technische universität
dortmund

Arbeit zur Erlangung des akademischen Grades
eines
Doktor der Naturwissenschaften
(Doktor rerum naturalium)

Bad Moon Rising?

Studies on the Performance of the First G-APD Cherenkov Telescope under Bright Light Conditions using SiPMs for Gamma-Ray Observations

Jens Björn Buß

geboren in Hagen-Haspe

2020

Lehrstuhl für Experimentelle Physik V
Fakultät Physik
Technische Universität Dortmund

Erstgutachter:	Prof. Dr. Dr. Wolfgang Rhode
Zweitgutachter:	Prof. Dr. Bernhard Spaan
Abgabedatum:	7. Juli 2020

The First G-APD Cherenkov Telescope (FACT) during observations in a full Moon night six month after its first light.

Kurzfassung

Diese Dissertation präsentiert eine Studie über den Einfluss des Nachthimmelhintergrunds (NSB) auf die Leistungsfähigkeit des First G-APD Cherenkov Telescope (FACT), welches das erste abbildende atmosphärische Cherenkov-Teleskop (IACT) mit einer Silizium-Photomultiplier-Kamera (SiPM-Kamera) ist. Der bisherige Stand der Technik, photomultiplier tubes (PMTs), kann durch helles Mondlicht sehr leicht schwer beschädigt werden. SiPMs sind ein alternativer robuster Detektortyp für imaging atmospheric Cherenkov telescopes (IACTs), der eine Maximierung der Beobachtungszeit durch Ausdehnung auf extreme NSB-Bedingungen ermöglicht, z. B. direktes Vollmondlicht. Die Leistungsfähigkeit wurde anhand von Beobachtungen des Krebsnebels aus dem Winter 2015/16 für alle beobachteten NSB-Niveaus bestimmt. Dedizierte Monte-Carlo-Simulationen wurden durch einen neuen Ansatz, der NSB-Messungen und simulierte ausgedehnte Luftschauer überlagert, auf die Lichtverhältnisse der Datensätze maßgeschneidert.

Die verwendete Analysekette verwendet maschinelle Lernverfahren sowie Entfaltungstechniken zur Rekonstruktion des Energiespektrums. Sie wurde im Laufe dieser Studie für verschiedene NSB-Werte optimiert. Die dedizierten Monte-Carlo-Simulationen werden verwendet, um maschinelle Lernverfahren zu trainieren sowie um deren Leistungsfähigkeit in Abhängigkeit vom NSB zu bewerten. In Vorbereitung auf diese Analyse musste ein Verfahren zur Auswahl optimaler Reinigungsstufen für die beobachteten Lichtverhältnisse verbessert werden, wie in dieser Arbeit vorgestellt wird. Mit diesen Verbesserungen werden die typischen Leistungskennzahlen für ein IACT evaluiert. Bis hin zu einem NSB-Niveau, das zwölfmal heller ist als die dunkelsten Nächte, wurde der Krebsnebel mit Signifikanzen von $\approx \frac{5\,\sigma}{\sqrt{h}}$ detektiert. Bei noch höheren NSB-Niveaus konnte die Quelle noch mit einer Signifikanz von $\approx \frac{3.4\,\sigma}{\sqrt{h}}$ nachgewiesen werden. Die zugehörigen NSB-Werte entsprechen dem direkten Mondlicht bei 60 % Mondphase. Darüber hinaus hat sich gezeigt, dass die integrale Sensitivität von FACT mit dem NSB-Niveau von 10 % auf 20 % des Krebsflusses abfällt, der für einen Nachweis mit $5\,\sigma$ Signifikanz in 50 h effektiver Beobachtungszeit notwendig ist. Die Hauptwirkung eines steigenden NSBs wurde als Anstieg der unteren Energieschwelle identifiziert, was sich auch in einer verschobenen Niedrigenergiekante der effektiven Sammelfläche sowie deren genereller Abnahme mit dem NSB äußert. Das Energiespektrum des Krebsnebels wurde in einem Energiebereich von 450 GeV bis 30 TeV für verschiedene NSB-Pegel erfolgreich rekonstruiert, bis hin zu den oben genannten Lichtverhältnissen. Entsprechend der ansteigenden Energieschwelle musste der untere Rand des entfalteten Energiebereichs auf bis zu 600 GeV erhöht werden, um das Energiespektrum bei höheren NSB-Pegeln zu entfalten. Abgesehen von den oben erwähnten Befunden wurden keine signifikanten Hinweise auf systematische Effekte hinsichtlich der entfalteten Spektren gefunden. Diese Arbeit zeigt überdies, dass die Spektren mit diesen Anpassungen weiterhin in guter Übereinstimmung miteinander und auch mit Referenzspektren von MAGIC und FACT sind.

Zusammenfassend zeigen die Leistungswerte vielversprechende Ergebnisse für Beobachtungen mit FACT bei erhöhten NSB-Pegeln. Sie unterstreichen die Verwendung von SIPMs als eine potenzielle Alternative zu anderen Ansätzen zur Ausdehnung der IACT-Beobachtungszeiten auf helle Lichtverhältnisse.

Abstract

This dissertation presents a study on the influence of the night sky background (NSB) on the performance of the First G-APD Cherenkov Telescope (FACT), which is the first imaging atmospheric Cherenkov telescope (IACT) with a silicon photomultiplier (SiPM) camera. The up till now state-of-the-art, photomultiplier tubes (PMTs), can be easily and severely damaged by bright moonlight. SiPMs are an alternative robust photon detector for IACTs allowing for maximization of observation time by extending towards extreme NSB conditions, e.g., direct full moonlight. The performance has been determined on observations of the Crab Nebula from winter 2015/16 for all observed NSB levels. Dedicated Monte Carlo simulations have been tailored to the light conditions of the data sets by a new approach superimposing NSB measurements and simulated extensive air showers.

The used analysis chain features machine-learning and unfolding techniques to reconstruct the energy spectrum and has been optimized in the course of this study for various NSB levels. The dedicated Monte Carlo simulations are used to train machine-learning models and allow for evaluation of their performance and dependency on the NSB. In preparation for this analysis, a procedure to select optimum cleaning levels for the observed light conditions needed to be improved as introduced in this thesis. With these enhancements, the typical performance metrics for an IACT are evaluated. The Crab Nebula has been detected with significances of $\approx \frac{5\,\sigma}{\sqrt{h}}$ up to an NSB level twelve times brighter than the darkest nights. At even higher NSB level, the source could still be detected with a significance of $\approx \frac{3.4\,\sigma}{\sqrt{h}}$ at NSB levels corresponding to direct moonlight at a 60 % lunar phase. Furthermore, it has been shown that the integral sensitivity of FACT degrades with the NSB level from 10 % to 20 % of the Crab flux necessary for detection with $5\,\sigma$ significance in 50 h effective observation time. The main effect of rising NSB has been identified as an increase of the energy threshold, which has also been evident in a shifted low-energy edge of the effective collection area as well as its general decline with the NSB. The Crab Nebula energy spectrum has been successfully reconstructed in an energy range of 450 GeV to 30 TeV for various NSB levels up to these light conditions. According to the rising energy threshold, the lower edge of the unfolded energy range had to be increased up to 600 GeV in order to unfold the energy spectrum at higher NSB levels. Other than the above-mentioned findings, no significant indication for systematic effects on the unfolded spectra have been found. This work shows furthermore that with these adjustments the spectra are still in good agreement with each other and also with reference spectra from MAGIC and First G-APD Cherenkov Telescope (FACT).

In summary, the performance values show promising results for observations with FACT at increased NSB levels. They underline the use of SiPMs as a potential alternative to other approaches for extending IACT observation times to bright light conditions.

for Karina, Liane and Hedda
your light shines brighter than anything else!

Contents

1 Introduction

Over the course of the last three decades, ground-based gamma ray astronomy with imaging atmospheric Cherenkov telescopes (IACTs) has evolved into the established channel to observe the VHE (very high energy)[1] gamma sky. Typically, the detected radiation comes from sources like supernova remnants (SNRs) and active galactic nuclei (AGNs). The goal of these measurements is to determine the properties of these sources and in particular the origin of the emitted radiation. Generally, a very dense central source, i.a., a neutron star or a (supermassive) black hole is the central machine for the emission processes. The variability and energy distribution of the emitted radiation especially is key information of the sources since they provide insight about the emission and acceleration processes in these objects.

In support of this, the detection of their radiation requires sensitive instruments that provide a decent amount of high-quality data in a short amount of time. Additionally, reliable and gapless measurements are crucial to determining the time-dependent component of the emissions from the observed sources, as flux variabilities were measured even at scales of a few minutes. Moreover, monitoring with minimized outages increases the probability for overlap with observations of other experiments, which provides for inherent Multi-wavelength and Multi-messenger observations [31, 99].

Nevertheless, the visibility of the sources and the environmental conditions of an IACT restrict the effective observation time heavily. Bad weather and increased ambient light conditions are the main causes of gaps in their observation schedule since the IACT technique uses the Earth's atmosphere as detector volume in which extensive air showers are measured indirectly via their Cherenkov light. Accordingly, measurements have to be optimized, in order to minimize these gaps and render the data sample as dense as possible.

Ever since the first detection of the Crab Nebula above 0.7 TeV by the Whipple 10 m telescope [68] in 1989, IACTs have improved massively in precession, sensitivity, efficiency and robustness. However, in particular, the robustness of the photon detectors used to measure the Cherenkov light is the major limiting factor to the observation time.

[1] The electro-magnetic spectrum in the range of 100 GeV to 100 TeV.

Conventionally, photomultiplier tubes (PMTs) are used for this task. Unfortunately, while being very sensitive to the faint Cherenkov flashes, these devices are easily damaged by high luminosities of background light. Moreover, these devices suffer from accelerated aging when exposed to a high light yield [8, 14]. This has the drawback that observations with such devices are generally restricted to conditions with low ambient light. Consequently, theses limitations cause gaps in the observation schedule and decrease the potential duty cycle of an IACT. The application of specialized, low-gain PMTs and UV filters allows for an extension to brighter light conditions [75].

In recent years, improvements in the development of solid-state photon detectors, so-called silicon photomultipliers (SiPMs), emerged as a possible alternative to this field of conflict. These devices are known to be very robust for a large light yield [86]. The First G-APD Cherenkov Telescope (FACT) was designed to assess and (finally) prove the applicability of this novel sensor approach to IACTs. Since October 2011, it has been pioneering the field of ground-based gamma ray astronomy with the first camera equipped and operating with SiPMs. Their use allows FACT to expand its duty cycle even to bright full moon nights with neither danger of damaging its photon detectors nor the need of filters. No indication of aging of the SiPMs has been found so far.

Consequently, this technology appears as a promissing solution to extend IACT observations to conditions of high night sky background (NSB) luminosities. Nevertheless, this also demands a deeper understanding of the properties of an instrument equipped with such devices. Especially FACT's performance at high NSB levels is relevant with regard to the quality of data and benefit in observation time. Moreover, the lifespan of the SiPMs used under such harsh conditions in the field has to be evaluated.

This thesis aims to determine the performance of FACT with respect to the influence of NSB going up to the conditions of full Moon nights. To achieve this goal, an analysis of data from observations of the Crab Nebula, taken in winter 2015/16, is carried out. Dedicated simulations of extensive air showers in the presence of a variety of NSB levels are produced and used to optimize the analysis for the different light conditions. Moreover, these simulations are used to train machine-learning models for high-level parametrization of properties of the primary gamma rays.

Based on these optimizations, both data and simulations are used to provide typical performance measures, e.g., the analysis' sensitivity for detection of a gamma-ray source, the systems' spectral acceptance, its angular resolution, or the energy threshold. Finally, the Crab Nebula's energy spectrum is derived and compared to reference spectra. In order to determine the NSB's influence, these studies are carried out for several NSB conditions and compared with each other.

In order to achieve the defined goals, this thesis is structured as follows:

Chapter 2 – Earth-Bound Gamma-Ray Astronomy summarizes the astro- and particle physics that the FACT experiment aims to investigate. The sources of the detected gamma rays are addressed briefly and the topic of monitoring AGNs is touched upon in order to motivate the maximization of observation time by extending observations to bright light conditions. Furthermore, the formation of extensive air showers in the Earth's atmosphere is discussed in context with the detection of their secondary radiation with an IACT. Related work from studies on past and current IACTs on the topic of bright NSB conditions is summarized briefly.

Chapter 3 – The FACT Experiment addresses the IACT at the foundation of the presented thesis. The telescope and its camera are presented, with a focus on the components that influence or are influenced by increasing levels of the NSB. Special focus is placed on the novel solid-state photon detectors, the SiPMs, which allow for a larger light yield than the conventionally used PMTs. The various ambient light conditions, at which FACT has been operated since 2011, are put in context with the presence of the Moon in order to define an NSB unit, used to interpret light conditions in this thesis and to structure the observations accordingly.

Chapter 4 – Analysis Chain and Applied Methods presents the analysis methods and tools necessary to perform the presented analysis. It further introduces typical metrics and parametrizations used by the machine-learning and the astroparticle community to measure the performance of their methods, analyses and experiments.

Chapter 5 – Selection of Data and Generation of Monte Carlo Simulations defines the datasets, their structure and conditions as used to carry out the presented performance study on observations of the Crab Nebula at different levels of the NSB. Furthermore, the generation of dedicated Monte Carlo simulation (MC) simulations for these light conditions is presented. These simulations are necessary to train the machine-learning models needed for the analysis of the data. Both, data and MCs, are the foundation on which to determine the performance of FACT.

Chapter 6 – Analysis Optimizations at Various Light Conditions explains how the analysis was optimized to the different light conditions. A new method to select appropriate cleaning levels is introduced. This method is necessary to adapt the analysis to these light conditions and to achieve a maximized performance.

Chapter 7 – NSB Performance presents the results of this study and, thus, the performance of FACT at increasing ambient light conditions, as an example of an IACT with SiPMs. These are the typical performance measures to assess the capability of FACT to determine the core information of detected gamma rays, i.e., rejection of background events and selection of gamma events with high probability, reconstruction of their energy and their spatial origin. Finally, energy spectra of the observed Crab Nebula are presented for the NSB samples.

Chapter 8 – Final Conclusion and Future Prospects contains the final discussion of the presented results of the performance study. Conclusions are drawn with regard to the performance at different light conditions and the benefit of extending observations there. Potential improvements to this work for future studies are outlined.

2 Earth-Bound Gamma-Ray Astronomy

This thesis aims to determine the performance of the FACT telescope to detect gamma rays at increased levels of background light. The origins of these gamma rays are galactic and intergalactic sources like, e.g., SNRs and AGNs. This chapter provides a short introduction to these sources and the physics involved to detect gamma rays that generate extensive air showers. The source under scrutiny in this thesis, namely the Crab Nebula, is briefly introduced. Furthermore, this chapter describes the working principle of the IACT technique to measure this radiation by use of the Earth's atmosphere, as well as the formation of the extensive air showers. The constraints of this method are discussed with respect to restrictions on a data analysis when conducting such measurements . Possible background phenomena are therefore outlined, e.g., Hadrons and photons from the night sky background (NSB).

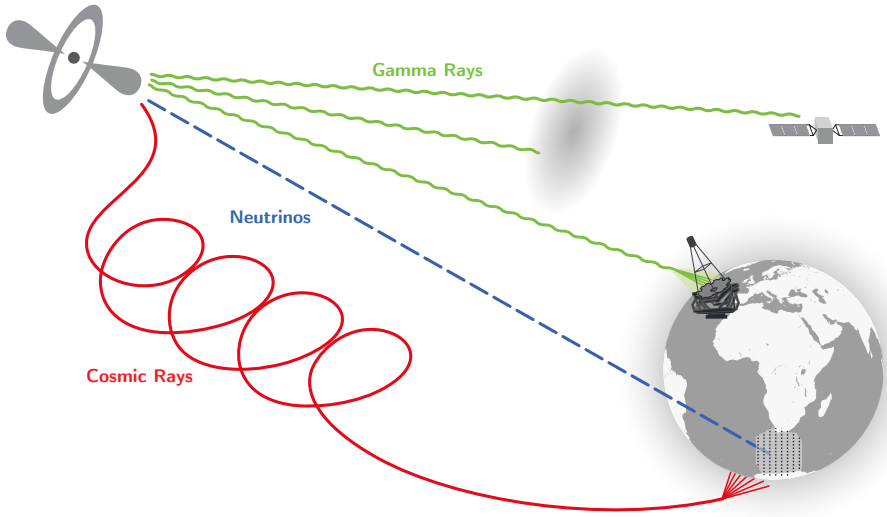

Figure 2.1: Overview of cosmic messenger particles in astroparticle physics and their propagation towards planet Earth (*image source:* [48]). The origin of gamma rays and neutrinos can be localized to the source of radiation, while charged particles in cosmic rays, like protons, are deflected by inter-galactic magnetic fields. The lines indicate an example of each messenger particle's trajectory when detected on planet Earth. The coloring of lines represents the particle types.

2.1 Multi-Messenger Astroparticle Physics

Every second, planet Earth is hit by a plethora of particles with inter- and extra-galactic origin. When detected, these particles reveal information about their source, their distribution in space, or interactions on their way. Figure 2.1 shows a sketch of the propagation of key messenger particles from a given source to planet Earth. SNRs and AGNs are among the sources that form the origins of these messenger particles.

AGNs emit large amounts of radiation driven by their central machine, i.e., an accreting super massive black hole. Due to the accretion, a hot plasma is ejected in the form of two relativistic jets, that emit radiation, back to back, and perpendicular to the accretion disk of the black hole. The subclass of Blazars is distinguished by the orientation of their jets which pointing in a direct line towards planet Earth (or away from it respectively). Their power output is dominated by non-thermal radiation and they belong to the most energetic particle accelerators in the universe. As such, a variety of messenger particles from these sources arrive at planet Earth [88].

The spectral energy distribution (SED) of photons from Blazars covers the entire electromagnetic spectrum and is characterized by the typical "double humped" shape. Thus, simultaneous multi-wavelength observations of experiments in the different energy ranges of the SED are of the utmost interest. The low-energy component (IR to X-ray) is generally believed to derive from the synchrotron radiation of electrons in moving magnetic fields, whereas the origin of the high-energy component of the SED (gamma rays) is under debate [73, 88]. There are mainly two competing models: a leptonic and a hadronic model. The leptonic models explain gamma ray emission with inverse Compton scattering of electrons in the jet with a photon field, i.e., either their own synchrotron emission or an external photon field [88]. However, hadronic models consider high-energy protons as the gamma ray's origin. Here gamma rays are produced by synchrotron radiation of the hadrons [3] or in photo-meson interactions (π_0 decay) [77]. In the latter case, a Blazar would also emit neutrinos [88]. Accordingly, finding neutrino counterparts to gamma ray emitters allows for a deeper understanding of the acceleration processes, which motivates multi-messenger observations and long-term monitoring of AGNs [31].

Neutrinos, for instance, are produced in hadronic processes and have the capacity of showing low interaction probabilities with fields or matter on their way [106]. This has the advantage, that the direction of their source is conserved in their trajectory (see figure 2.1, blue dashed line). Due to their low interaction probability, however, they pose the challenge that their detection requires large detector volumes, e.g., realized with the IceCube Neutrino Observatory (IceCube) [106].

Figure 2.2: A composite image of the Crab Nebula showing X-ray in blue, optical in green, and radio in red [35].

Gamma rays, on the other hand, are easier to detect. Further, their directional information is conserved in their trajectory, since they are not deflected by magnetic fields (see figure 2.1, green wavy lines). However, they may be absorbed by interstellar dust clouds or in interactions with the extra-galactic background light (EBL) [44, 88]. Once they arrive at Earth, they can either be detected directly with satellites in the orbit or they are measured indirectly via extensive air showers, which they produce in the atmosphere.

Nevertheless, charged particles, such as protons and other hadrons, also produce air showers when they enter the Earth's atmosphere. Unfortunately, these cosmic rays are deflected by magnetic fields. The directions of their trajectories cannot be matched with a specific source. Accordingly, they are detected as an isotropic background to the gamma rays. Moreover, the flux of cosmic rays outnumbers the flux of gamma rays by several magnitudes, in particular 10^3 to 10^4 times more cosmic rays in the VHE regime [5, 65, 105]. This makes sophisticated background rejection algorithms necessary to filter for gamma rays from an observed source.

In addition to AGNs, the class of SNRs forms a group of galactic gamma-ray sources. Especially the subclass of pulsar wind nebulae (PWNs) contains the largest population emitting radiation at TeV energies [65, 96]. Among them, the Crab Nebula, which was formed in the supernova of 1054 CE, is the brightest known gamma-ray source. At its center is a pulsar, a rapidly rotating neutron star with

a strong magnetic field. Figure 2.2 shows a composite image of the Crab Nebula, compiled from measurements at radio, optical, and X-ray wavelengths.

The generation of gamma rays is well explained by *inverse Compton* scattering of relativistic particles in the shocked wind and their self-emitted synchrotron photons in the magnetic field of the pulsar [52]. Crab is known to provide a (mostly)[1] steady VHE emission and, furthermore, the highest known gamma ray flux [66]. It is thus known as the "standard candle" of ground-based gamma ray astronomy and is widely used as a calibration source for the IACT community [40, 41].

2.2 Air Showers

Once the primary radiation from the previously mentioned sources enters the Earth's atmosphere, the primary particles interact with the present atoms. In the case of both gammas and hadrons, an extensive air shower is initiated that evolves in a forward direction deeper into the atmosphere. The schematic development of these two types of air showers is illustrated in figure 2.3. Depending on the primary particle, different physical processes are involved, which define the properties and appearance of the air showers.

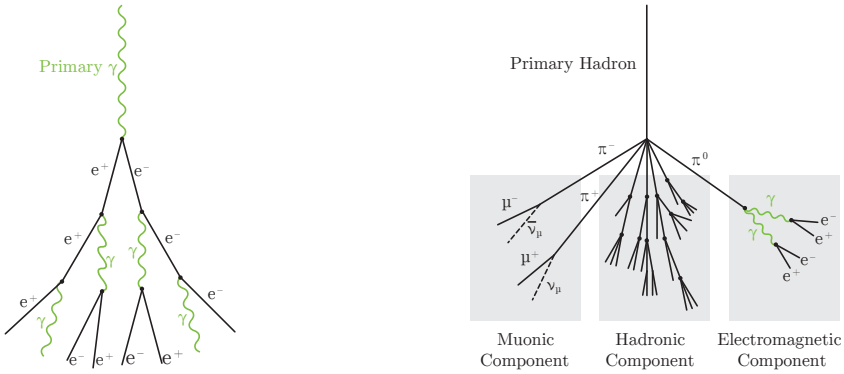

(a) Gamma shower **(b)** Hadron shower

Figure 2.3: Schematic development of air showers from a gamma ray (a) and a cosmic ray (b). The processes in a gamma shower are dominated by a cascade of pair production and bremsstrahlung. Hadronic showers undergo a variety of interactions, which can be divided into three components: a hadronic component, a muonic and an electromagnetic component. The latter two derive from pion decays (*image source:* [48]).

[1] At energies below ~1 GeV, multiple day-scale flaring events have been detected, but so far none in VHE, which is not necessarily in conflict with future findings [66].

2.2.1 Air Showers from Gamma rays

At an altitude of about 20 km above sea level (a.s.l.), incoming gamma rays initiate an extensive air shower by *pair production*. As a result, an electron-positron pair is emitted in a forward direction and conserves the energy of the primary γ particle. These particles interact with air molecules and again produce high-energy photons via *bremsstrahlung*. This process is repeated in a cascade of multiple bremsstrahlung/pair-production processes until the energy of secondary particles is to low for these interactions. The electromagnetic cascade is illustrated in figure 2.3a. In the case of electrons, positrons and photons, the cascade is tightly bunched along the projection of the trajectory of the initial gamma ray. The direction of a gamma ray's origin is thus reconstructable from the trajectory of the electromagnetic air shower [105].

In this process the large kinetic energies of primary and secondary particles yield velocities ($\sim 1\, c_0$) beyond the phase velocity in the atmosphere. In this case, Cherenkov radiation is emitted. Accordingly, each secondary particle produces a column of Cherenkov light in a forward direction. Thus, the air showers are visible by their pool of Cherenkov light, and its brightness is proportional to the energy of the primary particle. The schematics of this light pool are shown in figure 2.4 [105].

2.2.2 Air Showers from Cosmic rays

Cosmic rays also interact with the atmosphere and produce air showers similar to those of gamma rays. Among their primaries are all sorts of ions. The majority are protons (>80 %), followed by helium ions (~10 %). The interactions involved are illustrated in figure 2.3b [69]. Compared to gamma rays, a larger variety of interactions occur which can be subdivided into three main components: (i) a muonic, (ii) an electromagnetic, and (iii) a hadronic component. The first two are the result of pion decays, whereas the last produces a cascade of secondary hadrons. Similar to gamma rays these processes repeat until the available energy per secondary is too low for, e.g., pion generation [69, 105].

Again, Cherenkov radiation is emitted due to the high velocities of the particles. However, the hadronic cascade is wider and more scattered than the electromagnetic cascade, and secondary products show larger angles of emission. The Cherenkov light distribution is thus also broader, with a wider time spread [105].

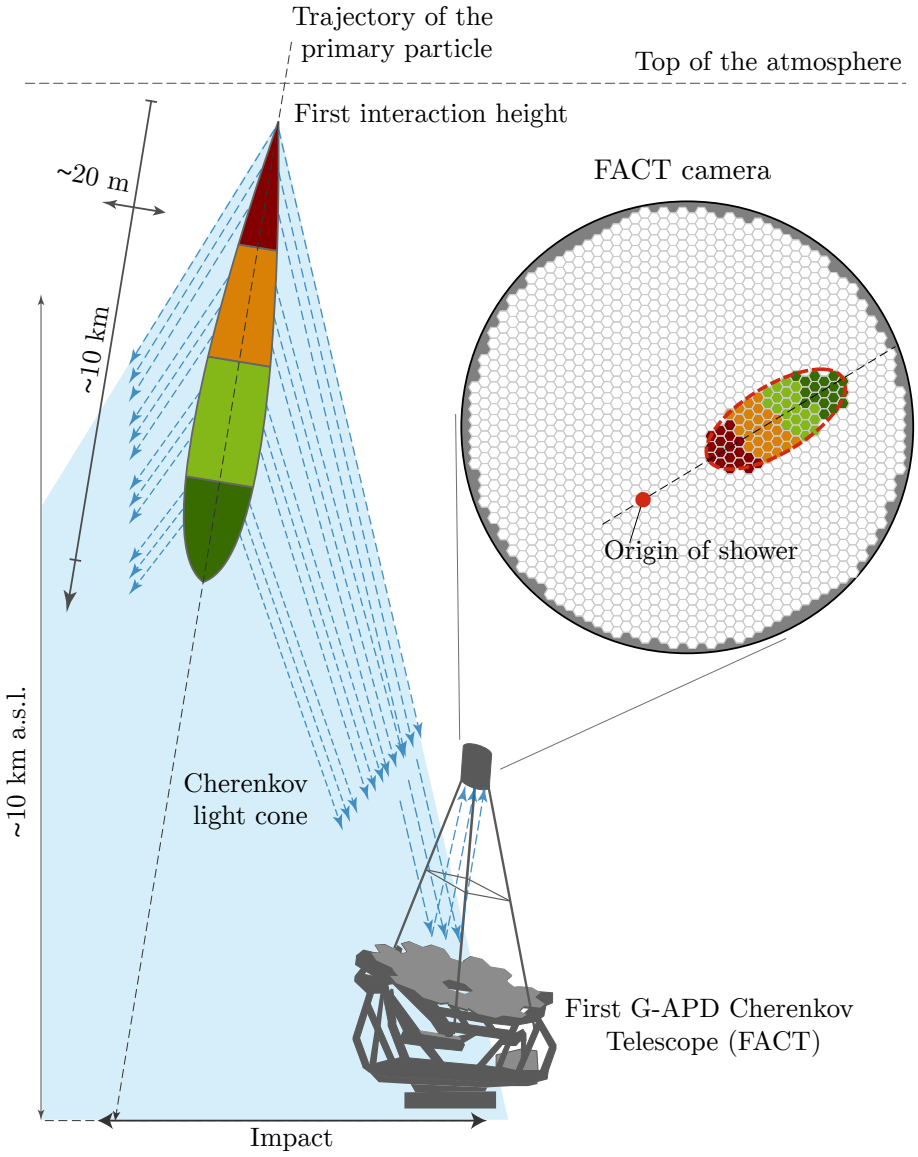

Figure 2.4: Illustration of the working principle of an IACT that is detecting Cherenkov photons form an extended air shower with about 1 TeV energy in the atmosphere. Cherenkov light of secondary particles is emitted in a light cone with the opening heading towards the direction of the primary particle. The light is reflected into the camera plane and produces a 2D projection of the showers Cherenkov light as visible in the pixels of the camera on the right-hand side. The coloring indicates the spatio-temporal structure of the air shower and the projected image in the camera. The coordinate system parallel to the trajectory of the primary particle (dashed line) indicates the typical dimensions of an electromagnetic shower. The typical height of the main emission regions is roughly at $(6-10)$ km, depending on the primary particle, energy, and atmospheric density.

2.3 The IACT Technique

Extensive air showers, as discussed in the previous section, produce a Cherenkov light cone in a forward direction of its trajectory. Cherenkov radiation is emitted by the secondaries in a light cone with a maximum emission angle, which depends on the atmospheric depth [69]. Typically, the produced light pool of a shower has a radius of $\approx 120\,\mathrm{m}$ [105].

An IACT, when placed inside this radius, is able to detect the air shower as a 2D projection in the plane of its multi-pixel camera. Figure 2.4 visualizes the detection of an extensive air shower. The general structure of an IACT is simple. The basic components are: (i) a (segmented) reflector and (ii) a (pixelized) camera in the focal plane. With this, the Cherenkov photons are projected by the mirrors in the camera plane. In this projection, the extensive air shower appears roughly as an ellipse with its semi-major axis pointing to the showers origin [4].

From this image the key information of a gamma ray are deduced [4]:

I. the origin of the gamma ray correlates with the orientation of the ellipsis,

II. the total energy of the primary particle correlates with the total intensity of the collected Cherenkov photons, and

III. different particle types of the primaries, mainly gammas and hadrons, are distinguished by the morphology of the light distribution of the Cherenkov photons.

Since the atmosphere is used as a calorimeter by the IACT technique, the detection principle relies heavily on atmospheric conditions, i.a., temperature, pressure, humidity, and cloud coverage. Unfortunately, gamma ray astronomers have no control over these. Monitoring of the atmospheric conditions is therefore necessary in order to discard troublesome data in the analysis or use tailored MC simulations for the observed conditions [105].

The presence of light from the NSB has an especially large influence on the detection of extensive air showers, because not only Cherenkov photons are reflected into the focal plane. A variety of natural and artificial sources emit photons into the night sky. While artificial sources, e.g., satellites, airplanes, beacons, and city lights can often be minimized by the choice of the telescope's location[2], the natural causes are mostly inevitable [105]. Typical natural sources are, e.g., (i) the Sun, (ii) the Moon, (iii) direct light from stars and the Milky Way, (iv) diffuse stellar light scattered

[2] On La Palma the light pollution is minimized by law since it is the location of the European Northern Observatory.

in the atmosphere, (v) direct and reflected moonlight, (vi) scattered light from the rising or dawning Moon, (vii) airglow, (viii) and the Zodiacal light [15, 79, 91]. Furthermore, the intensity and influence of these light sources is strongly influenced by the conditions in the atmosphere, e.g., the presence of clouds, haze, and Calima, since these effects scatter the present photons [32]. The involved sources of NSB are schematically illustrated in figure 2.5.

Unfortunately, photons from these processes enter the camera either directly or reflected by the IACT's mirrors. This creates a spatial and temporal uniform background over all pixels, or may even appear as a group of pixels with a higher background, if, e.g., a star is in the field of view [105].

Depending on the NSB level, the energy threshold of detectable air showers is, thence, shifted towards larger values since the Cherenkov light can only be identified if it is brighter than the background. Obviously, this is not the case for fainter, low-energy showers. Accordingly, this limits the sensitivity of an IACT to the present light conditions [105]. For this reason, for a long time, observations were only possible in the absence of moonlight [69].

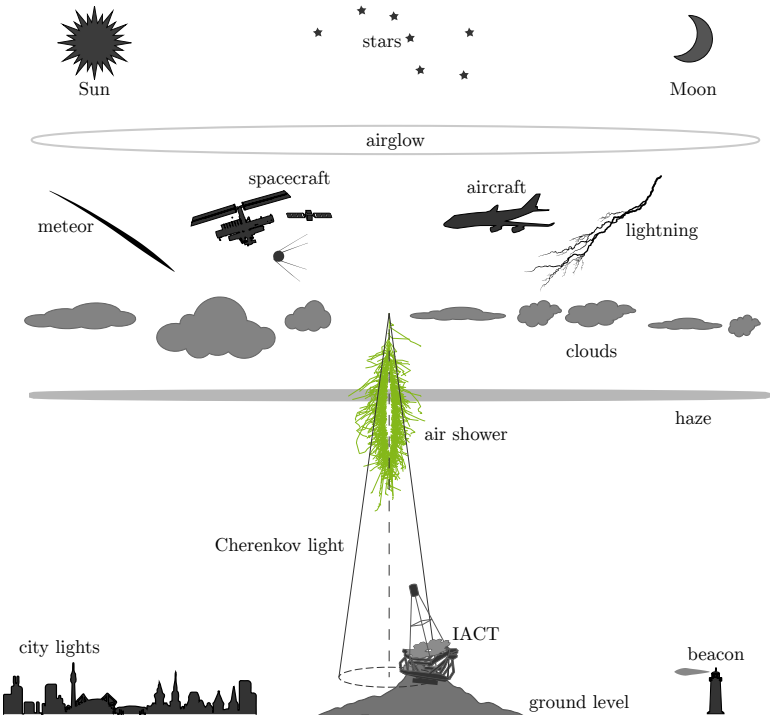

Figure 2.5: Illustration of potential light sources contributing to the NSB, which introduces a photonic background to observations with an IACT (*inspired by:* [105]).

2.4 Observations with IACTs at Bright Light Conditions

In the previous section, limits to an IACT's duty cycle due to bright ambient light have been addressed. Many of the past and present experiments thus have been aiming to extend their observations to increased NSB levels up to observations with moonlight. However, bright light conditions can severely damage PMTs, which have been the state-of-the-art devices in the gamma-ray community. Accordingly, most of the experiments focus on solutions to protect their PMTs from bright light. A good overview of different approaches to this issue is presented in [14]. A summary of these issues and a categorisation of the approach chosen by FACT is given in the following.

2.4.1 Approaches to Extending Observations to Bright Moonlight

The approaches for operating an IACT at bright ambient light can be divided into three main categories:

I Lowering of the PMT's gain,

II Optical filtering of NSB-dominated wavelengths,

III Alternative detector technologies, e.g., SiPMs.

Figure 2.6 shows the spectral acceptance of examples for these approaches in relation to the spectrum of Cherenkov light from a 1 TeV shower and NSB of different intensities. The approaches are discussed in more detail in the following.

Lowering of the PMT's gain aims to diminish the damage to the dynodes and aging of a PMT. Hence, the gain is lowered either with a reduced voltage at the high voltage supply (HV) of the PMTs, special low-gain PMTs, or a combination of both. In all three cases, aging of the sensors remains a general problem, compensated by occasionally increasing the HV to stabilize the gain. The reduced voltage approach was pioneered by the HEGRA Collaboration [71] and is used by MAGIC [8, 75] and VERITAS [14]. However, it has the disadvantage of signal-to-noise ratios increasing with the NSB level, due to contributions from the NSB (see fig. 2.6, grey and black dashed lines), which reduce the effective collection area of an IACT [14]. In progression from this approach, MAGIC uses low-gain PMTs., which allow for operation under moderate moonlight without lowering the HV, or, in combination with lowered HV, at even brighter light conditions [75].

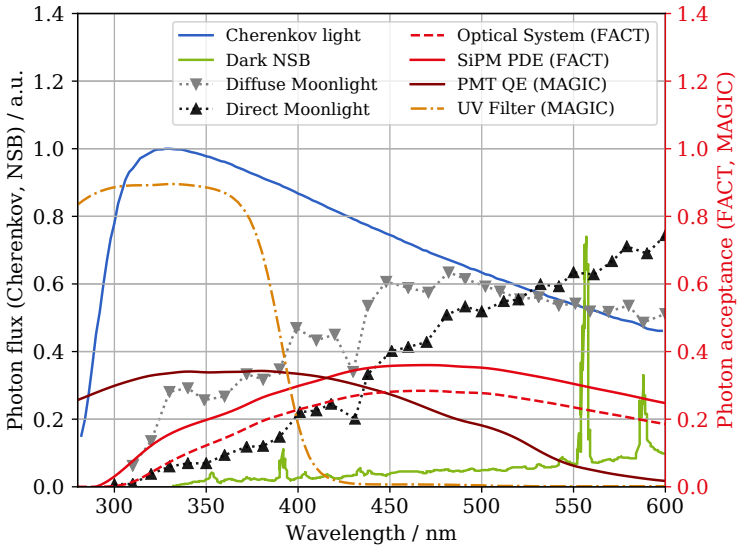

Figure 2.6: Spectra of the two main light phenomena (NSB and Cherenkov photons) detected by an IACT in the context of the spectral efficiencies of photon detector components (SiPMs [13], PMTs [8], and UV filters [8]). A spline interpolation of the Cherenkov light spectrum for a vertical, 1 TeV gamma-ray shower detected at an altitude of 2200 m a.s.l. is marked in blue [8, 46]. NSB spectra are shown for the darkest light conditions measured on La Palma (green line) [15], diffuse (grey dotted line) and direct moonlight (black dotted line) [8, 56, 57]. These curves are scaled by arbitrary normalization factors with the ordinate on the left hand side. Spline interpolations of photon acceptances of the photon detector components is given for FACT's optical system (dashed red line), its SiPMs' PDE (solid red line), MAGIC's PMT quantum efficiency (QE) (solid brown line), and the transmission of MAGIC's UV filters (dotted dashed orange line). The values of these four acceptances are given on the ordinate on the right hand side. The abscissa represents the wavelength dependency of the illustrated light spectra and component's acceptances. It is evident that the photon acceptance of FACT's SiPMs is less optimal than MAGIC's PMTs with regard to light spectra of both Cherenkov light and NSB.

Optical filtering of NSB-dominated wavelengths mainly comprises the use of UV filters to modify the wavelength-dependent acceptance of the optical system. For this purpose, filters with low/no transmission above 400 nm cover the PMTs to block the intensive parts of the NSB light spectrum. This approach has the advantage of improving the signal-to-noise ratio for high NSB compared to the reduced voltage method. However, it requires mantling and dismantling the UV filter [8, 14]. The Whipple Collaboration pioneered this approach and demonstrated

operation under moderate moonlight with a combination of solar-blind PMTs and a liquid UV filter [42, 43, 104]. Currently, UV filters are used by both the MAGIC and the VERITAS Collaboration for severe moonlight (~80 %). MAGIC in particular is using them to extend observations to full Moon nights [8, 14].

Alternative detector technologies aim to devices that fulfill the requirements for an IACT but are not/less impaired by a large light yield. Solid-state detectors, i.e., SiPMs, neither show signs of aging, nor are they damaged by a large light yield, which is a clear advantage for high NSB observations [13]. This allows for operations during all NSB levels and even direct light from the full Moon, as demonstrated by the FACT Collaboration [70]. Unfortunately, for SiPMs the spectral acceptance is still an issue with regard to the spectrum of the ambient light, as their peak PDE is roughly at 400 nm. However, current developments of SiPMs are improving towards near UV sensitivity, as presented, e.g., in [12, 59, 98].

In the case of FACT, a commercially available SiPM has been used, which has its peak PDE at ~440 nm, and is thus sensitive to large fractions of the NSB spectrum [13, 17]. It is therefore to be expected that the signal-to-noise ratio degrades with increased light conditions and, thus, energy threshold and effective collection area [14].

2.4.2 Impact on Analysis Results

The impact of high NSB data to the analysis of an IACT, as presented by the experiments above, is outlined briefly in the following. In general, these experiments agree that the energy threshold is increasing with the NSB, which is resulting in the effect of a declining sensitivity and effective collection area[3]. They claim that the factor of this effect is determined by the used hardware modifications (reduced HV and UV filters) and by the chosen analysis settings (mainly image cleaning levels), which have to be optimized for each cleaning/hardware setting.

Increasing the Energy Threshold The factor at which the energy threshold increases with the NSB depends on the hardware trigger and the settings of image cleaning and parameter cuts. Optimizing the analysis (cleaning levels and cuts) for different NSB bins allows a minimal energy threshold. Additionally, MAGIC and VERITAS state that the reduction of the energy threshold is more striking due to hardware modifications (reduced HV and UV filters) than for increasing NSB at nominal voltage. This effect is most prominent for the UV filter approach [8, 14, 71, 101].

[3] Details of these performance parametrizations are given in Chapter 4

Reduced Effective Collection Area VERITAS and MAGIC report on a decline of the effective collection area that is most prominent at energies below 1 TeV due to the energy threshold effect. Above this energy the effective areas appear almost unaffected [8, 14].

Reduced Sensitivity A lower sensitivity at increased moderate moonlight has already been stated by Whipple [42]. MAGIC and VERITAS account for a decline in sensitivity depending on a NSB/hardware modification, which is most prominent when utilizing UV filters (VERITAS ~50 % and MAGIC ~(60 – 80) %) [8, 14].

Distorted Image Parametrisations of Fainter Showers MAGIC claims that, above a Cherenkov light yield of 200 p.e., image parametrizations do not show differences for different light conditions. Below this level, these features are distorted [75]

Angular Resolution Whipple and VERITAS note that their angular resolution declines with the NSB [14, 101], whereas MAGIC states an angular resolution independent of the ambient light conditions [8].

Crab Detection Both HEGRA and Whipple already reported a lower significance of detection for Crab Nebula observations under moonlight conditions [71, 101]. HEGRA reported on generally higher background rates with reduced HV and over-estimated fluxes due to over-estimation of the effect of HV reduction [71]. More recently published results from VERITAS and MAGIC show that both experiments are able to detect Crab at elevated NSB levels. Furthermore, they state that the reconstructed spectra remain comparable over all studied illumination levels, given an optimized analysis. Additionally, MAGIC reported that fluxes are systematically underestimated when using only the standard analysis. Both claim an absence of significant additional systematics on the spectral slope [8, 14].

The feasibility of the SiPMs mentioned earlier for the detection of gamma rays at bright ambient light is subject to the work presented in the following chapters. With regard to the presented findings on the PMT approaches, the performance of FACT is investigated as an example for the SiPM approach. In preparation, FACT, its camera, and SiPMs are discussed in the next chapter.

3 The FACT Experiment

The First G-APD Cherenkov Telescope (FACT) is the first ever IACT equipped and operating with so-called silicon photomultipliers (SiPMs) aka Geiger-mode-Avalanche-Photo-Diodes (G-APDs). It has been pioneering the use of these semiconductor detectors in gamma ray astronomy since October 2011.

Figure 3.1: FACT in the morning after being placed in its in parking position. In the picture, the segmented mirror dish with its 30 hexagon shaped single mirrors is visible. The camera is located in a cylinder attached to four masts as seen on the right hand side of the picture.

In this chapter, the telescope and camera of FACT will be introduced. For this purpose, the properties and objectives of this instrument are presented. In particular, its speciality, the application of SiPMs to the IACT technique, is discussed in more detail. The sensor's detection principle is outlined briefly together with its advantages and the involved restrictions due to various noise phenomena in the sensor. The chapter will explain the exceptional robustness of these sensors and the consequent ability to observe at severe NSB conditions.

3.1 Introduction to FACT

FACT is a small IACT with a total mirror area of about 9.5 m^2 that was designed as a prototype to prove the concept of SiPMs in gamma-ray astronomy. It is also used as a monitoring experiment with the goal of gapless observations of TeV Blazars in the northern sky. Thus, it aims at a maximized duty cycle by, e.g., also operating at bright light conditions.

For this purpose, an old mount[1] of the former HEGRA telescope array was refurbished and equipped with a novel camera. The telescope is located at the Observatorio del Roque de los Muchachos on La Palma, Canary Islands, next to the MAGIC telescopes, at an altitude of ~2200 m above sea level. An overview of the properties of FACT is presented in table 3.1.

The telescope uses a segmented reflector with 30 hexagon-shaped single mirrors that have been aligned in *Davies-Cotton-parabola-hybrid* geometry since May 2014 [2]. Before, a pure *Davies-Cotton* geometry was used. A picture of the telescopes with a view on the mirrors is shown in figure 3.1. The mirrors are attached to the massive steel structure of the alt-azimuth mount of the former HEGRA CT3. Opposite the mirrors, the camera is mounted in the focal point of the reflector at a distance of ~4.9 m [13].

For the camera, a fully integrated concept was chosen, meaning that all readout electronics are contained in the camera housing. Only the high-voltage supplies are located in the counting house. More detail on the camera is given in section 3.2.

The front window of the camera has a diameter of 53 cm and consists of Polymethyl Methacrylate (PMMA), aka "plexiglass". It protects the light guides on which the SiPMs are glued, as shown in figure 3.4b. These light guides are solid PMMA cones with a hexagonal shape on the front side. Their purpose is to translate from the squared active detection area of the SiPMs to a hexagonal shape, which allows for a better distribution of the pixels for a round field-of-view (FOV). With this design, FACT has a FOV of 4.5°.

The camera has 1440 pixels that consist of one silicon photomultiplier (SiPM) each. These SiPMs are semi-conductor-based photon counting devices that comprise 3600 G-APDs in a squared active detection area of 3 mm × 3 mm. In section 3.3 these devices are discussed in more detail.

With the design presented above, FACT has been operating since 2011 on a nightly basis. Control has been carried out remotely from Central Europe for several years. This means that there is no crew on site except for staff visiting the island

[1] The mount of HEGRA Cherenkov telescope 3 (HEGRA CT3) was used.

occasionally for maintenance work. Regular operations are only interrupted during the three nights around full moon, for safety reasons since no MAGIC shift crew are present on site. However, due to the robustness of the SiPMs, observations are even possible under severe Moon light. This allows FACT to operate during full moon [70]. The duty cycle was thus more increasingly optimized over the past few years, resulting in some 95 % data-taking efficiency. The camera and the SiPMs are discussed in more detail in the next sections.

Properties	Value
Location	Observatorio del Roque de los Muchachos, La Palma, Canary Islands (Spain)
Altitude	2200 m a.s.l.
Mount	former HEGRA CT 3
First light	October 2011
Focal length	4.9 m
No. of mirrors	30
Total mirror area	9.5 m^2
Field-of-view (FOV)	4.5°
Camera diameter	53 cm
Camera weight	150 kg
Photon detector (pixel)	SiPM
No. of pixels	1440
No. of cells per pixel	3600 G-APDs
Light guides	solid Polymethyl Methacrylate (PMMA, “plexiglass”) cone
Trigger logic	Sum trigger: 160 trigger patches (sum of 9 pixels)
data acquisition (DAQ)	domino ring-sampling chip - type 4 (DRS4)
DAQ sampling frequency	2 G*samples*/s

Table 3.1: Overview of the properties of FACT.

3.2 The First G-APD Camera

After introducing FACT in the previous section, the camera and its electronics are discussed in this section in more detail. For a deeper insight into the camera electronics of FACT refer to [13, 102].

Figure 3.2a shows a picture of the camera with open housing during its assembly. One property of FACT's camera is that all readout electronics are fully integrated in the camera. Only the voltage supplies and the computing systems are in the *counting house*, which is a 20 ft intermodal container. These computers are used to control the telescope and store the data to hard disk drives. The camera's simplified schematics are illustrated in figure 3.2b. It shows the four main sections in which the camera electronics are structured: (i) sensor compartment, (ii) preamplifier boards, (iii) trigger system, (iv) and data acquisition system.

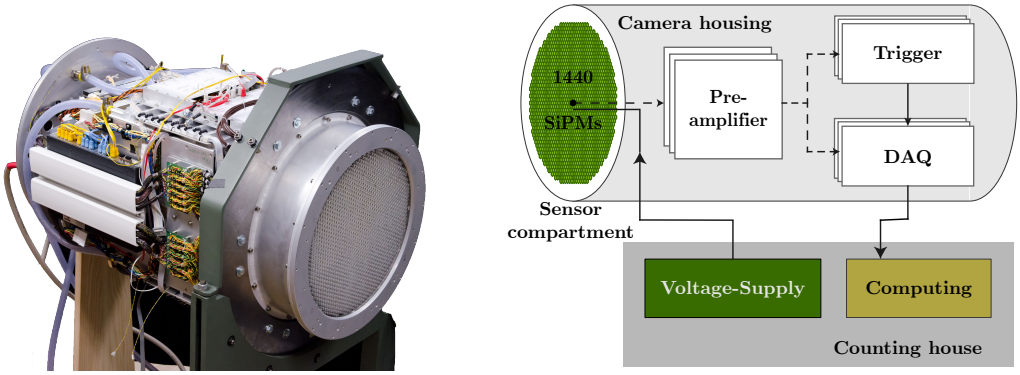

(a) FACT camera.

(b) Camera schematics.

Figure 3.2: Picture of the FACT Camera with open housing during its assembly (a) and simplified schematics of the main components of the camera (b). The only main components that are not integrated in the camera are the voltage supplies and computing resources (e.g., the data storage).

Cherenkov photons from extensive air showers and NSB photons enter the sensor compartment through the PMMA front window and light guides. They are detected in the SiPMs which are connected to the preamplifer boards. After the preamplifiers, the signal is split into a trigger and a read-out branch. In the latter, signals are constantly digitized, stored and overwritten in a ring buffer, waiting for a positive trigger decision. In the trigger branch the signal is modified and compared to a defined trigger threshold that, if exceeded, causes the signals in the ringbuffer to be stored to hard disk drives.

3.2.1 Sensor Compartment and Preamplifiers

The 1440 pixels are hosted in the sensor compartment. They are glued to the light guides and together they are placed on the front window in a hexagonal grid, forming an almost round camera plane, as visible in figure 3.3. A group of nine adjacent pixels is called a (trigger-)patch.

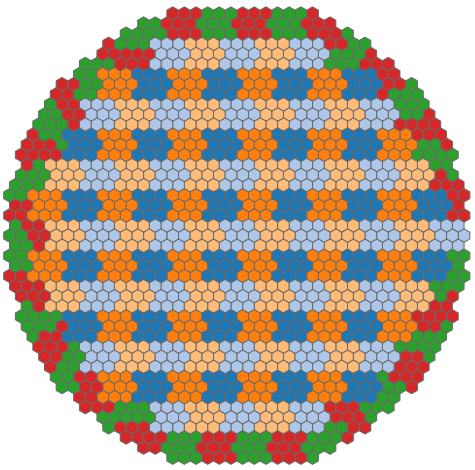

Figure 3.3: Distribution of pixels and trigger patches in the camera plane. A trigger patch is a group of nine adjacent pixels. The patches are marked in alternating colors.

Incoming photons are measured in the SiPMs as a voltage drop on a load resistor. From there, the SiPMs are capacitively coupled to the preamplifier boards, which is called an AC-coupling. Thus, only the alternating component of the current in the SiPM is measured. As a result, the baseline of the time series of a SiPM is slightly shifted downwards to negative voltages, if a continuous noise with a few MHz, e.g., NSB photons, is present. Accordingly, the baseline amplitude depends heavily on the NSB level.

As mentioned before the preamplifier signal is split. The signal on the readout branch is routed to the data acquisition (DAQ) board, whereas the signal on the trigger branch is handed to the so-called FTUs (FACT trigger unit boards) For the trigger branch, the signals of nine adjacent, non-overlapping pixels of a patch are summed. The trigger patches are indicated by the coloring in figure 3.3. Cable-based clipping is used to shorten the summed signal. The signal is then provided to the trigger. Both branches are discussed in the following.

3.2.2 Trigger

The purpose of the trigger system is to provide a very basic pre-selection of events. This has the aim to filter for showers and to reduce the number of NSB-dominated events that are stored to hard disk drives. FACT uses a simple sum trigger that applies a threshold to the signal of a patch. This threshold is adjusted with the ambient light conditions to the lowest possible level to be dominated by shower events, rather than those containing only NSB photons. A cascaded 2-level decision logic is realised in 40 FTUs and the FTM (FACT trigger master board).

trigger units The FTUs are pre-triggers for the individual patches. They provide so-called trigger primitives, which are realized in a *N-out-of-4* logic of neighboring patches that send a positive trigger to the FTM if N patches of a FTU have a signal above the threshold. The threshold is set with a 12 bit resolution digital-to-analog converter (DAC) in a comparator circuit on the preamplifier boards.

trigger master The trigger primitives of the 40 FTUs are further processed to the FTM which provides the final trigger decission, a *N-out-of-40* coincidence of trigger primitives. The current settings of FACT are: $N_{FTU} = 1$ and $N_{FTM} = 1$. This means the camera is triggered if a single patch is above the threshold.

In addition to this *physics-trigger* mode, special calibration trigger modes are available, e.g., triggers with a fixed clock of defined frequency. These triggers provide random events that mostly contain NSB photons, whereas Cherenkov photons are unlikely in this mode. Measurements in this mode are called *pedestal* runs, as they provide examples for the signals underlying the shower events, in particular, the background provided by the light of the night sky folded with the phenomena occurring the SiPMs.[2]

3.2.3 Data Acquisition

The second branch in the signal pipeline is responsible for the acquisition of data, which is provided in the domino ring-sampling chip - type 4 (DRS4).[3] For this purpose, the DRS4 holds nine ring buffers that are used to constantly write and overwrite the signals of each pixel of one patch, as it is measured after the preamplifier. Each ring buffer comprises 1024 capacitors to buffer the signal. The time series of a signal is thus divided into intervals, so-called time slices, of 1024 signal amplitudes.

The DRS4 chips are operated at a clock frequency of 2 G*samples*, which leads to an interval width of 500 ps/*samples*.

However, the timing of the individual samples causes a systematic delay that has to be calibrated in the analysis, in order to have the signal times in units of ns. Furthermore, each capacitor has an individual offset and dynamic range, which also has to be calibrated later in the analysis. These calibration steps are referred to as DRS-calibration and DRS-time-calibration.[4]

[2] The mentioned phenomena are briefly addressed in section 3.3
[3] The DRS4 was developed at the Paul Scherrer Institute [97]
[4] The implemented calibration is briefly adressed in chapter 4.2.1.

Once the signal in a patch exceeds the trigger threshold, the FTM board sends a trigger, so the buffer content is digitized by an analog-to-digital converter (ADC), and then stored to hard disk on a computer in the counting house.

After having described the basic processing of electronic signals from the SiPMs, their properties and funcionality are addressed in the next section.

3.3 Solid-State Photon Detectors: SiPMs

FACT, as mentioned in the introduction to this chapter, is the pioneer, and by this the proof of concept, for the use of SiPMs in an IACT. Before FACT, photomultiplier tubes (PMTs) were the state-of-the-art detector type for this application. The common purpose of both devices is the translation of an incoming photon into an electronic signal by multiplication of charged carriers. While PMTs tackle this task with a configuration of a photoncathode and multiple dynodes that require bias voltages in the kV regime [94], SiPMs address this issue with a semi-conductor that is operated at voltages below 100 V [13, 107].

A SiPM is a matrix of several thousands of Avalanche-Photo-Diodes (APDs) that are operated in *geiger-mode*. These Geiger-mode-Avalanche-Photo-Diodes (G-APDs) are solid-state photon-diodes that are operated with reverse bias above the *break-down voltage*. In this operation mode, a single photon initiates a self-perpetuating avalanche of electron-hole-pairs measured as a current flow in the diode. The avalanche is stopped by the use of (*here:* passive) quenching. By this, each G-APD is capable of detecting a single photon and needs to recharge afterwards [58, 107].

The SiPMs used in FACT are manufactured by Hamamatsu Photonics as type Multi-Pixel Photon Counter (MPPC) SI0362-33-50C [13, 58]. A picture of the device is shown in figure 3.4a.

The properties and advantages of SiPMs, with special focus on the operation during bright light conditions, are discussed in this section. The effects impairing the performance of a SiPM and its main features are addressed briefly.

3.3.1 Properties

The properties of FACT's SiPMs are summarized in table 3.2. The used MPPC SI0362-33-50C comprises 3600 G-APDs connected in parallel, on an active area of $3\,\text{mm} \times 3\,\text{mm}$. The signal in a SiPM is, thus, the superimposition of signals from its G-APDs.

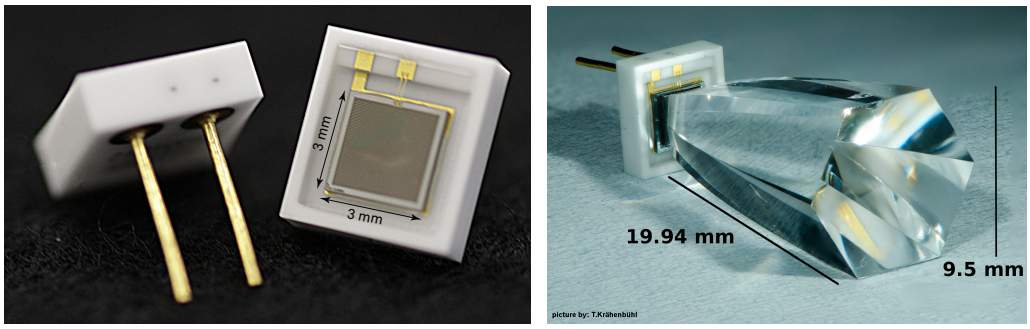

(a) Front and back of FACT's SiPMs.

(b) SiPM glued to a solid light guide.

Figure 3.4: Photographs of the SiPM type (Hamamatsu Photonics, MPPC SI0362-33-50C) used in FACT. Figure (a) shows the front side with the photon sensitive G-APD array on the right and the backside of the SiPM with connectors on the left. Figure (b) displays a SiPM glued to a solid light guide, as they are used in the FACT camera.

These SiPMs are able to detect light in the wavelength range of $(230-900)\,\mathrm{nm}$, peaking at about 440 nm, which covers a wide range of the Cherenkov light spectrum of extensive air showers. Apart from this, SiPMs show several advantages that make them suitable for gamma-ray astronomy and, in particular, for observations during bright light conditions, including the following characteristics:

- a relatively high gain 10^5 to 10^6 [107],
- a low operation voltage at $\approx 70\,\mathrm{V}$ [58, 107]
- insensitivity to magnetic fields [107],
- mechanical and electronic robustness [107],
- no damage when exposed to high luminosities [86], which allows for operation under bright light conditions without the use of UV filters or a reduced gain [39, 70],
- no known signs of aging [86, 94, 95],
- operation at room temperature without the need for active cooling [86],
- a standardized signal response for single photon events [86].

On the contrary, PMTs show aging effects, a loss in gain, when exposed to bright light conditions for a longer time [8]. This is an effect of aging of the dynodes, which occurs at a rate correlated with the integrated anode current. Very bright light conditions can even damage the PMTs [8, 14].

Property	Value
Photon detector (SiPM)	MPPC SI0362-33-50C
Manufacturer	Hamamatsu Photonics
No. of cells (G-APDs)	3600
SiPM active area	3 mm × 3 mm
Cell size	50 µm × 50 µm
Fill factor	61.5 %
Wavelength acceptance range	(320 – 900) nm
Peak sensitivity wavelength	440 nm
Operation voltage	70 V
Mean dark count rate	6 MHz
Peak PDE, at 1.4 V over-voltage	~36 %
Crosstalk probability	~13 %
Dead time	(50 ± 7) ns

Table 3.2: Overview of the properties of SiPMs used in the FACT camera.

Moreover, SiPMs operate at relatively low dark count rates $< 1\,\mathrm{MHz/mm^2}$ [107], which is in total $\approx 6\,\mathrm{MHz}$ per SiPM – given room temperatures (~25 °C) – and thus almost three times lower than the expected NSB rate from a dark night sky ($\approx 22\,\mathrm{MHz}$) [70]. Nevertheless, this effect is accompanied by characteristic effects of SiPMs, e.g., crosstalk and afterpulses. These effects and the signal generation in a G-APD are addressed in the following.

3.3.2 Signal Generation in G-APDs

A photon that impinges on a G-APD cell of a SiPM creates free carriers, i.e., an electron-hole-pair. This causes the rise of an avalanche of further free carriers due to ionization, with the result of a Geiger-type discharge. When operated above breakdown voltage, both electrons and holes are accelerated towards the electrode of opposite potential due to the applied bias voltage. As a result, an incoming photon causes a distinctive single photon signal that is measured as the current of free carriers through the G-APD [94].

Nevertheless, such avalanches are not only initiated by photons but also by thermal effects. The three dominating effects are addressed in the following as well as the temporal behavior of the G-APDs.

Dark counts cannot be distinguished from the signal of an incoming photon. They are initiated by thermal generation or tunneling of free carriers in the G-APD. Thus, the thermal generation is temperature-dependent [94]. Furthermore, the thermal generation is proportional to the depleted volume in the semi-conductor and scales with the active area of the device. The dark count rate has a strong dependence on the applied bias voltage due to field-assisted enhancement of the emission rate and an increase of the avalanche triggering probability. [45, 95].

Optical crosstalk occurs as one or several coincident avalanches of neighboring G-APDs as a result of an initially triggered G-APD due to a dark count or a photon. This process is initiated by a microplasma that is formed during the breakdown of a cell. Due to this plasma, electrons are lifted to higher bands. During the relaxation of this process photons are emitted. These photons can travel through the substrate of the semi-conductor and trigger avalanches in neighboring cells [94].

Afterpulses are the result of charge carriers from an initial avalanche being trapped in energy states in the band gap. After a stochastical detrapping lifetime, such a carrier is released with exponentially falling probability and can initiate another, delayed avalanche [67]. Depending on the duration of trapping, this results in a delayed signal or a prolonged recharging time for the G-APD. For the SiPMs in use, two typical time constants of 50 ns and 140 ns have been measured [47, 95].

All these phenomena produce an avalanche and are thus indistinguishable from the signal of a detected photon. Thus, they contribute to the number of extracted photons as a uncertainty factor to the true number of Cherenkov photons. They also influence the dead and recovery time of a G-APD.

Recovery time and dead time appear whenever a G-APD is triggered. Afterwards, it cannot measure a successive photon for a certain time, called *dead time*, until it is recharged enough to produce a new avalanche [54]. Furthermore, the duration until the G-APD is fully recharged is even longer, referred to as *recovery time* [93]. As a result, SiPMs show non-linearities between the numbers of incoming and triggered photons when exposed to massive photon quantities. In this situation the probability of a photon hitting a G-APD in dead time is increasing.

In the case of the used SiPMs (see table 3.2), *Grodzicka et al.* showed that at above a light yield of 1000 p.e. per SiPM the number of triggered cells is becoming significantly lower than the number of incoming photons hitting the sensor. Accordingly, a too low amplitude is measured and the photon counts are underestimated. They further measured the effective *dead time* of this device to be (50 ± 7) ns [54].

While at low light conditions such high quantities are rarely encountered in a single pixel, at brighter light conditions this might become an issue. Therefore, the feasibility of SiPMs for high NSB observations has been questioned by parts of the gamma-ray astronomy community. Consequently, FACT also aims to evaluate this influence on the operation of a SiPM camera. The general aims of FACT are discussed in the next section.

3.4 Objectives of FACT

In the previous sections, the telescope and its hardware have been described. The scientific goals and, accordingly, the purpose of FACT are outlined in this section.

The current generation of operating IACTs such as MAGIC, H.E.S.S., and VERITAS reach much higher sensitivities than FACT. They are focusing on the discovery of new sources as well as observations of a plethora of galactic and extragalactic gamma-ray sources. Their observation time is thus too valuable for a long-term monitoring of well-known sources. Nevertheless, there are strong reasons for a continuous monitoring of the few exceptionally bright Blazars with dedicated monitoring telescopes, for instance:

- Flux variations of theses sources,
- Multi-wavelength observations for comparison with other ranges of the electromagnetic spectrum, e.g., radio or X-ray observations,
- Multi-messenger studies, aiming for coincidence measurements with other particle channels, e.g., neutrinos and gravitational waves.

The latter two require a maximized overlap with other experiments in the field, whereas investigations on flux variations benefit heavily from dense light curves. Such variabilities have been detected on scales of days down to several minutes [9]. Obviously the astroparticle domain also profits from alerts being provided for extreme flares of the monitored sources. In both cases, long-term monitoring and rapid follow-up observations are solid ways to address these objectives [31, 99].

Thus, FACT was designed to provide for a monitoring experiment observing well-known Blazars in the TeV regime, i.e., Mrk 421, Mrk 501, 1ES 1959+50, and

1ES 23444+51.4. Accordingly, one of FACT's main objectives is to maximize its duty cycle in order to aim for gapless observations of such sources. Among other things, this was achieved by the use of solid-state photon detectors [31].

It furthermore functions as a protoype for this detector technology for future telescopes, e.g., for the Cherenkov Telescope Array (CTA) [1] and for dedicated prospect monitoring facilities such as, for instance, the proposed Cherenkov Telescope Ring (CTR) [99]. In the latter case, the experience of FACT helps to draw conclusions for the design and requirements for future monitoring telescopes.

In order to maximize its duty cycle, FACT focuses on two main objectives:

I. Firstly, the prolonging of observation times by additionally observing at more severe data-taking conditions, e.g., bright light conditions, lower zenith angles and bad weather conditions [70].

II. Secondly, the minimization of downtime due to maintenance and human interaction, via robotic operation and a robust telescope system with a long lifecycle [19].

For this reason, FACT was designed as a robust instrument with a stable and maximized performance aiming for the trade-off between inexpensiveness and high performance in order to scale out to several instruments as needed, for instance, for CTR [31, 99].

Due to their robustness and low costs, the decision for SiPMs supports many of these requirements. In consequence, FACT is today not only the first SiPM telescope but also the first almost robotic IACT. It has been shown in [70] that SiPMs are so robust that even observations with the full moon in the camera's focus are possible without instant damage.

Nevertheless, when maximizing observation time by going to bright light conditions, it is necessary to judge the effective improvement by evaluation of FACT's performance with an analysis chain optimized for these light conditions. Furthermore, the robustness and supposedly long life time of the SiPMs in use have to be evaluated to prove the absence of aging effects. This thesis aims to answer this question. The potential benefits are described in the following section.

3.5 Extension of Observations to Bright Light Conditions

As presented earlier in this chapter, one of FACT's objectives is to maximize its duty cycle by operating at severe light conditions. The benefit in doing so is addressed in this section with regard to the data collected with FACT so far. The light

conditions at which these data were taken are discussed briefly in the context of influential effects, which are dominated by the Moon. The analysis of this data requires adaptions to the analysis chain, which will be presented in chapter 6.

3.5.1 Distribution of Ambient Light in Data Collected with FACT

Even though FACT is able to observe at bright ambient light, its observations strategy aims for high quality, respectively low NSB, observations. Thus, most observations are at low NSB. Nevertheless, due to the periodicity of the Moon, nights close to full Moon are dominated by bright light conditions.

In good approximation, the light conditions can be quantified with the DC current in the pixels of FACT. For this reason, the average of currents in all pixels over the duration of a run (observation interval of typically ~5 min) is used to approximate the NSB level of an observation. Figure 3.5 shows the distribution of light conditions of runs from all sources, taken since the end of commissioning in May, 2012. Most of the observations populate at dark night conditions with currents of ~4 µA. In order to compare light conditions in the later analysis, this condition is used to define a NSB unit, hereafter called $\mathrm{NSB}_{\mathrm{Dark}}$, with:

$$1\,\mathrm{NSB}_{\mathrm{Dark}} \mathrel{\hat{=}} 4\,\mu\mathrm{A}. \tag{3.1}$$

The current standard analysis is optimized for observations at dark night conditions ($\leq 2\,\mathrm{NSB}_{\mathrm{Dark}}$). With this, already a large fraction of roughly 66 % of observations are covered. This is marked with the dark green area in figure 3.5. However, the brighter light conditions (marked in bright green) are currently excluded from the analysis, which means that about 34 % of observations are not considered here.

Moreover, the total number of observations at a given light condition is specific for each source due to several factors, e.g., angular distance to the Moon, zenith distribution of a source's observations, and the duration of observations during those conditions. The gain of observation time with light conditions beyond a dark night scenario varies thus with the observed source.

Figure 3.6 shows the gain in observation time by including observations up to a given light condition. The four main sources of FACT are given as an example. Dark night conditions cover a large fraction of the observed data. Nevertheless, some sources benefit more than others from including observations at brighter light conditions. Furthermore, the overall gain of additional data from extending to brighter light conditions saturates since these light conditions are intrinsically less observed.

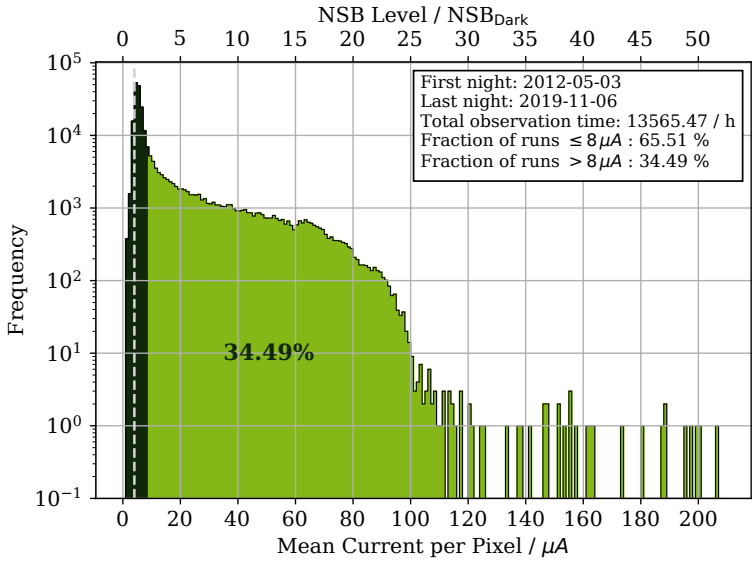

Figure 3.5: Distribution of the average current per pixel and observation run of typically 5 min. The abscissa represents the average of currents in all pixels over the duration of a run, which correlates with the NSB level. The top axis represents the ambient light in units of dark night conditions referred to as $\mathrm{NSB}_{\mathrm{Dark}}$. The dashed line at ~4 µA indicates the currents at dark night conditions in the absence of the Moon. Light conditions for which the current *fact-tools* analysis is optimized are marked in dark green. NSB levels that are not considered in the *fact-tools* standard analysis yet are marked in light green. They constitute 34.49 % of all observations.

The Crab Nebula, for example, has been observed a lot during dark night conditions. Thus, almost 70 % of Crab observations are covered by the standard analysis. However, 1ES 2344+514, for instance, has less overall observation time than Crab and apparently less at dark light conditions. One reason for this is that, on average, this source is more often only visible at lower zenith angles than Crab. Consequently, observations $\leq 2\,\mathrm{NSB}_{\mathrm{Dark}}$ cover almost 60 % of the observed data. Moreover, this source benefits even more than the other four sources from extending the standard analysis up to light conditions 20 times higher than dark nights.

Nevertheless, there is not only a benefit in total observation time by going to brighter light conditions. As FACT's monitoring purpose aims at the detection of flare states with increased, short time luminosities of the observed sources, a timely dense monitoring is required. Observations at increased NSB levels thus allow for avoidance of missing flares due to interrupted observations caused by moonlight.

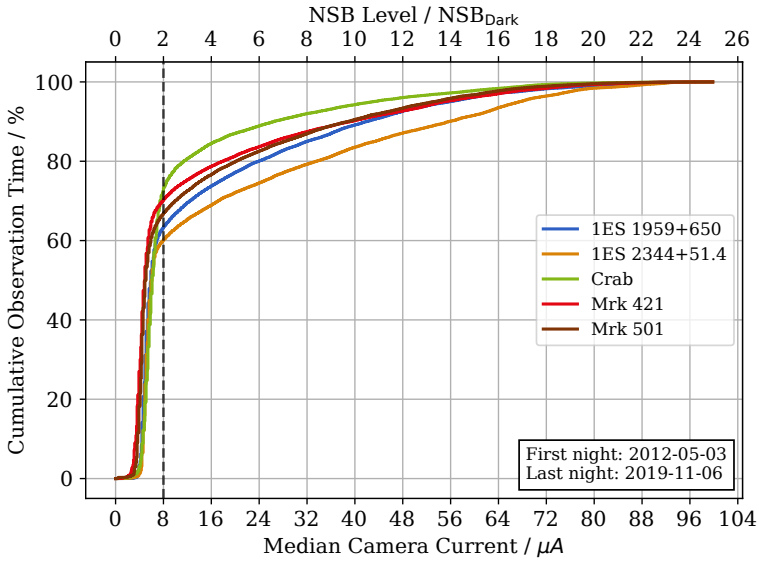

Figure 3.6: Fraction of the accumulated observation time of all observations up to a given light condition relative to the total observation time opf a source. The observation time is represented by the ordinate. The light conditions are given on the abscissas in units of the camera's average current (bottom) and in units of dark night conditions (top). The colors represent each of the five main sources monitored with FACT. The dashed line indicates the highest light condition considered in the standard analysis (with *fact-tools*). Large fractions of observations are covered by the standard analysis. However, some sources benefit strongly from going beyond the standard analysis margins.

3.5.2 NSB Levels in the Context of the Moon

The ambient light conditions, with which FACT is confronted are a result of several natural and artificial sources of light, which were introduced in chapter 2.3. Nevertheless, the Moon, when present, is the dominating factor for FACT, since it is the largest reflector of sunlight in the night sky and FACT does not observe sources near to the bulge of the Milky Way. Thus, in order to understand the circumstances of different NSB levels, it makes sense to determine them with regard to the presence of the Moon. The most influential factors for the NSB level in the camera are (i) the angular distance between an observed source and the Moon, (ii) the zenith angle of the Moon, (iii) and the Moon phase.

Figure 3.7 shows the dependency of the ambient light conditions to the angular separation of the Moon and the observed source with regard to the Moon phase. Obviously, the closer an observed source is to the Moon and the more of the Moon is

illuminated, the higher the detected NSB. As visible, observations in the presence of the full Moon increase the NSB beyond a factor of ten, depending on the distance to the Moon. When pointing close to the full Moon, NSB levels as high as 180 $\mathrm{NSB_{Dark}}$ are likely.

The light conditions presented in this figure are used in reference to the NSB levels discussed later in this work. The dotted lines represent four NSB levels used on the Crab sample analysed in this thesis. The figure shows further that the NSB samples chosen later in chapter 5.1 cover light conditions from dark night up to observations in the presence of the full Moon.

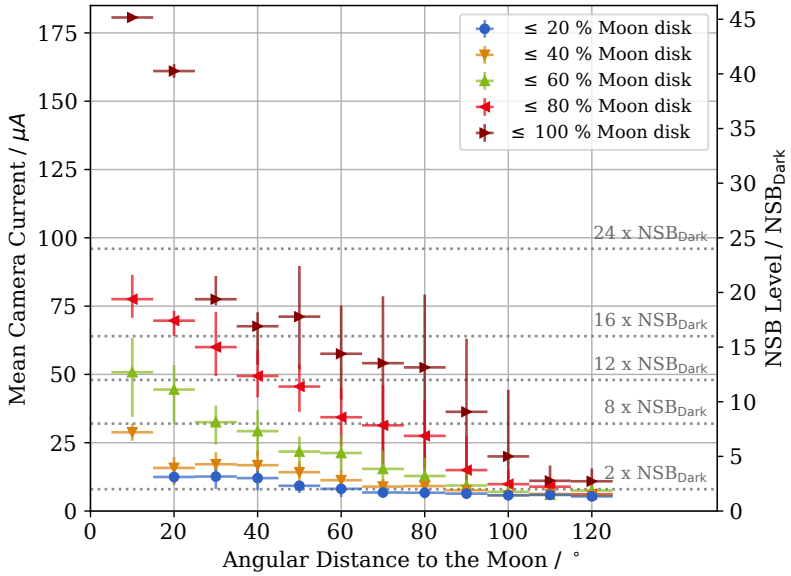

Figure 3.7: The dependency of the angular separation of an observed source to the Moon, with respect to the Moon phase, shows increasing NSB levels the closer a source is to the Moon and the more of the Moon is illuminated. The angular separation is represented by the abscissa. The colors stand for five Moon phases, from new Moon to full Moon. Horizontal error bars represent the width of bins in angular distance. Vertical error bars mark the $1\,\sigma$ environment of the NSB level in a bin. The mean DC current per run is given on the left ordinate and the self-defined NSB level as ordinate on the right hand side. Five representative NSB levels are marked with the dotted horizontal lines. The top line represents the maximum NSB considered in this work. The lowest line represents dark night conditions. The data were collected from observations of all sources between May, 2012 and November, 2019.

This concludes the discussion of FACT, its SiPMs, and its objectives. As outlined, it is the aim of this thesis to extend the analysis of observations to bright light conditions (see chapter 6). Moreover, the performance of their analysis, and thus the performance of FACT for high NSB conditions, will be evaluated (see chapter 7). The methods needed for this are explained in the next chapter.

4 Analysis Chain and Applied Methods

The analysis performed in this study requires a pipeline of several analysis steps, some of which must be taken out in a specific order. This chapter will outline the necessary steps and methods used for the analysis of Crab Nebula data in the winter season 2015/16 at light conditions from "dark night" to almost "full moon". The presented analysis chain is universal in its structure, and it is applied to extract an observed source's physical properties (i.a., its differential energy spectrum) from the raw data level. The required methods are explained in the following.

Due to the absence of a test beam in gamma-ray astronomy, simulations of particle showers are essential for the methods presented in this section. The machine-learning algorithms in particular, require data with ground truth in order to train and evaluate a model. More details to the MCs are provided in chapter 5.2

4.1 Analysis Chain

An overview of the analysis pipeline used in this study is illustrated in figure 4.1. The pipeline starts at raw data level, reading events from FITS files, and processes the events through a chain of programs dedicated to particular steps of the analysis to reach the final gamma level. After this level, reconstructed gamma-ray events are available, with information about their energy, origin and predicted event class (*hereafter:* `gammaness`)[1].

The methods used in this thesis and the provided performance study require a good understanding of the analysed data. Due to the lack of a test beam in astroparticle physics, sophisticated Monte Carlo simulation (MC)[2] are mandatory to gain insight in the involved processes. They are necessary to provide ground truths for the training of machine-learning methods and allow for an evaluation of their performance. Furthermore, they are used to investigate the performance of the telescope, respectively, the analysis.

[1] The confidence level (between 0 and 1) of the classifier for having detected a gamma event (see section 4.4.2).

[2] Monte Carlo simulation: A method to provide simulations based on random sampling of the desired processes [20]

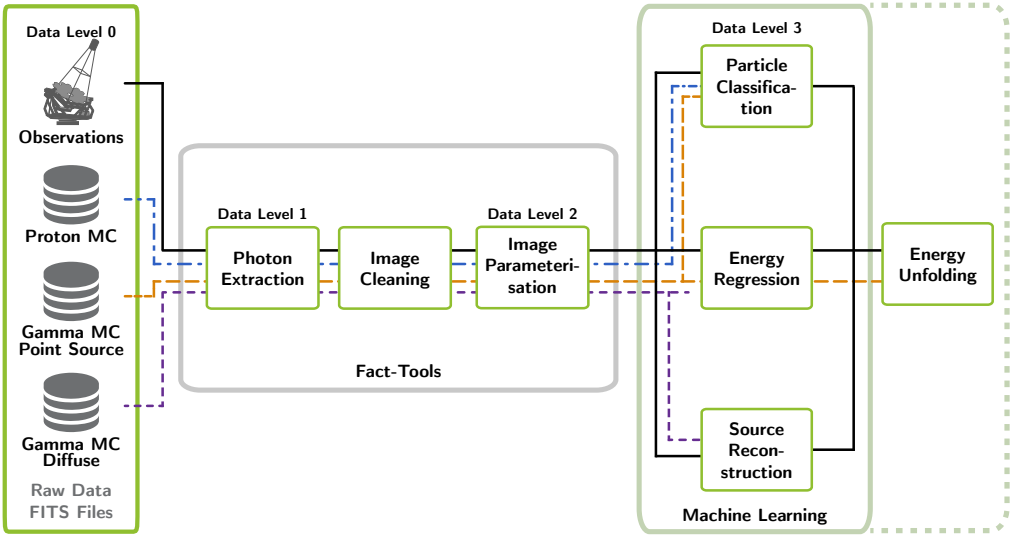

Figure 4.1: Overview of the analysis chain used in this thesis in order to progress from raw data level to gamma level. After the final analysis steps, high-level information about the source are available, i.e., its energy spectrum and gamma luminosity. The analysis is applied to both data and MC simulations. Dashed lines indicate the flow of training data from simulations. Solid lines indicate the flow of data from observations used for the application of trained machine-learning models.

The simulations are thus later split into training and evaluation sets, which both are propagated through the analysis pipeline. Data and MCs are both stored in FITS files. Their properties, selection and generation are discussed in chapter 5.

The pipeline consists of three main processing steps:

I. the **feature extraction** that provides a parametrization of the shower stored in the raw data files,

II. the **training and prediction** of the main properties of showers based on features generated in the first step,

III. the **unfolding** of the energy spectrum from gamma rays of the observed source, given their properties from step two.

In the case of the following FACT analysis, the feature extraction is conducted with the low-level analysis framework *fact-tools* [23, 34] (details in section 4.2). It is responsible for reading data and MCs at raw data level from FITS files and calibrating their time series. These calibrated time series are used to extract features at pixel level, i.e., photon charges (number of photons) and arrival times.

Afterwards, the image cleaning filters pixels that contain mostly Cherenkov photons, and it provides an image of the extensive air shower. These shower images are parameterised and deliver a feature set at shower level that is used in the following step.

The identification of gamma ray events and suppression of hadronic background events is realised with machine-learning methods, in particular by training a *random forest classifier* with gamma ray and proton events to distinguish these two classes. The reconstruction of particle energy and origin is also performed with these techniques. In both cases, the target value (e.g., particle energy or distance to the source) is estimated by a *random forest regressor* which was trained on gamma ray events (details in section 4.3). Applying these models to data provides features at gamma level and allows the analyst to define a final cut on `gammaness` and the events' angular distance to the source, `angular_distance` (θ). The use of these cuts enables the analysis to provide high-confidence gamma rays with estimated energies for the last step of this analysis chain.

In this step, the differential energy spectrum of an observed source is unfolded. Due to the fact that the energy of the primary particle can only be measured indirectly, its resolution is limited by the combination of detector and analysis. The true energy distribution is thus folded with their joined response. Such situations are known as inverse problems [78] with unfolding being a way to solve them [78]. The unfolding approach used in this thesis is addressed in section 4.5.4.

In combination with the unfolding, detector acceptance, normalization with observation time, and the background correction are applied to calculate a flux and determine the differential energy spectrum of the source.

The software components used for these steps will be discussed in the following sections in more detail.

4.2 Raw Data Analysis and Feature Extraction

The feature extraction from FACT's raw data is performed with the low-level analysis package *fact-tools* [23]. It is based on the *streams* analysis framework by Christian Bockermann et al. [21, 22]. Both software packages have been developed at the collaborative research center (CRC 876) at TU Dortmund University. The *fact-tools* are the result of close and fruitful collaboration of computer scientists and physicists within the CRC 876.

The *streams* framework aims at consecutive data with large volumes (Big Data) and provides a well-defined and performing infrastructure for this. It is implemented

in *Java*. Computing tasks are defined in so-called processors and their consecutive order of execution is defined in an abstraction layer outside of the code in *XML*. This concept allow for separation of the code's implementation, which has to be compiled, and the design and definition of analysis chains [21].

The *fact-tools* are a *streams* based library of processors implemented for the use in Cherenkov astronomy, and for FACT in particular. In this study, *fact-tools* version 1.0.3 is used. Their code is open source and hosted on github [34].

The generation of NSB simulations for the later analysis was also performed in *fact-tools* and can be found in section 5.3.2. The tasks performed for the low-level analysis and a selection of methods important for this thesis are explained in the following.

4.2.1 Calibration

The FITS files' raw data contain the time series of every pixel and event in a run. However, due to the nature of the DAQ (see section 3.2.3) and for the sake of reducing the data's volume,[3] the files contain uncalibrated time series as digitized by the DRS4 [7]. In the first step, a calibration is thus necessary before extracting photon charges and arrival times from the time series.

The uncalibrated data is stored for each pixel in 300 time slices[4] with amplitudes in units of the used ADC. Each sample corresponds to a capacitor in the DRS4 chip with an individual offset - regarding the amplitude and timing - and an individual dynamic range of the amplitude. These are the effects that have to be calibrated. The calibration step in *fact-tools* is responsible for the following tasks:

- DRS calibration: Calibration of the slices' amplitudes to mV.
- DRS time calibration: Calibration of the slices' timing to ns.
- Removal of artifacts produced by the DRS4 in the DAQ, e.g., DRS spikes and DRS jumps.
- Interpolation of broken pixels with their neighbors.

The time series are thus available with floating point resolution and valid units ($\Delta t \approx 0.5\,\mathrm{ns}$ and $\Delta A \approx 0.5\,\mathrm{mV}$). Furthermore, the amount of noise on the time series is reduced.

[3] Calibrated data are floating points numbers, while uncalibrated data is stored as integer.
[4] 300 slices is FACT's region of interest. For some measurements the full 1024 slices are read.

4.2.2 Photon Extraction

In the photon extraction step, the number of photons - often called photon charge - and the average arrival time of such a photon bunch are extracted for each pixel. Photons produce an avalanche in a SiPM with a distinctive signal, which is visualized in figure 4.2. For each pixel, the largest amplitude is searched in a time window of 45 ns close to the beginning[5] of the time series, which is divided into time slices 0.5 ns wide. The timing of triggered air shower events is determined by the trigger electronics and thus always close to time slice 50 of a pixel.

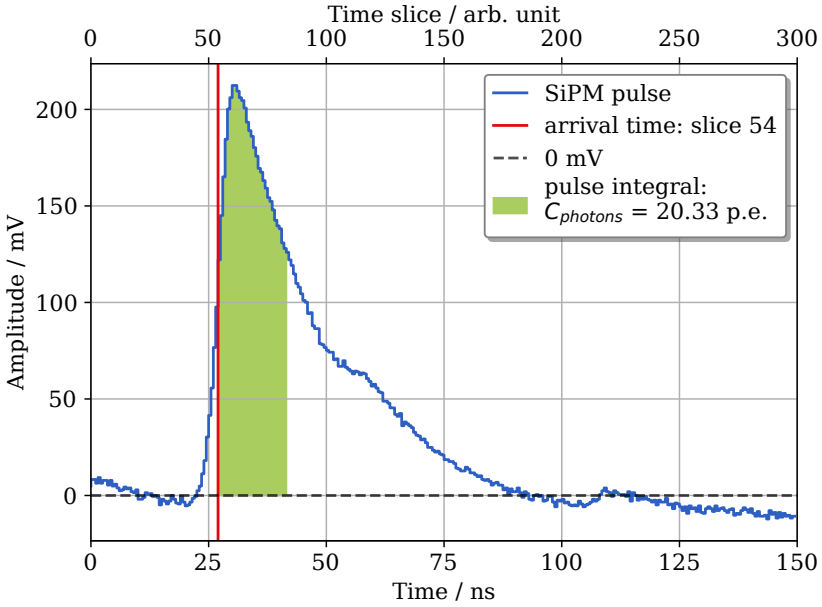

Figure 4.2: Time series of a single pixel with a SiPM pulse with a photon charge $C_{\text{photons}} \approx 10$ p.e. and an arrival time at slice 54 ($t \approx 27$ ns). The red line marks the arrival time, which is given on the abscissa in units of DRS4 cells (top) and calibrated time in ns (bottom). The green area indicates the pulse integral used to determine the photon charge. The ordinate shows the SiPM's current's amplitude measured as a voltage drop at a capacitively coupled resistor. Negative amplitudes, due to a baseline shift, are neglected in the integration. This reduces the contribution from NSB to the photon charge.

Signals of detected pulses are integrated over 30 time slices (15 ns). This integral is divided by the gain of a pixel's SiPM, in order to determine the number of photons in units of photon equivalent (p.e.). This gain is defined as the integrated signal

[5] In the current version the search window starts at time slice 35 of the time series.

of a single photon in a given time window of, again, 15 ns. The gains of all pixels are measured in dedicated runs at the beginning of each night. Details to these calibration measurements can be found in [18].

In the case of very large events with quantities of more than 200 p.e. the pre-amplifier on the FACT preamplifier boards (FPA) saturates. These events are reconstructed from their signal width at a threshold of 1800 mV.

The arrival time is determined on the sharp leading edge of a pulse by fitting a third order polynomial to it. After this, value pairs of photon charge and arrival time are available for every pixel.

However, Cherenkov photons and avalanches from NSB photons or from dark counts cannot be distinguished by their signal shape. Only their different time structures allow for a reduction of the impact of this kind of noise. Cherenkov photons arrive in a very narrow window of ≈ 10 ns, while NSB photons and dark counts are uniformly distributed. This can be used to determine the NSB level directly and also its contribution to the extracted signal – the dark count rate is smaller, shows little variance over an observation, and can thus be neglected.

Variance of the Pedestal Signals

The variance of the pedestal signals (`ped_var`) is a feature that is sensitive to this contribution of NSB [72]. It was added to *fact-tools* as part of this study in order to measure the NSB directly in shower events.

In this implementation, the feature is determined by dividing the time series of a pixel into randomly sampled consecutive subsamples. An illustration of the randomly sampled integration windows is shown in figure 4.3. The width of the subsample's binning is chosen in accordance with the size of the photon extraction's integration window. The random sampling is achieved by starting in a uniform random slice of the time series and looping over it in a circular manner. Accordingly, the time series is integrated in several windows separately.

The variance, more precisely the standard deviation, of these integrals is defined as the feature called variance of the pedestal signals (`ped_var`). It is derived on pixels dominated by NSB and it is proportional to the level of NSB since it increases with the fluctuation of the time series.

Typically, it makes more sense to estimate the NSB level on pixels without Cherenkov photons. The `ped_var` of all pixels that are discarded by an image cleaning are thus used for an event-wise representation. `Ped_var` is later used to add information about light conditions to machine-learning steps like the gamma/hadron separation.

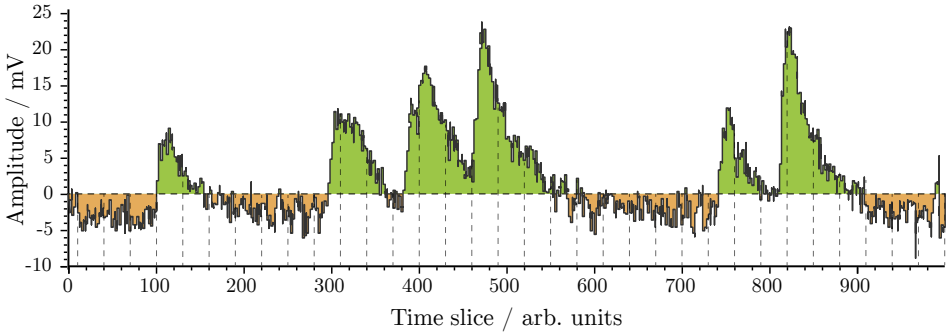

Figure 4.3: Illustration of the feature called variance of the pedestal signals (`ped_var`), which is calculated here on a time series with 1024 time slices divided into consecutive samples with a random starting point and the size of the typical integration window of 30 time slices. The dashed lines indicate the integration window. The time is given on the abscissa in units of DRS4 cells. The ordinate shows the SiPM's current's amplitude measured as a voltage drop at a capacitively coupled resistor. Green areas mark positive and orange areas indicate negative contributions to the integral.

4.2.3 Image Cleaning

Image cleaning is responsible for determining the shower image by distinguishing pixels with Cherenkov photons from those dominated by NSB. The algorithm used in *fact-tools* is called a two-level time-neighbor cleaning and is a threshold value method introduced in [87].

Figure 4.4 illustrates the image cleaning and the relevant features based on an exemplary shower. The cleaning is mainly controlled by the following parameters:

- **The core threshold**, which defines the minimum photon charge of the core pixels[6] (default: $N_{core} \geq 5\,\text{p.e.}$),
- **The neighbor threshold**, which defines the minimum photon charge of neighbor pixels[7] (default: $N_{neighbor} \geq 2.5\,\text{p.e.}$),
- **The time limit**, which defines the maximum arrival time coincidence of adjacent pixels (default: $T_{max} \leq 10$ time slices ($\hat{=}\ 5\,\text{ns}$)), and
- **The min. number of pixels**, which defines the minimal size of a pixel cluster to survive (default: $N_{pixel} \geq 2$)).

[6] Name for the brightest inner pixels of a shower
[7] Name for the fainter, outer pixels of a shower or pixels in separated clusters

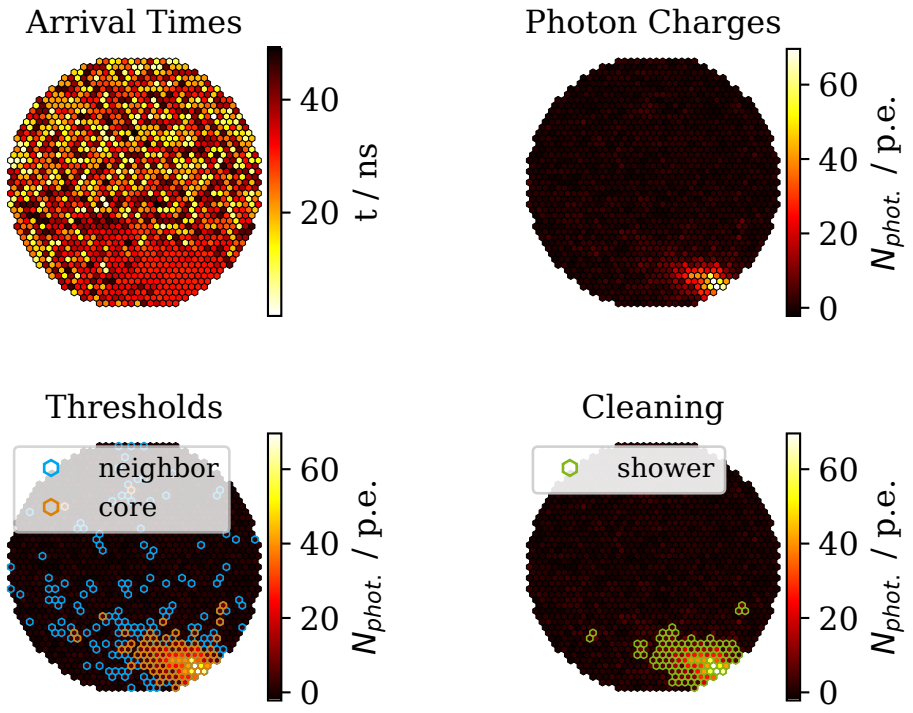

Figure 4.4: Camera views of an exemplary shower event, showing (LRTB): the distribution of arrival times, photon charges, all pixels above the core and neighbor threshold (orange and blue), and shower pixels selected by the image cleaning (green). The latter is parametrized to provide features for the further analysis steps. Here several pixel "islands" are visible with a large area main island and several small islands that might belong to the shower or are induced by NSB. If the cleaning levels have been tuned well, the average number of island should be independent of the light conditions.

In addition, the current implementation also discards cluster originating from stars in the field-of-view. A shower is identified if one or several clusters of pixels apply to these constraints [33].

Obviously, these thresholds depend on the behavior of the NSB. The default values were chosen for "dark night" conditions. With increased NSB, however, they have to be adapted to reduce the distortion of shower images. But, at the same time two high thresholds will discard Cherenkov photons as well and increase the energy threshold of the analysis. Thus, cleaning levels have to be optimized with care for different light conditions, as will be done in section 6.2.

4.2.4 Image Parametrization

After the image cleaning, pixels are separated into shower pixels and pedestal pixels. Typically, the shower pixels are used to extract features from their distribution to parametrize the image. Nevertheless, the pedestal pixels can also be used to simultaneously parametrize the noise (i.e., the NSB), for example by use of `ped_var`, which was introduced in section 4.2.2.

Extensive air showers, especially gamma ray showers, produce shower images with an elliptic shape in the camera plane. The first set of image parameters was introduced by Hillas [64]. Several more additional parametrizations have been implemented since, and the development of new algorithms is an on going process. A sketch of these features is illustrated in figure 4.5.

The current version of *fact-tools* extracts more than 200 features (independent and correlated). This requires the selection of a subset of mostly uncorrelated features. An excerpt of features, important in this thesis, is listed and briefly explained below:

- `width` and `length` parametrize the spread of the semi-minor and semi-major axis of the two-dimensional shower distribution (see fig. 4.5).
- `delta` is the rotation of the shower with regard to an arbitrarily orientated Cartesian coordinate system (see fig. 4.5).
- `numIslands` represents the number of separated clusters in the shower image (see fig. 4.5).
- `size` accounts for the total number of photons in the shower pixels.
- `mean_arrival_time` is the average arrival time of detected photons in all pixels (shower and pedestal).
- `concentration_cog` is the ratio of `size` to photons at the center of gravity of the shower's light distribution (`COG`).
- `leakage1` (and `leakage2`) are ratios between `size` and the photon contents of the outer most ring of pixels (or the two outermost rings).

Furthermore, all basic statistical properties (e.g., quantity, mean, standard deviation, kurtosis and skewness) are calculated on the distribution of `ped_var`, photon charge, and the arrival time of shower and pedestal pixels.

The feature `DISP` delivers the distance between the `COG` and the reconstructed origin of the shower (see figure 4.5), and is necessary to calculate the angular distance between reconstructed and actual source position referred to as `angular_distance` (θ).

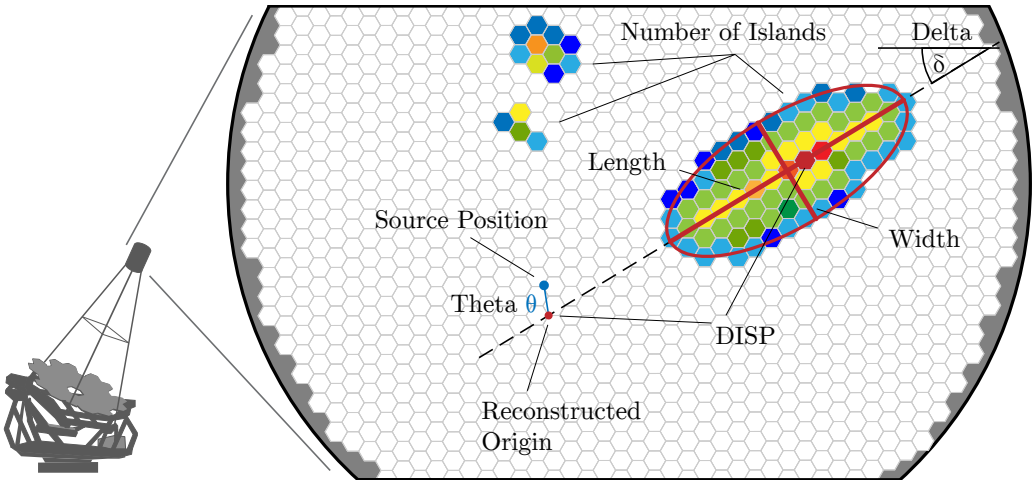

Figure 4.5: Illustration of geometrical image parameters determined by the shower's distribution of pixels and their photon charges in the camera plane. The shower pixels and photon charges are indicated by the coloring of the pixels. Dark red pixels have much photon content, blue pixels the least. The main island is marked with a red ellipsis which represents the projection of the light's 2D Gaussian distribution. Separated pixel clusters are called islands and are more frequent in hadron events. `DISP` is the distance between the reconstructed source position and the light distribution's center of gravity. The angular distance between reconstructed and known source position refers to the angle θ.

This thesis uses a machine-learning approach introduced by [83] to determine this feature. This has the advantage of a better angular resolution than the deterministic approach used so far in [100]. The machine-learning part will be explained in the next section.

4.3 Machine Learning

The high-level features in the analysis (gamma level) are determined with machine-learning methods. The tasks related to these features comprise (i) particle classification for the gamma/hadron separation, (ii) energy regression and (iii) source reconstruction, which means the regression of `DISP`. The implementations of the machine-learning tasks are collected in the *python* package *aict-tools* [84], which was developed at TU Dortmund University. All three machine-learning tasks use the *random forest* algorithm based on an implementation of the *python* package *scikit-learn* [89].

Brief overview of the *random forest* algorithm is given in this section. *Random forests* are applicable to both classification and regression problems, as shown in the following. Furthermore, methods and metrics to evaluate the performance of these models are summarized in this section. An explanation of the machine-learning tasks performed are provided in section 4.4 (gamma/hadron separation and source reconstruction) and 4.5 (energy regression).

4.3.1 Introduction to Random Forests

A *random forest* [27] is a robust, supervised ensemble learning method formed by a combination of decision tree-based predictors. Each decision tree is trained with a bootstrap sample (i.e., multiple sub-samples drawn with replacement) of annotated data containing the ground truth of the task to be learned. Figure 4.6 shows a sketch of such decision trees.

During the training of each individual tree, at each node a random sample of features is drawn and the best binary split of the data is determined. The number of features (`max_features`) and the decision criterion (`criterion`) can be specified by the user. Since each split adds a new layer to the tree, it can grow to a certain depth. The maximum depth (`max_depth`) is thus a parameter of the random forest that constrains the size of each tree. The leaves of the decision tree contain the class ratios remaining after the chain of splits up to that leaf. Such a tree gives thus a probabilistic prediction of the class for each event when applied to a dataset.

The decision of several trees in a forest is combined through a forest of given size (`n_estimators`). Their decision is the result of a majority vote or, as in the case of *scikit-learn*, the class with the maximum mean confidence among all trees or the mean predicted value in case of a regression task. This strategy, in combination with the random sampling, makes a *random forest* very robust against overfitting. Moreover, k-fold *cross-validation* [60] is used to test a model during training for overfitting by estimating the prediction error, as will be explained in section 4.3.2.

Random Forest Classifier In the case of a classification between two (or several) classes, a *random forest* is used as described above. A model is trained based on a data sample containing the labels of the classes as a special attribute. The criterion for the best split can either be Gini impurity[8] (`gini`) or information gain[9] (`entropy`). The leaves of the decision tree contain the class ratios remaining after the chain of splits up to that leaf (see figure 4.6a). By applying such a model to

[8] Reduction of class impurity after a split with the used feature.
[9] Reduction of entropy in a sample after a split with the used feature.

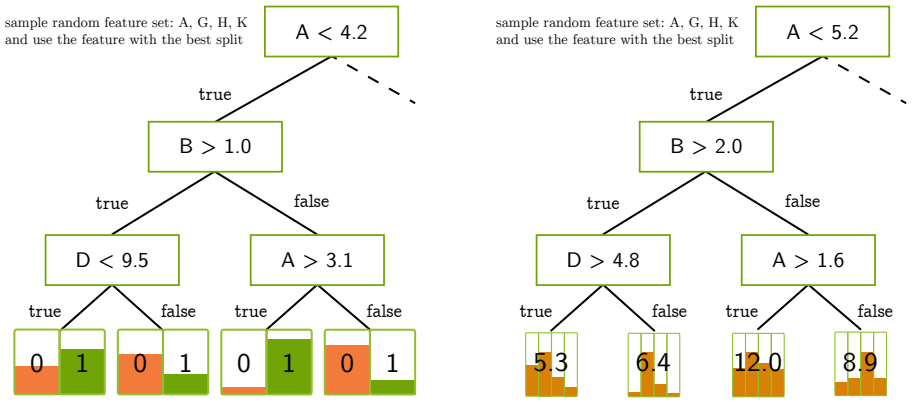

(a) Decision Tree **(b)** Regression Tree

Figure 4.6: Sketch of decision trees as used in a random forest for classification (a) and regression (b). The wide rectangles represent the nodes with the split condition in the node and the decision on the edges. The leaves are at the bottom of the tree. In the case of the classifier they contain a (binary) class distribution. In the regression case, they hold the distribution of the target variable or a representation of it, e.g., the distribution's mean or a linear regression model. Both cases show a tree with limited depth.

data the trees return their class prediction and the result of the forest is the average of the class predictions $P \in [0,1]^C$ for C classes. The final decision, e.g., in a binary classification, is achieved by applying a threshold to the class predictions in order to decide for one class at a defined confidence level.

Random Forest Regressor Regression problems are approached with a *random forest* that is formed by trees which predict numerical values instead of class labels [27]. A sketch of such a tree is depicted in figure 4.6b. A model is trained on a sample containing the ground truth of a numerical value that is predicted in the application case.

The prediction of a given leaf is simply the mean of the target variable's values in that leaf. Nodes are split again with binary decisions on the randomly sampled features. The splits have the aim to minimize the variance of the target variable. A typical criterion for the best split is minimizing the mean squared error (MSE). In the application case, the *random forest* estimates the value of the target variable based on the given feature set by averaging over the predictions of all regression trees.

4.3.2 Evaluation of Machine-Learning Tasks

The use of machine-learning models, as discussed in the previous section, requires independent methods and metrics to assess the performance of their predictions. Before applying a model to data, it is necessary to know how accurate it predicts. Furthermore, it is mandatory to test for overfitting to guarantee that a trained model generalizes well in order to predict on an unknown data set.

In this section the methods and metrics used for the evaluation of the machine-learning tasks are thus introduced briefly. They are used for the machine-learning steps presented in chapter 6 and the evaluation of the NSB performance in chapter 7.

Cross-Validation is one of the most widely used methods for estimating prediction errors. For this purpose, the training set is split into k mutually distinct subsets, as outlined in figure 4.7. In each iteration, the training is conducted on $k-1$ subsets, whereas the k^{th} set is used to apply the model and test the performance with a given metric [60]. Typical metrics are, e.g., accuracy (for classification problems) and R^2-score (for regression problems).

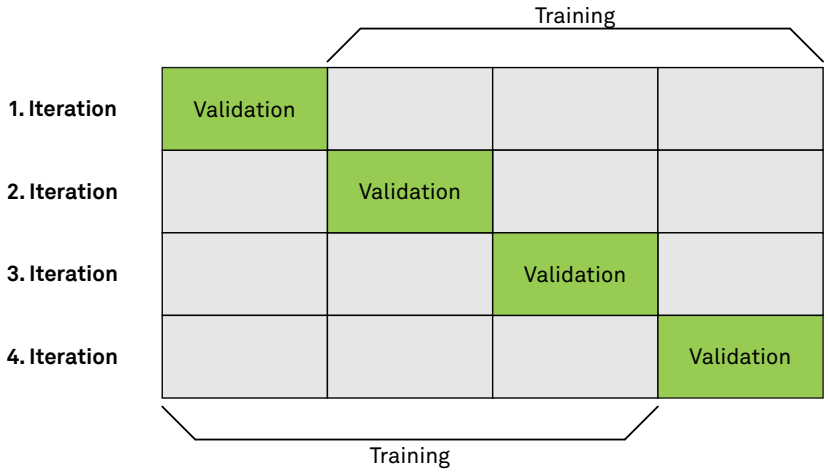

Figure 4.7: Sketch of a 4-fold *cross-validation*. At the beginning of the *cross-validation*, the full data set is split into $k = 4$ subsets. The grey boxes indicate the training sets and the green boxes represent the validation sets. Each line symbolises an iteration. The composition of the subsets remains unchanged during the *cross-validation*. In each iteration the selection of validation and training sets is permuted.

In order to test for the fluctuation of the generated models on independent data sets, train and test sets are iterated as indicated by the green boxes in figure 4.7. From the results of each iteration, the mean and standard deviation of the k metrics are calculated, which allows for the prediction error to be estimated. The evaluation of the machine-learning models addressed above uses a 20-fold *cross-validation*, which is applied during training.

Bootstrapping is used to assess statistical accuracies in order to estimate the (prediction) error of a determined value or model. In contrast to *cross-validation*, *bootstrapping* resamples with replacement from a dataset Z used for training or to derive a certain value from the data set, e.g., the median of a distribution. Each sample has the same size as the original dataset. Accordingly, the new dataset will contain multiple instances of the same original data events and will omit other original events. This procedure is repeated k times, in order to estimate the distribution of any quantity $S(Z)$ computed from Z. Then the operation that was applied to the original set is also applied to the bootstrap samples. This method allows the analysis, for instance, to assess the expected value or the uncertainty of an operation applied to Z, by computing the mean and standard deviation of the methods results on the k bootstrap samples [60].

The R^2-score refers to the coefficient of determination and is used to measure the performance of a regression with the following equation:

$$R^2 = 1 - \frac{\sum_i (y_i - f_i)^2}{\sum_i (y_i - \bar{y})^2}. \tag{4.1}$$

In this equation, y is the dependent variable, i.e., the ground truth to be predicted, with a mean value $\bar{y}$ and a prediction f. R^2-score determines the proportion between the variance of residuals and the variance of the true value. It is thus a measure of how well data points are approximated by the regression predictions.

The Area under the ROC curve (AUC) is a measure of the performance of a classifier. A Receiver-Operator-Curve (ROC) visualizes the true positive rate[10] versus the false positive rate[11] by altering the prediction threshold of the model that is evaluated. An example for such a ROC curve is depicted in figure 4.8. The area under this curve is referred to as area under the (ROC-) curve (AUC). It is a metric

[10] The fraction of correctly predicted signals.
[11] The fraction of background events being incorrectly predicted as signals

to determine the performance of the classifier invariant to the prediction threshold. The closer its value to the optimum, which is 1, the better the performance of the classifier [26].

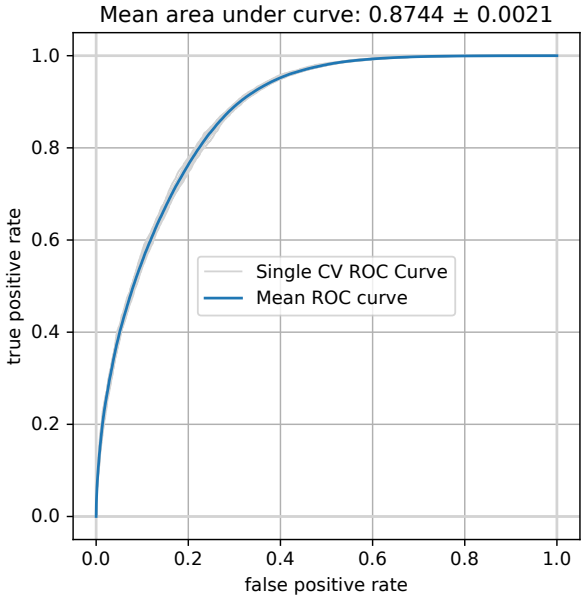

Figure 4.8: Example for a ROC curve. The vertical axis represents the true positive rate, which is the fraction of correctly predicted signals. The horizontal axis represents the false positive rate, which is the fraction of background events being incorrectly predicted as signals. The curve is the result of a scan of a classifier's prediction threshold from 0 to 1, while measuring, e.g., the true/false positive rates at the same time. The AUC is the area under this curve and is a quality metric for the classification's performance. High AUCs ($\geq 80\,\%$) indicate a good performance, while a classification with an AUC of $\approx 50\,\%$ is not better than random sampling.

4.4 Background Suppression and Source Detection

The detection of a gamma-ray source requires the reconstruction of a shower's spatial origin and the suppression of the overwhelming amount of hadronic showers in these observations. The methods discussed in the previous section are thus used in the following to perform these two tasks, namely, (i) the `DISP` regression and (ii) the background suppression, also known as gamma/hadron separation. The settings of the *random forests* used for these steps are listed in table 4.1.

Nevertheless, a remaining background of non-gamma events, surviving the gamma/hadron separation, have to be considered in the further analysis. A simultaneous measurement of this background and the showers from the observed source is therefore outlined in section 4.4.3. This information is used to determine the significance of a detection after applying these methods to observations. The computation of this quality measure is described in section 4.4.4. In that sense, an IACT's ability to detect a VHE gamma-ray source is referred to as its sensitivity and allows for comparison of the performance of different IACTs. The sensitivity of an IACT is thus summarized in section 4.4.5.

Setting	Separation	Energy regression	DISP regression	DISP (sign) classification
`n_estimators`	200	200	200	200
`criterion`	entropy	mse	mse	gini
`max_features`	sqrt	5	sqrt	sqrt
`max_depth`	15	15	20	20
`min_samples_split`	2	3	2	2
`n_signal`	120 000	120 000	120 000	120 000
`n_background`	120 000			
cross-validation metric	Accuracy	R^2-score	R^2-score	Accuracy
k-fold *cross-validation*	20	20	20	20

Table 4.1: Settings (*scikit-learn*) for training of the machine-learning models in this study. The `DISP` method has two columns because it uses both a *random forest classifier* and a *random forest regressor*. The criterion setting defines the optimization strategy for the *random forest* i.e., reduction of class impurity (gini), reduction of entropy aka increase of information gain (entropy), or the mean squared error (mse). The number of features (`max_features`) can be chosen to a fixed number or the squareroot of the total number of features $\sqrt{\texttt{n\_features}}$.

4.4.1 Source Reconstruction (DISP Regression)

The reconstruction of the spatial origin of a shower is estimated based on the image parametrization. In this study DISP, the distance between the COG and the reconstructed origin of the shower, is determined with a *random forest*. Its settings are listed in table 4.1.

The following approach for the DISP regression has been introduced in [83]. It is actually based on two machine-learning models:

- a *random forest regressor* that estimates $\texttt{DISP}_{\text{abs}}$, the numerical distance of the reconstructed source position to the showers COG, and
- a *random forest classifier* predicting the $\texttt{sign}_{\texttt{DISP}}$ of its direction on the shower axis.

However, the ground truth for this task depends on the low-level analysis chain. COG and delta are features that are generated within *fact-tools*. Therefor, they cannot be simulated directly. The target values are thus calculated as follows:

- $\texttt{DISP}_{\text{true}}$, the ground truth for distance of COG and source position, is estimated as the Euclidean distance of simulated source position (know from MCs) and COG (extracted in *fact-tools*),
- $\texttt{delta}_{\text{true}}$, the ground truth for the shower's rotation around the COG, is determined as the rotation of the vector spanned by COG and the simulated source positions, and
- $\texttt{sign}_{\text{true}}$, the ground truth for the sign of the shower's direction, is calculated from the sign of the difference of delta and $\texttt{delta}_{\text{true}}$ with:

$$\texttt{sign}_{\text{true}} = \text{sgn}\left(|(\texttt{delta} - \texttt{delta}_{\text{true}})| - \frac{\pi}{2}\right)$$

.

This step is trained on a sample of diffuse gamma MCs, i.e., gamma rays simulated with an isotropically distributed source position in the camera plane. The features used for the DISP regression are listed in appendix A.4.3. When applying this model to data, $\texttt{DISP}_{\text{abs}}$ and $\texttt{sign}_{\texttt{DISP}}$ are predicted separately and the final DISP is calculated as:

$$\texttt{DISP} = \texttt{sign}_{\texttt{DISP}} \cdot \texttt{DISP}_{\text{abs}}. \tag{4.2}$$

The souce position of a detected shower is then reconstructed to the coordinates:

$$\vec{s}_{\text{est.}} = \begin{pmatrix} \texttt{COG}_x + \texttt{DISP} \cdot \cos(\texttt{delta}) \\ \texttt{COG}_y + \texttt{DISP} \cdot \sin(\texttt{delta}) \end{pmatrix} \tag{4.3}$$

4.4.2 Background Suppression (Gamma/Hardron Separation)

Gamma rays are the minority class and the analysis is confronted with a majority of showers being induced by hadrons. In order to filter the desired gamma events and to reduce this large background, the class of the primary particle of recorded events has to be determined. In this sense, the gamma/hadron separation is a binary classification, addressed here with a *random forest classifier*. The *random forest*'s settings used for this step are listed in table 4.1.

Due to the lack of a test beam in the real world, the model is trained on gamma and proton simulations, with a balanced class distribution. This step uses gamma events simulated in so-called Wobble-Mode, i.e., the off-axis simulation of a point source (see section 5.2.2). The Wobble-Mode is explained in the following section, while the different simulation sets are presented in chapter 5.2.

Gamma rays are marked with the class label 1 and protons with the class label 0. The probability for having detected a gamma is thus larger if the *random forest*'s prediction is closer to one. Accordingly, in the case of the gamma/hadron separation the class prediction is hereafter called `gammaness`. The features used for this step are listed in appendix A.4.1.

4.4.3 Estimation of the Residual Background in Wobble Mode

The telescope can be operated in Wobble-Mode. This mode provides a simultaneous measurement of gamma showers from the observed point source and a residual, isotropic background that survives the gamma/hadron separation. A sketch of this observation mode is depicted in figure 4.9.

In Wobble-Mode, the pointing is moved to a location on a ring around the camera center. In the case of FACT, the radius is typically 0.6°. The location of the source on this ring is called the ON-position and is chosen arbitrarily. Additionally, a set of evenly distributed locations of OFF-positions is defined on the same ring. This mode has the benefit of measuring the background simultaneously with data from a source. The number of OFF-positions is a matter of choice. This work uses five OFF-positions in order to have enough statistics and to avoid an overlap of neighboring OFF-positions with the ON-position.

During data taking the pointing of the telescope is altered in order to compensate for inhomogeneities of the NSB, e.g., due to stars in the FOV. The ON-position can thus be at different locations of the ring around the camera's center. The number of these altered positions is also arbitrary. In the case of FACT, typically two opposite locations are selected.

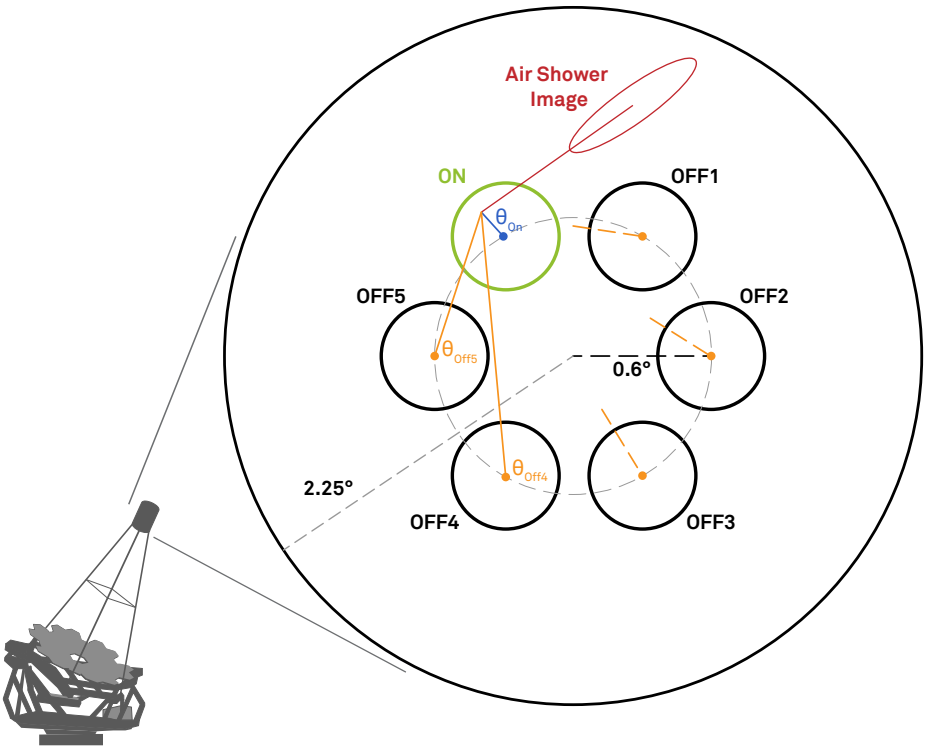

Figure 4.9: Sketch image to describe the Wobble-Mode, which allows for simultaneous measurement of signal and background. The camera pointing is adjusted with the actual source position off-axis by 0.6°. The `angular_distance` (θ) between the reconstructed and actual source position can therefore be determined for each shower with regard to the ON-position (θ_{On}) and five OFF-positions (θ_{Off_n}). The illustrated situation shows a shower coming from the source's region. Gamma-ray events from a point source at the ON-position accumulate in its vicinity, while the diffuse background is distributed isotropically over the camera and would cause a uniform distribution of θ^2 regarding the OFF-positions.

The simultaneous estimation of the background is achieved by deriving the angular distance θ of a shower's reconstructed source position[12] with regard to both the ON-position (θ_{On}) and the OFF-positions (θ_{Off_n}). The reconstructed origins of gamma showers from an observed source are expected to accumulate near the ON-position. On the other hand, the source positions of misclassified events, which survived the gamma/hadron separation, are isotropically distributed in the camera. The OFF-positions are thus used to estimated their contribution to the distribution of gamma-like events near the ON-position.

[12] see section 4.4.1, equation 4.3.

With this procedure, the number of signal and background events are counted for a given data set of observations. The number of signal events N_{on} is counted in the neighborhood of the ON-position, whereas the number of background events N_{off} is derived in the five OFF-positions. This neighborhood is defined by constraining the `angular_distance` (θ) to a certain maximum. These numbers allow for the determination of a detection significance of an observed source as described in the following.

4.4.4 Significance of Detection

In gamma ray astronomy, it is common to determine the statistical significance of detection of an observed source with the Li&Ma significance [74]:

$$s(N_{\text{on}}, N_{\text{off}}, \alpha) = \sqrt{2 \cdot \left(N_{\text{on}} \ln \left[\frac{1+\alpha}{\alpha} \left(\frac{N_{\text{on}}}{N_{\text{on}} + N_{\text{off}}} \right) \right] + N_{\text{off}} \ln \left[(1+\alpha) \left(\frac{N_{\text{off}}}{N_{\text{on}} + N_{\text{off}}} \right) \right] \right)}. \tag{4.4}$$

In this equation, N_{on} is the number of events from the source and N_{off} the number of background events. α is the weight determining the ratio between the number of background and signal measurements. In the case of a measurement in Wobble-Mode, as described in section 4.4.3, α is the reciprocal number of OFF-positions, and $N_{\text{on,off}}$ are the event quantities in the according positions.

4.4.5 Sensitivity

The sensitivity of an IACT is mainly determined by its optical components (mirror area and reflectivity), the quantum efficiency of its sensors (here SiPMs), and the final trigger threshold [92]. In the gamma-ray community, Crab Nebula measurements are utilized in order to determine the sensitivity of the system. This property can thus be used to compare different IACTs with each other. The sensitivity is determined as the minimum flux of the Crab Nebula giving $5\,\sigma$ significance of detection (Eq. 4.4) within 50 h effective observation time [11]:

$$s\left([S_{\text{rel}} \cdot (N_{\text{on}} - \alpha \cdot N_{\text{off}}) + \alpha \cdot N_{\text{off}}] \cdot \frac{50\,\text{h}}{T_{\text{obs}}}, N_{\text{off}} \cdot \frac{50\,\text{h}}{T_{\text{obs}}}, \alpha \right) = 5\sigma \tag{4.5}$$

This expression contains the relative sensitivity $S_{\text{rel}}(N_{\text{on}}, N_{\text{off}}, \alpha, T_{\text{obs}})$ and is determined numerically for a given sample of observations.

Differential Sensitivity

In order to determine the performance of a telescope for sources with a spectral shape different to that of the Crab Nebula, the differential sensitivity is computed. According to the definition commonly used in gamma-ray astronomy, the sensitivity is evaluated separately in narrow energy bins in a logarithmic scale [76].

4.5 Reconstruction of the Energy Spectrum

Deriving the gamma-ray flux coming from an observed source is one of the main goals of an analysis in gamma-ray astronomy, as it is a proxy to the properties of that source. This section summarizes the required steps to determine the differential gamma-ray flux, also known as energy spectrum. The mathematical formulation of the differential energy spectrum is provided in the following section 4.5.1.

In order to derive this spectrum, the energies of gamma rays have to be estimated based on the image parametrization described earlier in this chapter, which is addressed in section 4.5.3. Due the detector's limited and energy-dependent efficiency, a limited energy resolution and a remaining bias of the this method, the actual energy spectrum is not directly measured. This restriction is compensated by facilitating deconvolution or unfolding as introduced in section 4.5.4. The detection efficiency, also being called detector acceptance, requires a correction of the event rates, which is determined on MC simulations as described in section 4.5.2.

4.5.1 Differential Energy Spectrum

The differential photon spectrum[13] (also known as energy spectrum) is defined by the differential gamma-ray flux of a given source:

$$\frac{\mathrm{d}F}{\mathrm{d}E}(E) = \frac{\mathrm{d}N_\gamma}{\mathrm{d}E\,\mathrm{d}A_{\mathrm{eff}}\,\mathrm{d}t_{\mathrm{eff}}}. \tag{4.6}$$

In this equation A_{eff} is the effective collection area and t_{eff} is the effective observation time of the observed source [103]. $\mathrm{d}N_\gamma$ is the number of gamma events per energy bin $\mathrm{d}E$. A_{eff} is further described in section 4.5.2. In the case of FACT, t_{eff} is calculated from the observation's duration and the detector efficiency, which is determined by the trigger dead time. Both values are stored in a database for every single run.

[13] A good summary and a general overview of a typical gamma ray analysis is given in the PhD thesis of Robert Wagner [103].

The light curve is defined as the energy spectrum discretized in time bins. In this case equation 4.6 changes to:

$$\frac{\mathrm{d}F}{\mathrm{d}E}(E,t) = \frac{\mathrm{d}N_\gamma}{\mathrm{d}E\,\mathrm{d}A_{\mathrm{eff}}(t)\,\mathrm{d}t_{\mathrm{eff}}(t)} \tag{4.7}$$

The integral flux is used in case the amount of observations do not allow a light curve or a spectrum to be compiled, as defined above. In this case, equation 4.6 is integrated over the whole energy range above a given energy E_0:

$$F_{E>E_0}(E,t) = \frac{\mathrm{d}N_\gamma(t)}{\mathrm{d}A_{\mathrm{eff}}\,\mathrm{d}t_{\mathrm{eff}}} \tag{4.8}$$

4.5.2 Effective Collection Area

The effective collection area is equivalent to the detector acceptance. It combines the area in which air showers are observable with the telescope's detection efficiency at gamma level [103]:

$$A_{\mathrm{eff}}(E,\theta) = \int_0^{2\pi}\int_0^{\infty} \epsilon(E,\theta,\phi,p)\; p\,\mathrm{d}p\,\mathrm{d}\phi = \epsilon(E,\theta,\phi,p)\cdot A_0(E) \tag{4.9}$$

The detection efficiency is determined from MCs as the ratio of simulated and surviving gamma events:

$$\epsilon(E,\theta,\phi,p) = \frac{\mathrm{d}N_{\mathrm{survived}}}{\mathrm{d}N_{\mathrm{simulated}}} \tag{4.10}$$

In this equation $N_{\mathrm{simulated}}$ represents the number of simulated showers, whereas N_{survived} defines the number of events that survived at gamma level. The collection area A_0 is determined as a circle on the ground around the telescope with the simulated, maximum impact parameter p of extensive air showers as radius:

$$A_0 = 2\pi \cdot p^2.$$

In order to derive the differential energy spectrum, the effective collection area and the effective observation time are used to correct the energy-dependent detection rates. They are determined from an energy estimation of the observed extensive air shower. This energy estimation is presented in the following section.

4.5.3 Energy Estimation

Similar to the particle class, a primary particle's energy cannot be measured directly and so has to be estimated based on features from the image parametrization. The energy regression is done with a *random forest regressor* (see section 4.3.1) that is trained on a sample of gamma MCs. The target value for the training is the energy of a simulated shower's primary particle. As this value is not available in observations, only simulations of extensive air showers can provide ground truth for the training of the *random forest regressor*. In this study the showers are simulated with the software CORSIKA (COsmic Ray SImulations for KAscade) [61], which is discussed in more details in section 5.2.1.

The regression model is trained in a 20-fold *cross-validation* on a set of gamma events simulated in Wobble-Mode. The *random forest*'s settings used for this step are listed in table 4.1. In order to be sensitive to the influence of NSB to the energy estimation, `ped_var` is included as a feature in the training. The features used for this step are listed in appendix A.4.2.

The estimated energies from this procedure alone do not follow the true spectrum, due to a remaining bias and a limited resolution. Their correction is addressed in the following section.

4.5.4 Introduction to Unfolding

Image parametrization based energy regression can only estimate the detectors response to an incoming particle. Unfolding, or deconvolution, of this signal and the detector's properties is thus required to reconstruct the true energy spectrum of the observed source. Such a problem is referred to as an inverse problem and can be described by the Fredholm integral equation of the first kind [24, 51, 78]:

$$g(y) = \int A(x, y)\ f(x)\, dx + b(y)\,. \tag{4.11}$$

In this equation, $g(y)$ is the distribution of observable features y, e.g., the estimated energy, and $f(x)$ the truly generated distribution of energies x, e.g., the source's spectrum. The function $b(y)$ in this equation represents a remaining and known background within $g(y)$. This background is estimated in the OFF-positions introduced in section 4.4.3. $A(x, y)$ is called the response function of the detector and describes all effects[14] involved in producing the observed features. In practice,

[14] This includes the properties of the atmosphere, the creation and propagation of air shower particles, the telescope and camera with all their properties, and the analysis chain up to the point of unfolding.

finding an analytical and continuous description for f, g, A, and b is not feasible. Therefore, the problem must be discretized in order to be solved. MC methods are thus required to determine the response function. From these considerations, equation 4.11 translates to the following linear model:

$$\vec{g} = \underset{m \times n}{\mathbf{A}} \vec{f} + \vec{b}, \tag{4.12}$$

with m, the number of bins in the observables space, and n, the bins in the space of the true distribution. $\mathbf{A}$ is called the response matrix of the detector. The distributions $\vec{g}$, $\vec{f}$ and $\vec{b}$ are understood as vectors in their according spaces. In the case of MC simulations, they are well-known and allow for a computation of the response matrix, which is required for the unfolding. Given $\vec{g}$, $\mathbf{A}$ and $\vec{b}$, the unfolding algorithm is then computing a suitable $\vec{f}$ [24, 78].

4.5.5 The Used Unfolding Algorithm: *funfolding*

The unfolding technique applied in this thesis is implemented in the *python* package *funfolding* [25], which was developed in the course of the PhD thesis of Mathis Börner at TU Dortmund University [24]. The algorithm is based on a Bayesian approach to solving the inverse problem mentioned above. In order to estimate the spectrum, a likelihood function can be formulated as follows:

$$\mathcal{L}\left(\vec{g}|\vec{f}\right) = \prod_{u}^{m} \frac{\lambda_u\left(\vec{f}\right)^{g_u}}{g_u!} \exp\left(-\lambda_u\left(\vec{f}\right)\right) \tag{4.13}$$

This binned likelihood function compares the number of measured events $\vec{g}$ in bins of the observable space with the prediction of a model λ_u, given a vector $\vec{f}$ of the true spectrum. The likelihood is formulated under the assumption that the observable bins in $\vec{g}$ following a Poission distribution with rate $\mathbf{A}\vec{f}$. In the sense of equation 4.12, the model λ_u translates to $\mathbf{A}\vec{f}$ [24].

In order to estimate the likelihood function above, *funfolding* uses the *Markov-Chain-Monte-Carlo method* (MCMC)[15] to estimate the likelihood function. By estimating the likelihood it attempts to model the true (energy) distribution $\vec{f}$ of a dataset with a given set of observables $\vec{g}$.

For the sake of completeness, it should be mentioned that this method also supports regularisation. However, no regularization was used to produce the spectra shown in this thesis.

[15] *funfolding* uses the MCMC implementation from the python package *emcee* [50, 53].

4.5.6 Application of Unfolding and Acceptance Correction

The application of this algorithm and the acceptance correction must be tailored to FACT. They are thus implemented in the dedicated package *fact-funfolding* [82], which is wrapped around *funfolding*. The observables $\vec{g}$ used for the linear model (eq. 4.12) are the estimated energies from 4.5.3. The model $\mathbf{A}\vec{f} + \vec{b}$ itself is then generated in combination with MC simulations of gamma events in Wobble-Mode (the simulations are described in chapter 5.2.2). These gamma events were processed with the whole analysis chain described in this chapter, as sketched in figure 4.1. The *Markov-Chain-Monte-Carlo* based spectrum estimation is finally applied to data from observations and to MC simulations for validation.

The acceptance correction is carried out with the effective collection area, which is calculated from the area in which air showers are observable. Equation 4.9 thus translates to:

$$A_{\text{eff}}(E) = 2\pi \cdot p^2 \cdot \frac{\mathrm{d}N_{\text{survived}}(E)}{\mathrm{d}N_{\text{simulated}}(E)} \tag{4.14}$$

$N_{\text{simulated}}$ and p are set by the MC simulation, i.e., CORSIKA, whereas N_{survived} is a result of each individual analysis in this study. The event numbers of the used simulations are listed in table 5.3. The effective collection area is determined in the same energy bins as the true energy spectrum $\vec{f}$. The differential energy spectrum is then calculated from the unfolding with equation 4.6, given the binned number of unfolded gamma rays $\mathrm{d}N_{\text{survived}}$.

This concludes the summary of the analysis chain and the techniques used in this thesis. In the following chapter, data and simulations are discussed on which these methods are performed.

5 Selection of Data and Generation of Monte Carlo Simulations

The required analysis steps and methods to detect a gamma ray source have been discussed in chapter 4. As this thesis aims to investigate the performance of FACT for different NSB conditions, representative data samples from the Crab Nebula are selected for a variety of light conditions. The selection of these samples and their properties are explained hereafter.

This chapter will also present, the generation of MCs as training data and as the foundation for the later performance analysis. The software and production chain used for these MCs is outlined briefly, alongside two complementary methods to generate NSB events in the simulation.

5.1 Crab Nebula Data Sets

In the gamma-ray astronomy community, the Crab Nebula is widely used as a "standard candle" since its flux is known to encounter no significant variability in the VHE regime. It can therefore be used as a test source to evaluate and compare the performance of different instruments and analyses. The evaluation of FACT's performance for different NSB conditions, as presented in this thesis, is performed on a data sample of the Crab Nebula from the winter period 2015/2016.

5.1.1 Definition of Environment Conditions

In order to use data from well-defined environment conditions, e.g., good weather conditions or low zenith angles, a certain set of constraints to meta attributes of the observations is applied to the data. The FACT collaboration stores such meta attributes in the so-called `RunInfo` database that holds meta information about each run, i.e., a sequence of events measured with FACT.

This analysis is limited to low zenith measurements below 30°. Furthermore, only events with a reasonable trigger rate are selected. The full set of chosen constraints is listed in table 5.1.

5.1.2 Definition of NSB Samples

The Crab sample is further divided into six subsamples with different light conditions. Figure 5.1 illustrates the distribution of runs in these six samples with regard to light conditions at which they where observed. The NSB level of an observation is proportional to the mean current measured of all pixels during the observations, which is stored as `fCurrentsMedMeanBeg` in the `RunInfo` database. Accordingly, the samples are defined in intervals of this attribute. The intervals are selected in equidistant bins of the mean current (see table 5.2), except for the two lowest bins.

The `no moonlight` sample corresponds to so-called "dark night" conditions, which are the best conditions for observations. Prior performance studies on FACT where carried out on a Crab sample from 2013/14 with these conditions. In order to compare the results from this thesis to those studies, the constraints in listing 5.1 are thus applied to the `no moonlight` sample in addition to those in table 5.1.

The number of data runs, data events and observation times resulting after applying these constraints to the samples are illustrated in table 5.2. Furthermore, the third column of table 5.2 contains NSB levels defined as sky brightness in units of the average current of the "dark night" conditions, which corresponds to a mean current of 4 µA.

Constraint (`RunInfo` DB)	Description
`fSourceName` = Crab	Selection of the gamma source
`fNight` $\geq$ 2015-09-01	First Night
`fNight` $\leq$ 2016-04-01	Last Night
`fZenithDistanceMean` $>$ 5.5	Minimum zenith angle [°]
`fZenithDistanceMean` $<$ 30.5	Maximum zenith angle [°]
`fTriggerRateMedian` $<$ 85	Maximum of the median trigger rate [a.u.]
`fThresholdMinSet` $<$ (14 $\cdot$ `fCurrentsMedMeanBeg` + 265)	Relation between trigger threshold at beginning of an observation to the mean currents in the camera

Table 5.1: Constraints applied to the meta attributes in the `RunInfo` database in order to obtain the 2015/16 Crab sample.

```
fMoonZenithDistance > 100
fEffectiveOn > 0.95
fTriggerRateMedian > 40
fThresholdMinSet < 350
```

Listing 5.1: Additional cuts on the `RunInfo` database for "dark night" conditions

The observation time, and with it the number of runs and events decreases with the NSB level. The size of the six NSB samples thus also declines with the brightness (see figure 5.1). This has several reasons, e.g.:

- FACT's observation strategy aims to maximize good quality observations by switching to a different source as soon as the current source is too close to the Moon or the horizon.
- For safety reasons, FACT is only operated when the MAGIC shift crew is present on site. Consequently, it does not take data during the three nights around full moon, which have the highest NSB even though it would be technically possible.
- At the brightest light conditions the software that controls the trigger threshold takes longer to adjust the threshold to stabilize the trigger rate.

NSB Sample	Current Interval [µA]	NSB level Interval [NSB units]	Number of Data Runs	Number of Crab Events	Observation Time [h]
no moonlight	(0,8]	(0,2]	999	17 889 056	74.64
low moonlight	(8,16]	(2,4]	386	2 924 550	22.26
slight moonlight	(16,32]	(4,8]	244	1 297 470	17.49
moderate moonlight	(32,48]	(8,12]	115	343 088	8.03
increased moonlight	(48,64]	(12,16]	24	60 298	1.82
strong moonlight	(64,96]	(16,24]	9	12 794	0.40

Table 5.2: Properties of the six NSB samples used in this thesis. The samples are defined by applying the current interval to the `fCurrentsMedMeanBeg` attribute in the `RunInfo` database.

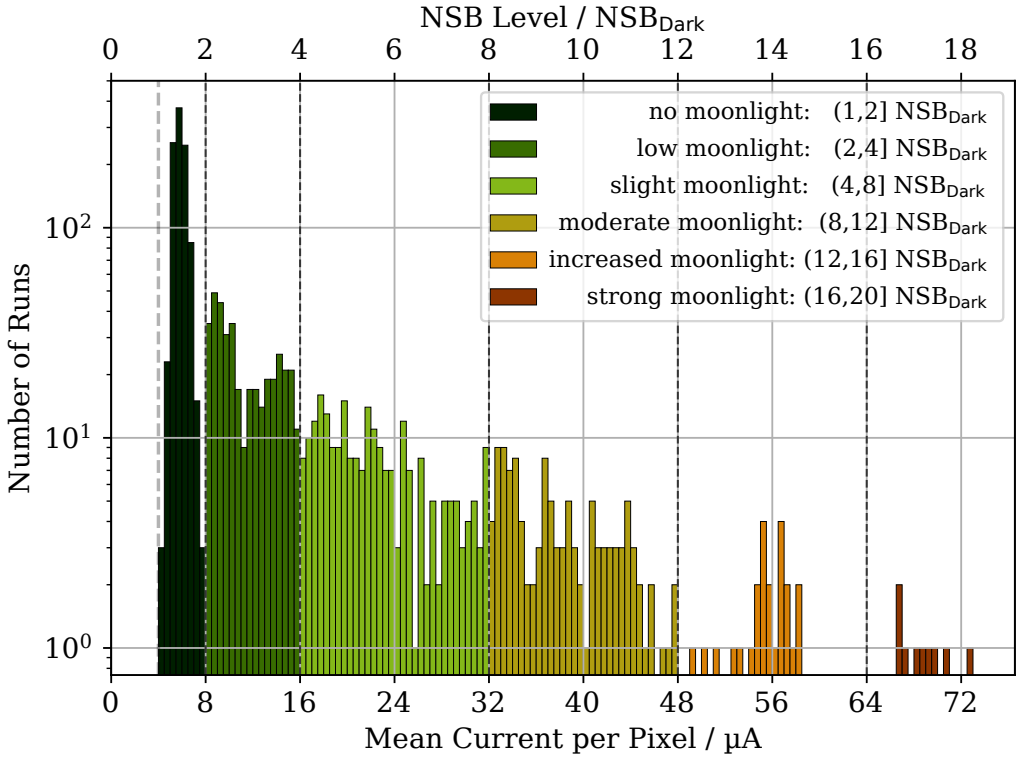

Figure 5.1: Distribution of data runs of Crab Nebula observations with regard to the light conditions at the beginning of the observations. The abscissa represents the average of currents in all pixels at the begin of a run, which correlates with the NSB level. The top axis represents the ambient light in units of dark night conditions referred to as $\mathrm{NSB}_{\mathrm{Dark}}$. The thick grey dashed line marks the $1\,\mathrm{NSB}_{\mathrm{Dark}}$ light level. The six NSB samples used in this study are indicated with the coloring of the histogram. The thin black dashed lines indicate the margins of the samples. The number of runs is decreasing with the NSB since the observation strategy of FACT aims to maximize the number of high-quality low-nsb observations. High NSB observations are therefore rare.

5.2 Monte Carlo Simulations

In gamma-ray astronomy, simulations are the foundation for most analyses. Due to the lack of a test beam, simulations of particle showers are necessary to deliver ground truth for the properties of data and effects to be investigated. In this sense simulations are used in this study for two main purposes:

- Annotating data for the training of supervised machine-learning techniques, i.e., a particle's type/class, its energy, or its location.
- Delivering test sets with well-known properties in order to provide the conventionally used performance measures of the different analysis steps.

In particle physics, such simulations are typically based on the so-called Monte Carlo technique, which is used to sample the behavior of the physical processes involved [20]. Monte Carlo simulations (MCs) in gamma-ray astronomy generally consist of two main steps:

I. the simulation of air showers from different primary particles (in the atmosphere) and

II. the simulation of the particle detector (i.e., telescope and camera).

In the case of FACT, air showers are simulated with CORSIKA (COsmic Ray SImulations for KAscade) [61]. The simulation of FACT in particular, its reflector and camera electronics, is realised with CERES (Camera Electronics and REflector Simulation), which is an executable in the ROOT-based framework MARS CheObs (Modular Analysis and Reconstruction Software - Cherenkov Observatory Edition [28, 30]. The files of the first production step mainly contain quantities and locations of the Cherenkov photons produced in a shower. The output of CERES is stored in FITS files [7] and contains time series of the pixels' response to the extensive air shower, as does the data from observations. The production chain used, notably these two software components and the settings used for the simulations, are outlined in the following. Special focus is placed on the simulation of the SiPMs. Furthermore, the simulation of NSB levels as compared to those in section 5.1.2 is explained in more detail.

5.2.1 Air Shower Simulations with CORSIKA

CORSIKA is a software package for the simulation of extensive air showers that are initiated by high energy cosmic particles. It allows for a variety of primary particles, e.g., photons, protons, and light or heavy nuclei up to iron. The package

is responsible for simulating the propagation and decay of the primary particle and its cascade of secondaries in the atmosphere [61].

The choice of interaction models is modular in CORSIKA and depends on quality and runtime constraints as specified by the user. The extensive air showers in this study were simulated with the following combination of interaction models:

- low-energy hadronic interactions ($< 80\,\mathrm{GeV}$):
  FLUKA (FLUktuierende KAskade)[49] is responsible for inelastic hadron cross-sections with the components of air [62].

- high-energy hadronic interactions ($\geq 80\,\mathrm{GeV}$):
  QGS-JETII (Quark Gluon String model with JETs) [85] is utilized for elastic hadron-nucleon scattering at higher energies, including minijets to describe the hard interactions [62].

- electro-magnetic interactions:
  EGS4 (Electron Gamma Shower) [81] is responsible for the coupled transport of electrons and photons at energies between some keV to several hundreds of GeV [62].

The simulations used in this thesis were produced with an adapted version of CORSIKA (Version 6.005), called MMCS (MAGIC Monte Carlo Simulation), that mainly samples a wavelength for the Cherenkov photons and manipulates the impact plane of the photons on the ground.

In order to provide training data for the gamma/hadron separation, both point source gamma events and isotropically distributed protons are simulated. The main settings of the CORSIKA simulation runs are summarized in table 5.3. The input-cards[1] are listed in appendix A.1.

The settings, in particular energy range, impact, and viewcone, were estimated large enough to contain all (or at least the vast majority) of the showers that FACT might be able to see. The slope of the proton's energy spectrum was selected with regard to the spectral index of the cosmic-ray flux from [16]. In the case of the gamma ray's energy spectrum, a slope $\alpha = -2.7$ that is close to that of Crab but not exactly the same value as was measured by other telescopes (e.g., [6]: $\alpha_{Hegra} = -2.62$), was chosen. The simulation of protons requires a lot of computation time. The protons were thus simulated with the Reuse option, which reuses a shower for different, simulated telescope locations in order to reduce the production time. As for the observations, low zenith angles were produced.

[1] This is what CORSIKA calls a config file used for a simulation run.

Simulation settings	Proton	Gamma
Energy range	100 GeV to 200 TeV	200 GeV to 50 TeV
Slope of the simulated spectrum	-2.7	-2.7
Viewcone	5°	0°
Event reuse	20	0
Maximum impact parameter	400 m	270 m
Zenith range	(0 – 30)°	
Azimuth range	(0 – 0)°	
Atmosphere	Atmospheric Model 11 (MAGIC winter)	
Number of resulting events	780 046 520	18 000 000

Table 5.3: Settings for simulations of proton and gamma sets with CORSIKA.

The resulting event quantities are also listed in table 5.3. The events are stored in output files containing information about the impact locations and wavelength of the Cherenkov photons, and about the simulated showers. In the next simulation step, these files are read into CERES and the simulation of FACT is performed.

5.2.2 Telescope Simulation with CERES

The program CERES is responsible for the simulation of the telescope and its response to the Cherenkov photons. CERES is part of the framework MARS, which is implemented in C++ and uses ROOT as its underlying platform [28, 30]. It is publicly available at [29]. CERES follows a modular design strategy to reconstruct the signal path of the Cherenkov photons and to adapt the order of physical effects they are confronted with. For this it provides routines, i.a., for the following effects and components:

- **Atmospheric absorption**: Acceptance of incoming photons with regard to their wavelength or incident angle due to absorption by Rayleigh scattering, ozone and aerosols (Mie scattering).

- **Light of the night sky background (NSB)**: Calculation of the NSB rate by either sampling photons from the NSB spectrum and folding them with all acceptance effects or sampling with a given rate from a Poisson distribution.

- **Optical system/Reflector**: Reflexion of photons in the mirrors and acceptance with regard to reflectivity and point spread function (PSF) of the mirrors.
- **Light guides**: Angular acceptance and transmission of photons entering the Winston-Cones towards the SiPMs.
- **Photon detectors**: Response of SiPMs to photons and simulation of their properties, e.g., PDE, dark counts, crosstalk, and afterpulses.
- **Camera electronics**: Simulation of the electronic components, i.a., data acquisition (DAQ) and trigger electronics, including electronic noise and the formation of a pixel's time series with regard to a photon's pulse shape.

The settings of these components are controlled via a config-file.[2] This allows the properties of these components to be modified with the aim of producing simulations at different conditions of FACT and its environment. Furthermore, the settings of these components are used to tune the simulations to observations in order to reduce Data-Monte-Carlo mismatches.

The effects and components most relevant for this thesis are explained briefly in the following. Details about the simulated effects are documented directly in the MARS code [29]. The simulation of different NSB levels is discussed in greater detail in section 5.3.

Optical System The Cherenkov photons from CORSIKA are further processed in CERES. For this purpose, their trajectories are transformed into the telescope's coordinate frame with regard to the telescope's pointing position. The reflector simulation reflects the photons on the mirrors and stores those which hit the focal plane. Photons hitting the camera or its holding before hitting the mirrors are rejected. The normal vector of each mirror is blurred with a random Gaussian to emulate the single mirror PSF. All photon-absorbing processes, i.e., atmosphere,

PDE, mirror reflectivity, and transmission of the light guides, are simulated via rejection sampling [90] with their (empirical) probability density function (PDF) regarding the wavelength of the photons. The incident angle of the photons is utilized in the same manner for the PDF of the light guides' angular acceptance.

In the used version of CERES, NSB photons are not propagated through the reflector simulation. However, the mirror area is considered and the absorption effects are applied to the NSB photons. Nevertheless, direct starlight is not simulated in the current version.

[2] In CERES the term "rc-file" is used. Examples of a config file are presented in appendix A.2.

Telescope Pointing The general pointing of the telescope is simulated with respect to the direction of the showers origin. However, CERES offers three different scenarios for the pointing relative to the shower's origin, which are steered with the `OffTargetDistance` setting:

I. On-target Mode: `OffTargetDistance` $= 0°$

II. Wobble Mode: `OffTargetDistance` $> 0°$

III. Diffuse Mode: `OffTargetDistance` $< 0°$

The On-target mode is used for particles with an isotropic distribution (e.g., protons) or in order to have a point-like source (e.g., gammas) in the camera center. The wobble mode allows to simulate Off-target observations with a point-like source at a fixed distance to the camera center. In diffuse mode, `OffTargetDistance` defines a radius of a disk around the camera center. The pointing position is randomly distributed in this disk. This allows CERES, for example, to simulate diffuse gamma events.

SiPM Simulation The SiPMs are simulated on a microscopic level, in the sense of simulating individual G-APDs. Their properties (e.g., crosstalk, dead-time, recovery-time, and afterpulse) are defined in the config-file.

At first, the PDE is applied to the list of remaining photons, given their wavelength. Dark counts are treated as random photons. Thus, the dark count rate and NSB rate are combined. NSB and Cherenkov photons are processed in the chronological order of their arrival time at a pixel. For each photon a random G-APD is sampled. Photons hitting a G-APD during its dead-time are ignored. Otherwise, the photon is further processed.

The recovery-time, which determines the pulse amplitude, is taken into account to simulate crosstalk and afterpulses, as their probability depends on the signal amplitude. Crosstalk events are sampled from a Poisson distribution, whereas the afterpulses are produced via rejection sampling from the experimental afterpulse probability density functions. Signals generated due to these two effects are processed recursively equal to the list of photons. With this procedure, SiPMs are simulated accurately, which was determined by comparing data and simulations on a single photon level as shown in [39].

Electronics Simulation The simulation of the camera electronics is responsible for generating the voltage curves as measured in the FACT camera. By applying the typical SiPM pulse shape to the photon arrival times, a continuous time series is achieved. Electronic noise is added to the time series as white noise with Gaussian sampling. The timing of individual photons or pixels can be manipulated to add time jitters and shifts as they occur, e.g., due to cabling.

In the simulation of the DAQ the time series is descretized to time slices of 500 ps. However, in the current version of CERES a complete simulation of the DRS4 has been omitted so far.

The trigger simulation operates on the continuous time series. The simulation is implemented analog to the real trigger with a summed signal of 9 pixels, cable clipping, a time-over-threshold discriminator, and the typical trigger logic (N-out-of-4 trigger coincidence and N-out-of-40 primitives) of FACT. The trigger threshold can be modified in the config-file. Once an event has exceeded the trigger threshold, it is digitized and written to a FITS file [7].

Simulation of Gamma Events in Diffuse and Wobble Mode The gamma events used in the following are simulated with two different pointings. For the training of the gamma/hadron separation and for the performance tests, gamma events were simulated in Wobble-mode with `OffTargetDistance` $= 0.6°$. This is the same off-axis distance that was used for the Crab obervations.

For the training of the `DISP` method,[3] diffuse gamma showers were randomly located within a 3° radius to the camera center, with `OffTargetDistance` $= -3.0°$.

5.3 NSB Simulation

The simulation of different NSB conditions is mandatory for the studies in this thesis. Two different approaches are evaluated. CERES provides an inherent method to generate NSB photons, used by all prior studies on FACT. Additionally, a method based on NSB measurements was developed for FACT and implemented in a master's thesis (see [36]) supervised by the author of this thesis. Both methods are described and compared in the following.

[3] see chapter 4.4.1

5.3.1 GenNSB: Generation of NSB Photons by Sampling a Poissonian

The inherent method of CERES to simulate NSB photons samples their arrival times according to an exponential distribution, given a defined event rate (NSB rate). The number of NSB photons in the pixels thus follows a Poisson distribution. This approach generates each NSB photon for each pixel separately and is herafter referred to as NSB simulation with generated night sky photons (GenNSB).

The generated photons are added to the list of Cherenkov photons from the shower simulation. The final signal, in the sense of the time series in a pixel, is essentially generated by superimposing the single photon pulse shapes of all photons of a pixel. Higher light conditions are generated by increasing the mentioned NSB rate. The NSB rate can either be set as a value in the CERES config or by providing a measured NSB spectrum (wavelength distribution) for a certain light condition. In the latter case, this spectrum is folded with the acceptance PDFs mentioned earlier and a NSB rate is calculated from that.

However, a disadvantage of sampling single NSB photons is that the runtime of the simulation increases massively with higher NSB rates, since every NSB photon is sampled individually. Simulating high rates, as required for this thesis, would cause additional simulation times of several months for different light conditions. This method was therefore avoided for light conditions other then “dark night”.

5.3.2 ObsNSB: Sampling of NSB Events from Observations

An alternative approach to simulating different NSB levels utilizes so-called pedestals that mostly only contain random photons from the NSB and noise from the SiPMs. These measurements are conducted on a regular basis along with observations of FACT before each set of observations and within each run as interleaved pedestals. Accordingly, they contain the same ambient light conditions as these observations.

The principle idea of this NSB simulation approach is to superimpose simulated air showers with measured pedestal events. These pedestal events are thus sampled from the same distribution of NSB conditions as the observations to be analysed. The benefits of this procedure are simulated air showers with a defined energy, particle type, direction, and an NSB that corresponds to the actual ambient conditions of the observed showers.

This method is hereafter referred as ObsNSB (Observed night sky background superimposition) and is implemented in a subpackage of *fact-tools*. It is based on a concept[4] used in MAGIC to simulate higher order NSB levels.

In contrast to NSB simulation with generated night sky photons (GenNSB), the runtime of a simulation with ObsNSB is not affected by the NSB rate since full time series of 300 time slices (150 ns) are superimposed with the simulated time series of air showers from CORSIKA and CERES. Additionally, any other artifacts from the camera , e.g., noise from the DAQ (DRS4 chip), electronic noise, light flasher malfunctions, reflections, or defective pixels, will also be in the simulated data after this step. Acceptance effects of the NSB photons (e.g., mirror reflectivity, cone transmission and angular acceptance) are inherently in the data, as well as star light (e.g., Ceta Tauri for Crab). This method should thus lead to a more realistic simulation of the background in the shower images.

Nevertheless, the NSB photons from this method are not considered in the simulation of the SiPMs. Thus, an increased NSB rate will not cause more G-APDs in dead-time. In fact, at high photon rates the number of detected photons of the SiPM becomes non-linear with the number of incoming photons due to this effect, as presented in [54] and [95]. Consequently, the MCs generated with this method might contain too many Cherenkov photons, while the non-linearity in the NSB photons is inherently contained. This would cause a Data-Monte-Carlo mismatch, increasing with the NSB in image features that are proportional to the number of photons such as the `size`.

Accordingly, the use of ObsNSB is based on the assumption that this effect is negligible for the number of Cherenkov photons in a single pixel adding to the NSB. Nevertheless, a potential influence is investigated with Data-Monte-Carlo mismatch control plots in section 5.4 and section 6.2.6. Furthermore, a comparison of simulations of data with both the standard GenNSB and the adaptive ObsNSB approach at “dark night” conditions is carried out in subsection 5.4.

CERES Simulation for ObsNSB The superposition of pedestals and simulations requires a special configuration of CERES. As electronic noise, dark counts, and NSB photons are already in the pedestals, these components have to be switched off. Accordingly, the settings have to be changed in the CERES config used for the standard simulation (see appendix A.2) to the values in listing 5.2.

[4] No publication for this method was found.

```
MSimRandomPhotons.FrequencyFixed: 0.0   #Dark count rate
MSimRandomPhotons.FileNameNSB:          #NSB spectrum
MSimRandomPhotons.FrequencyNSB:   0.0   #NSB rate
MSimCamera.DefaultNoise:          0.0   #Electronic noise
```

Listing 5.2: Specific CERES settings without noise for ObsNSB. CERES requires a blank in place of the file name in order to simulate NSB according to the NSB frequency.

Superposition of Events for ObsNSB The superposition of events is implemented in *fact-tools* (subpackage fact.pedestalSuperposition) [34]. Both the CERES output and the pedestal files are stored in FITS files. The underlying method in *fact-tools* streams the MC events, samples a random pedestal event, and sums up both time series element-wise regarding the time slices and the pixel. Details of this can be found in [36] and the used *fact-tools* process can be found in appendix A.3.1.

Suitable pedestal files are chosen with the constraints from table 5.1, in order to fulfill the same environment and quality conditions as the Crab data. Additionally, the samples for the NSB conditions are again defined by applying the constraints in table 5.2 to the pedestal files. Random sampling with replacement of the events of such a set of pedestal files is utilized with the aim of gaining a random pedestal event composition and to enrich its quantity. To minimize a potential bias of changing NSB with the zenith of the observation, MCs and pedestals are binned in zenith bins of width 3°. The brighter light conditions have a larger zenith binning with 6° for increased and 9° for strong moonlight because they contain fewer events than the lower NSB levels.

The random sampling is performed on a database [37] holding information about all pedestal events (i.e., `night`, `run_id`, `event_id`, `event_type`, and `run_type`), joined with additional information from the `RunInfo` database (i.e., currents and zenith angles of the observations) for the constraints mentioned. This procedure allows for saving runtime and I/O for sampling from the pedestal files.

After superimposing, the events are stored again in a FITS file. With the procedure outlined above, MCs with the same light conditions as the Crab data are generated. ObsNSB MCs were generated for all three particle types, protons, (Wobble-Mode) gammas, and diffuse gammas.

5.3.3 Resulting Monte Carlo Sets from ObsNSB and GenNSB

The properties of the MC sets[5] simulated with ObsNSB and GenNSB are listed in table 5.4. It provides additional information on the ObsNSB MCs and the pedestals used. The pedestal event numbers shown are reached by using both pedestal runs and interleaved pedestal events from the data runs. The number of pedestal events also fall with higher NSB. Only a few thousand events are thus available at the highest light conditions. The sampling with replacement mentioned above is therefore a compromise in order to generate NSB events for these sets. Furthermore, the larger zenith binning for these two light conditions binnings also mentioned above was chosen in order to find enough matching pedestals.

The comparison of event numbers after CERES show fewer ObsNSB than GenNSB events in general. This is an effect of the simulated trigger threshold. The trigger threshold was not changed when simulating without NSB. For this reason, those events triggered only due to NSB are contained in GenNSB but not in ObsNSB.

[5] Note that the simulated event numbers are lower for the increased moonlight sample due to a failure in the processing with *fact-tools*. A few runs were not processed because of this malfunction.

Properties of sample	GenNSB	no moonlight	low moonlight	slight moonlight	moderate moonlight	increased moonlight	strong moonlight
Current [µA]		(0,8]	(8,16]	(16,32]	(32,48]	(48,64]	(64,96]
NSB level [NSB units]		(0,2]	(2,4]	(4,8]	(8,12]	(12,16]	(16,24]
Pedestal Zenith:							
Min. [°]		6.36	6.36	6.36	6.36	7.78	9.25
Max. [°]		30.45	29.33	30.25	30.03	30.49	30.32
Number of events (in thousands):							
pedestals		277.9	82.88	65.11	29.88	6.78	1.5
proton	509.65	467.19	467.19	467.19	467.19	425.01	467.35
gamma (wobble)	2 870.62	2 703.36	2 703.36	2 703.36	2 703.36	2 432.96	2 704.32
gamma (diffuse)	1 244.26	1 162.25	1 162.25	1 123.61	1 162.25	1 045.69	1 170.76

Table 5.4: Properties of proton and gamma simulations with GenNSB and ObsNSB. Event numbers are rounded to thousands with two digits and illustrate how many of the showers of CORSIKA survive the trigger of CERES. The minimum and maximum zenith angles of pedestals indicate the zenith range from which pedestals where sampled for the superimposition.

5.4 Comparison of ObsNSB and GenNSB with Crab Nebula Data

The adaptive ObsNSB approach is prospected to deliver a more realistic simulation of the background due to ambient light conditions. In order to identify the improvement or possible flaws of this approach compared to the standard simulation GenNSB, simulations with both methods are compared to data taken with FACT. For this purpose proton simulations are generated at dark night NSB conditions. The observation data are from a Crab sample from winter 2015/2016. Only quality pre-cuts defined in listing 5.3 were applied to all three samples in order to reduce well-known remaining Data-Monte-Carlo mismatches.

```
num_pixel_in_shower >= 10
        num_islands <  8
              width <  35
           leakage1 <  0.6
           leakage2 <  0.85
             length <  70
```

Listing 5.3: Quality cuts used in this study to reduce remaining Data-Monte-Carlo mismatches.

No classification cuts were applied to the Crab sample. We can therefor assume that this sample is dominated by hadrons and a comparison with proton MCs is valid.

The distributions of image parameters of shower events after image cleaning are compared. For this purpose, representative spatial and temporal image parameters are investigated, namely, the Hillas parameters `width`, `length`, and `size`, as well as the concentration of Cherenkov photons at the center of gravity of the light distribution (`concentration_cog`), the mean variance of the pedestal signals of non-shower pixels (`ped_var_mean`), and the average arrival time of photons in all pixels of the camera (`arrival_time_mean`). The feature distributions are illustrated in figure 5.2.

Spacial attributes, such as the `length`, the `width` and the `concentration_cog`, show no signifficant difference between GenNSB and ObsNSB, apart from a reduced rate (see figures 5.2a, 5.2f, and 5.2e). Compared to the Crab data no improvement is visible. The `size` distributions agree for both methods, as shown in figure 5.2b.

Differences between both methods are visible for all features that are either extracted or contain information from non-shower pixels. This is, e.g., the case for the

`arrival_time_mean` as it contains arrival times from both shower and non-shower pixels (see figure 5.2c). In the case of this feature, the distribution of ObsNSB is closer to the Crab data. The `ped_var_mean` is also improved by use of ObsNSB. Nevertheless, in both distributions a difference between the data and MCs is still visible.

Discussion The main goal of ObsNSB is to provide a more realistic NSB background. Accordingly, it should mostly be affecting features that represent this background. This is the case for these kinds of features, as shown above.

Furthermore, features extracted based on shower pixels should not be impaired by ObsNSB at dark night conditions, as these pixels should not be dominated by NSB photons. The distributions of the spatial features of GenNSB and ObsNSB are in first order in good agreement and show mostly the same differences to the Crab sample.

In conclusion, using ObsNSB provides a more realistic NSB background than GenNSB without impairing shower features that are crucial for the further analysis. Thus, the further analysis steps are based on the assumption that ObsNSB simulations at higher NSB levels provide still valid results, which is investigated in chapter 6.2.6.

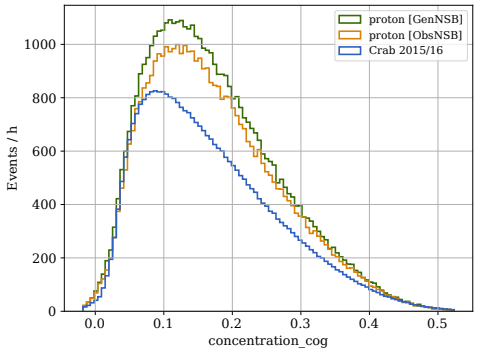

(a) Concentration of Cherenkov photons at the center of gravity of the light distribution (`concentration_cog`).

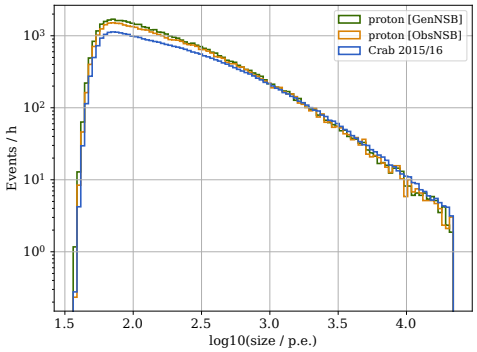

(b) Total number of photons in the shower pixels (`size`).

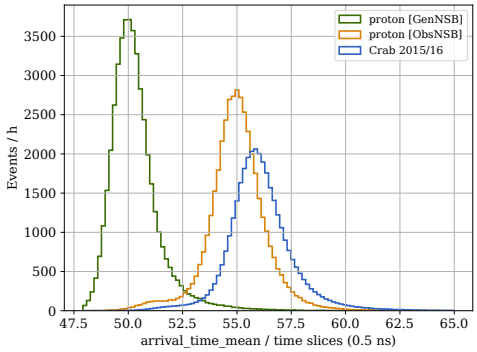

(c) Average arrival time of photons in all pixels of the camera (`arrival_time_mean`).

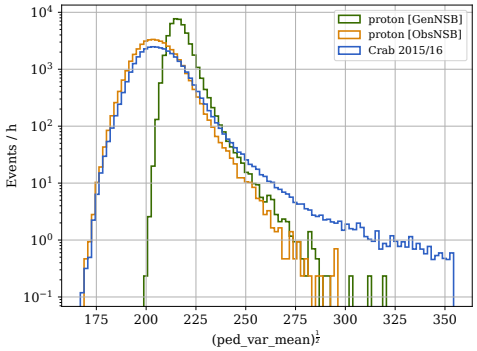

(d) Mean variance of the pedestal signals of non-shower pixels (`ped_var_mean`).

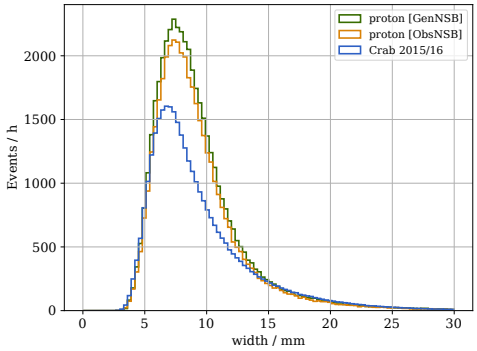

(e) Width of the light distribution along a shower's semi-minor axis (`width`).

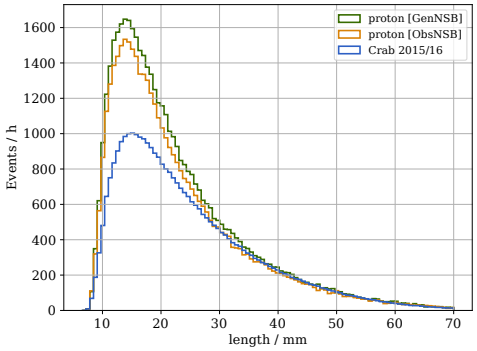

(f) Length of the light distribution along a shower's semi-major axis (`length`).

Figure 5.2: Comparision of image parameter distributions of Crab Nebula data and simulations with ObsNSB and GenNSB. The Crab Nebula data and the pedestal data for ObsNSB were taken at $(0-2)\,\mathrm{NSB}_{\mathrm{Dark}}$. The horizontal axis represents the values of the extracted image parameters, while the vertical axis provides the event rates. The event rates have been normalized to observation times in order to compare distributions from data and MCs.

6 Analysis Optimizations at Various Light Conditions

The general analysis chain and the data sets used for this thesis have been discussed in the previous chapters. As mentioned before, the objective of this thesis is to investigate the performance of FACT at different light conditions. Thus, the analysis chain has to be optimized to provide the best possible results at these conditions.

Chapter 4.2.3 already addressed the fact that the image cleaning needs to be optimized and adapted to the light conditions encountered. Features from the image parametrization are likely to be influenced by the NSB, which may have potential consequences for the machine-learning steps and the results at gamma level.

Consequently, the aim of this chapter is to provide optimized settings for the analysis chain described in chapter 4. In particular, the cleaning will be optimized and based on that, suitable machine-learning models are trained. For this purpose, the ObsNSB MCs from chapter 5 will be used, as they contain the ground truth required for the optimization. The chapter is structured as follows.

At first, it will explain how the ObsNSB simulations are prepared for the image cleaning. This involves the development and application of a trigger emulation for the MCs, which is necessary since in the real world the trigger threshold is adapted to the light conditions.

Afterwards, a strategy to optimize cleaning levels for different light conditions is proposed and carried out. How and which cleaning levels were found for the performance analysis will be discussed. The impact of the cleaning levels on the performance of the machine-learning steps is investigated and compared to the standard cleaning levels. Alongside the image cleaning, the two NSB simulation techniques are compared with each other in order to determine whether there is a potential improvement in machine-learning performance.

Finally, a set of suitable cleaning levels will be selected. Based on this step, feasible values for the prediction threshold (`gammaness`) and the `angular_distance` (θ) limit will be selected for the performance analysis in chapter 7.

6.1 Trigger Emulation for the ObsNSB Simulations

The cleaning optimization in section 6.2 requires similar properties of data and MCs. Unfortunately, simulations with ObsNSB take place after the trigger simulation. Without the trigger, events that otherwise would have been discarded remain in the sample and may impair the result of the optimization. Furthermore, during observations the trigger threshold is adapted to rising NSB levels. A posterior emulation of the trigger's behavior is thus necessary.

A software trigger with a similar behavior to that of the hardware trigger[1] has been implemented in *fact-tools* within the course of this study.[2] This software trigger applies a given threshold to observed and simulated events, thus guaranteeing that the same selection process is applied to both. The threshold is applied to the summed signal of 9 adjacent pixels. In order to determine valid thresholds the conversion from software trigger to hardware trigger thresholds (back and forth) is required.

The emulation of the trigger signal in the software trigger has been applied to Crab observations in order to determine feasible thresholds. All events in the observed data obviously survived the hardware trigger. They are used to determine the highest possible software threshold (T_{max}) to keep all of them. This minimal T_{max}, hereafter called $\min(T_{\mathrm{max}})$ is determined for each run. This value is then related to the current at the beginning of the run, as this represented the NSB conditions before the run started. The current at the beginning of a run has been also stored in the `RunInfo` data base.

The behavior of $\min(T_{\mathrm{max}})$ is shown in figure 6.1. The software trigger criterion found shows a similar behavior to that of the hardware trigger and rises continuously with the NSB level. Nevertheless, the threshold values of the software trigger are smaller than those of the hardware trigger. This is due to an unknown conversion factor of DAC units of the hardware trigger to the units of the software trigger. A power function is fitted to the data points to extract the following simple model for an estimate of a trigger criterion based on the light conditions:

$$T\left(I_{\mathrm{beg}_{\mathrm{mean}}}\right) = (41.2 \pm 7.6)\,\frac{1}{\mu\mathrm{A}} \cdot {I_{\mathrm{beg}_{\mathrm{mean}}}}^{(0.5510 \pm 0.0003)}. \tag{6.1}$$

For the following optimization of cleaning levels, this trigger threshold is applied to every event according to the mean current of the pedestal file used for the superposition in ObsNSB.

[1] The behavior of the hardware trigger is explained in section 3.2.2

[2] The initial idea for this software trigger was implemented in the MARS analysis chain and was presented in [63].

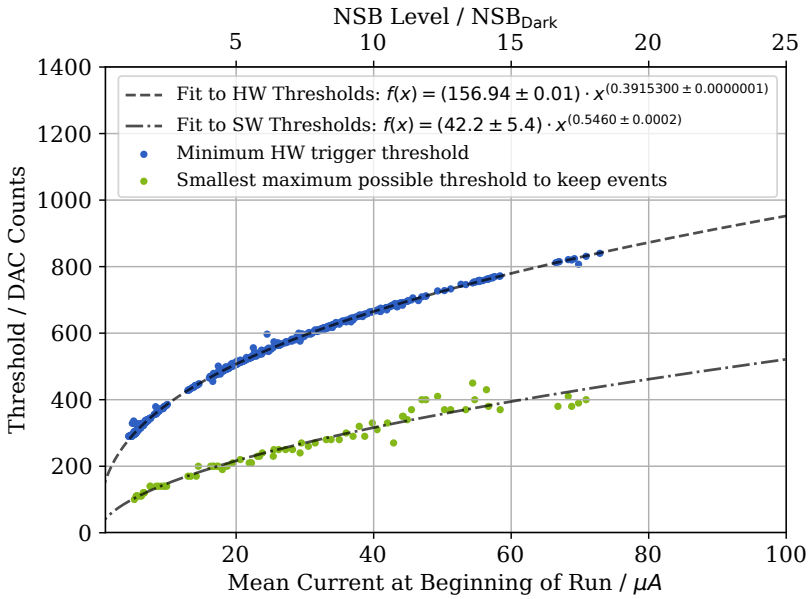

Figure 6.1: Distribution of the determined software trigger threshold estimate $\min(T_{\max})$ (green) and the used hardware trigger's threshold (blue) for observations of the Crab Nebula at various NSB levels. The light conditions are given on the abscissas in units of the camera's average current (bottom) and in units of dark night conditions (top). The dependency of trigger threshold and light conditions is modeled with a power function (dashed lines). The $\min(T_{\max})$ model (dashed dotted line) is used to apply a comparable trigger criterion to both data and MCs.

6.2 Cleaning Optimization

The aim of this section is to find the best possible cleaning levels for various light conditions. It is therefore necessary to define a suitable optimization criterion.

MAGIC, for example, tuned the cleaning for their standard analysis by demanding that only 6 % of pure NSB events survive the cleaning [76]. This criterion is hereafter called *pedestal impurity*. Furthermore, in a study dedicated to Moon observations they found higher cleaning levels for higher light conditions by tuning their cleaning to the *mean number of islands* by constraining it to $\hat{N}_{\text{islands}} \leq 2$ [32]. This is due to the fact that `number of islands` has its origin in the structure of hadron initiated showers, which tend to produce more subshowers than electromagnetic showers. If the cleaning is well tuned to the light conditions, the average number of islands is expected to be independent of them.

In the following, these constraints are investigated for FACT. Furthermore, the fraction of surviving gamma ray events (hereafter called *gamma efficiency*) is introduced as an additional constraint to maximize the number of detected gamma rays from an observed source.

In order to investigate these criteria for different cleaning levels and light conditions, a grid search is carried out on gamma MCs (*gamma efficiency*), Crab data (*mean number of islands*) and pedestal events (*pedestal impurity*). Both cleaning level parameters are scanned in a range of $T_{\text{core}} \in [1.5, 9.5]$ p.e. and $T_{\text{neighbor}} \in [1.0, 9.0]$ p.e. The maximum arrival time coincidence of adjacent pixels ($T_{t_{max}} \leq 10$ time slices ($\hat{=} 5$ ns)) is kept fixed and thus not optimized here. The trigger thresholds from the previous section are applied afterwards.

6.2.1 Mean Number of Islands Criterion

The current standard 5.0-2.5 cleaning ($T_{\text{core}} = 5.0$ p.e. and $T_{\text{neighbor}} = 2.5$ p.e.)[3] is investigated with the suggested *mean number of islands* criterion for different light conditions of Crab observations. Additionally, three exemplary, randomly selected cleaning levels with higher thresholds are tested. If the cleaning is well tuned to the light conditions, the average number of islands is expected to be independent of them. Figure 6.2 shows the NSB dependency of the *mean number of islands* for these cleaning settings.

The blue markers indicate the behaviour of the standard image cleaning. Below $5\,\text{NSB}_{\text{Dark}}$ the *mean number of islands* is almost independent of the light conditions. However, with higher light conditions the *mean number of islands* increases rapidly, which is an effect of the contributions from more intense NSB. As discussed earlier, this effect is reduced with adapted, higher cleaning levels. For the medium light conditions range ($(8-12)\,\text{NSB}_{\text{Dark}}$) a 6.0-4.5 cleaning appears to be feasible given the $\hat{N}_{\text{islands}} \leq 2$ constraint. For more extreme light conditions these thresholds need to be increased again, e.g., to a 7.5-4.0 cleaning.

This behavior of the *mean number of islands* suggests that cleaning levels should be inceased for observations at brighter light conditions. Potentially good cleaning levels aim to minimize the light dependence while keeping core and neighbor threshold as low as possible. This minimization thus requires a criterion of its own.

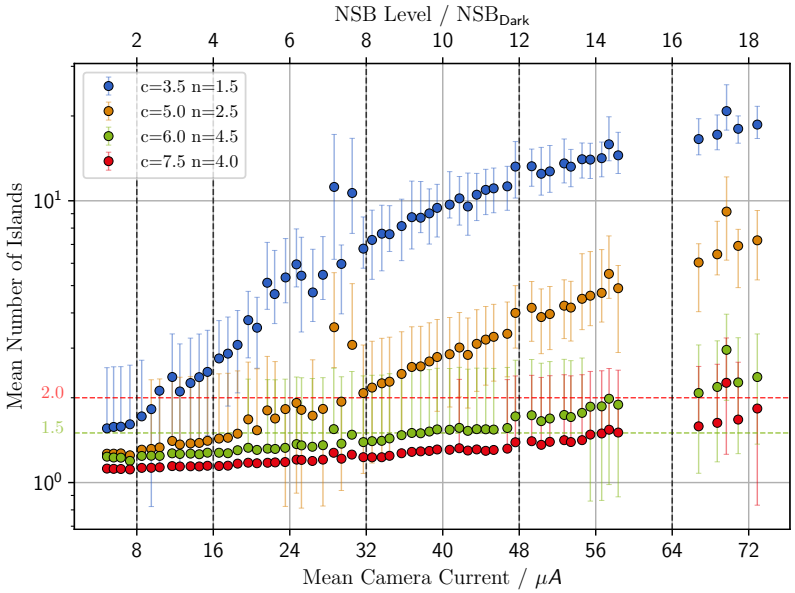

Figure 6.2: Dependency of the average number of islands of the light conditions and three different cleaning levels. The abscissa represents the average of currents in all pixels over the duration of a run, which correlates with the NSB level. The top axis represents the ambient light in units of dark night conditions referred to as NSB_{Dark}. The average number of islands is represented by the ordinate. The standard cleaning levels are marked in blue. Three random, additional higher cleaning levels are marked in orange, green, and red. The $\hat{N}_{\text{islands}} \leq 2$ limit is indicated as a red dashed line. Additionally, a more conservative limit is marked with the green dashed line. The error bars represent the 25th/75th-percentile to indicate the spread of the `number of islands (numIslands)` distribution. The light conditions are structured in 1 µA bins. The vertical dashed grey lines indicate the margins of the NSB samples.

6.2.2 Pedestal Impurity Criterion

An alternative optimization is to constrain the *pedestal impurity* [76]. The cleaning is thus tested on pure pedestal runs with regard to how many events survive the cleaning. The surviving events are those events that would superimpose with the Cherenkov photons of showers during observations. They distort the shower images if the cleaning levels are too low. Thus, the pedestal runs give an estimate for the contribution of NSB noise to the shower images. MAGIC demands a maximum *pedestal impurity* of $< 6\%$.

[3] See section 4.2.3.

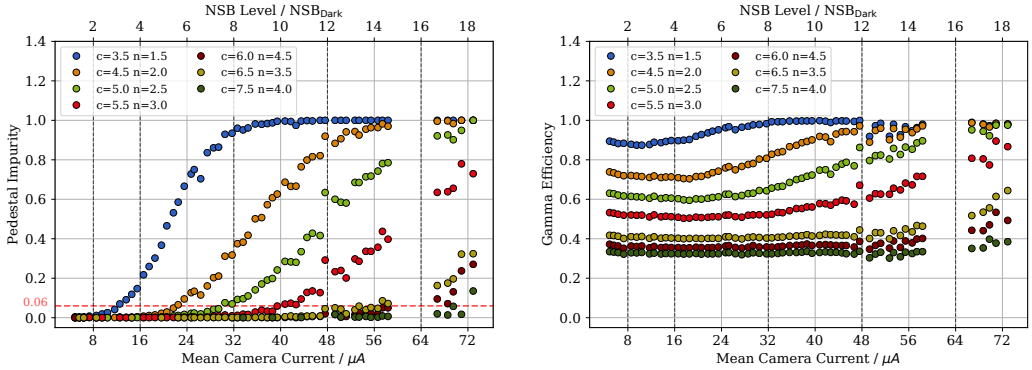

(a) *pedestal impurity* vs. NSB

(b) *gamma efficiency* vs. NSB

Figure 6.3: Dependency of *pedestal impurity* (a) and *gamma efficiency* (b) on the light conditions and three different cleaning levels. The abscissa represents the average of currents in all pixels over the duration of a run, which correlates with the NSB level. The top axis represents the ambient light in units of dark night conditions referred to as $\mathrm{NSB_{Dark}}$. The constraint on *pedestal impurity* of 6 % is indicated by the horizontal red dashed line in (a). The light conditions are structured in 1 µA bins. The vertical dashed grey lines indicate the margins of the NSB samples.

Figure 6.3a shows the dependency of the *pedestal impurity* on the light conditions and for a variety of higher and lower cleaning settings as compared to the standard cleaning. The standard cleaning levels exceed the *pedestal impurity* constraint (grey dashed line) at about $8\,\mathrm{NSB_{Dark}}$, which is roughly the upper boundary of the slight moonlight sample. However, at light conditions below $2\,\mathrm{NSB_{Dark}}$ a lower 3.5-1.5. cleaning seems to be still sufficient. A similar situation can be found with rising light conditions where lower thresholds reach the *pedestal impurity* limit and even higher cleaning levels are required. Consequently, settings can be chosen for the specific light conditions.

Nevertheless, optimizing only for the *pedestal impurity* neglects the goal to keep as many gamma events as possible. Furthermore, it is not trivial to find an optimum point for a certain combination of cleaning levels. Figure 6.4 shows the result of the *pedestal impurity* for the grid search on the range of cleaning levels mentioned. Several combinations of neighbor and core threshold are fulfilling the *pedestal impurity* constraint. This underlines the need for a second criterion representing the entity to be kept.

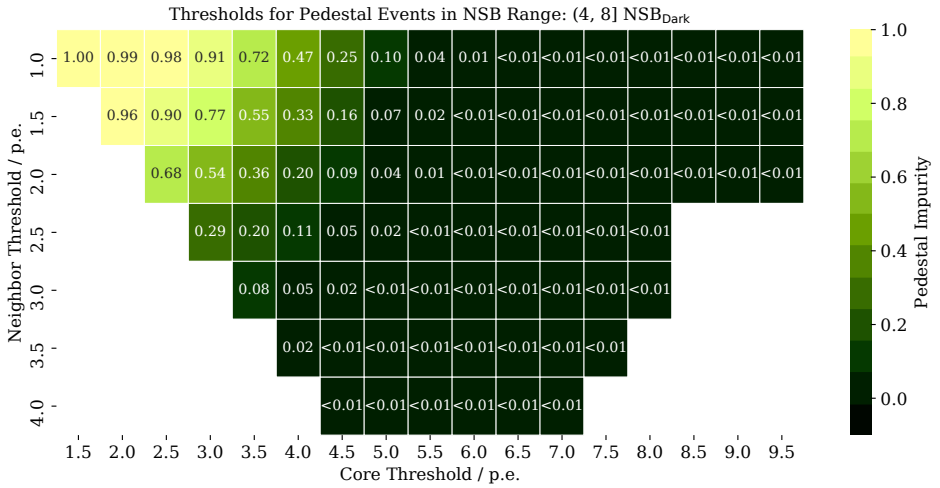

Figure 6.4: Example of a result from a grid search of cleaning thresholds for the slight moonlight sample ($(4-8)\,\mathrm{NSB_{Dark}}$) with regard to the *pedestal impurity*. Cleaning level combinations with neighbor thresholds larger than core thresholds have not been considered. The coloring indicates the level of *pedestal impurities* and the rounded values are printed in each bin. Cleaning levels without coloring either did not contain any events. Grid searches for the other light conditions are shown in appendix in figure B.1 and figure B.2.

6.2.3 Gamma Efficiency Criterion

In order to find a clearer constraint for the cleaning settings, the efficiency of detecting gamma events is included. The goal of every gamma analysis is to maximize the number of gamma events from the observed source. Thus, the fraction of true gamma events surviving the analysis chain, and the image cleaning in particular, is a suitable, additional optimization criterion to quantify this goal.

Figure 6.3b shows the fraction of gamma events surviving the image cleaning depending on the chosen cleaning levels and light conditions. It is evident that the *gamma efficiency* is independent of the light conditions up to a critical NSB level. This behavior can be observed for all cleaning thresholds. After this level the fraction of surviving gamma events increases as more pixels exceed the cleaning thresholds. This critical NSB level is mainly determined by the chosen cleaning levels and shifts towards higher NSB levels with higher cleaning levels.

Furthermore, the *gamma efficiency* is generally reduced with increased cleaning levels, as expected. This circumstance will also increase the energy threshold, as fainter showers are discarded. The aim is thus again to use the lowest possible

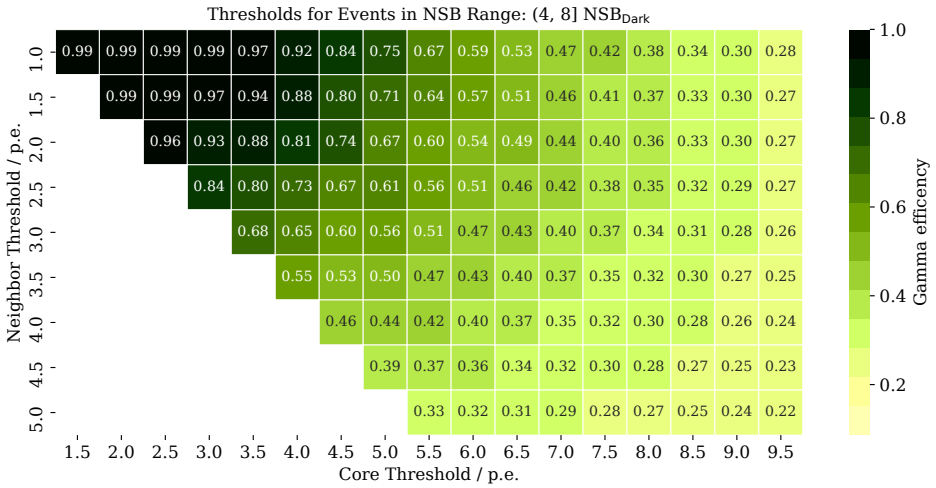

Figure 6.5: Example of a result from a grid search of cleaning thresholds on pedestal data for the slight moonlight ($(4-8)\,\mathrm{NSB_{Dark}}$) sample with regard to the *gamma efficiencies*. Cleaning level combinations with neighbor thresholds larger than core thresholds have not been considered. The coloring indicates the level of *gamma efficiency* and the rounded values are printed in each bin. Cleaning levels without coloring either did not contain any events. Grid searches for the other light conditions are shown in the appendix in figure B.3 and figure B.4.

cleaning levels that diminish the effect of increased NSB and provide the maximum *gamma efficiency*. In fact, the situation here is the same as with the *pedestal impurity*, as the grid search reveals that several combinations of core and neighbor thresholds lead to the same *gamma efficiency*. The result of the grid search on the *gamma efficiency* is depicted in figure 6.5.

Accordingly, in the case of all three optimization criteria, one would always aim for the lowest possible cleaning levels. However, it is difficult to determine a optimum point that accounts for this goal and defines a suitable combination of core and neighbor thresholds for a single criterion, thus an approach to combine them is carried out in the following.

6.2.4 Selection of Suitable Cleaning Levels

The previous section has shown that a combination of the criteria mentioned above is beneficial to find a suitable set of cleaning levels. An approach to combine *gamma efficiency* and *pedestal impurity* will be presented first. The *mean number of islands* criterion is incorporated afterwards.

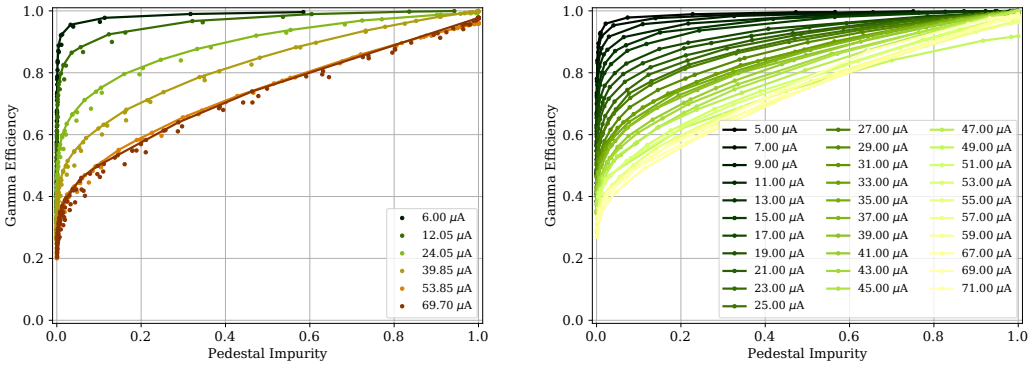

(a) Pareto frontiers grouped by ranges of the mean camera current of the six light conditions.

(b) Pareto frontiers grouped by the mean camera current binned with 2 µA wide bins.

Figure 6.6: Pareto frontiers of *pedestal impurity* vs. *gamma efficiency* for different combinations of cleaning settings grouped by different light conditions. Each data point represents a combination of both cleaning levels. The pareto frontier contains all sets of cleaning levels with an optimum combination of *pedestal impurity* and *gamma efficiency*. The colored lines indicate the convex hull of the pareto frontiers and indicate the smallest convex sets of data points on the pareto frontier. Subfigure (a) shows the pareto frontiers for the six NSB samples. In subfigure (b) only the convex hull is displayed, which has been determined for several light levels with a finer binning of 2 µA width. In both cases, the labels in the legend represent the mean current of a bin.

An optimal cleaning would lead to a *pedestal impurity* of 0 % and a *gamma efficiency* of 100 %. In order to find the setting that is the closest to this optimum, the grid search results from the previous sections are visualized in figure 6.6.

In this image, each data point represents a combination of both cleaning levels. The aggregated efficiencies are grouped by the six light conditions used in this study. In all six cases the different settings form a so-called pareto frontier.[4] This pareto frontier contains an optimal set of cleaning levels with regard to the desired combined criterion. The settings that are the closest to the optimum are indicated by a convex hull. Consequently, all settings on this hull are optimum regarding the problem and indicate that there are no better combinations.

As illustrated in figure 6.1, improving one criterion, e.g., *gamma efficiency*, diminishes the other, e.g., *pedestal impurity*. Furthermore, it is evident that the further the convex hull from the optimum, the higher the NSB level.

[4]Set of all states that have an optimum combination of the desired criteria

Current Bin [µA]	Core Threshold [*p.e.*]	Neighbor Threshold [*p.e.*]
(4.0, 8.0]	3.5	1.5
(8.0, 16.0]	4.5	2.0
(16.0, 32.0]	5.5	3.0
(32.0, 48.0]	6.5	3.5
(48.0, 64.0]	6.0	4.5
(64.0, 100.0]	7.5	4.0

(a) Pareto optimal cleaning levels, with progressive constraints: *pedestal impurity* < 0.01. The efficiencies where weighted with w(*gamma efficiency*)=1 and w(*pedestal impurity*)=0.1.

Current Bin [µA]	Core Threshold [*p.e.*]	Neighbor Threshold [*p.e.*]
(4.0, 8.0]	4.0	1.0
(8.0, 16.0]	5.0	1.5
(16.0, 32.0]	6.0	2.5
(32.0, 48.0]	6.5	3.5
(48.0, 64.0]	8.0	3.5
(64.0, 100.0]	9.0	4.5

(b) Pareto optimal cleaning levels, with conservative constraints: $\hat{N}_{\text{islands}} \leq 1.5$ and *pedestal impurity* < 0.01. The efficiencies where weighted with w(*gamma efficiency*)=1 and w(*pedestal impurity*)=0.1.

Table 6.1: Sets of pareto optimal cleaning levels with progressive (a) and conservative (6.1b) optimization constraints for the six NSB ranges. The NSB levels are represented by the mean camera current binned in the according ranges. The thresholds are given in units of p.e.

Figure 6.6b gives a more detailed binning of the pareto fronts with respect to the average current in the camera. Also in this representation, the tendency of the pareto front towards the desired optimum behaves reciprocally to the current.

In order to find a suitable setting for the image cleaning at each light condition, the setting closest to the optimum is searched for. For the further analysis, two sets of cleaning levels are defined. These cleaning sets are summarized in the tables 6.1a and 6.1b.

The first considers an optimum point of gamma efficiency and *pedestal impurity* by additionally demanding a *pedestal impurity* $< 1\,\%$ and weighting the impurity with 0.1. This setting is hereafter called progressive cleaning.

The second set of cleaning levels extends these constraints by additionally coercing the *mean number of islands* criterion to below 1.5 on average. This levels are called conservative cleaning levels in the following.

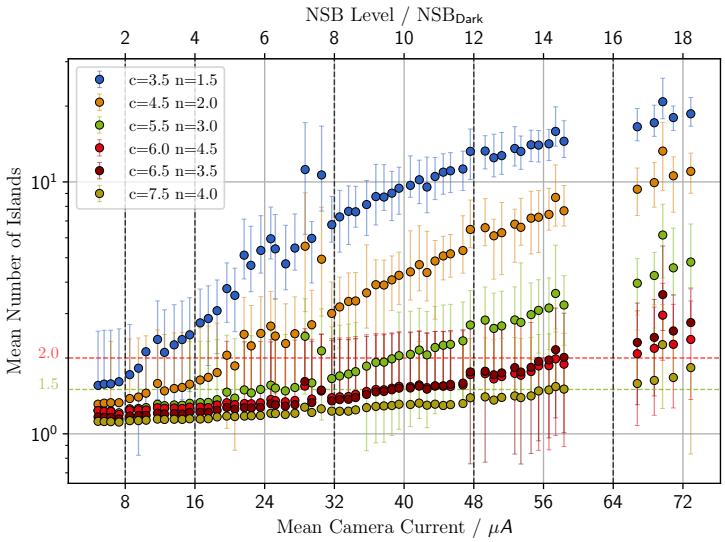

Figure 6.7: Dependency of the average number of islands on light conditions if progressive cleaning settings have been used. The abscissa represents the average of currents in all pixels over the duration of a run, which correlates with the NSB level. The top axis represents the ambient light in units of dark night conditions referred to as $\mathrm{NSB}_{\mathrm{Dark}}$. The average number of islands is represented by the ordinate. The $\hat{N}_{\mathrm{islands}} \leq 2$ limit is indicated as a red dashed line and the $\hat{N}_{\mathrm{islands}} \leq 1.5$ limit with the green dashed line. The error bars represent the 25th/75th precentile to indicate the spread of the `numIslands` distribution. The light conditions are structured in 1 µA bins. The vertical dashed grey lines indicate the margins of the NSB samples. Cleanings for these light conditions are presented in ascending order from top to bottom in the legend. The chosen cleaning levels stay below the $\hat{N}_{\mathrm{islands}} \leq 2$ limit in their dedicated NSB range.

6.2.5 Effect on Number of Islands

The cleaning settings found in the previous section are chosen to provide an optimal result in terms of *gamma efficiency* and *pedestal impurity*. Furthermore, contributions of NSB-dominated pixels to shower images are potentially minimized. Accordingly, the average `numIslands` should be stable within the NSB range in which its cleaning settings are optimized.

As visible in figure 6.7 and figure 6.8, the average `numIslands` fulfills this constraint for both new cleaning settings and shows an average of less than 1.5 islands. Furthermore, the conservative cleaning levels, as expected, constrain the `numIslands` harder than the progressive cleaning levels. In both cases it has to be acknowledged

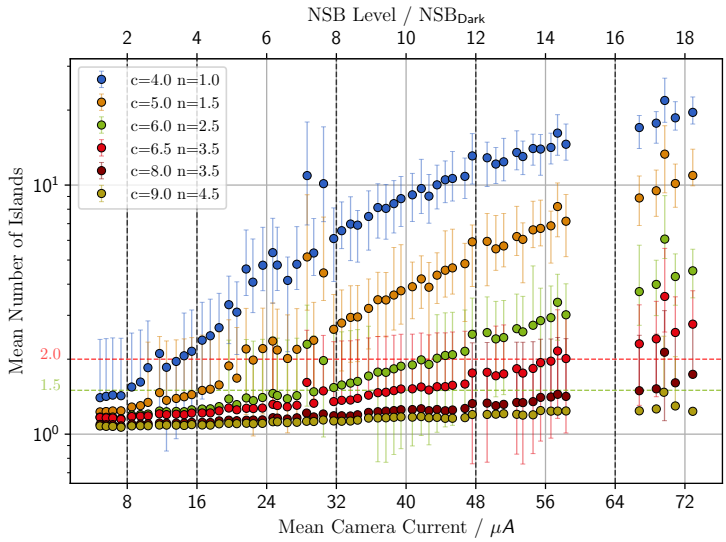

Figure 6.8: Dependency of the average number of islands on light conditions if conservative cleaning settings have been used. The abscissa represents the average of currents in all pixels over the duration of a run, which correlates with the NSB level. The top axis represents the ambient light in units of dark night conditions referred to as $\mathrm{NSB}_{\mathrm{Dark}}$. The average number of islands is represented by the ordinate. The $\hat{N}_{\mathrm{islands}} \leq 2$ limit is indicated as a red dashed line and the $\hat{N}_{\mathrm{islands}} \leq 1.5$ limit with the green dashed line. The error bars represent the 25th/75th precentile to indicate the spread of the `numIslands` distribution. The light conditions are structured in 1 µA bins. The vertical dashed grey lines indicate the margins of the NSB samples. Cleanings for these light conditions are presented in ascending order from top to bottom in the legend. The chosen cleaning levels stay below the $\hat{N}_{\mathrm{islands}} \leq 1.5$ limit in their dedicated NSB range.

that this parameter still shows a systematic rise with the NSB, even within the optimized NSB range. Nevertheless, it can be kept below the $\hat{N}_{\mathrm{islands}} \leq 2$ constraint in both cases.

In summary, this section has shown how to define cleaning levels with a combined optimization criterion. The decision to limit the number of cleaning settings to six NSB ranges was a compromise. Yet the relative rise of `numIslands` is rather small within these ranges and the cleaning settings found appear to be promising for the further analysis. The shower images of these two cleaning settings are thus studied in the following section. In particular, the match of data and simulation are investigated on an image parameter level.

6.2.6 Comparison of Image Parameters from Data and MC

In the previous section, a strategy to optimize cleaning levels for various light conditions was introduced. With these cleaning levels, shower images are extracted for those NSB levels. In order to legitimize the features from the image parametrization for the following machine-learning steps, the image parameters are compared for data and MC simulations. The result of this comparison is discussed in this section.

For this purpose, the features `size` and `length` are shown as examples for the impact of the new cleaning levels on the image parameters. Furthermore, only feature distributions from the progressive cleaning are shown, as those of the conservative cleaning behave similarly. Moreover, the comparison plots show also features generated with the standard cleaning levels in order to compare them to the new cleaning levels and to indicate the improvement between them.

A general comparison shows that simulated and observed features mostly agree in their shape and general structure. The Data-Monte-Carlo mismatches that accounted for the "dark night" conditions, mostly remain. A slight improvement is visible at higher NSB rates and higher cleaning levels.

The comparison of standard and progressive (or conservative) cleaning levels shows a clear improvement with the new cleaning levels at the brighter light conditions. This is, for example, clearly visible for `size` at the highest NSB as shown in figure 6.9f. Similar to this, `length` shows a clear improvement at the highest light conditions cleaned with the new levels (see figures 6.10d and 6.10f). At lower NSB all three cleanings show similar behavior in terms of Data-Monte-Carlo mismatches. Nevertheless, the new cleaning levels show generally higher event rates (e.g., in figure 6.9a).

In conclusion, the new cleaning levels provide sufficient results in regard to the evaluated image parameters. The agreement of data and simulation allows for their use in the machine-learning steps in the following chapter. In particular, at the higher NSB levels the standard cleaning is outperformed by the new cleaning levels. At these light conditions, the standard cleaning levels for many of the features are massively distorted and smeared out. The new cleaning levels, on the other hand, do not feature this problem.

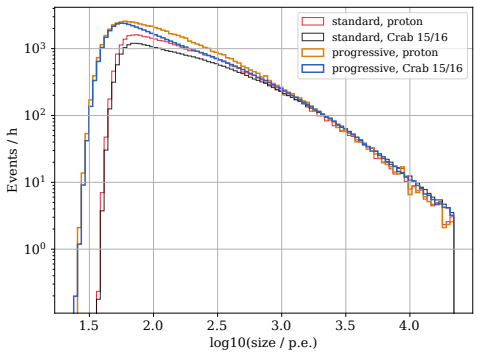

(a) no moonlight: $(0-2)\,\mathrm{NSB}_{\mathrm{Dark}}$.

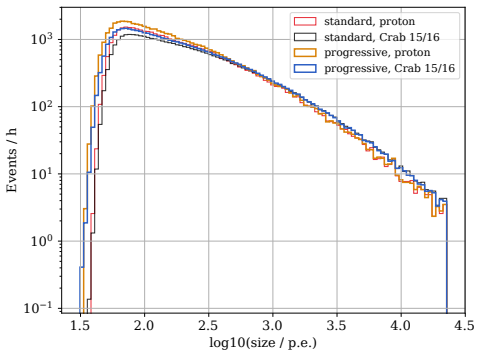

(b) low moonlight: $(2-4)\,\mathrm{NSB}_{\mathrm{Dark}}$.

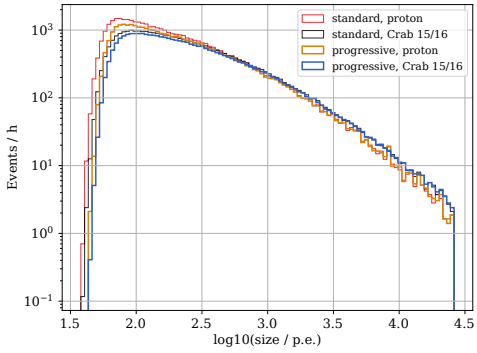

(c) slight moonlight: $(4-8)\,\mathrm{NSB}_{\mathrm{Dark}}$.

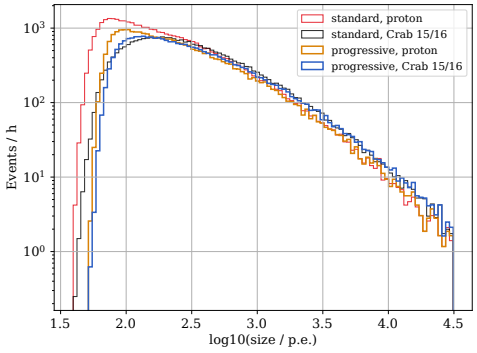

(d) moderate moonlight: $(8-12)\,\mathrm{NSB}_{\mathrm{Dark}}$.

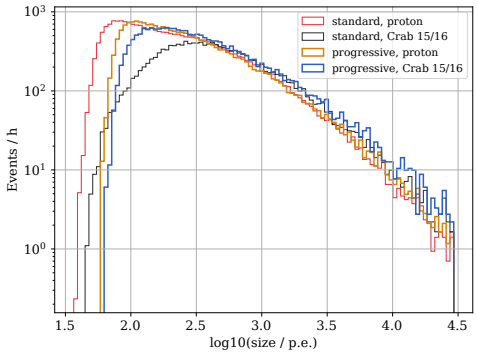

(e) increased moonlight: $(12-16)\,\mathrm{NSB}_{\mathrm{Dark}}$.

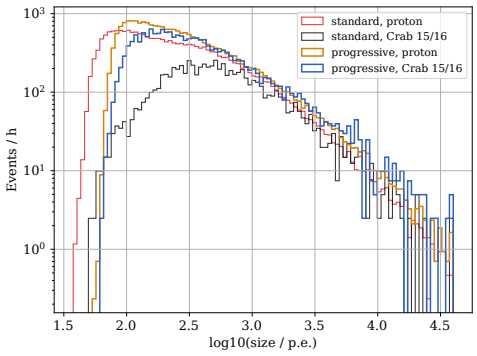

(f) strong moonlight: $(16-24)\,\mathrm{NSB}_{\mathrm{Dark}}$.

Figure 6.9: Comparison of observations and MC simulations based on the distributions of the feature `size` for six representative light conditions. The distributions are normalized to observation times. Each plot contains four feature distributions from the same image parameters and light conditions. These distributions show proton events from the standard cleaning (black and red) and the progressive cleaning (blue and orange) for Crab data (black and blue) and proton simulations (red and orange).

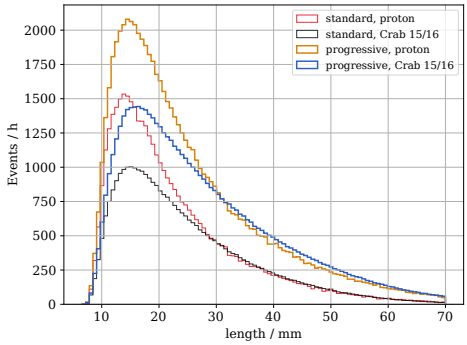

(a) no moonlight: $(0-2)\,\mathrm{NSB}_{\mathrm{Dark}}$.

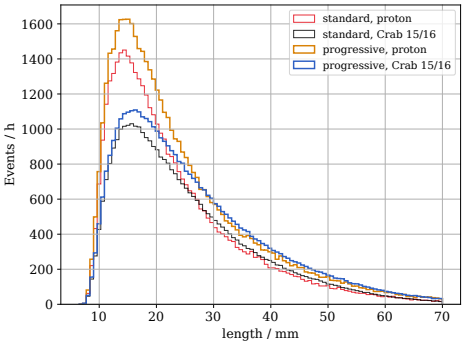

(b) low moonlight: $(2-4)\,\mathrm{NSB}_{\mathrm{Dark}}$.

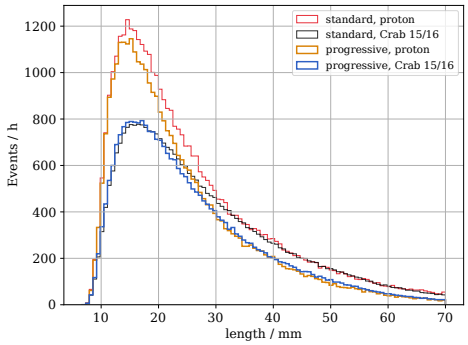

(c) slight moonlight: $(4-8)\,\mathrm{NSB}_{\mathrm{Dark}}$.

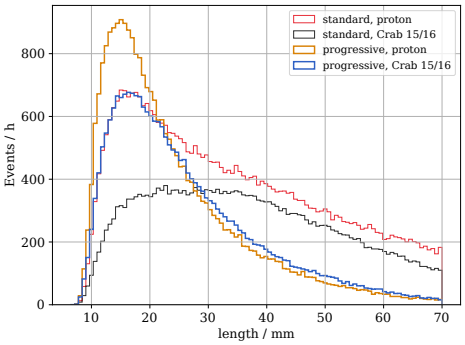

(d) moderate moonlight: $(8-12)\,\mathrm{NSB}_{\mathrm{Dark}}$.

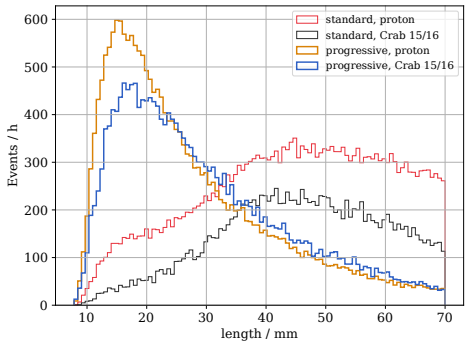

(e) increased moonlight: $(12-16)\,\mathrm{NSB}_{\mathrm{Dark}}$.

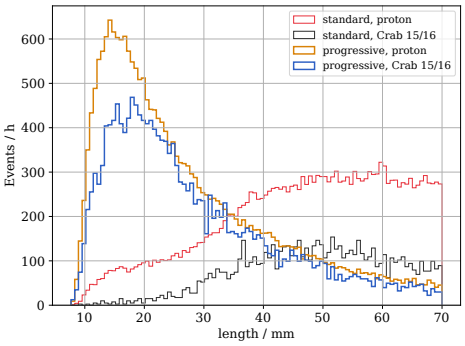

(f) strong moonlight: $(16-24)\,\mathrm{NSB}_{\mathrm{Dark}}$.

Figure 6.10: Comparison of observations and MC simulations based on the distributions of the feature `length` for six representative light conditions. The distributions are normalized to observation times. Each plot contains four feature distributions from the same image parameters and light conditions. These distributions show proton events from the standard cleaning (black and red) and the progressive cleaning (blue and orange) for Crab data (black and blue) and proton simulations (red and orange).

6.3 Model Performances

In the previous section, optimized cleaning levels have been ascertained and two settings per light condition have been selected for further evaluation. Their impact on the performance of the machine-learning steps in this study (i.e., DISP regression, energy regression and gamma/hadron separation) is discussed in this section. The aim of this section is to finally determine one cleaning setting per light condition.

For this purpose, image parameters are generated with these cleaning levels from the ObsNSB datasets. Machine-learning models for the steps mentioned above are trained on their features. In order to evaluate the methods used, an independent gamma test sample from these simulations is prepared for each light condition and excluded from the training.

In addition to the new cleaning levels, features from standard cleaning levels are also generated and used for an independent model. Moreover, additional models using a combination of GenNSB samples and standard cleaning levels are trained. Models from these two samples are used as a baseline that is compared to the new cleaning settings. This has the purpose of indicating potential improvement. The performance of the specific machine-learning tasks is discussed hereafter in more detail.

6.3.1 Performance of the Source Reconstruction

The regression of DISP, as introduced in section 4.4.1, is responsible for reconstruction of the location of the showers' origin. A *random forest* regression model is trained for this analysis step. In order to understand the influence of the light condition to training and application data, the performance of the regression is evaluated on a dedicated test samples of simulated diffuse gamma showers in the following.

Figure 6.11 shows the performance of the DISP regressions for the test samples introduced at the beginning of this section. The R^2-score was chosen as performance metric since it is a commonly used metric for regression problems. The R^2-score was introduced in chapter 4.3.2. Its values range typically from 0 to 1, with 1 indicating a perfect prediction of the target values of the test set. In the case of the implementation used from *scikit-learn*, negative values are also possible. They indicate a bad performance of the predicting model.

The R^2-score is depicted in relation to the light conditions of the test samples with increasing light levels. The combination of cleaning levels and the two NSB simulations (ObsNSB and GenNSB) is indicated by the coloring.

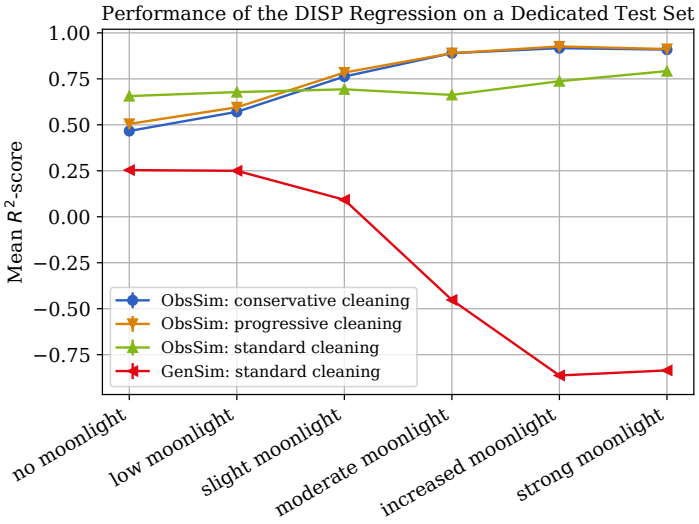

Figure 6.11: Performance of the source reconstruction with `DISP` regression determined on a dedicated test gamma sample. Involved cleaning levels and simulation samples are indicated by the coloring. Data points are connected with lines to indicate related settings. They do not indicate any linearity. The ordinate represent the R^2-score and the abscissa categorizes the six NSB samples. The R^2-score was determined with a bootstrapping of the test sample. The mean R^2-score of the predictions is indicated by the data points. The error bars are calculated from the bootstrap samples' standard deviation. However, they are smaller than the size of the markers's data points. The models from the optimized cleaning outperform the standard cleaning at higher NSB levels. At lower NSB levels the standard cleanig performs better.

The source reconstruction clearly benefits from the more realistic NSB conditions in the ObsNSB MCs. For all light conditions, they outperform the predictions from a GenNSB based model, which even shows a negative score at moderate moonlight conditions. Regarding the cleaning levels, the `DISP` regression seems to benefit from higher cleaning levels, as the new cleaning levels start to show better predictions once they are higher than the standard. The latter show a stable performance over all light conditions, whereas the performance of the new cleaning levels improves with rising NSB and, thus, rising cleaning thresholds. A comparison of the two new cleanings does not show a clear result as the progressive cleaning seems to be only insignificantly better than the conservative cleaning.

However, the apparent improvement of the `DISP` regression with higher cleaning levels has to be put in context of the whole analysis. With increased cleaning levels more showers are rejected before the machine-learning steps and, especially, smaller,

fainter, showers that are harder to reconstruct are missing in this performance evaluation. Nevertheless, even with constant cleaning levels a better performance is achieved with ObsNSB than with GenNSB.

6.3.2 Performance of the Background Suppression

The classification between gamma rays and hadronic showers is performed with a *random forest classifier*, as described in section 4.4.2. The performance is evaluated in a 20-fold *cross-validation*. The GenNSB model can only be evaluated within the *cross-validation* on the the lowest light conditions, as this is the only light condition it contains. In addition, dedicated test samples with gammas and protons are evaluated with bootstrapping to determine the influence of the chosen cleaning settings on data from a specific light condition and also show the performance of the GenNSB model to higher light conditions. Due to insufficient proton simulations only a small test sample is available for them, which has been chosen to 10 % of the full proton set defined in table 5.4 in order to have sufficient proton events for training.

The AUC[5] is investigated in order to quantify the performance. Bootstrapping is used in order to estimate the uncertainty of the measured AUC in case of the test sample. In both cases (*cross-validation* and bootstrapping) the performance values are given as mean values of the AUC and their uncertainties are estimated with the standard deviation.

Figure 6.12b shows the results of the model application from test samples (figure 6.12b) and the *cross-validation* (figure 6.12a), both with various light conditions. At lower light conditions, models based on the standard cleaning levels with any one of the two NSB simulations (GenNSB and ObsNSB) show the best performance. With increasing light conditions, the mean AUC of these models decreases. GenNSB has the worst AUC for higher light conditions. ObsNSB with standard cleaning levels also shows a smaller AUC at more severe light conditions. Again, both the conservative and progressive cleaning levels with ObsNSB show a mostly stable performance for all light conditions. For strong moonlight, the conservative cleaning level shows a slightly higher AUC.

In order to investigate the performance of the gamma/hadron separation models in the real world situation, they are evaluated on Crab observations in the next section.

[5] See section 4.3.2.

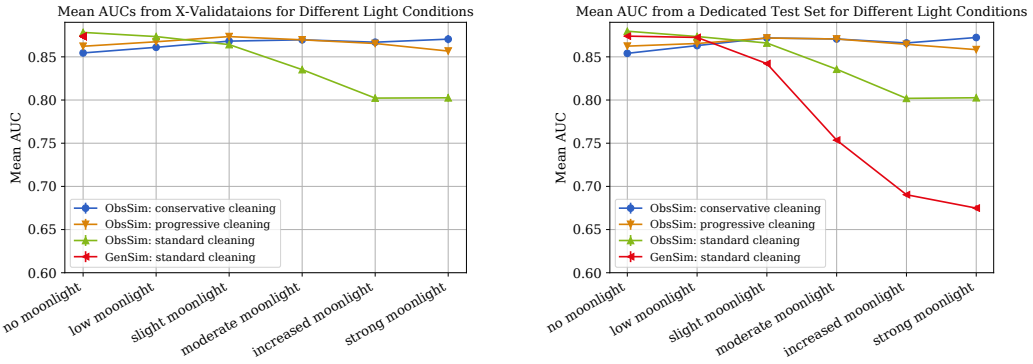

(a) Mean AUC of gamma/hadron separations determined in a 20-fold cross-validation during the training.

(b) Mean AUC of gamma/hadron separations applied to a dedicated gamma test sample with bootstrapping.

Figure 6.12: Performance of the gamma/hadron separation for increasing light conditions. The chosen performance metric is the AUC of the models. Involved cleaning levels and simulation samples are indicated by the coloring. Data points are connected with lines to indicate related settings. They do not indicate any linearity. The ordinates represent the AUC and the abscissas categorizes the six NSB samples. The performance was evaluated both in a 20-fold *cross-validation* (a) and also with bootstrapping on an independent test sample (b). For both samplings the mean AUC of the predictions is given by the data points, whereas the error bars are calculated from the bootstrap samples standard deviation, but may be smaller than the data points' markers. The models from the optimized cleaning outperform the standard cleaning at higher NSB levels. At lower NSB levels the difference in performance of all models is less striking.

Detection of the Crab Nebula

The gamma/hadron separation's performance on observations is determined here with data from Crab Nebula observations. Since an IACT analysis aims for the purest gamma sample possible, a high significance of the detection of the VHE "standard candle", Crab Nebula, is a suitable performance measure for this application. For this purpose, the significance (Li&Ma) of Crab's detection is compared for each model and light condition, as introduced in chapter 4.4.4.

The resulting significance of detection is illustrated in figure 6.13. Since FACT's observation plan is optimized to maximum observation time at the best environment conditions, most of the data is taken at the lowest light conditions. This has the result of more statistics and thus a higher significance at lower NSB levels in general. In order to allow for a comparison between light conditions, significances are normalized to the observation time in $\sqrt{\text{h}}$, as shown in figure 6.14.

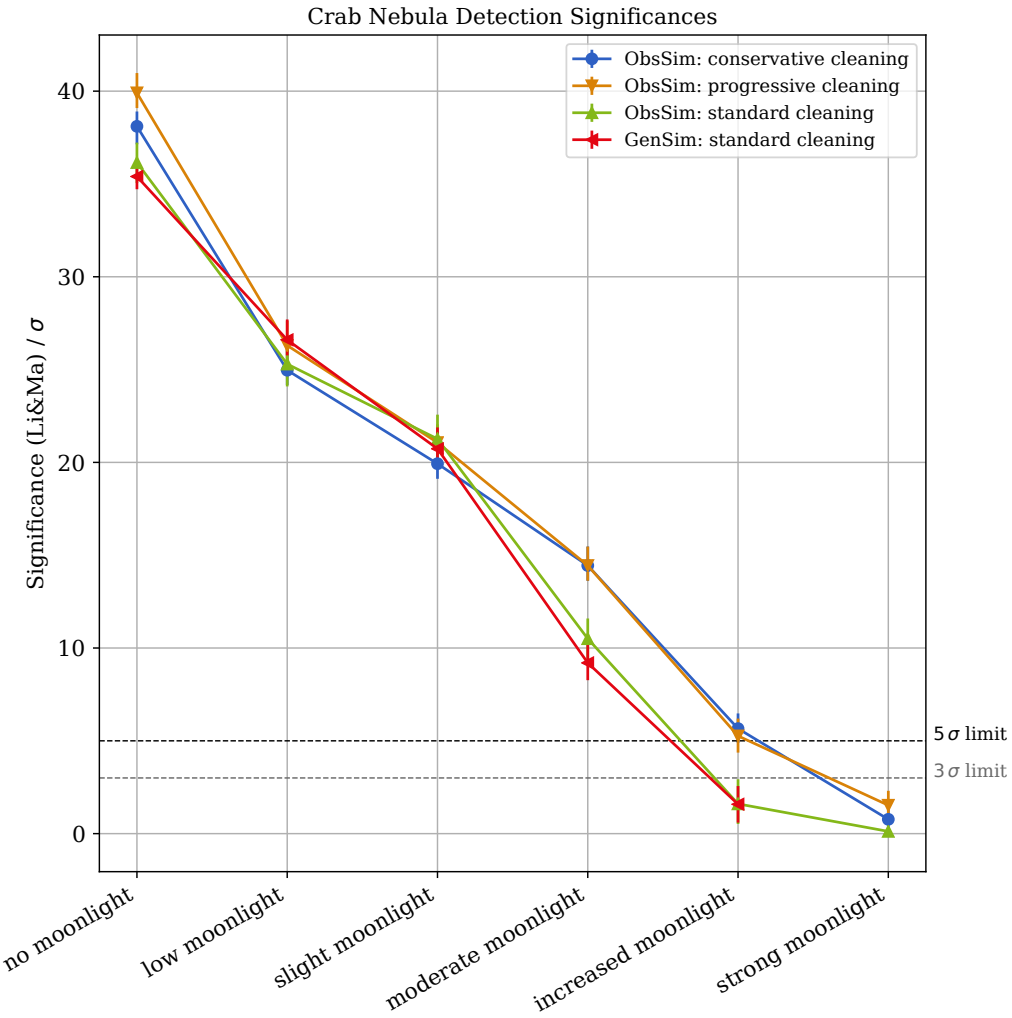

Figure 6.13: Comparison of the significance (Li&Ma) of detection of the Crab Nebula with data from dedicated light conditions for different cleaning settings and MC simulations. Involved cleaning levels and simulation samples are indicated by the coloring. The ordinates represent the significance (Li&Ma) and the abscissas categorizes the six NSB samples. Data points are connected with lines to indicate related settings. They do not indicate any linearity. The performance was evaluated with bootstrapping. The mean significance is given by the data points. Error bars are calculated from the bootstrap samples' standard deviation, but may be smaller than the data points' markers. A `gammaness` cut of $G_{\text{min}} = 0.85$ and a θ^2-cut of $\theta^2_{\text{max}} = 0.025°$ have been applied to the Crab Nebula data in order to achieve the shown examples. The $5\,\sigma$ and the $3\,\sigma$ detection limit are marked by the black and grey horizontal, dashed lines.

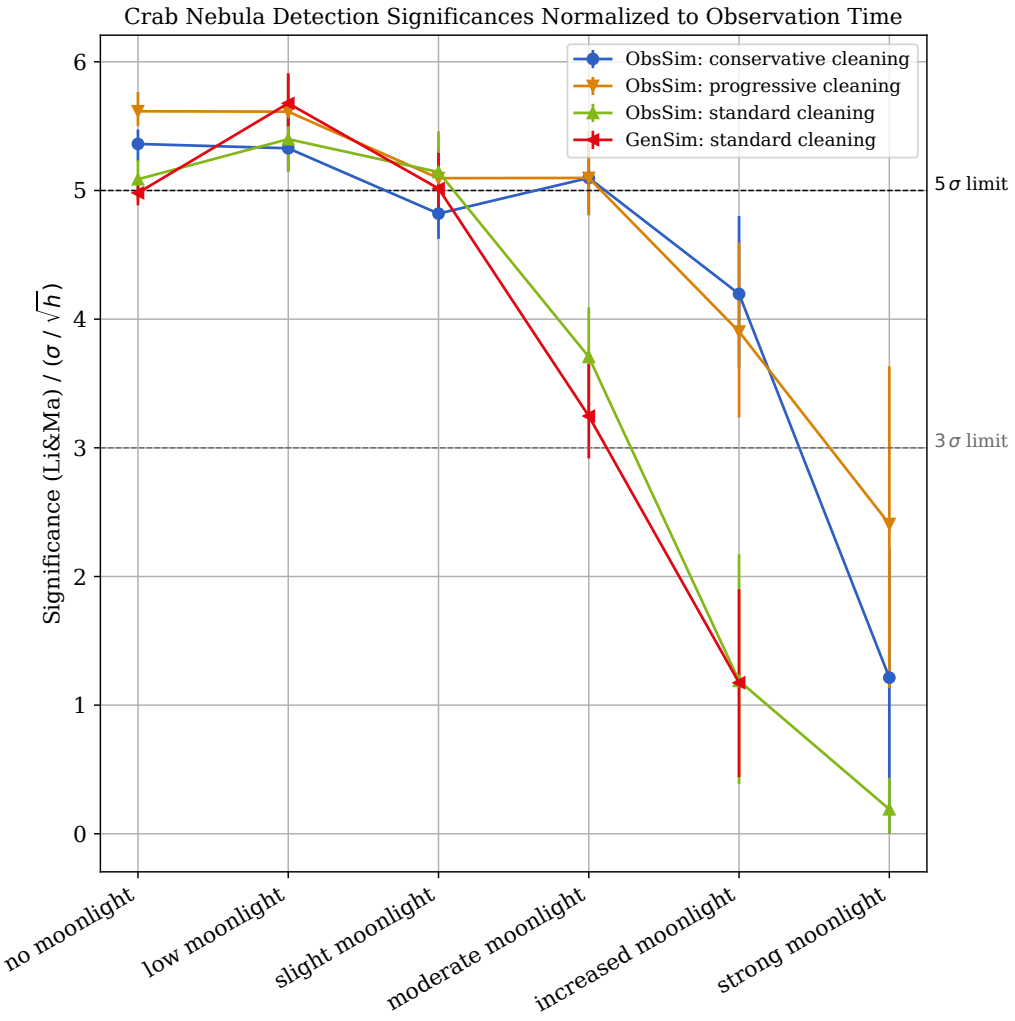

Figure 6.14: Comparison of the significance of detection of the Crab Nebula with data from dedicated light conditions for different cleaning settings and MC simulations, normalized by observation times ($1/\sqrt{h}$). Involved cleaning levels and simulation samples are indicated by the coloring. The ordinates represent the normed significance (Li&Ma) and the abscissas categorizes the six NSB samples. Data points are connected with lines to indicate related settings. They do not indicate any linearity. The performance was evaluated with bootstrapping. The mean significance is given by the data points. Error bars are calculated from the bootstrap samples' standard deviation, but may be smaller than the data points' markers. A `gammaness` cut of $G_{\text{min}} = 0.85$ and a θ^2-cut of $\theta^2_{\text{max}} = 0.025°$ have been applied to the Crab Nebula data in order to achieve the shown examples. The $5\,\sigma$ and the $3\,\sigma$ detection limit are marked by the black and grey horizontal, dashed lines.

.

Using the models trained with ObsNSB simulations and the use of optimized cleaning levels results in a higher or at least equally high significance of detection of Crab. In the case of increased light conditions, the new model allows for a detection with more than 5σ with the given Crab sample.

A comparison of ObsNSB and GenNSB models with standard cleaning does not show a significant difference of these two models in regard to the Crab Nebula detection performance.

The combination of ObsNSB and progressive cleaning levels provides a relatively stable significance per square root hour with more than $5\,\frac{\sigma}{\sqrt{\mathrm{h}}}$, as shown in figure 6.14. The standard cleanings perform comparably to the new cleaning levels at lower light conditions. For the highest light conditions ($\geq 12\,\mathrm{NSB_{Dark}}$) the significance rate of the new cleaning levels drops below four and two sigma per square root hour. With standard cleaning this drop already appears in the range of $(8-12)\,\mathrm{NSB_{Dark}}$. At light conditions brighter than $8\,\mathrm{NSB_{Dark}}$, ObsNSB and the new cleaning levels thus seem to allow for a better detection performance than the standard cleaning.

6.3.3 Performance of the Energy Regression

The energy reconstruction is performed by use of a *random forest regressor* (see section 4.5.3). The R^2-score is evaluated analogous to the `DISP` regression. The according performance on the gamma test samples is visualized in figure 6.15.

The outcome is slightly different to the performance of the previous machine-learning steps. The performance of GenNSB with standard cleaning levels is again the worst of the models, degrading gradually with increasing NSB. The three ObsNSB models show mostly comparable behavior for all light conditions. At a closer look, the comparison of the two new cleaning levels indicate a slightly better performance of the conservative cleaning at the highest light conditions than the progressive cleaning levels. At low light conditions no significant difference is visible for the R^2-scores of the models, with the standard cleaning appearing to be slightly better there.

Surprisingly, the standard cleaning levels also perform better for the two highest light conditions. This might indicate that the energy estimation benefits from lower cleaning levels in general, due to more light per event. On the other hand this could also be an effect of the low statistics of pedestal events in these samples, which, as mentioned before, were a compromise. With lower cleaning levels at these light conditions, more NSB contributes to the shower images and therefore to `size`, which is one of the most important energy-dependent features. Due to a smaller variety of NSB examples in both the training and the test set, the *random forest regressor*

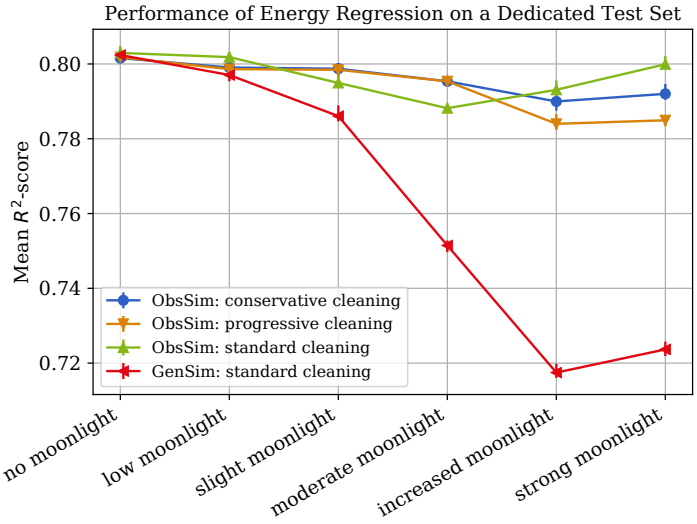

Figure 6.15: Performance of the energy regression determined with the R^2-score on a dedicated test gamma sample. Involved cleaning levels and simulation samples are indicated by the coloring. Data points are connected with lines to indicate related settings. They do not indicate any linearity. The ordinate represent the R^2-score and the abscissa categorizes the six NSB samples. The R^2-score was determined with the bootstrapping of the test sample. The mean R^2-score of the predictions is indicated by the data points. Error bars are calculated from the bootstrap samples standard deviation, but may be smaller than the data points' markers. The models based on ObsNSB MCs show better results than those from GenNSB. They show similar results for all light conditions. However, the optimized cleaning seems better at medium light conditions and the standard cleaning at higher NSB levels. At low NSB levels the performance differs insignificantly.

might have overfitted to the nsb events in both sets. The estimated performance thus might be less realistic. The new cleaning levels are further above the NSB and would thus be less afflicted by this effect. The true nature of this effect has not be determined in this study. Nevertheless, the performance of all three ObsNSB models differs insignificantly at these light conditions.

In conclusion, the performance of the energy estimation also suggests using ObsNSB MCs for the energy estimation, especially with increasing light conditions. A difference in performance for the three ObsNSB cleaning settings is less striking and even shows a slightly better performance for the standard cleaning. For a closer examination, the *bias* and *resolution* of the energy estimations are compared in the following.

Energy Resolution In order to determine the effect of the chosen cleaning and simulation method on the energy reconstruction, its energy-dependent bias and resolution are evaluated for each light condition and model.

Three examples, the lowest, the highest, and one intermediate light condition are illustrated in figure 6.16. It is visible that above a certain energy threshold of about 1 TeV, bias is not significantly influenced by the choice of cleaning and simulation method. However, the resolution shows behavior similar to that for the R^2-score. With increasing light conditions, GenNSB and standard cleaning levels show the worst resolution, the new cleaning levels appear mainly independent, and ObsNSB and standard cleaning levels improve with increasing light conditions. The new cleaning levels show smoother curves with smaller error bars, while the standard cleaning has larger bin to bin fluctuations in the high energy regime.

At energies below 1 TeV, a tendency towards worse performance results is visible with increasing cleaning levels, which can be expected, as with higher cleaning levels less information is at hand on showers with low energies. At low light conditions the models using the new (here lower) cleaning levels and ObsNSB show a slightly better bias and resolution. In contrast, with increasing light conditions the standard cleaning levels are lower and seem to deliver better performance results, with GenNSB providing slightly better performance results than ObsNSB. The behavior in bias and resolution thus confirms the trend seen for the R^2-score of the energy estimations, which indicated that it seems to benefit from comparably lower cleaning levels.

6.3.4 Results and Discussion

In the previous paragraphs, the performance of machine-learning models trained with the cleaning levels from section 6.2 have been discussed. Based on these performances, one set of cleaning levels is selected for the further analysis as outlined in the following.

ObsNSB or GenNSB? In general, the models trained with ObsNSB show a overall better and more stable performance for the chosen light conditions. The negative trend of GenNSB with increasing light conditions suggests the use of ObsNSB for the further analysis.

Adaptation of Cleaning Levels in ObsNSB The general trend of the performance of background suppression and angular resolution with increasing light conditions indicates the benefit of adapting cleaning levels to the light conditions. The improvement with the new cleaning levels is clearly visible, especially with regard to the

significance of the source detection. However, for the energy estimation the situation is less clear. Here we must distinguish between low and high NSB conditions.

Low Light Conditions At the two lowest light conditions the standard cleaning shows the best results for all three machine-learning steps. Nevertheless, in the case of the regression tasks the performances of all three cleanings are very similar. Moreover, bias and resolution indicated a insignificantly better performance of the new cleaning levels.

Bright Light Conditions With increasing light conditions the new cleaning levels show a clearly better performance regarding the gamma/hadron separation, both for the AUC score and the significance of the source detection. The regression of `DISP` in particular shows a significantly better result.

Surprisingly, the energy regression shows slightly better results for the standard cleaning regarding R^2-score, and bias and resolution. As mentioned earlier, this could be due to overfitting caused by low statistics of NSB samples at these light conditions, or are benefit from generally lower cleaning levels. Nevertheless, the improvement is less striking than in the case of background suppression and angular resolution.

Comparison of Progressive and Conservative Cleaning Levels Models trained with the progressive cleaning levels, show in almost all steps the better performance or at least nearly the same as those trained with conservative cleaning levels.

Determining Cleaning Settings for all Light Conditions Based on the previous considerations, the decision for one specific set of cleaning thresholds for the various light conditions is a trade-off between separation performance and energy estimation. Since the differences in the energy estimation are less prominent and focus on the energy regime below 1 TeV, the models with higher significances are chosen for the following evaluation. For all light conditions the models trained with ObsNSB simulations and progressive cleaning levels (see table 6.1a) show a good trade-off and are used in the following discussion of the performance of FACT for different light conditions.

The choice of suitable limits for `angular_distance` (θ) and thresholds for the predictions of the gamma/hadron separation are discussed in the next section.

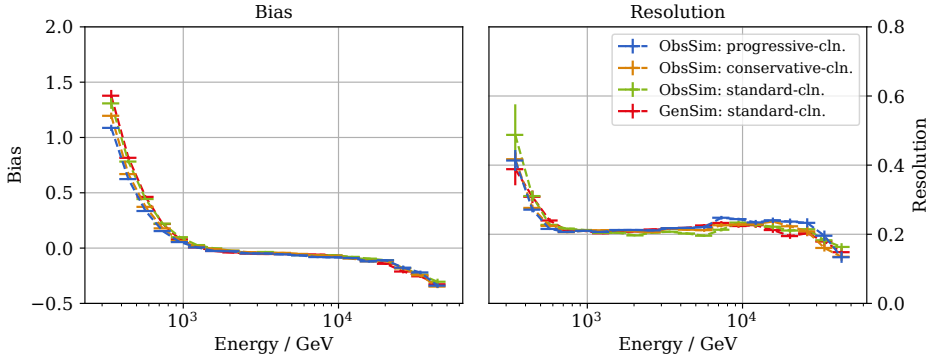

(a) No moonlight: $(0-2)\,\mathrm{NSB}_{\mathrm{Dark}}$

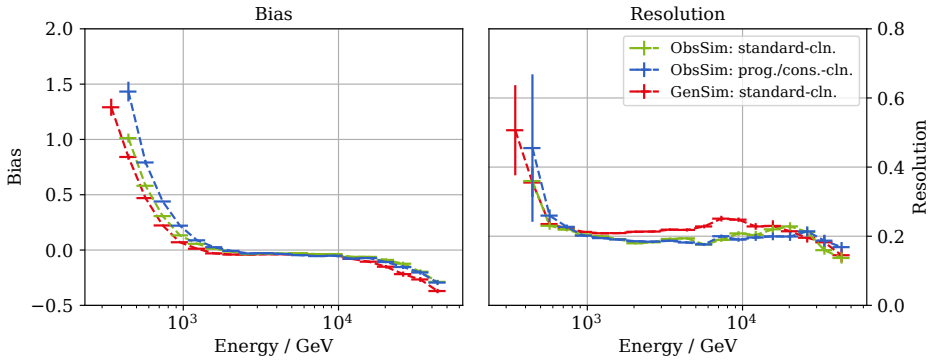

(b) Moderate moonlight: $(8-12)\,\mathrm{NSB}_{\mathrm{Dark}}$

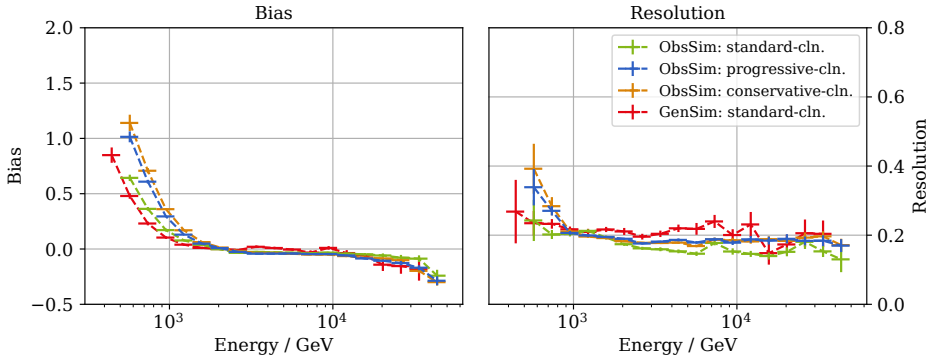

(c) Strong moonlight: $(16-24)\,\mathrm{NSB}_{\mathrm{Dark}}$

Figure 6.16: Comparison of machine-learning models with regard to bias and resolution of the energy regressor. Involved cleaning levels and simulation samples are indicated by the coloring. Data points are connected with dashed lines to indicate related settings. They do not indicate any interpolation. Bias and resolution were determined with bootstrapping of the test sample. Their mean values are represented by the data points, whereas the error bars are calculated from the samples as the percentiles representing the $\pm 1\sigma$ environment.

6.4 Cut Selection for Angular Distance and Gammaness

The final classification of the primary particle and supression of the hadronic background depends on the choice of a sufficient `gammaness` threshold (G_{min}), which reflects the confidence of the *random forest classifier*. Furthermore, the sample are also constrained in the maximum angular distance (θ^2_{max}) of reconstructed gamma events in order to reduce the number of events with bad directional reconstruction. In both cases this is done to maximize the significance of the source detection.

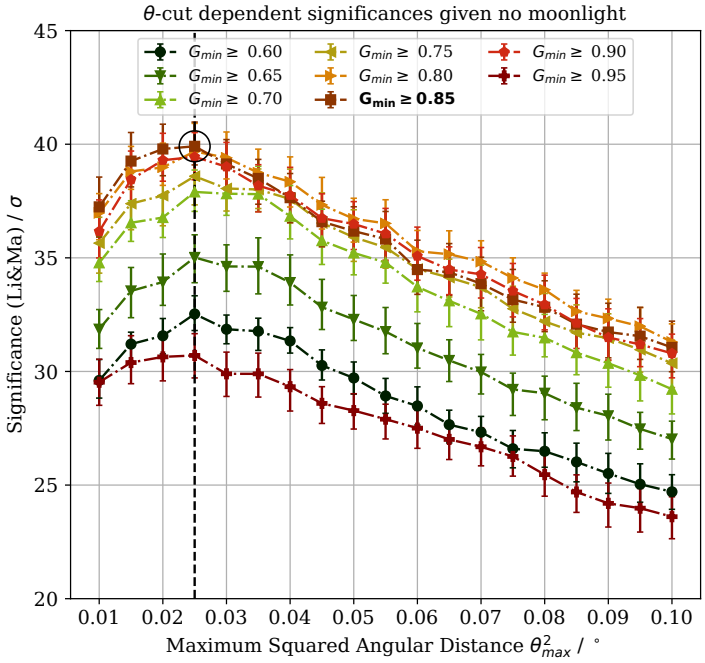

Figure 6.17: Dependency of the significance of detection (Li&Ma) to the choice of maximum angular distance (θ^2_{max}) and prediction threshold with progressive cleaning levels for the no moonlight sample. The significance is on the ordinate, the evaluated θ^2_{max} is on the abscissa, and the curves are grouped by the chosen prediction threshold. Lines do not indicate linearity but connect data points with the same prediction threshold. The data points mark the significance for the data set with the given combination of θ^2_{max} and prediction threshold. The significance was determined in a 100-fold bootstrapping, with the mean as a data point and the standard deviation as an estimator of the error bars. The θ^2_{max} chosen for this thesis is indicated by the dashed vertical line and the chosen `gammaness` threshold is printed in bold letters in the legend. The resulting significance is marked with a black circle.

The influence of the choice of θ^2_{max} and `gammaness` on the significance of detection of the Crab Nebula was determined in a grid search. An example of this is visualized in figure 6.17. The resulting dependencies of all light conditions can be found in appendix B.4 of this thesis (see figure B.11 – B.13). Independent of the choice of θ^2_{max}, prediction thresholds in a range of $[0.75, 0.9]$ show the highest significances. Furthermore, the choice of θ^2_{max} defines the overall maximum possible significance. It is visible that the maximum significance is almost always found for a $\theta^2_{\text{max}} \leq 0.03°$.

This concludes the optimization of the analysis in order to provide optimum results for the evaluation of FACT's performance at various NSB levels. In the following analysis a `gammaness` of $G_{\text{min}} = 0.85$ and a θ^2-cut of $\theta^2_{\text{max}} = 0.025°$ is chosen, since they provide reasonable significances for the detection of the Crab Nebula. The progressive cleaning levels, respectively the models trained with them on ObsNSB simulations, are used for accordingly.

7 NSB Performance

FACT's SiPMs are a robust photon detector that allows FACT to operate under severe light conditions without the need for UV filters or operation with reduced bias voltage. Nevertheless, operating under such conditions increases the noise in shower images and requires adaptations to the trigger threshold and cleaning levels, as presented in the previous chapters. Consequently, this impairs the performance of the whole system, notably detector and analysis.

The dependency of NSB conditions on the performance of FACT with respect to the analysis of Crab is presented in this chapter. The analysis is based on the optimimun cleaning levels, machine-learning models, and cuts in `gammaness` and `angular_distance` (θ) defined in chapter 6. In order to determine the performance, typical parametrizations, which were introduced in section 4.4.4 to 4.5.2, are applied to independent gamma MC sets and the Crab Nebula observations, defined in chapter 5. In this chapter, the evaluation of FACT's performance is therefore carried out as follows:

Gamma simulations are utilized, for instance, for the investigation of the effect of NSB on the energy distribution, energy threshold, the angular resolution and the effective collection area.

Based on the Crab observations, the influence on the image parameters after cleaning is investigated. Moreover, they are used to evaluate the NSB dependency on the significance[1] of the Crab Nebula's detection and FACT's sensitivity[2]. Furthermore, the energy spectra of Crab Nebula are unfolded for various NSB levels and compared with each other as well as with results from other analyses and experiments, with the aim to identify weather the spectrum reconstruction is effected by the NSB or if the spectra correspond.

In order to document the improvement with the analysis presented, the results achieved with the standard analysis are shown and compared.

[1] Introduction to significance (Li&Ma) in section 4.4.4
[2] Introduction to sensitivity in section 4.4.5

7.1 Influence of NSB on the Image Parameterization

Increasing light conditions and the choice of cleaning levels have an impact on the morphology of shower images and thus on the features generated from them. The influence on the distributions of image parameters is the focus of this section. A comparison of example feature distributions after image cleaning and quality cuts[3] for Crab Nebula observations at different NSB levels is illustrated in the following.

In figure 7.1, `length` is shown as an example for a spatial Hillas parameter. The optimized analysis shows comparable distributions independent of the light conditions with regard to shape and location of the distributions mode. The distributions only differ by their relative event rate, which decreases with the NSB levels as expected for increasing cleaning levels.

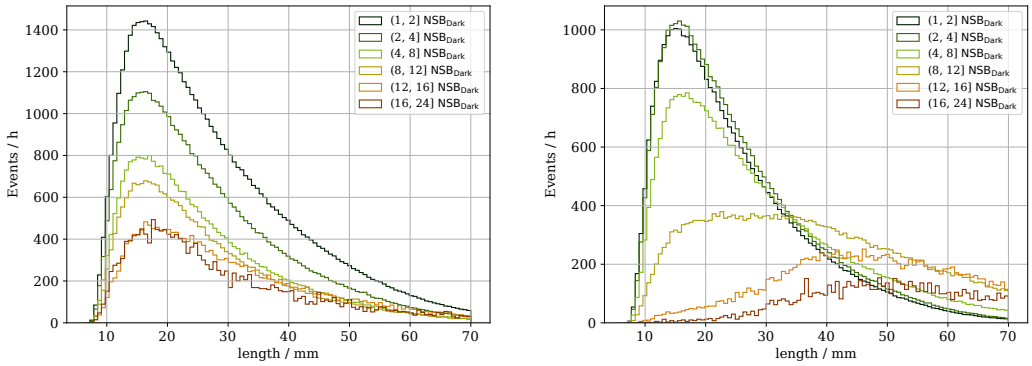

(a) Optimized analysis.

(b) Standard analysis.

Figure 7.1: Distribution of `length` after quality cuts from Crab observations grouped by light conditions (indicated by coloring). Results are shown for the optimized and for comparison also for the standard analysis.

In comparison, the standard cleaning only shows a comparable behavior at low NSB conditions. Above 8 $\mathrm{NSB}_{\mathrm{Dark}}$ the distributions become smeared out and the mode is shifted to larger values. As `width` and `length` play an important role in, e.g., reconstruction of directional information of the showers, the optimized cleaning levels indicate a clear improvement.

This observation is supported by the distribution of the `concentration_cog` (see fig. 7.2a), which is a measure for the relative amount of photons at the center of the shower ellipsis compared to the total amount of photons.

[3] The quality cuts are shown in listing 5.3

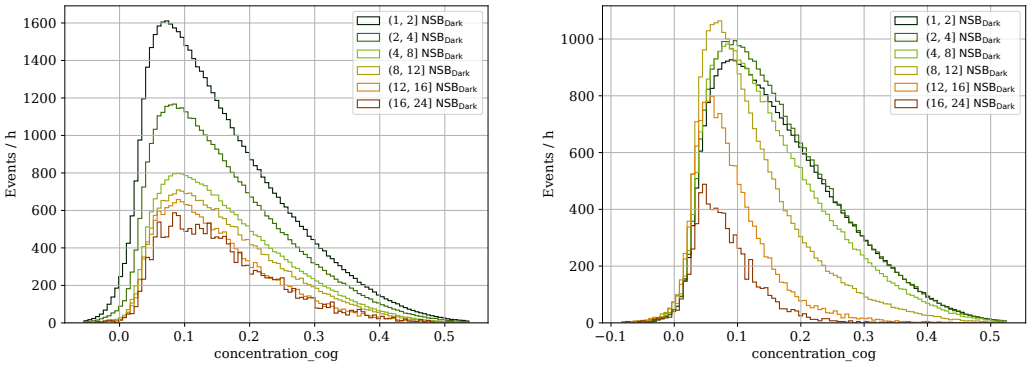

(a) Optimized analysis. **(b)** Standard analysis.

Figure 7.2: Distribution of concentration of the shower core (`concentration_core`) after quality cuts from Crab observations grouped by light conditions (indicated by coloring). Results are shown for the optimized and for comparision also for the standard analysis.

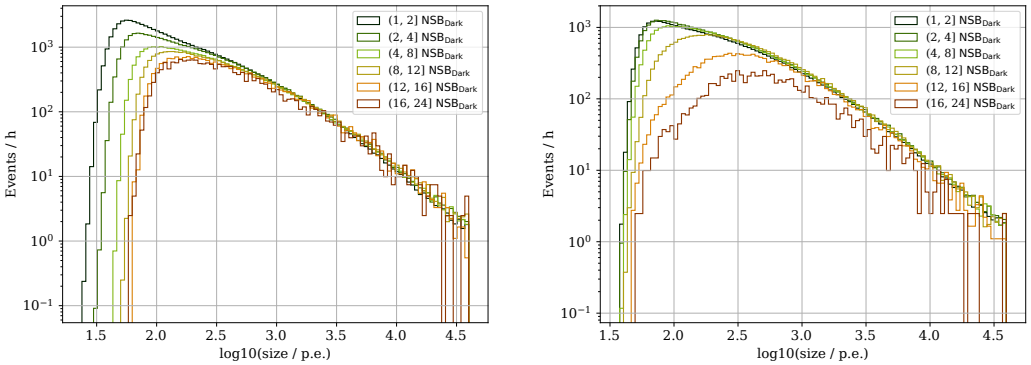

(a) Optimized analysis. **(b)** Standard analysis.

Figure 7.3: Distribution of `size` after quality cuts from Crab observations grouped by light conditions (indicated by coloring). Results are shown for the optimized and for comparision also for the standard analysis.

With the standard cleaning the distributions of the high NSB samples are shifted towards smaller values, whereas the new cleaning, again, conserves the shape of the distributions. This indicates that the ratio of `size` to light at the `COG` is stable and the photons are concentrated in an rather compact area, as expected for Cherenkov photons.

The total amount of light in the shower is indicated by `size` (see figure 7.3). As visible, the low edge and the mode of `size` are shifted towards higher values with increasing NSB levels. Due to the power-law nature of air showers, faint, low-energy showers, which are responsible for events with a small `size`, show the highest rates and populate close to the low edge and the mode of the distribution. Their shift is thus a consequence of the increased cleaning levels that reduce NSB contributions but increase the threshold for fainter showers. Nevertheless, the `size` distributions correspond above 300 p.e. respectively at high energies, which is important for the energy estimations.

On the contrary, the standard cleaning shows this agreement only for `size`s > 300 p.e. and only for light conditions lower than 16 $\mathrm{NSB}_{\mathrm{Dark}}$. Moreover, the higher the NSB level, the more the shapes differ and a lack of fainter showers is visible.

An example for a temporal feature is given with the average time of the arrival of photons on pixels associated with the shower (`arrival_time_shower_mean`). Again, for the optimized cleaning the main difference occurs in lower rates with higher NSB. Nevertheless, it appears that the mode of the `arrival_time_shower_mean` distribution shifts towards higher values with higher NSB, as an effect of remaining NSB photons contributing to the arrival time distribution. This effect is even stronger for the generally less rigid cleaning levels of the standard analysis. Here, the arrival time distributions are generally shifted towards larger values with rising NSB and the location of the mode is less stable.

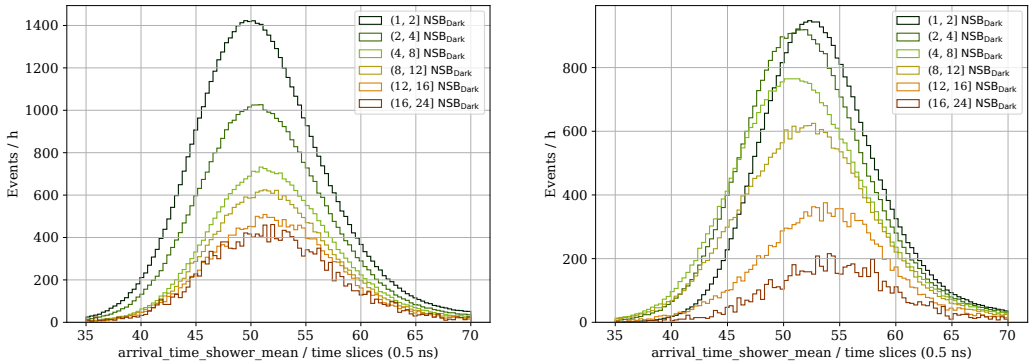

(a) Optimized analysis. **(b)** Standard analysis.

Figure 7.4: Distribution of the `arrival_time_shower_mean` after quality cuts from Crab observations grouped by light conditions (indicated by coloring). Results are shown for the optimized and for comparision for the standard analysis.

7.2 Energy Threshold

The energy threshold, in the sense of the mode of the energy distribution, is commonly used in gamma ray astronomy to quantify the energy dependency of an IACT. In this study, the mode of the energy distribution is determined by fitting a Gaussian curve to the top of the energy distribution and using the curve's center as value for the mode. Despite the name, an IACT can detect gamma rays below this threshold. Nevertheless, this value allows gamma astronomers to compare different telescopes and analyses. In the case of, for instance, HEGRA, the energy threshold of the whole system was determined to 500 GeV at dark light conditions [92].

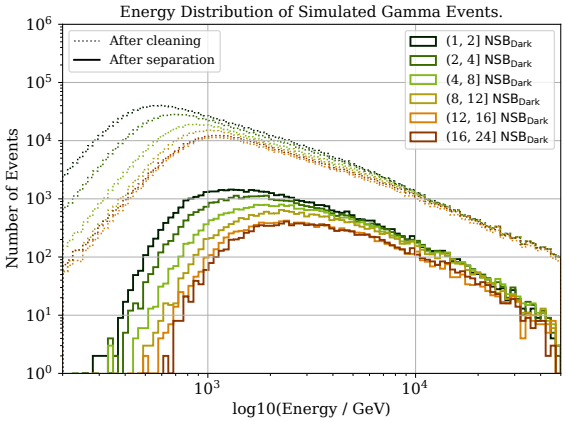

Figure 7.5: Dependency of the energy distribution to different light conditions indicated by the coloring. The optimized cleaning levels have been applied. The dotted lines represent the distributions after the image cleaning, whereas the solid lines indicate the distribution after gamma/hadron separation with $G_{\text{min}} = 0.85$ and a θ^2-cut of $\theta^2_{\text{max}} = 0.025°$.

Figure 7.5 shows the energy distributions of the dedicated NSB sets produced with ObsNSB. The distributions are displayed for the situation after the image cleaning (dashed lines) and after the application of the gamma/hadron separation (solid lines). The whole energy distribution and, thus, the energy threshold shifts with rising NSB towards higher energies. Furthermore, as for the image parameters, the detection rate of gamma rays decreases with the NSB, which is mostly an effect of the higher cleaning levels.

In order to understand this dependency in more detail, the energy threshold is plotted against the mean camera current in figure 7.6. Each data point represents

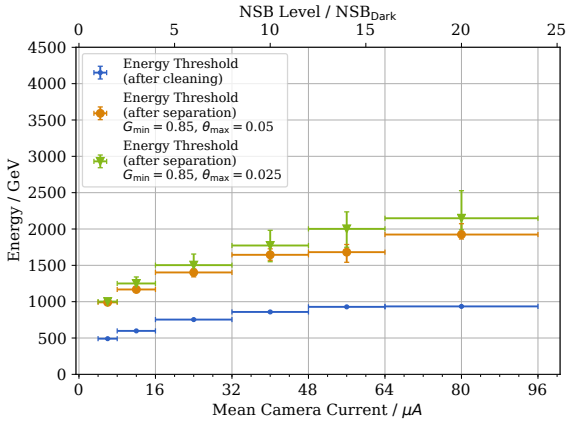

Figure 7.6: Dependency of the energy threshold on different light conditions with the optimized analysis. The coloring represents the threshold after cleaning and after the background suppression with two different limits for the `angular_distance` (θ). The ordinate represents energy thresholds. The light conditions are given on the abscissas in units of the camera's average current (bottom) and in units of dark night conditions (top). The data points are the mode of the energy distribution, determined by fitting a Gaussian to the top of the energy distribution. Values and horizontal error bars are determined in a 100-fold bootstrapping of the fit. Vertical error bars indicate the width of the NSB bins.

the energy threshold estimated by fitting a Gaussian curve to a region near the maximum of the energy distribution. The fit is performed in a 100-fold bootstrapping to estimate the uncertainty of the threshold estimation. The error bars indicate the standard deviation of the bootstrap folds. Furthermore, the threshold is plotted in this visualisation for the situations after the image cleaning and after the gamma/hadron separation for different θ^2-cuts. The resulting energy thresholds thus found are listed in table 7.1.

It is evident that the energy threshold rises with the NSB level. Before the gamma/hadron separation, the threshold rises quickly with the background light and cleaning levels. It seems to converge towards a plateau slightly below 1 TeV. At the lowest light conditions, the energy threshold is roughly at 500 GeV, while at high NSB it exceeds 1 TeV. Comparable behavior can be seen for events after a gamma/hadron separation with a `gammaness` > 0.85 and a θ^2-cut at 0.05°. The energy threshold rises from ≈ 1 TeV at dark night conditions to slightly below 2 TeV at strong moonlight conditions. With the harder limit on the `angular_distance` (θ) the energy threshold rises even above 2 TeV at the brightest light conditions. The uncertainties of the energy threshold increase with NSB due to a broadening of the energy distributions and a decline of event numbers in these samples.

NSB set	NSB level (range) [$\mathrm{NSB_{Dark}}$]	Min. Energy (optimized) [GeV]	Energy Threshold (optimized) [GeV]
After cleaning:			
no moonlight	(0,2]	200±0	491±2
low moonlight	(2,4]	200±0	598±3
slight moonlight	(4,8]	200±0	754±3
moderate moonlight	(8,12]	200±0	859±6
increased moonlight	(12,16]	201±0	929±5
strong moonlight	(16, 24]	200±0	935±4
After separation: $G_{\mathrm{min}} = 0.85$, $\theta^2_{\mathrm{max}} = 0.025°$			
no moonlight	(0,2]	330±32	1002±37
low moonlight	(2,4]	354±23	1251±79
slight moonlight	(4,8]	378±64	1503±115
moderate moonlight	(8,12]	369±114	1773±192
increased moonlight	(12,16]	466±60	2002±253
strong moonlight	(16, 24]	706±20	2148±248
After separation: $G_{\mathrm{min}} = 0.85$, $\theta^2_{\mathrm{max}} = 0.05°$			
no moonlight	(0,2]	267±15	991±28
low moonlight	(2,4]	248±33	1168±36
slight moonlight	(4,8]	339±28	1402±70
moderate moonlight	(8,12]	328±72	1645±91
increased moonlight	(12,16]	452±44	1682±115
strong moonlight	(16, 24]	564±67	1924±107

Table 7.1: Energy thresholds determined for different light conditions after cleaning and after the background suppression with two different limits for the `angular_distance` (θ). Energy thresholds are listed for the optimized analysis. Furthermore, the minimum energy in the gamma sample is also listed. The energies and their uncertainties are the result of a 100-fold bootstrapping. Both are rounded to integers.

7.3 Angular Resolution

The energy-dependent angular resolution is used to determine the performance of the directional reconstruction of events from a point source, depending on the event's energy. Based on simulated point source like events, the angular resolution is evaluated here in the sense of a 68 % containment interval of angular distances of reconstructed event directions. While large, high-energy events contain more information to reconstruct their origin, the reconstruction of the direction of low-energy events is more difficult and has a larger uncertainty.

In this section, the NSB-dependent angular resolution of FACT is determined on point source like gamma events from simulations in Wobble-Mode. The evaluated events are constrained to a `gammaness` of $G > 0.85$. The energy is binned by the simulated true energy.

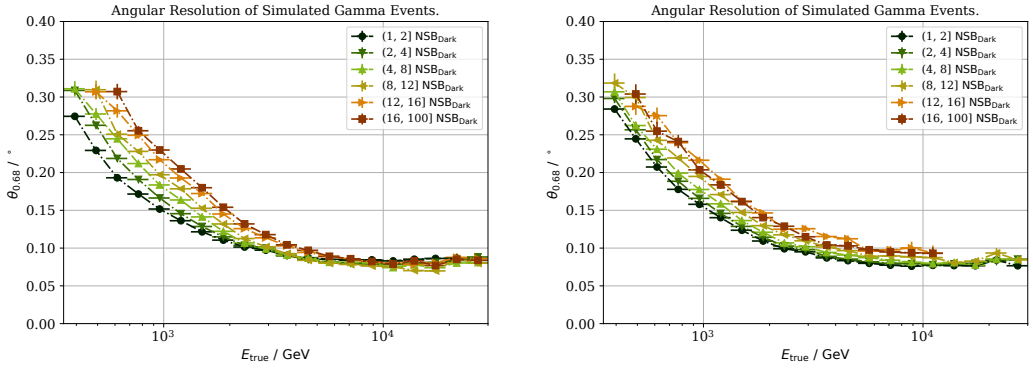

(a) Optimized analysis.

(b) Standard analysis.

Figure 7.7: Dependency of the angular resolution on the light conditions for the progressive cleaning (right) and the standard cleaning levels (left) of events after gamma/hadron separation with a prediction threshold of $G > 0.85$ confidence. The evaluated events are from an energy range of 350 GeV to 30 TeV. The data points represent the mean from a 100-fold bootstrapping and the horizontal error bars indicate its standard deviation. Vertical error bars indicate the width of the energy bins. Dashed lines connect the data points in order to guide the reader's eye towards related data sets. They do not indicate any linearity.

Figure 7.7 shows the angular resolution achieved with the optimized analysis (fig 7.7a) and, to illustrate a possible improvement, also the angular resolution achieved with the standard analysis (fig 7.7b). In general, the results from both analyses provide similar results for the angular resolution. The new cleaning levels seem to improve the angular resolution of events at high NSB levels ($> 32\,\mu A$) with energies above

2 TeV. The high energy segment beyond the 10 TeV mark in particular benefits from this optimization. However, at lower energies, below 2 TeV, the standard analysis provides slightly better results for these light conditions and, also at lower light conditions below 32 µA, the standard analysis provides mostly better results.

Regarding the NSB dependency of the angular resolution, figure 7.7 shows a decrease in resolution with increasing background light. In particular, the angular resolution of a given energy bin increases with rising NSB. Events with an energy of, e.g., ≈ 1 TeV reach from 0.15° at dark night conditions to $\approx 0.23°$ at the highest light conditions. This trend is visible for all energy ranges, but becomes less prominent with higher energies. In the worst case, the difference in resolution between light conditions is $\approx 0.1°$

In summary, it seems that the angular resolution is mostly affected by moonlight in the lower energy range below 2 TeV. Not surprisingly, the directional reconstruction of high energy showers is almost unaffected by the NSB as their light distribution is well above the NSB. In order to investigate the impact of the angular resolution to observations, the detection of Crab is discussed in the following section, alongside the spatial distribution of excess events in skymaps.

7.4 Source Detection

The results for the source detection of the Crab Nebula in the defined NSB ranges are summarized in table 7.2. The table shows that the significance of detection declines with the NSB level. Both analyses in use are able to detect the Crab Nebula up to $(8-12)\,\mathrm{NSB}_{\mathrm{Dark}}$ with more than $5\,\sigma$ significance, the optimized analysis even up to $(12-16)\,\mathrm{NSB}_{\mathrm{Dark}}$. At the same time, however, the observation times also decline.

In order to determine the detection performance of Crab independent of the overall statistics of a NSB sample, the significance can be normalized to the square root of observation time in hours, as done in section 6.3.2. Up to $(8-12)\,\mathrm{NSB}_{\mathrm{Dark}}$, the Crab Nebula is detected with $S_{\mathrm{norm}} \approx 5\,\frac{\sigma}{\sqrt{\mathrm{h}}}$, given optimized cleaning levels. Above these light conditions, S_{norm} decreases with the NSB level and detection with more than $5\,\sigma$ is not possible with the samples used.

The situation is similar for the standard analysis, and here the detection performance also declines with the background light. Evidently, the performance of detecting Crab improves with optimized cleaning levels.

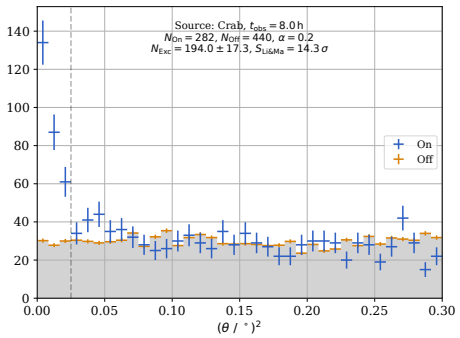

(a) Optimized analysis: $(8-12)\,\mathrm{NSB_{Dark}}$

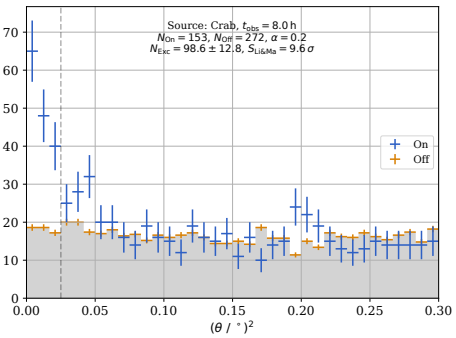

(b) Standard analysis: $(8-12)\,\mathrm{NSB_{Dark}}$

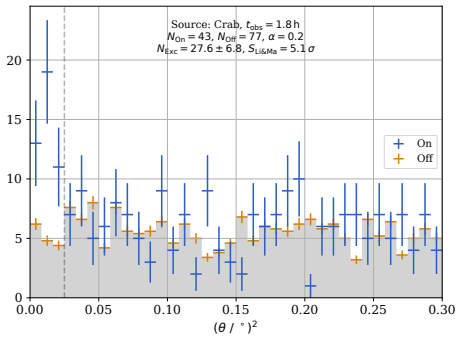

(c) Optimized analysis: $(12-16)\,\mathrm{NSB_{Dark}}$

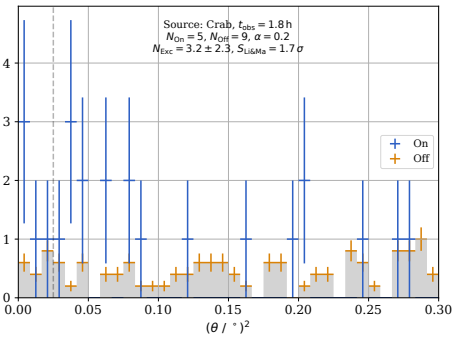

(d) Standard analysis: $(12-16)\,\mathrm{NSB_{Dark}}$

Figure 7.8: Examples for the distribution of the squared angular distance of reconstructed and actual source position (θ^2-plots) of Crab Nebula observations at moderate moonlight (a and b) and increased moonlight conditions (c and d). The squared distances θ^2 are binned on the abscissa and the total number of events is given on the ordinate. The plots on the left (a and c) are achieved with the optimized analysis, whereas those on the right (b and d) with the standard analysis. Blue points represent data from the ON-position, while the average rates from the OFF-positions are indicated in orange. A `gammaness` cut of $G > 0.85$ has been applied to the Crab Nebula data in order to achieve the shown examples. The value of the θ^2-cut of $\theta^2_{\mathrm{max}} = 0.025°$ is indicated by the vertical grey, dashed line. The optimized analysis shows higher excess rates and significances of the detection, as well as smoother distributions. At increased moonlight the standard analysis is not able to detect the Crab Nebula.

7.4.1 Angular Distribution of Detected Gamma-Like Events

The angular distribution of detected gamma-like events is visualized in a θ^2-plot, which shows the quantity of detected events with regard to the ON-position and the distribution of the background estimated in the five OFF-positions, as described in

section 4.4.3. The background distribution can be found in such a plot as mostly uniform distribution. Examples for θ^2-plots are given for two light conditions in figure 7.8. The chosen examples show the θ^2-plots of both analyses for light levels $(8-12)\,\mathrm{NSB_{Dark}}$ and $(12-16)\,\mathrm{NSB_{Dark}}$. The θ^2-distributions of all NSB samples can be found in appendix C.1.

For both NSB levels, the optimized analysis provides a more significant detection and the θ^2-distribution shows a more distinctive and narrower peak at the location of the source, which is at $\theta^2 = 0°$. In the sample with a light range of $(12-16)\,\mathrm{NSB_{Dark}}$, an excess is clearly visible for the optimized analysis, even though the detection does only just exceed a $5\,\sigma$ confidence threshold. In contrast, for the standard analysis, Crab is invisible in this sample.

At the brightest light conditions, $(16-24)\,\mathrm{NSB_{Dark}}$, both analyses are unable to detect Crab, although the optimized analysis shows a small excess, which, however, is compatible with the background within the error limits.

7.4.2 Distribution of Detected Gamma-Like Events on Sky Maps

The spatial distribution of detected gamma-like events regarding the observed sky region is called a sky map. The reconstructed[4] position of an event's origin is estimated as equatorial coordinates right ascension (RA) and declination (dec). By this procedure, the two-dimensional distribution of the reconstructed origins is put in context with the sky region actually observed and the location of the emitting source, the Crab Nebula.

Examples for the sky maps of the two light conditions discussed in the previous section are displayed in figure 7.9, for both analyses. The sky maps of all NSB samples can be found in appendix C.1.

In these sky maps the location of Crab is indicated by a grey circle at the center of the map. The number of events is indicated by the coloring. It is evident that the largest cluster of events accumulates at this location.

This behavior is similar for all light conditions below $(12-16)\,\mathrm{NSB_{Dark}}$. For these light conditions, the sky maps for both analyses are very similar. Starting with the range $(8-12)\,\mathrm{NSB_{Dark}}$, the sky maps of the standard analysis lose their quality since the accumulation of events at the location of Crab Nebula is less concentrated. Even less events are in the skymap at the highest NSB levels. No accumulation of events can thus be detected at the location of the Crab Nebula when using the standard cleaning.

[4] See chapter 4.4.1.

The sky maps confirm the observations from the θ^2-plots earlier in this section. For both analyses, the accumulation point is concentrated at the source position, but the pictures of the standard cleaning are more distorted. Moreover, it is more washed out for the standard cleaning. Additionally, at the highest NSB levels, the Crab Nebula can barely be seen with optimized cleaning, whereas with the standard cleaning the few surviving events are scattered over the map.

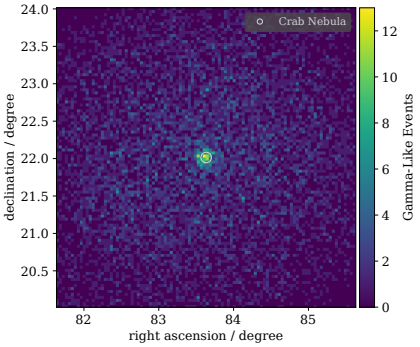

(a) Optimized analysis: $(8-12)\,\mathrm{NSB}_{\mathrm{Dark}}$

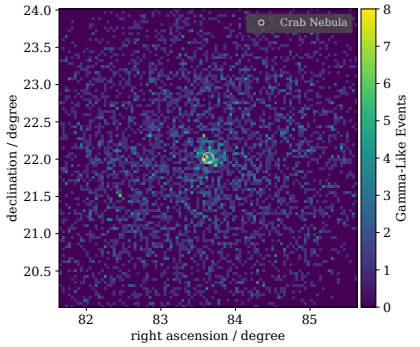

(b) Standard analysis: $(8-12)\,\mathrm{NSB}_{\mathrm{Dark}}$

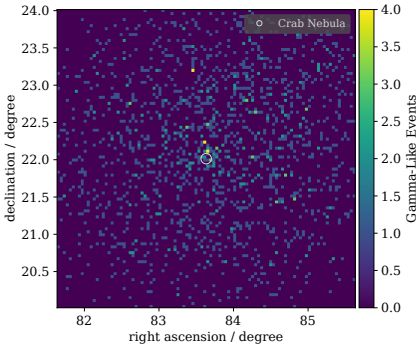

(c) Optimized analysis: $(12-16)\,\mathrm{NSB}_{\mathrm{Dark}}$

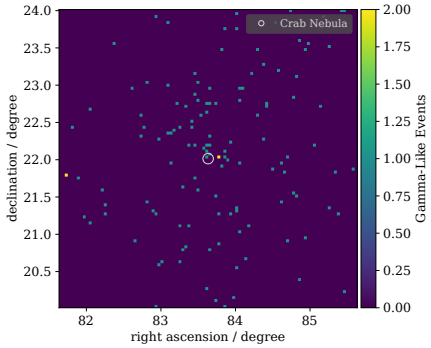

(d) Standard analysis: $(12-16)\,\mathrm{NSB}_{\mathrm{Dark}}$

Figure 7.9: Sky maps of gamma-like events in the observed sky region with the source position of Crab in the centers. Two examples of NSB conditions are presented: moderate moonlight and increased moonlight. The latter are the highest possible with a minimum significance $> 3\sigma$. The source location is indicated by the grey circle. The two plots on the left (a and c) are achieved with the optimized analysis, whereas the two on the right (b and d) show the same data processed with the standard analysis. The coloring indicates the frequency of events from a certain direction given in equatorial coordinates right ascension and declination. The data are constrained to a `gammaness` of $G > 0.85$. At moderate moonlight events accumulate at the location of Crab is clearly visible.

	no moon	low moon	slight moon	mod. moon	incr. moon	strg. moon
Current [µA]	(0,8]	(8,16]	(16,32]	(32,48]	(48,64]	(64,96]
NSB level [$\mathrm{NSB_{Dark}}$]	(0,2]	(2,4]	(4,8]	(8,12]	(12,16]	(16,24]
θ^2_{max} [°]	0.025	0.025	0.025	0.025	0.025	0.025
t_{obs}[h]	50.5	22	17.1	8	1.8	0.4
Optimized analysis:						
N_{On}	2 047	964	672	282	43	7
N_{Off}	3 084	1 496	1 116	440	77	19
N_{Exc}	1 430.2	664.8	448.8	194	27.6	3.2
$S_{\mathrm{Li\&Ma}}$ [σ]	39.5	26.6	21.2	14.3	5.1	1.3
$S_{\mathrm{norm}}\left[\frac{\sigma}{\sqrt{\mathrm{h}}}\right]$	5.56	5.67	5.13	5.06	3.8	2.06
Standard analysis:						
N_{On}	2 125	1 067	714	153	5	0
N_{Off}	3 773	1 755	1 266	272	9	,
N_{Exc}	1 370.4	716	460.8	98.6	3.2	-0.2
$S_{\mathrm{Li\&Ma}}$ [σ]	35.8	26.8	20.8	9.6	1.7	0
$S_{\mathrm{norm}}\left[\frac{\sigma}{\sqrt{\mathrm{h}}}\right]$	5.04	5.71	5.03	3.39	1.27	0

Table 7.2: Statistics of the detection of Crab with optimized (top) and standard cleaning levels (bottom), grouped in NSB condition samples. All results are provided with the same θ^2-cut at $\theta^2_{\mathrm{max}} = 0.025°$. Also the observation times t_{obs} are independent of the analysis. N_{On} and N_{Off} represent the number of events from the ON-position and the OFF-positions. N_{Exc} indicates the number of On-events exceeding the background that was estimated in the OFF-positions. The significance of the source detection is given as $S_{\mathrm{Li\&Ma}}$ and additionally as normed to the square root of observation time by S_{norm}.

7.5 Sensitivity

In order to evaluate the performance for detecting different sources at given light conditions, the sensitivity of the telescope and analysis are determined as described in section 4.4.5. Accordingly, the integral sensitivity per light condition and the differential sensitivity of the given analysis are compared for different light conditions. Furthermore, the impact of the chosen analysis (optimized or standard analysis) is investigated in the following.

7.5.1 Integral Sensitivity

The integral sensitivity is the overall minimum flux – in units of Crab (C.U.) – needed to detect a source with $5\,\sigma$ significance in 50 h effective observation time, given that the source has a similar spectral index. Figure 7.10 shows the integral sensitivity at a given light condition achieved with a `gammaness`-cut $G_{\text{min}} = 0.85$ and a θ^2-cut of $\theta^2_{\text{max}} = 0.025°$, and an additional, looser, θ^2-cut with $\theta^2_{\text{max}} = 0.05°$, depending on the NSB level. Sensitivies are shown for both analyses.

In comparison, the two analyses in figure 7.10b also reflect the improvement due to the optimized analysis with new cleaning levels. In particular, for high NSB levels the sensitivities have been improved significantly. Especially in the $(12-16)\,\text{NSB}_{\text{Dark}}$ bin, the sensitivity of the standard analysis cannot be determined, since Crab was not detected there, as was shown in the previous section. Only the optimized analysis provides an estimate for the sensitivity of $S_{\text{rel.}}\,((12-16)\,\text{NSB}_{\text{Dark}}) = 0.17^{+0.04}_{-0.05}\,\text{C.U.}$

The overall sensitivity of the analysis decreases with rising NSB levels (see figure 7.10a). Given the tighter θ^2-cut, the sensitivities are less than 0.1 C.U. at the lowest light conditions. In the middle range $(4-12)\,\text{NSB}_{\text{Dark}}$ they increase slightly to about 0.11 C.U. sensitivity. Above $12\,\text{NSB}_{\text{Dark}}$ roughly a flux of about 0.17 C.U. is required to exceed the $5\,\sigma$ confidence threshold[5] of the significance of detection.

For the larger θ^2-cut, the trend is similar but sensitivities range from 0.12 C.U. to 0.3 C.U. Moreover, the uncertainties of the determined sensitivity in the range $(12-16)\,\text{NSB}_{\text{Dark}}$ are larger due to the lower significance in the Crab sample.

A sensitivity for the highest NSB levels could not be calculated as the source was not detected with sufficient significance by either analysis. Consequently, the sample with the NSB range $(16-24)\,\text{NSB}_{\text{Dark}}$ is excluded from the further analysis.

[5] The agreement on a $5\,\sigma$ confidence threshold in astroparticle physics was concluded at the International Cosmic Ray Conference (ICRC) in 1985 and is mentioned in [44]

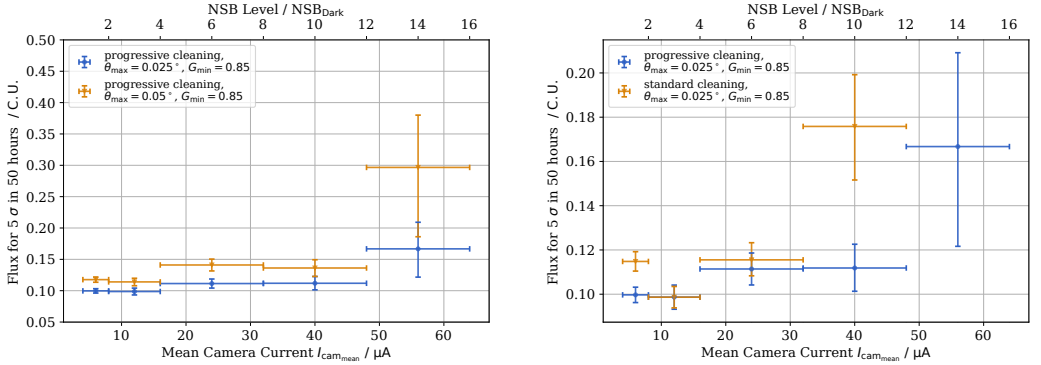

(a) progressive cleaning **(b)** Comparison of cleanings

Figure 7.10: Integral sensitivity for six different light condition samples for the optimized analysis a) and a comparison with the standard analysis b) after the gamma/hadron separation. The relative Crab Nebula flux for 5 σ in 50 h observation time is given on the ordinate in Crab units (C.U.). The light conditions are given on the abscissas in units of the camera's average current (bottom) and in units of dark night conditions (top). The prediction threshold for the gamma/hadron separation and the θ^2-cut are presented in the legends of the plots. The sensitivities were estimated in a 1000-fold bootstrapping and the data points represent the mean integral sensitivity over the boot strap samples. The horizontal error bars indicate the width of the current bin. The vertical error bars indicate the confidence interval by means of the 1 σ environment of the determined integral sensitivity. It is evident that the integral sensitivity slightly declines with the NSB level and a longer observation time is required. The standard analysis shows generally worse sensitivities than the optimized analysis.

7.5.2 Differential Sensitivity

In order to determine the performance for sources with a different spectral index than the Crab Nebula the differential sensitivity is determined as described in section 4.4.5. For this purpose, the events are binned by their estimated energy in 10 logarithmic bins in a range from 400 GeV to 30 TeV.

The relative sensitivity is calculated for each energy bin separately. The uncertainty of the sensitivity is determined in a 1000-fold bootstrapping. In order to diminish small systematic discrepancies (as suggested in [11]) sensitivities with $N_{\text{excess}} \leq 10$ and $N_{\text{off}} \leq 10$ are neglected in each bootstrap step. Furthermore, only bins with a valid sensitivity in at least 90 % of bootstrap steps are displayed.

The differential sensitivities for the optimized analysis are illustrated in figure 7.11. The sensitivity curves of the remaining light conditions are similar over wide ranges.

The lowest energy bin evaluated moves towards higher energies with the NSB level as the energy threshold is also shifted. Accordingly, only for the $(0-2)\,\mathrm{NSB_{Dark}}$ sample a sensitivity could have been estimated for an energy range of $(400-600)\,\mathrm{GeV}$. In the range $(600-950)\,\mathrm{GeV}$ samples up to $8\,\mathrm{NSB_{Dark}}$ are represented and show a clear degradation of the sensitivities with the light conditions.

In the central energy range at about 1 TeV to less than 4 TeV all shown light conditions show comparable sensitivities in the margin of their uncertainties, despite the sample above $12\,\mathrm{NSB_{Dark}}$, which has the worst sensitivity for energies of about 1 TeV. However, there is a slight trend of decreased sensitivity with the light conditions in this energy range, with the $(4-8)\,\mathrm{NSB_{Dark}}$ sample being the exception as it has slightly worse sensitivities than the $(8-12)\,\mathrm{NSB_{Dark}}$ sample.

Especially for the light conditions in a range of $(12-16)\,\mathrm{NSB_{Dark}}$, sensitivities can only be determined in the central energy range of $(0.95-2.3)\,\mathrm{TeV}$. Due to low statistics at these light conditions, it was only possible to evaluate two energy bins.

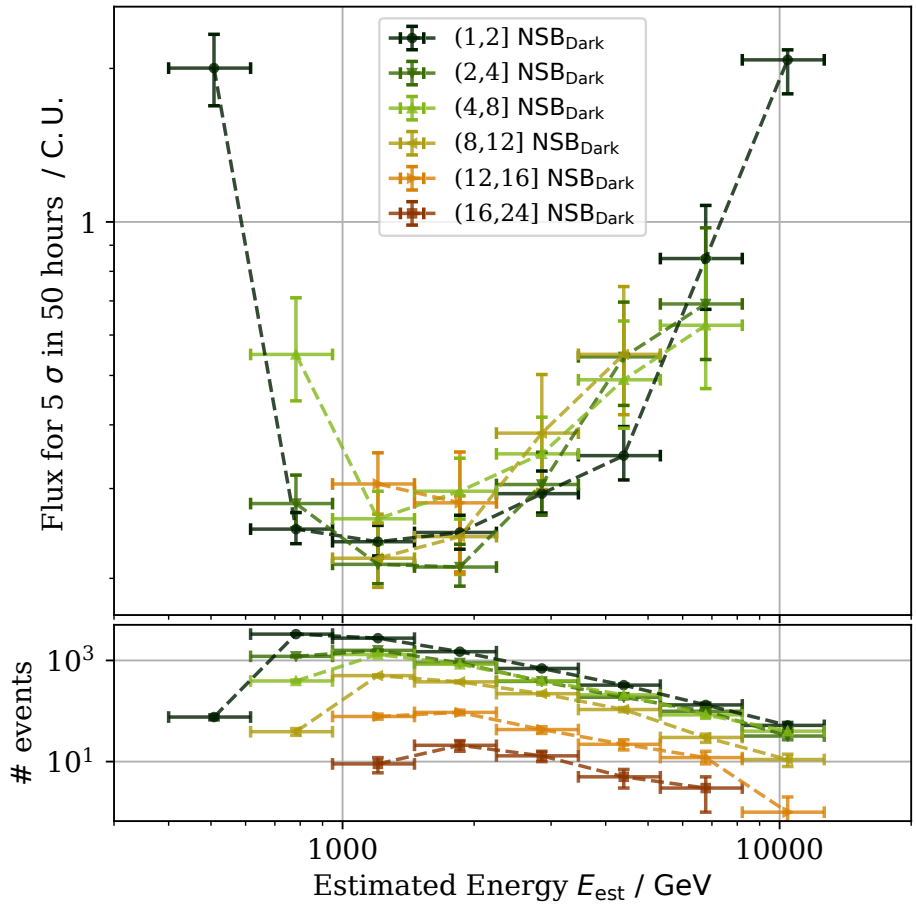

Figure 7.11: Differential sensitivity for six different light condition samples for the optimized analysis after the gamma/hadron separation. The gamma/hadron separation was performed with a `gammaness`-cut of $G_{min} = 0.85$ and a θ^2-cut of $\theta^2_{max} = 0.025°$. The relative Crab Nebula flux for $5\,\sigma$ in 50 h observation time is given on the ordinate in Crab units (C.U.). The abscissa represents the estimated energy in GeV. The horizontal error bars indicate the width of the energy bins, whereas vertical error bars indicate the confidence interval by means of a $1\,\sigma$ environment of the relative sensitivity determined in 1000-fold bootstrapping. The dashed lines connect the data points from the same NSB sample and do not indicate an interpolation between bins. In the lower panel, the energy distribution is plotted as a reference for the statistics in each bin.

7.6 Effective Collection Area

The effective collection area A_{eff} allows quantification of the detection efficiency of the whole analysis chain as described in section 4.5.2, by calculating the ratio of simulated and surviving events after all analysis steps. This is performed in log space energy bins for the desired energy range of the simulated gamma events. In order to identify the impact of light conditions on the detection efficiency, this procedure is carried out and evaluated for each light condition sample.

Figure 7.12 shows the effective areas for all six NSB samples with optimized and standard cleaning levels after application of the gamma/hadron separation with a `gammaness`-cut $G_{\text{min}} = 0.85$ and a θ^2-cut of $\theta^2_{\text{max}} = 0.025°$.

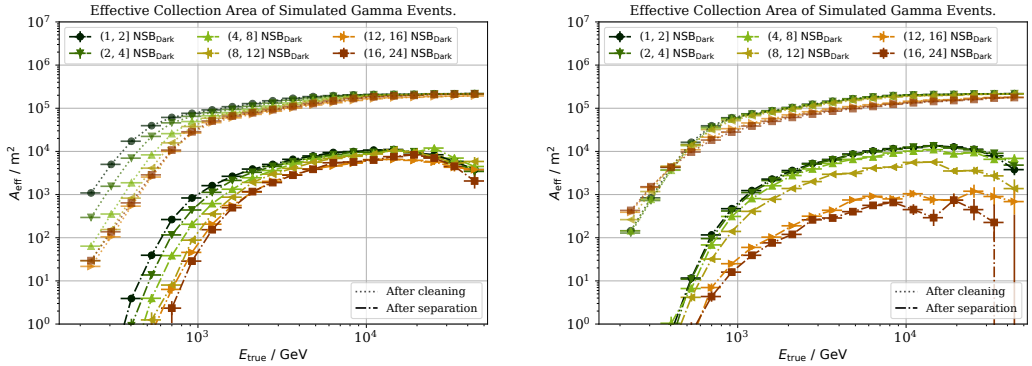

(a) Optimized analysis **(b)** Standard analysis

Figure 7.12: Effective collection areas for six different light condition samples, compiled with the optimized (a) and the standard analysis (b). The abscissa represents the simulated energy in GeV, whereas the ordinate shows the effective collection areas. The connecting lines group data points from the same NSB sample and do not indicate any interpolation. Dotted lines indicate the effective collection areas after the image cleaning, whereas the dashed lines represent the situation after a gamma/hadron separation with a `gammaness` threshold $G_{\text{min}} = 0.85$ and a θ^2-cut of $\theta^2_{\text{max}} = 0.025°$. The horizontal error bars represent the width of the energy bin and vertical error bars indicate the confidence interval of the determined effective area with regard to the ratio of simulated and triggered events in a bin. This interval is estimated as a binomial proportion confidence interval.

The comparison of figure 7.12a and figure 7.12b shows a clear improvement by using the optimized cleaning levels. The effective collection areas of samples with high NSB levels ($>8\,\text{NSB}_{\text{Dark}}$) are significantly smaller for the standard analysis than those for optimized analysis. Accordingly, the detection efficiency at higher NSB

levels is significantly improved by the optimized analysis. The structures of effective collection areas from the optimized analysis appear flatter and smoother, while the results of standard analysis are more unsteady especially in the high-energy regime. At lower NSB levels ($<8\,\mathrm{NSB_{Dark}}$) improvement in effective area is less striking but still present.

The comparison of effective collection areas for different light conditions reveals a decline of A_{eff} with rising NSB. This decline is effecting both the overall detection efficiency and the effective areas at the low bound of the detectable energy regime. Below 4 TeV the effective area is a rather steep function. It reaches a plateau at about 7 TeV. With increasing NSB levels, the low-energy edge of A_{eff} is shifted towards higher energies, which is partly a result of the artificially higher energy threshold due to the chosen image cleaning. Accordingly, this shift of the lower edge is less prominent for the effective areas generated with the standard analysis.

For showers at energies almost at 1 TeV the effective collection area differs from $A_{\mathrm{eff}} \approx 5000\,\mathrm{m^2}$ at dark night conditions of $(0-2)\,\mathrm{NSB_{Dark}}$ to less than $A_{\mathrm{eff}} \approx 300\,\mathrm{m^2}$ at the brightest light conditions with $(16-24)\,\mathrm{NSB_{Dark}}$. Within the plateau A_{eff} is the highest at about $40.000\,\mathrm{m^2}$ for dark night conditions and the lowest with less than $20.000\,\mathrm{m^2}$ at bright light conditions.

At about 15 TeV the effective areas after gamma/hadron separation decrease again. This is the high-energy region, with comparably less events due to the power-law nature of the energy spectrum. Moreover, these showers are often not fully contained in the field of view because of their large size.

The acceptance correction, which is needed to compile the energy spectrum, uses generally the same effective areas as those presented in this section. More precisely, in case of the unfolding performed in the following section 7.7 to generate energy spectra of the Crab Nebula, the effective collection areas are compiled together with the spectrum.

7.7 Crab Energy Spectrum

The energy spectrum is one of the main goals of each source's analysis. The impact of the NSB levels to the energy spectrum is investigated in the following. Only NSB samples with significances of detection of more than $5\,\sigma$ are considered as they provide sufficient statistics and excess events in particular. Thus, the samples at the highest NSB conditions at $(16-24)\,\mathrm{NSB_{Dark}}$ are excluded here. However, the standard analysis' sample at $(12-16)\,\mathrm{NSB_{Dark}}$ is also unfolded in order to be compared with the optimized analysis, which is just above the $5\,\sigma$ limit there.

Each energy spectrum is unfolded separately for each of the given NSB samples. As shown in section 7.2, the energy threshold increases with rising NSB for the analysed MCs. To compensate for this effect, the unfolded energy range is adapted accordingly. The decline of event rates is further compensated by reducing the number of unfolded bins. Both effects have been discussed in the previous sections.

The unfolded spectrum is then compared to already published Crab Nebula energy spectra from MAGIC [10] and FACT observations from 2013/14 [100]. Furthermore, each spectrum is compared to the spectrum for the lowest NSB from this study with conditions of $(0-2)\,\mathrm{NSB}_{\mathrm{Dark}}$. This allows for determination of the limitations for unfolding at different NSB levels. For comparison, spectra unfolded with both analyses are shown.

7.7.1 Unfolding Result of the Optimized Analysis

The result of the optimized analysis with progressive cleaning levels and ObsNSB MCs is illustrated in figure 7.13. The figure shows the unfolded energy spectrum for each NSB level. A fitted parametrization of each published spectrum is illustrated with a solid line. Additionally, the energy distribution of events remaining after gamma/hadron separation is depicted together with the unfolded count spectrum.

Up to an NSB level of $< 16\,\mathrm{NSB}_{\mathrm{Dark}}$ the energy spectrum of Crab Nebula can be successfully unfolded. The majority of spectral data points are in agreement with the two published spectra within statistical fluctuations. However, the margin energy bins ($\leq 1\,\mathrm{TeV}$ and $\geq 10\,\mathrm{TeV}$) differ with rising NSB and show a slight tendency of over-estimation compared to the published results. A comparison of the different spectra with the unfolded spectrum at dark night conditions underlines this observation. In the case of the low energy edge, this is a result of the combination of small entries in the effective collection area and lower event rates at theses energies. The effect of low event rates can also be seen in the energy distribution of remaining events after gamma/hadron separation for the Crab samples. These rates are displayed at the side of each spectrum. Nevertheless, these energy bins still fit the reference spectra within margins of their error bars.

NSB levels $< 12\,\mathrm{NSB}_{\mathrm{Dark}}$ have sufficient statistics to determine the expected structure of the energy distribution. In the case of the $(12-16)\,\mathrm{NSB}_{\mathrm{Dark}}$ sample, the unfolded event distribution shows that only a few events with large relative errors are available, and no events above 10 TeV have been detected. As shown earlier this sample does only just exceed the $5\,\sigma$ significance limit. Nevertheless, a spectrum can be unfolded with a massively reduced number of bins. It still agrees with the reference spectra, however, their error bars are significantly larger than those of the lower NSB ranges.

In particular, the high-energy bins ($> 10\,\mathrm{TeV}$) show a lerger over-estimation of bins due to the lack of high-energy events, which is mainly caused by low statistics for the highest NSB levels due to small observation times at these conditions.

7.7.2 Unfolding Result of the Standard Analysis

Similar to the optimized analysis, the energy spectra are unfolded for the standard analysis. The results are visualized in figure 7.13, and are mostly comparable to the results discussed in the last section. However, the lowest energy bin at $(0-2)\,\mathrm{NSB}_{\mathrm{Dark}}$ is over-estimated. In this energy range the fluxes estimated with the optimized analysis chain are closer to the reference spectra. Apart from the this bin and the general event rates no significant difference can be noted for the spectra of both analyses up to $(8-12)\,\mathrm{NSB}_{\mathrm{Dark}}$. Above $12\,\mathrm{NSB}_{\mathrm{Dark}}$ only a few events survive the gamma/hadron separation. Less energy bins can thus be unfolded successfully. As a consequence of a lack of statistics, especially in the high energy regime, the unfolded spectrum does thus not correspond to the reference spectra.

In summary, the Crab energy spectrum can be reconstructed up to an NSB level of $12\,\mathrm{NSB}_{\mathrm{Dark}}$ with an analysis chain based on both standard and progressive cleaning levels. The unfolding result seems to be mainly independent of the chosen cleaning levels and NSB simulation (ObsNSB or GenNSB), but the unfolded spectra with optimized cleaning levels fit better to the reference spectra and a allow to go lower in energy. In the case of the $(12-16)\,\mathrm{NSB}_{\mathrm{Dark}}$ sample only the optimized analysis corresponds in all bins to the reference spectra in the margin of uncertainties. Above $12\,\mathrm{NSB}_{\mathrm{Dark}}$ the higher detection rate of the optimized analysis thus indicates an clear advantage over the standard analysis.

7.7.3 Comparison with Reference Spectra

In both analyses, the energy spectrum of Crab Nebula can be reconstructed safely up to light conditions $\leq 12\,\mathrm{NSB}_{\mathrm{Dark}}$. Despite low event numbers, the unfolding evan seems to provide a reasonable spectrum for the $(12-16)\,\mathrm{NSB}_{\mathrm{Dark}}$ range when using the newly optimized cleaning levels. This shows that observations up to this level are still feasible to provide valid energy spectra, which are in agreement with the reference spectra from MAGIC and FACT.

The comparison to FACT's Crab Nebula spectrum from winter 2013/14 indicates further that FACT's performance does not show any significant degradation for the time between these studies.

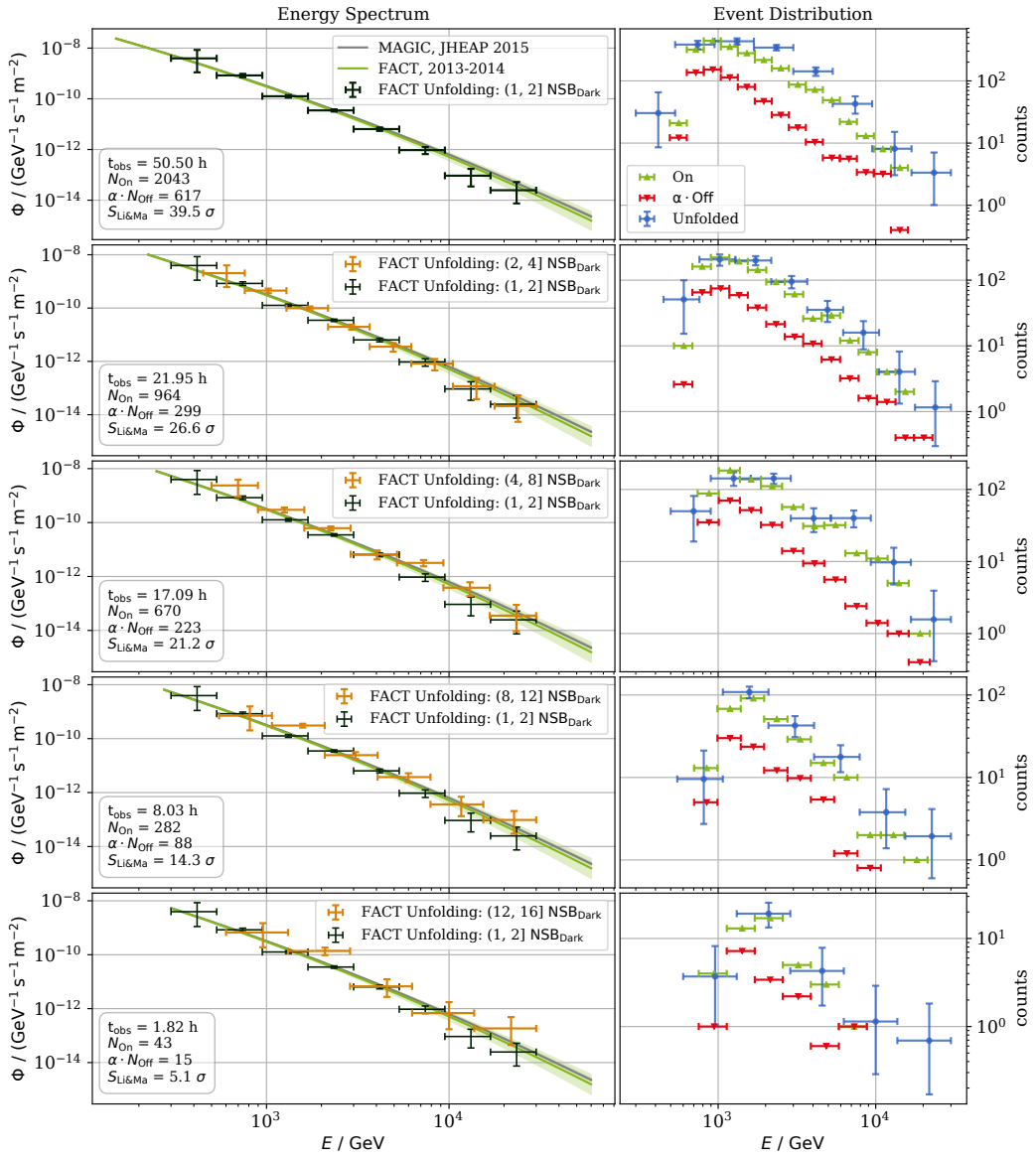

Figure 7.13: Energy spectra of the six NSB data sets that are unfolded with ObsNSB MCs and processed with progressive cleaning levels. The first column shows the energy spectra with the estimated flux on the ordinate and the unfolded energy on the abscissa. The second column shows the energy distribution of events before (green and red) and after unfolding (blue) with the event numbers on the ordinate on the left hand side and again the estimated energy on the abscissa. Each row shows the energy spectrum of a NSB sample (increasing brightness in ascending order), the energy spectrum at the lowest NSB level, and a fit of published reference energy spectra of FACT and MAGIC (green and grey solid lines). The uncertainty of the latter is indicated by an area with the same color. The values of the extracted spectra are listed in tables C.1 to C.5 in the appendix.

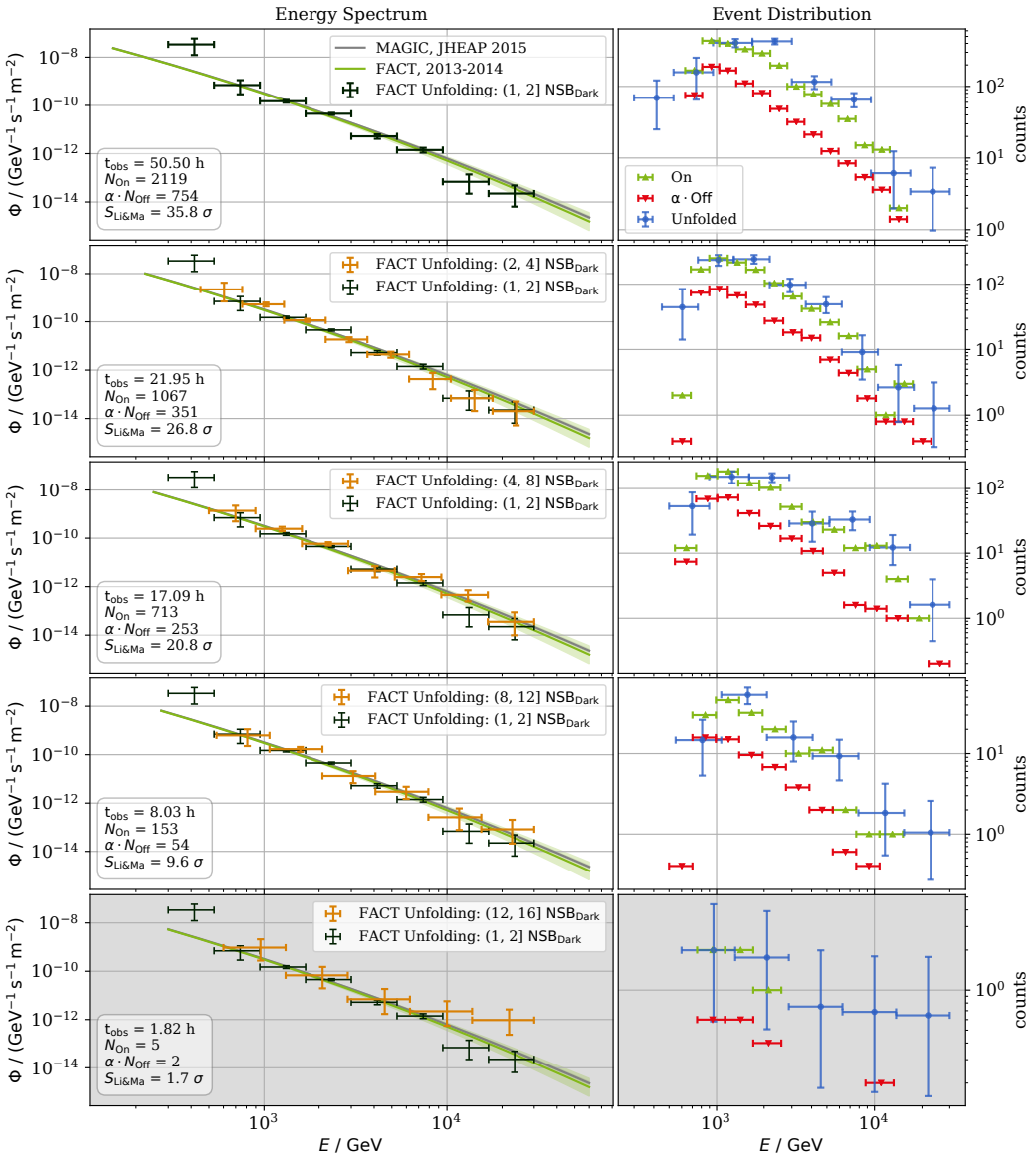

Figure 7.14: Energy spectra of the six NSB data sets that are unfolded with standard cleaning levels. The first column shows the energy spectra with the estimated flux on the ordinate and the unfolded energy on the abscissa. The second column shows the energy distribution of events before (green and red) and after unfolding (blue) with the event numbers on the ordinate on the left hand side and again the estimated energy on the abscissa. Each row shows the energy spectrum of a NSB sample (increasing brightness in ascending order), the energy spectrum at the lowest NSB level, and a fit of published reference energy spectra of FACT and MAGIC (green and grey solid lines). The uncertainty of the latter is indicated by an area with the same color. The energy spectrum at an NSB level of $(12-16)\,\mathrm{NSB}_{\mathrm{Dark}}$ is marked with a grey background as the significance of detection does not exceed the $5\,\sigma$ confidence threshold. The values of the extracted spectra are listed in tables C.6 to C.10 in the appendix.

8 Final Conclusion and Future Prospects

This thesis presents for the first time a detailed investigation of the influence of NSB on the performance of an IACT with a SiPM camera. FACT as the first IACT using this technology is used as a prototype and proof of concept. It has shown that extending observations to such light conditions maximizes the duty cycle of an IACT in terms of total observation time and gapless monitoring. In the case of FACT in particular, about 34 % of observations were executed under bright light conditions. With the optimized analysis shown in chapter 6, most of these observations can be analysed now. In contrast to standard PMT tube designs, SiPM cameras do not need UV filters or dedicated hardware modes which potentially diminish the performance of the instrument as well as achievable observation times.

The Crab Nebula was used as a benchmark source. On a data sample from winter 2015/16, this thesis has demonstrated for the first time that even observations in the presence of the full moon provide reasonable results, given the data analysis has been optimized. The Crab Nebula has been detected above the confidence threshold of $5\,\sigma$ significance up to an NSB level of $12\,\mathrm{NSB}_{\mathrm{Dark}}$ with a rate of $\approx \frac{5\,\sigma}{\sqrt{h}}$. Above these light conditions, the sensitivity degrades with the NSB level (e.g., $\approx \frac{3.4\,\sigma}{\sqrt{h}}$ below $16\,\mathrm{NSB}_{\mathrm{Dark}}$). Nevertheless, the source is still detectable at such light conditions, which correspond to direct moonlight at a lunar phase of more than 60 %.

Based on this analysis, the Crab Nebula energy spectrum has been successfully unfolded with FACT data at ambient light conditions up to $16\,\mathrm{NSB}_{\mathrm{Dark}}$. The limitation to this illumination is likely to be a result of the sample's low number of observations rather than the performance of the instrument. Thus, future investigations with a larger sample at high NSB are required to investigate the performance at even higher light conditions.

It has been demonstrated that the unfolded spectra from the chosen NSB samples correspond to a spectrum computed at the darkest light conditions. The binning and energy range of the unfolding however had to be adapted to the light conditions to compensate for shifted energy thresholds. With regard to NSB, no significant indication for systematic effects on the unfolded spectra have been found yet, despite over-estimation on the edges of the spectrum due to low event statistics and the shift of the energy threshold. A substantial influence of SiPM saturation to the energy estimation could not be determined at the investigated light conditions.

A comparison to reference spectra from MAGIC and FACT shows agreement within statistical fluctuations, which suggests that the use of SiPMs allows for reproduction of results achieved with the commonly used sensor type (PMTs). Furthermore, the correspondence to a FACT Crab Nebula spectrum from winter 2013/14 is an indication for the absence of significant aging of the SiPMs during this time.

The typical performance measures for FACT provided in this thesis widely confirm the findings of other IACTs with PMTs for observations under severe moonlight. An indication for a degrading angular resolution with the NSB level has been found and appears dominant for lower energies ($> 2\,\mathrm{TeV}$). This correlates with a shift of the energy threshold to higher energies with increasing NSB due to the chosen image cleaning, which is adjusted to compensate for increasing distortion of the shower images. Thus, the effective collection area also shows a general decline and a shifted low-energy edge. Consequently, this loss of low-energy showers results in a slowly decreasing integral sensitivity of the detector, ranging from fluxes $\approx 0.099^{+0.003}_{-0.003}\,\mathrm{C.U.}$ at the lowest NSB to $\approx 0.17^{+0.04}_{-0.05}\,\mathrm{C.U.}$ below $16\,\mathrm{NSB_{Dark}}$. Furthermore, he differential sensitivity appears comparable in a central energy range of $(1-4)\,\mathrm{TeV}$ with light conditions below $12\,\mathrm{NSB_{Dark}}$.

These results were achieved by improving the analysis chain of FACT during the course of the study. Additional event-wise feature representations of NSB in the camera were introduced to the *fact-tools* and fed to the machine-learning tasks in order to enable the models to consider the ambient light conditions. A crucial step was, the optimization of the image cleaning with NSB-dependent cleaning levels. As a result of this study, a novel optimization criterion was introduced, which is considering both a minimized impurity due to NSB-dominated events and a maximised efficiency to detect gamma rays.

Furthermore, this optimization requires MC simulations for the observed NSB levels. Since the established simulation software for FACT uses a rather slow simulation of NSB, a more resource-friendly approach was used that superimposes simulations of showers with actually measured images of the NSB.

The cleaning levels used in this study allow for better performance of the analysis compared to standard cleaning levels. It has been shown that the machine-learning tasks benefit from both the optimized cleaning levels and a training on simulations with tailored NSB conditions. The reconstruction of the particle class and its spatial origin achieve the largest benefit from this optimization. Consequently, the significance of detection on the Crab samples is systematically larger with the optimizations carried out in this study. However, the improvement of the energy regression is less striking and its evaluation indicates a larger benefit from generally lower cleaning levels.

A possible improvement for future work could thus be a combination of features from multiple cleaning levels on the same event in order to combine the different benefits mentioned, e.g., to gamma/hadron separation and energy estimation. This way their different advantages could be combined, e.g., by a better signal-to-noise ratio due to higher cleaning levels for the gamma/hadron separation and a higher light yield at low cleaning levels for the energy regression.

Furthermore, it has been shown that the evaluation of FACT's NSB-dependent performance is limited by the amount of data. Thus, it is beneficial to increase the number of available samples for the evaluation and the generation of MCs. For future work, this can be achieved by including additional years of observations of Crab and other sources. The latter enables the researcher to sample from even more pedestal events for the NSB MCs. Additionally, using all years of Crab observations enables future studies to increase the evaluation sample and allows for further investigation of the SiPMs long-term stability.

Nevertheless, observations during full moon are especially rare for the early years of FACT since operations were only possible with the MAGIC crew on site. Due to MAGIC's currently ongoing observations with UV filters during full moon, observations with FACT during these light conditions are more frequent now and allow for an increase of high NSB samples. This has the additional benefit of closing the full moon gap for other sources too. Furthermore, variability studies on the observed AGNs will benefit from the possibility to observe, detect and analyse gamma-ray events even during these gaps. This allows for an unbiased monitoring of these sources and increases the likelihood for detecting flares during high NSB conditions due to overall increased observation time. Additionally, the potential overlap in multi-messenger campaigns is also increased.

For the presented analysis, the machine-learning models were optimized separately for each NSB bin. However, in the use case of an analysis with all observed light conditions, data from these bins have to be combined to compute joined spectra and light curves. Furthermore, it might be beneficial to use the NSB binning only to adapt the cleaning levels. In this case, NSB and cleaning levels should be used as features in the machine-learning model to allow for decisions based on the chosen setting.

The utilized two-level time-neighbor cleaning itself contains room for improvement, as it is based on a rather simple thresholding of arrival time and photon charge of each pixel. The information from a 150 ns time series in each pixel and event is thus boiled down to these two features. Nevertheless, these time series contain additional information, e.g., arrival times and photon charges of NSB photons and other noise. Furthermore, pixels containing Cherenkov photons share similarities of their time series and show larger correlations than NSB-dominated pixels. In order

to take these information into account, a multivariate approach to image cleaning could be beneficial. This strategy may allow for a better adaptation of changing NSB levels by adding them as a feature to such a model. Further studies need to investigate which kind of algorithms, e.g., clustering methods or supervised decision algorithms, are feasible for this task. Deep learning, for instance, allows to start at raw data level without a hand-tailored cleaning and other NSB considerations as we have shown for FACT in [38].

In support of considering information from all photons in an event, a promising novel representation of photons in the pixels is the so-called *photon stream* [80]. Due to the exceptional single photon resolution of SiPMs, the time series of each pixel can be reduced to a list of arrival times of all single photons in a pixel. This list contains photon-like events from all the phenomena mentioned above. They can thus be rejected in more sophisticated algorithms still to be developed that are then tuned to the NSB level. In this representation, an extensive air shower appears as a dense cluster of photons in a three-dimensional space, surrounded by less densely uniformly distributed NSB photons. Brighter ambient light will thus increase the NSB photon density in this representation. Moreover, future studies should investigate whether tackling the identification of shower photons with modern clustering methods might have an advantage over standard image cleaning procedures, especially for bright light conditions.

Further potential for improvement of the IACT technique with SiPMs is mostly determined by the sensor itself. The SiPMs used in FACT are from an early generation of SiPMs that were commercially available in large quantities at the time. In fact, the wavelength dependency of their PDE is far from optimal, considering the wavelength distribution of observed Cherenkov light. Furthermore, their PDE reaches towards the IR regime where light from the NSB dominates, thus impairing the signal-to-noise ratio for the desired task. However, in the meantime manufacturers have optimized these devices for the needs of gamma-ray astronomers, extending the PDE towards near UV wavelengths. Future experiments with these UV-improved SiPMs will thus show better performances at bright ambient light conditions and will have a better sensitivity than FACT in the presence of high NSB. Nevertheless, with the current, new generation of SiPMs, the high sensitivities in IR remain, even if the peak PDE has been shifted more towards the maximum of the Cherenkov light distribution. This demands even further improvement of the PDE of SiPMs or a wavelength shift of incoming photons towards their PDE. An interesting approach for such an improvement of wavelength acceptance for SiPMs was introduced by Guberman et al. as the *Light-Trap* [55]. The device is based on a PMMA disk doped with a wavelength-shifting material that absorbs photons mainly in a $(300-400)\,\mathrm{nm}$ range and re-emits them at $(400-500)\,\mathrm{nm}$. The technique aims to improve the sensitivity in the near-UV range to this extent.

A Appendix: Reproducibility of this Thesis

This chapter contains the settings of the programs used in the study presented in this thesis in order to provide reproducibility. For this purpose, the thesis and the scripts to provide the presented analysis are stored in a *GitLab* repository at TU Dortmund University hosted at the following url: `https://git.e5.physik.tu-dortmund.de/jbuss/Dissertation`. A *Makefile* in this repository allows for reproduction of this study. The raw data processing with *fact-tools* and the processing of the NSB simulations with ObsNSB are stored in a separated repository at `https://git.e5.physik.tu-dortmund.de/jbuss/Dissertation-Processing`. The program calls and the pipeline structure are again documented in a *Makefile*. The following sections provide the reader of this thesis with an overview of the setting used for the study in this thesis.

A.1 CORSIKA Input Cards

This section presents exemplary *input cards* for CORSIKA which contain the configuration of a simulation run with CORSIKA. The following provides an overview of the parameters and their meaning aswell as an example *input card* for a proton and a gamma simulation each.

Parameter	**Description**
RUNNR	Run ID
EVTNR	Number of first shower event (ID)
NSHOW	Number of showers / primaries to be generated in a run
SEED	Seeds for the random number generators
PRMPAR	Particle type of the primary particle (code)
ERANGE	Energy range of the primary particle energy (GeV)
ESLOPE	Slope of differential primary energy spectrum

Continued on next page

Parameter	Description
THETAP	Zenith angle range of primary particle (°)
PHIP	Azimuth angle range of primary particle (°)
VIEWCONE	Inner and outer angle of viewing cone
FIXCHI	Starting altitude of primary particle
OBSLEV	Observation level a.s.l. (cm)
MAGNET	Earth's magnetic field at the telescopes location (µT)
ARRANG	Rotation angle (in °) between detector and magnetic north
ATMOSPHERE	External tabulated atmosphere model number
ATMLAY	Lower boundaries (in cm) for layers of atmo. model
RADNKG	Outer radius (cm) to calculate the NKG formula
ECUTS	Energy cuts: hadr. muon elec. phot. (GeV)
ECTMAP	Gamma factor cut for print out of particles
MUADDI	Activate additional muon information
MUMULT	Simulate muon multiple scattering by Moliere's theory
CWAVLG	Cherenkov wavelength band (nm)
CSCAT	Scattering distance Cherenkov events to core location (cm)
CERSIZ	Bunch size Cherenkov photons
CERFIL	Cherenkov output file
CERTEL	Telescope dimentions and locations
LONGI	Activates sampling of longitudinal shower development
MAXPRT	Max. number of printed events
PAROUT	Table Output
DATBAS	Write data base file
DEBUG	Debug flag, log. unit, delayed debug
DIRECT	Directory of particle output

Table A.1: Description of parameters used in the CORSIKA input cards. See [62] for details.

A.1.1 CORSIKA Input Card for a Proton Simulation

```
RUNNR     000001
EVTNR     1
NSHOW     1500
SEED      <seed_1_1> <seed_2_1> <seed_3_1>
SEED      <seed_1_2> <seed_2_2> <seed_3_2>
SEED      <seed_1_3> <seed_2_3> <seed_3_3>
PRMPAR    14
ERANGE    100.0 30000.0
ESLOPE    -2.700
THETAP    10.000 10.000
PHIP      0.000 0.000
VIEWCONE  0.000 5.000
FIXCHI    0
OBSLEV    220000.0
MAGNET    30.3 24.1
ARRANG    -7.0
ATMOSPHERE 11 yes
ATMLAY    775000.0 1650000.0 5000000.0 10500000.0
RADNKG    20000.0
ECUTS     0.3 0.3 0.02 0.02
ECTMAP    10000.0
MUADDI    no
MUMULT    yes
CWAVLG    290.0 900.0
CSCAT     20  0.0 40000.0
CERSIZ    1.0
CERFIL    yes
CERTEL    1 0.0 0.0 0.0 0.0 0.0 500.0 500.0
LONGI     no 20.0 no no
MAXPRT    0
PAROUT    no no
DATBAS    no
DEBUG     no 6 no 1000000
DIRECT    <scratchfolder>
USER      <username>
HOST      <hostname>
EXIT
```

Listing A.1: Exemplary CORSIKA *input card* of a set of protons in an energy range of 100 GeV and 30 TeV. The zenith angle and the seeds have been altered for the simulation. In this example, events have been sampled with a zenith angle of 10°.

A.1.2 CORSIKA Input Card for a Gamma Simulation

```
RUNNR     000001
EVTNR     1
NSHOW     3000
SEED      <seed_1_1> <seed_2_1> <seed_3_1>
SEED      <seed_1_2> <seed_2_2> <seed_3_2>
SEED      <seed_1_3> <seed_2_3> <seed_3_3>
PRMPAR    1
ERANGE    200.0 50000.0
ESLOPE    -2.700
THETAP    9.000 10.000
PHIP      0.000 0.000
VIEWCONE  0.000 0.000
FIXCHI    0
OBSLEV    220000.0
MAGNET    30.3 24.1
ARRANG    -7.0
ATMOSPHERE 11 yes
ATMLAY    775000.0 1650000.0 5000000.0 10500000.0
RADNKG    20000.0
ECUTS     0.3 0.3 0.02 0.02
ECTMAP    10000.0
MUADDI    no
MUMULT    yes
CWAVLG    290.0 900.0
CSCAT     1  0.0 27000.0
CERSIZ    1.0
CERFIL    yes
CERTEL    1 0.0 0.0 0.0 0.0 0.0 500.0 500.0
LONGI     no 20.0 no no
MAXPRT    0
PAROUT    no no
DATBAS    no
DEBUG     no 6 no 1000000
DIRECT    <scratchfolder>
USER      <username>
HOST      <hostname>
EXIT
```

Listing A.2: Exemplary CORSIKA *input card* of a set of gammas in an energy range of 200 GeV and 50 TeV. The zenith angle and the seeds have been altered for the simulation. In this example, events have been sampled with a zenith angle in a range of $(9-10)°$.

A.2 CERES Config-File for the Telescope Simulation

The simulation of FACT is provided by the software CERES. The basic configuration file used for all simulations in this thesis is given in the following. CERES calls its configuration files *rc-files*. The presented *rc-file* uses the GenNSB approach to simulate the NSB. The adapted settings used to provide telescope simulations for the ObsNSB approach are explained in the main part of this thesis in chapter 5.2.2.

```
# ============================================================================
############################################################################
# ============================================================================
#                                 General
# ============================================================================
############################################################################
# ============================================================================

# ----------------------------------------------------------------------------
# Use this if you want to setup the logging stream for the jobs
# (overwrites command line options)
# ----------------------------------------------------------------------------
MLog.VerbosityLevel: 4

# ============================================================================
############################################################################
# ============================================================================
#                                  Ceres
# ============================================================================
############################################################################
# ============================================================================

# ----------------------------------------------------------------------------
# Use this to setup binnings. For more details see: MBinning::ReadEnv
# ----------------------------------------------------------------------------
BinningImpact.Raw:  40 0 1000
BinningTrigPos.Raw: 300 -25 275

# ----------------------------------------------------------------------------
# Initialize random number generator (see MJob::InitRandomNumberGenerator)
# ----------------------------------------------------------------------------
RandomNumberGenerator: TRandom3

# ----------------------------------------------------------------------------
# Setup for the atmosphere. Default values below.
# ----------------------------------------------------------------------------
#MSimAtmosphere.FileAerosols: resmc/fact/atmopshere-aerosols.txt
#MSimAtmosphere.FileOzone:    resmc/fact/atmopshere-ozone.txt

# ----------------------------------------------------------------------------
# Poiting of the telescope. To switch on
# off-target observations set a value for the distance !=0 [deg].
# ----------------------------------------------------------------------------
MSimPointingPos.OffTargetDistance: 0.6

# ----------------------------------------------------------------------------
# Setup the reflector and camera geometry
# ----------------------------------------------------------------------------
Reflector.Constructor: MReflector

Reflector.FileName: [...]/fact-reflector_first_light_untill_May2014.txt
Reflector.SetSigmaPSF: 2.0

# --- FACT ---
MGeomCam.Constructor:   MGeomCamFACT();

# Set the APD type (1: 30x30 <default>, 2: 60x60, 3:60x60(ct=15%))
MSimAPD.Type:                   0
MSimAPD.NumCells:               60
MSimAPD.DeadTime:               3.0
MSimAPD.RecoveryTime:           8.75
MSimAPD.CrosstalkCoefficient:   0.1
MSimAPD.AfterpulseProb1:        0.14
```

```
MSimAPD.AfterpulseProb2:        0.11

MSimExcessNoise.ExcessNoise:    0.096

# ------------------------------------------------------------------------
# Setup the absorption, conversion efficiency and angular acceptance
# ------------------------------------------------------------------------
MirrorReflectivity.FileName: [...]/
    MirrorReflectivity_Lustermann_FACT_bearbeitet.txt
PhotonDetectionEfficiency.FileName: [...]/fact-pde-1.4V.txt
ConesAngularAcceptance.FileName:    [...]/fact-cones-angular-acceptance.txt
ConesTransmission.FileName: [...]/Transmittance_1439Cones_FACT_bearbeitet.txt

AdditionalPhotonAcceptance.Function.Name:     0.85
AdditionalPhotonAcceptance.Function.Npx:      100
AdditionalPhotonAcceptance.Function.Xmin:     290
AdditionalPhotonAcceptance.Function.Xmax:     900

# ------------------------------------------------------------------------
# Setup the dark counts (FrequencyFixed) and the NSB noise per cm^2
# ------------------------------------------------------------------------
# Dark Counts per APD: ~4MHz
MSimRandomPhotons.FrequencyFixed: 0.004

# NSB photon rate per cm^2 ~40MHz (folded with the cones' angular
# acceptance and the wavelength acceptance of the camera (window, apd, etc)
# 0.040 1/ns/cm^2 NSB-rate:
MSimRandomPhotons.FileNameNSB: resmc/night-sky-la-palma.txt
MSimRandomPhotons.FrequencyNSB: 0.0

# ------------------------------------------------------------------------
# Setup the trigger
# ------------------------------------------------------------------------
# This line could be omitted but then the discriminator would be
# evaluated for all pixels not just for the pixels which are
# later "connected" in the trigger (used in the coincidence map)
MSimTrigger.FileNameRouteAC: [...]/fact-trigger-sum.txt

# DiscriminatorThreshold
MSimTrigger.DiscriminatorThreshold: -192.387

MSimTrigger.CableDelay: 21.0
MSimTrigger.CableDamping: -0.96
MSimTrigger.CoincidenceTime: 0.5


# Every Pixel(!) should see the same signal independent of its size
MSimCalibrationSignal.NumPhotons: 24
MSimCalibrationSignal.NumEvents:  1000

IntendedPulsePos.Val: 26

# ------------------------------------------------------------------------
# Setup the FADC
# ------------------------------------------------------------------------

MRawRunHeader.SamplingFrequency: 2000
MRawRunHeader.NumSamples:        300
MRawRunHeader.NumBytesPerSample: 2
MRawRunHeader.FadcResolution:    12

MSimCamera.DefaultOffset:       -1850.0
MSimCamera.DefaultNoise:        2.8125
MSimCamera.DefaultGain:         22.553


# Value for the fudgefactor in the calculation of the accoupling:
MSimCamera.ACFudgeFactor: 0.3136
MSimCamera.ACTimeConstant: 20

# The number of sampling points is almost irrelevant because they
# are equidistant, i.e. calculated and no search is necessary.
# Nevertheless, you must make sure that there are enough points
# to sample the function accurately enough.
# Attention: x in the function is given in slices, so if you change the
sampling
# frequency you have to change also this function
PulseShape.Function.Name:
(1.239*(1-1/(1+exp((0.5*x-2.851)/1.063)))*exp(-(0.5*x-2.851)/19.173))
PulseShape.Function.Npx:   310
PulseShape.Function.Xmin:  -10
```

```
PulseShape.Function.Xmax:  300
# ------------------------------------------------------------------------
# This is a cut executed after the calculation of the image parameters
# ------------------------------------------------------------------------
Cut.Inverted: yes
Cut.Condition: MHillas.fSize>10.0

ContEmpty3.Condition: MPhotonEvent.GetNumPhotons<10

MFixTimeOffset.FileName: resmc/fact/pixel_delays_ALL_ZERO.csv
ResidualTimeSpread.Val: 0.0
GapdTimeJitter.Val: 1.5

# last line comment
```

Listing A.3: Exemplary CERES *rc-file* for simulating FACT and its environment, e.g., the Earth's atmosphere and the NSB. The latter is here simulated with the GenNSB approach. File paths with an absolute component are shortend by `[...]`.

A.3 Process XMLs for *fact-tools*

The raw data processing, i.a., feature extraction, and the NSB simulations with ObsNSB were performed with *fact-tools*. The analysis process is based on the standard analysis from the *fact-tools* repository. It has been adapt to use the `ped_var` feature. Furthermore, an adapted analysis process has been created for the cleaning study presented in section 6.2 aswell as the trigger emulation presented in section 6.1. All *fact-tools* processes presented in this thesis are stored in a dedicated repository at `https://git.e5.physik.tu-dortmund.de/jbuss/Dissertation-Processing`.

A.3.1 Process for ObsNSB

The following *XML* defines the *fact-tools* process for the ObsNSB approach presented in section 5.3.2.

```
<process id="1" input="fact">
    <fact.utils.Remapping
        key="Data"
        outputKey="Data"
    />
    <fact.datacorrection.DrsCalibration
        key="Data"
        outputKey="DataCalibrated"
    />
    <fact.datacorrection.RemoveSpikes
        dataKey="DataCalibrated"
        outputKey="DataCalibrated"
        startCellKey="StartCellData"
        leftBorder="${RemoveSpikes.leftBorder}"
        spikeLimit="${RemoveSpikes.spikeLimit}"
```

```
        topSlopeLimit="${RemoveSpikes.topSlopeLimit}"
        maxSpikeLength="${RemoveSpikes.maxSpikeLength}"
    />
    <fact.datacorrection.InterpolateTimeSeries
        calibService="calibService"
        dataKey="DataCalibrated"
        dataOutputKey="DataCalibrated"
    />

<!-- Sample Pedestal Event and calibrate it -->
    <fact.utils.SamplePedestalEvent
        prependKey="LONS_"
        noiseDatabase="${noiseDB}"
        dataFolder="${dataFolder}"
        dbBinningKey="Zd"
        itemBinningKey="MPointingPos.fZd"
        binning="${noiseBinning}"
        samplingTryKey="Tries"
    />
    <fact.datacorrection.DrsCalibration
        drsKey="LONS_drspath"
        key="LONS_Data"
        outputKey="LONS_DataCalibrated"
        startCellKey="LONS_StartCellData"
    />
    <fact.datacorrection.PatchJumpRemoval
        dataKey="LONS_DataCalibrated"
        outputKey="LONS_DataCalibrated"
        prevEventsKey="LONS_prevEvents"
        startCellKey="LONS_StartCellData"
        unixTimeKey="LONS_UnixTimeUTC"
        jumpLimit="${PatchJumpRemoval.jumpLimit}"
    />
     <fact.datacorrection.RemoveSpikes
        dataKey="LONS_DataCalibrated"
        outputKey="LONS_DataCalibrated"
        startCellKey="LONS_StartCellData"
        leftBorder="${RemoveSpikes.leftBorder}"
        spikeLimit="${RemoveSpikes.spikeLimit}"
        topSlopeLimit="${RemoveSpikes.topSlopeLimit}"
        maxSpikeLength="${RemoveSpikes.maxSpikeLength}"
    />
<!--url="${drstime}"-->
    <fact.datacorrection.DrsTimeCalibration
        startCellKey = "LONS_StartCellData"
        dataKey      = "LONS_DataCalibrated"
        outputKey    = "LONS_DataCalibrated"
    />
    <fact.datacorrection.InterpolateTimeSeries
        calibService="calibService"
        dataKey="LONS_DataCalibrated"
        dataOutputKey="LONS_DataCalibrated"
        badPixelKey="LONS_badPixel"
        unixTimeKey="LONS_UnixTimeUTC"
    />
    <fact.utils.CombineDataArrays
        firstArrayKey="DataCalibrated"
        secondArrayKey="LONS_DataCalibrated"
        outputKey="DataCalibrated"
        op="add"
    />
     <fact.datacorrection.DrsCalibration
        key="DataCalibrated"
        outputKey="Data"
        reverse="true"
    />
    <fact.utils.Remapping
```

```
        key="Data"
        outputKey="Data"
        reverse="True"
    />
    <!--<fact.ShowViewer key="DataCalibrated" />-->
    <fact.io.FITSWriter
        url="${output}"
        keys="${OUTPUT_KEYS}"
        headerKeys="CREATOR,NROI,NPIX,TELESCOP,RUNTYPE,CAMERA"
    />
</process>
```

Listing A.4: Process used in *fact-tools* to generate NSB simulations with ObsNSB approach. In the case of *fact-tools* processes are defined in *XML*. Each tag represents for a processor aka an analysis step that manipulates the data. The suffix LONS refers to the NSB measurements.

A.3.2 Process Template for the Trigger Emulation

The following *XML* defines the *fact-tools* process to perform a ratescan, which scans the number of triggering patches for a given trigger threshold. This ratescan is used to determine the software trigger threshold estimate $\min(T_{\max})$ as done for the trigger emulation in section 6.1. A repository with scripts to evaluate these ratescans are hosted at `https://github.com/fact-project/ratescan`.

```
<!-- This process performs a SW ratescan on the given data-->
<process id="1" input="fact">
  <include url="classpath:/analysis/init.xml" />
  <!-- This skips events created by our malfunctioning LED light pulser
      (27s Events) -->
  <Skip condition="%{data.saturated_slices_percentage} &gt; 0.2" />
  <!-- Only analyze physics trigger events -->
  <Skip condition="%{data.TriggerType} != 4" />

  <!-- Start with the standard analysis to determine the shower pixels
      -->
  <include url="classpath:/analysis/calibration.xml" />
  <include url="classpath:/analysis/extraction.xml" />
  <include url="classpath:/analysis/cleaning.xml" />

  <fact.features.source.PixelSetForSourcePosition
          starPositionKeys="Cetatauri"
          starRadiusInCamera="11.0"
          outsetKey="starset"
  />

  <!-- Determine all functioning pixels-->
  <fact.pixelsets.Invert
          insetKey="badPixels"
          outsetKey="goodPixels"
  />

  <!-- Define the set of functioning non-shower pixels as basis for
      pedestal pixels-->
  <fact.pixelsets.Difference
      setUKey="goodPixels"
      setAKey="shower"
      outsetKey="pedestal"
```

```
  />
  <fact.pixelsets.Length
    pixelSetKey="pedestal"
    outputKey="num_pixel_in_pedestal"
  />
  <!-- Compute pedestal only features, e.g. PedVar -->
  <Skip condition="%{data.num_pixel_in_pedestal} &lt; 1"/>
  <include url="classpath:/analysis/pedestalParameters.xml" />
  <!-- After this the trigger emulation starts -->
  <!-- Do the signal shaping -->
  <fact.filter.ShapeSignal
          key="DataCalibrated"
          outputKey="DataShaped"
          shift="20"
          factor="0.96"
  />
  <!-- Define pixels that should be excluded -->
  <fact.pixelsets.Union
          setAKey="badPixels"
          setBKey="starset"
          outsetKey="triggerPixelsExcluded"
  />
  <!-- Summation of pixels of a trigger patch -->
  <fact.TriggerEmulation.SumUpPatches
          key="DataShaped"
          outKey="SummedPatches"
          pixelSetExcludeKey="triggerPixelsExcluded"
  />
  <!-- Scan trigger rates vs. trigger threshold -->
  <fact.TriggerEmulation.Ratescan
          key="SummedPatches"
          nThresholds="1000"
  />
  <fact.utils.SanitizeKeys />
  <!-- its important that you output a valid json file for this to work
      in conjuction with gridmap -->
  <fact.io.JSONWriter
    keys="${event_metadata_common},${event_metadata_observations},${
        RatescanFeatures},${pointing},${pedestals}"
    url="${output}"
    writeListOfItems="True"
    pixelSetsAsInt="True"
    specialDoubleValuesAsString="True"
    jsonl="True"
  />
</process>
```

Listing A.5: Process used in *fact-tools* to perform a ratescan, which scans the number of triggering patches for a given trigger threshold. This ratescan is used to determine the software trigger threshold estimate $\min(T_{\max})$ used for the trigger emulation. In the case of *fact-tools* processes are defined in *XML*. Each tag represents for a processor aka an analysis step that manipulates the data.

A.3.3 Process Template for the Cleaning Study

The following *XML* defines a template for a *fact-tools* process to evaluate a cleaning level for the cleaning study. This template is used for each pair of cleaning levels introduced in section 6.2.

```
<!-- Image Cleaning with levels: Core: ${
    TwoLevelTimeNeighbor.coreThreshold}, Neighbor ${
    TwoLevelTimeNeighbor.neighborThreshold}-->
<fact.cleaning.TwoLevelTimeNeighbor
    calibService="calibService"
    photonChargeKey="photoncharge"
    arrivalTimeKey="arrivalTime"
    corePixelThreshold="${TwoLevelTimeNeighbor.coreThreshold}"
    neighborPixelThreshold="${TwoLevelTimeNeighbor.neighborThreshold}"
    timeLimit="${TwoLevelTimeNeighbor.timeLimit}"
    minNumberOfPixel="${TwoLevelTimeNeighbor.minNumberOfPixel}"
    starPositionKeys="<CETA_TAURI>"
    starRadiusInCamera="11.0"
    outputKey="shower_<CLEANING_LEVEL_NAME>"
/>

<!-- Count the number of pixels in a shower-->
<fact.pixelsets.Length
  pixelSetKey="shower_<CLEANING_LEVEL_NAME>"
  outputKey="num_pixel_in_shower_<CLEANING_LEVEL_NAME>"
  />

<!-- Prepare variables for this step and initialize with NaN-->
<SetValue key="num_islands_<CLEANING_LEVEL_NAME>" value="NaN" />
<SetValue key="size_<CLEANING_LEVEL_NAME>" value="NaN" />
<SetValue key="cog_<CLEANING_LEVEL_NAME>" value="NaN" />
<SetValue key="cog_<CLEANING_LEVEL_NAME>_x" value="NaN" />
<SetValue key="cog_<CLEANING_LEVEL_NAME>_y" value="NaN" />
<SetValue key="length_<CLEANING_LEVEL_NAME>" value="NaN" />
<SetValue key="width_<CLEANING_LEVEL_NAME>" value="NaN" />
<SetValue key="delta_<CLEANING_LEVEL_NAME>" value="NaN" />

<stream.parser.ParseDouble keys="num_islands_<CLEANING_LEVEL_NAME>,size_
    <CLEANING_LEVEL_NAME>,cog_<CLEANING_LEVEL_NAME>,cog_<
    CLEANING_LEVEL_NAME>_x,cog_<CLEANING_LEVEL_NAME>_y,length_<
    CLEANING_LEVEL_NAME>,width_<CLEANING_LEVEL_NAME>,delta_<
    CLEANING_LEVEL_NAME>"/>

<!-- Determine Hillas paramter and number of Islands if the shower has
    enough pixels.-->
<If condition="%{data.num_pixel_in_shower_<CLEANING_LEVEL_NAME>} >= 5">
    <fact.features.NumberOfIslands
      pixelSetKey="shower_<CLEANING_LEVEL_NAME>"
      outputKey="num_islands_<CLEANING_LEVEL_NAME>"
    />
</If>
<!-- Otherwise these features are NaN.-->
```

Listing A.6: Process used in *fact-tools* to evalutate a cleaning level pair for the cleaning study. In the case of *fact-tools* processes are defined in *XML*. Each tag represents for a processor aka an analysis step that manipulates the data.

A.4 Machine-Learning Settings

The machine-learning tasks for this study are based on the *python* package *aict-tools* (see doi:10.5281/zenodo.3338081, `https://github.com/fact-project/aict-tools`). The *aict-tools* use machine-learning methods implemented by the *scikit-learn* package. The features used for the machine-learning tasks presented in section 4.3 are listed in the following.

A.4.1 Feature List for the Background Suppression

The following list contains the features used for the Background Suppression presented in section 4.4.2.

```
- concentration_cog
- concentration_core
- concentration_one_pixel
- concentration_two_pixel
- leakage1
- leakage2
- size
- width
- length
- skewness_long
- skewness_trans
- kurtosis_long
- kurtosis_trans
- num_islands
- num_pixel_in_shower
- photoncharge_shower_mean
- photoncharge_shower_variance
- ped_var_median      # Only used for OBASS
- ped_var_mean        # Only used for OBASS
- ped_var_max         # Only used for OBASS

# Generated features:
- area: width * length * @pi
- log_size: log(size)
- log_length: log(length)
- size_area: size / (width * length * @pi)
- area_size_cut_var: (width * length * @pi) / log(size)**2
```

Listing A.7: Features from *fact-tools* and a feature generation with *aict-tools* used for the Background Suppression aka gamma/hadron separation.

A.4.2 Feature List for the Energy Regression

The following two list contain the features (and generated features) used for the energy regression presented in section 4.5.3.

```
- size
- width
- length
- skewness_trans
- skewness_long
- concentration_cog
- concentration_core
- concentration_one_pixel
- concentration_two_pixel
- leakage1
- leakage2
- num_islands
- num_pixel_in_shower
- photoncharge_shower_mean
- photoncharge_shower_variance
- photoncharge_shower_max
- ped_var_median      # Only used for OBASS
- ped_var_mean        # Only used for OBASS
- ped_var_max         # Only used for OBASS

# Generated features:
- log_size: log(size)
- size_area: size / (width * length * @pi)
- area: (width * length * @pi)
- cog_r: sqrt(cog_x**2 + cog_y**2)
```

Listing A.8: Features from *fact-tools* and a feature generation with *aict-tools* used for the energy regression.

A.4.3 Feature List for the Source Reconstruction

The following two list contain the features (and generated features) used for the source reconstruction presented in section 4.4.1.

```
- num_pixel_in_shower
- width
- length
- skewness_long
- kurtosis_long
- concentration_cog
- concentration_core
- leakage1
- leakage2
- slope_long
- time_gradient_slope_long
- photoncharge_shower_mean
- photoncharge_shower_variance
- ped_var_median      # Only used for OBASS
- ped_var_mean        # Only used for OBASS
- ped_var_max         # Only used for OBASS

# Generated features:
- area: width * length * @pi
- width_length: 1 - (width / length)
- log_size: log(size)
- log_size_area: log(size) / (width * length * @pi)
```

Listing A.9: Features from *fact-tools* and a feature generation with *aict-tools* used for the source reconstruction aka `DISP` regression.

B Appendix: Additional Information for the Analysis Optimizations

Chapter 6 presented an optimization of the analysis in in this study with regard to NSB. In particular, optimum cleaning levels have been found in a grid search in section 6.2. Moreover, final prediction cuts based the machine-learnig models have been defined in section 6.4. In both case the findings in these sections were illustrated with examples from some of the light conditions. This chapter contains thus additional information from all light conditions.

The full grid search on *pedestal impurity* and *gamma efficiency* for all light conditions is shown in the next section. The optimization in section 6.2 allowed this thesis to define cleaning levels with regard to six NSB level ranges. In extension to the image parameters presented in section 6.2.6, more feature distributions are presented in section B.3 for both new cleaning level sets. In addition to the defined six NSB ranges, cleaning levels for NSB bins with a smaller granularity are given in section B.2. The dependency plots of significance of detection (LiMa) and the choice of maximum angular distance (θ_{max}) and `gammaness` threshold for all light conditions are depicted in section B.4.

B.1 Results of the Grid Search on Cleaning Levels

In section 6.2 optimum cleaning levels have been searched in a combined grid search on *pedestal impurity* and *gamma efficiency*. The following shows additional examples for the heat maps presented in the figures 6.4 and 6.5. The illustration of the grid search on the *pedestal impurity* are presented in figure B.1 for NSB levels lower than $8\,\text{NSB}_{\text{Dark}}$ and figure B.2 for higher than $8\,\text{NSB}_{\text{Dark}}$. The heat maps for the *gamma efficiency* are depicted in figure B.3 for NSB levels lower than $8\,\text{NSB}_{\text{Dark}}$ and figure B.4 for higher than $8\,\text{NSB}_{\text{Dark}}$.

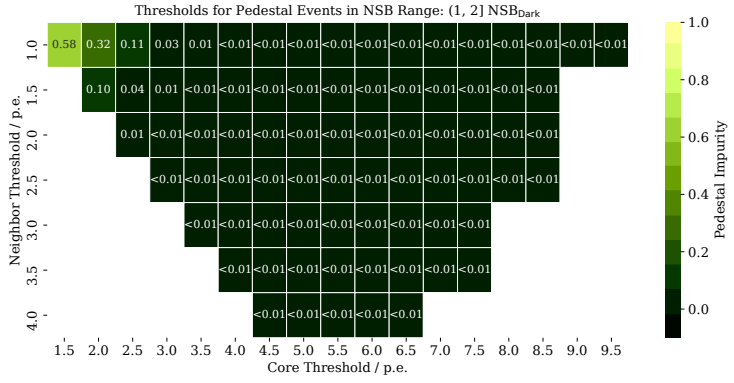

(a) No moonlight: $(0-2)\,\mathrm{NSB}_{\mathrm{Dark}}$.

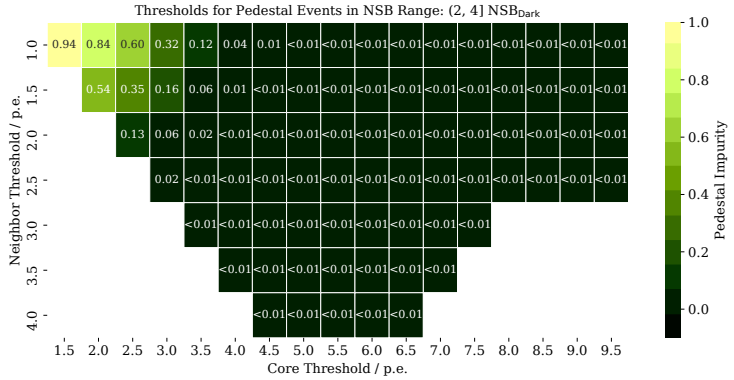

(b) Low moonlight: $(2-4)\,\mathrm{NSB}_{\mathrm{Dark}}$.

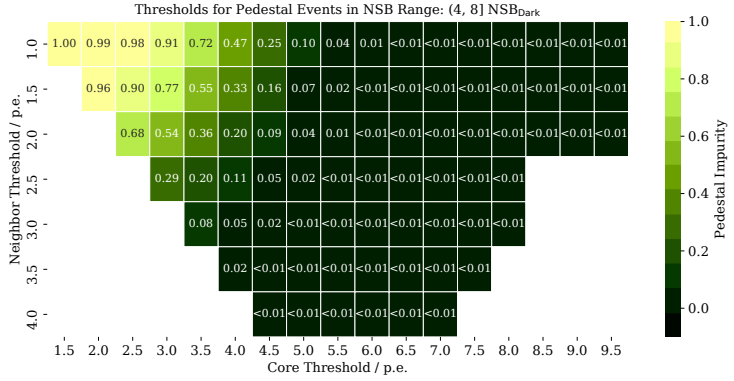

(c) Slight moonlight: $(4-8)\,\mathrm{NSB}_{\mathrm{Dark}}$.

Figure B.1: Result from a grid search of cleaning thresholds on pedestal data with regard to *pedestal impurities* at the three lower light conditions. The coloring indicates the fraction of surviving pedestal events relative to number of events in the sample. The brighter the color, the more pedestal events survived the cleaning.

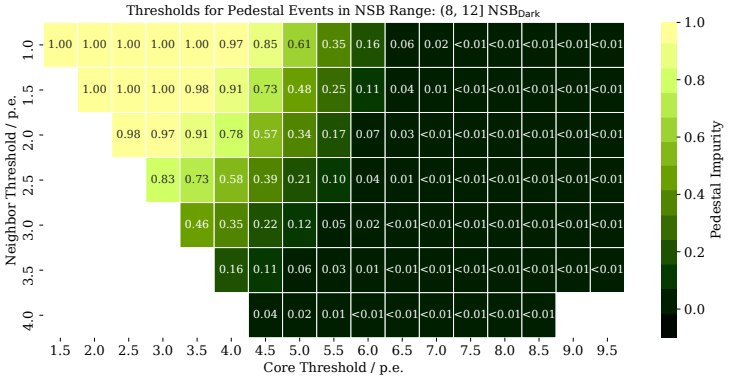

(a) Moderate moonlight: $(8-12)\,\mathrm{NSB}_{\mathrm{Dark}}$.

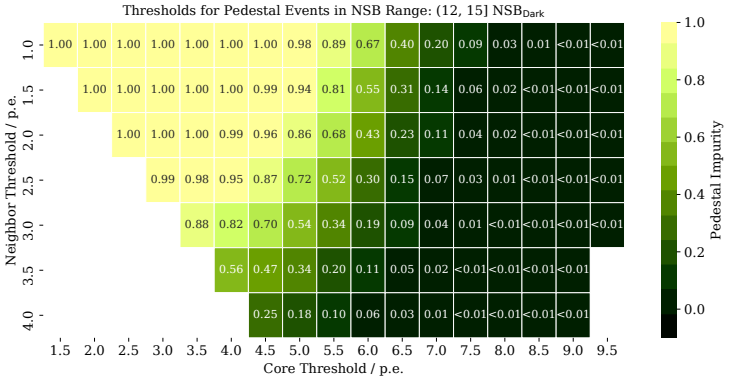

(b) Increased moonlight: $(12-16)\,\mathrm{NSB}_{\mathrm{Dark}}$.

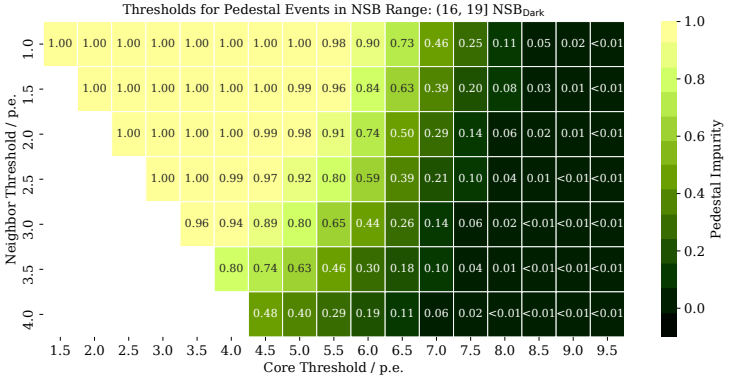

(c) Strong moonlight: $(16-24)\,\mathrm{NSB}_{\mathrm{Dark}}$.

Figure B.2: Result from a grid search of cleaning thresholds on pedestal data with regard to *pedestal impurities* at the three higher light conditions. The coloring indicates the fraction of surviving pedestal events relative to number of events in the sample. The brighter the color, the more pedestal events survived the cleaning.

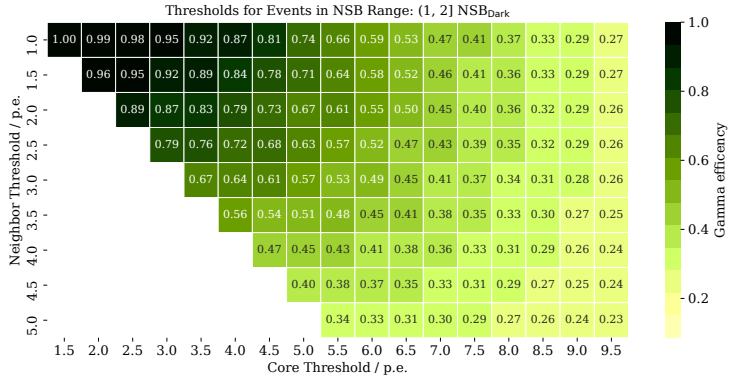

(a) No moonlight: $(0-2)\,\mathrm{NSB}_{\mathrm{Dark}}$.

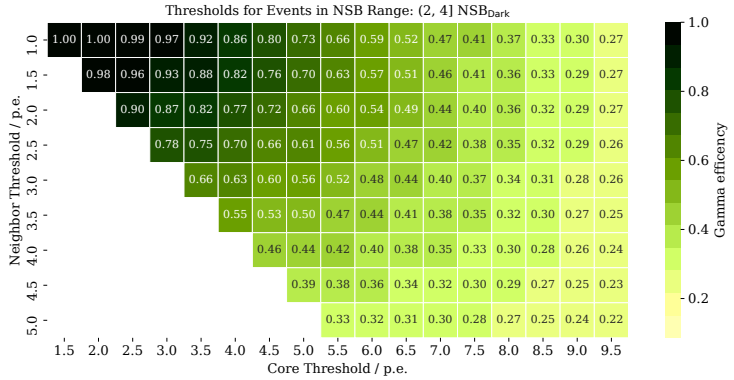

(b) Low moonlight: $(2-4)\,\mathrm{NSB}_{\mathrm{Dark}}$.

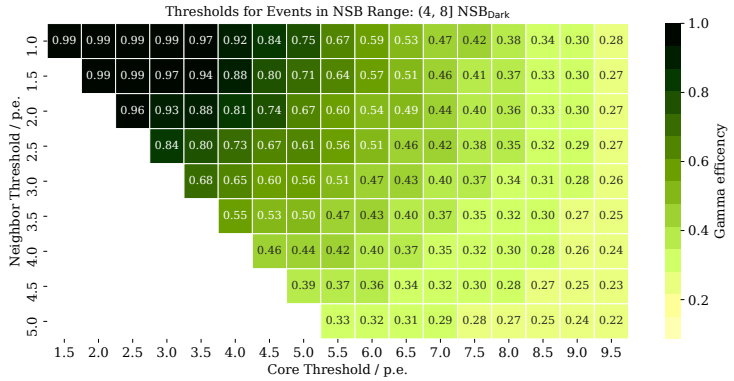

(c) Slight moonlight: $(4-8)\,\mathrm{NSB}_{\mathrm{Dark}}$.

Figure B.3: Result from a grid search of cleaning thresholds on gamma simulations with regard to the *gamma efficiencies* at the three lower light conditions. The coloring indicates the fraction of surviving gamma events relative to number of events in the sample. The darker the color, the more gamma events survived the cleaning.

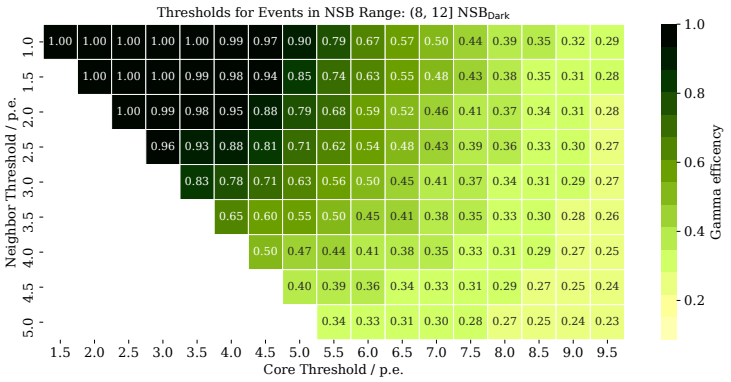

(a) Moderate moonlight: $(8-12)\,\mathrm{NSB}_{\mathrm{Dark}}$.

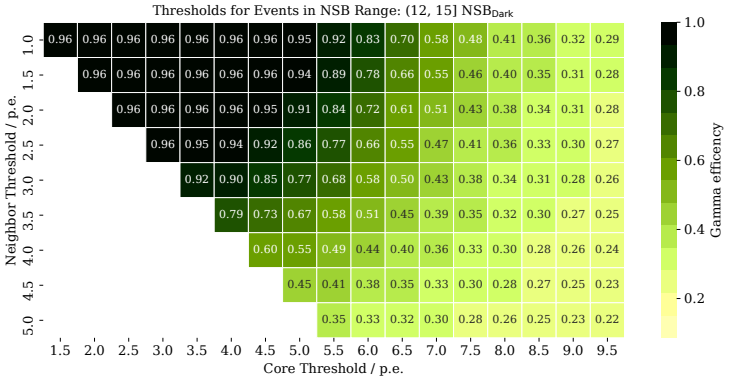

(b) Increased moonlight: $(12-16)\,\mathrm{NSB}_{\mathrm{Dark}}$.

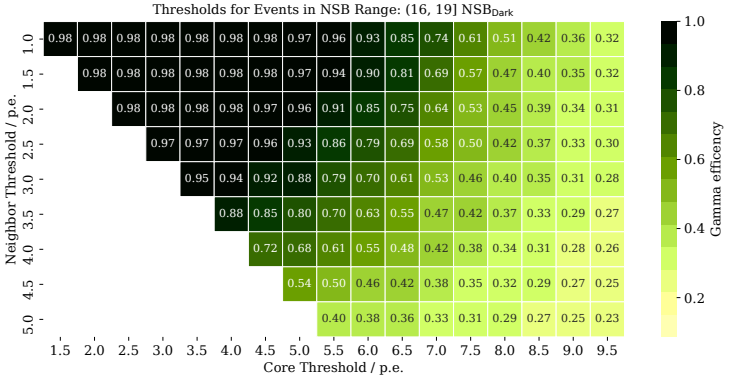

(c) Strong moonlight: $(16-24)\,\mathrm{NSB}_{\mathrm{Dark}}$.

Figure B.4: Result from a grid search of cleaning thresholds on gamma simulations with regard to the *gamma efficiencies* at the three higher light conditions. The coloring indicates the fraction of surviving gamma events relative to number of events in the sample. The darker the color, the more gamma events survived the cleaning.

B.2 Image Cleaning Levels with Finer NSB Binning

In section 6.2.4 optimum cleaning levels have been found with the use of pareto frontiers. Figure 6.6b has shown such pareto frontiers for an NSB binning with a finer granularity than the six NSB ranges used in this thesis. The following two lists contain cleaning levels with a finer NSB binning that have been determined with the same methods as described in section 6.2.4.

B.2.1 Progressive Cleaning Levels with Finer NSB Binning

Current Bin [µA]	Core Threshold [p.e.]	Neighbor Threshold [p.e.]	Average Number of Islands	Gamma Efficiency	Pedestal Impurity
(4, 5]	3.5	1.5	1.56	0.89	0.00
(5, 6]	3.5	1.5	1.58	0.89	0.00
(6, 7]	3.5	1.5	1.58	0.88	0.00
(7, 8]	4.0	1.0	1.43	0.87	0.00
(8, 9]	4.0	1.5	1.51	0.83	0.00
(9, 10]	4.0	1.5	1.56	0.82	0.00
(10, 11]	4.0	1.5	1.73	0.82	0.01
(11, 12]	4.0	2.0	1.80	0.76	0.00
(12, 13]	4.5	1.5	1.51	0.76	0.01
(13, 14]	4.5	1.5	1.55	0.76	0.01
(14, 15]	4.5	1.5	1.59	0.76	0.01
(15, 16]	4.5	2.0	1.57	0.71	0.00
(16, 17]	5.0	1.5	1.50	0.69	0.00
(17, 18]	5.0	2.0	1.47	0.64	0.00
(18, 19]	5.0	2.0	1.53	0.64	0.00
(19, 20]	5.5	1.5	1.63	0.62	0.00
(20, 21]	5.5	1.5	1.46	0.62	0.00
(21, 22]	5.5	2.0	1.65	0.59	0.01

Continued on next page

Current Bin [µA]	Core Threshold [p.e.]	Neighbor Threshold [p.e.]	Average Number of Islands	Gamma Efficiency	Pedestal Impurity
(22, 23]	5.5	2.0	1.56	0.60	0.01
(23, 24]	6.0	1.5	1.49	0.57	0.01
(24, 25]	6.0	2.0	1.50	0.55	0.00
(25, 26]	5.5	3.0	1.52	0.52	0.00
(26, 27]	6.0	2.0	1.41	0.54	0.00
(27, 28]	6.0	2.0	1.47	0.54	0.00
(28, 29]	6.5	2.0	2.07	0.49	0.01
(29, 30]	6.5	1.5	1.40	0.52	0.00
(30, 31]	7.0	1.5	1.57	0.47	0.00
(31, 32]	6.0	2.5	1.54	0.51	0.01
(32, 33]	7.0	1.5	1.34	0.46	0.00
(33, 34]	7.0	1.0	1.38	0.49	0.00
(34, 35]	6.5	2.5	1.45	0.47	0.00
(35, 36]	7.0	1.5	1.42	0.47	0.00
(36, 37]	7.0	2.0	1.43	0.46	0.01
(37, 38]	6.5	3.0	1.51	0.45	0.00
(38, 39]	6.5	3.5	1.50	0.42	0.00
(39, 40]	7.0	1.5	1.53	0.48	0.00
(40, 41]	7.0	2.5	1.46	0.44	0.01
(41, 42]	7.5	2.0	1.39	0.42	0.00
(42, 43]	7.0	3.0	1.42	0.41	0.00
(43, 44]	7.0	3.0	1.46	0.41	0.01
(44, 45]	7.0	3.0	1.46	0.41	0.00
(45, 46]	7.5	2.0	1.41	0.41	0.00
(46, 47]	8.0	1.5	1.33	0.38	0.00
(47, 48]	8.5	3.0	1.27	0.32	0.00

Continued on next page

Current Bin [µA]	Core Threshold [p.e.]	Neighbor Threshold [p.e.]	Average Number of Islands	Gamma Efficiency	Pedestal Impurity
(50, 51]	6.0	4.5	1.65	0.24	0.00
(51, 52]	7.5	2.5	1.50	0.27	0.00
(52, 53]	8.0	2.5	1.40	0.22	0.00
(53, 54]	8.5	1.0	1.34	0.24	0.00
(54, 55]	8.5	2.5	1.30	0.20	0.00
(55, 56]	8.5	2.5	1.35	0.22	0.00
(56, 57]	8.0	3.5	1.41	0.21	0.00
(57, 58]	8.5	3.0	1.36	0.21	0.00
(58, 59]	8.5	3.0	1.34	0.21	0.00
(66, 67]	9.0	3.0	1.29	0.30	0.00
(68, 69]	9.0	1.5	1.41	0.34	0.00

Table B.1: Pareto optimal cleaning levels, with progressive constraints: *pedestal impurity* $<$ 0.01. The efficiencies where weighted with w(*gamma efficiency*)=1 and w(*pedestal impurity*)=0.1.

B.2.2 Conservative Cleaning Levels with Finer NSB Binning

Current Bin [µA]	Core Threshold [p.e.]	Neighbor Threshold [p.e.]	Average Number of Islands	Gamma Efficiency	Pedestal Impurity
(4, 5]	4.0	1.0	1.40	0.88	0.00
(5, 6]	4.0	1.0	1.42	0.87	0.00
(6, 7]	4.0	1.0	1.43	0.87	0.00
(7, 8]	4.0	1.0	1.43	0.87	0.00
(8, 9]	4.5	1.0	1.38	0.80	0.00
(9, 10]	4.5	1.0	1.42	0.80	0.00
(10, 11]	4.5	1.5	1.49	0.76	0.00
(11, 12]	5.0	1.0	1.50	0.72	0.00
(12, 13]	5.0	1.0	1.38	0.73	0.00
(13, 14]	5.0	1.0	1.42	0.72	0.01
(14, 15]	5.0	1.0	1.44	0.73	0.01
(15, 16]	5.0	1.5	1.44	0.69	0.00
(16, 17]	5.0	1.5	1.50	0.69	0.00
(17, 18]	5.0	2.0	1.47	0.64	0.00
(18, 19]	5.5	1.0	1.43	0.64	0.00
(19, 20]	6.0	1.0	1.47	0.58	0.00
(20, 21]	5.5	1.5	1.46	0.62	0.00
(21, 22]	6.0	1.5	1.49	0.57	0.00
(22, 23]	5.5	2.5	1.49	0.56	0.00
(23, 24]	6.0	1.5	1.49	0.57	0.01
(24, 25]	6.0	2.5	1.46	0.51	0.00
(25, 26]	6.0	2.0	1.46	0.55	0.01
(26, 27]	6.0	2.0	1.41	0.54	0.00
(27, 28]	6.0	2.0	1.47	0.54	0.00
(28, 29]	8.0	1.0	1.36	0.38	0.00

Continued on next page

Current Bin [µA]	Core Threshold [p.e.]	Neighbor Threshold [p.e.]	Average Number of Islands	Gamma Efficiency	Pedestal Impurity
(29, 30]	6.5	1.5	1.40	0.52	0.00
(30, 31]	7.0	2.0	1.49	0.45	0.00
(31, 32]	6.5	2.0	1.43	0.49	0.00
(32, 33]	7.0	1.5	1.34	0.46	0.00
(33, 34]	7.0	1.0	1.38	0.49	0.00
(34, 35]	6.5	2.5	1.45	0.47	0.00
(35, 36]	7.0	1.5	1.42	0.47	0.00
(36, 37]	7.0	2.0	1.43	0.46	0.01
(37, 38]	6.5	3.5	1.47	0.42	0.00
(38, 39]	6.5	3.5	1.50	0.42	0.00
(39, 40]	7.0	2.0	1.48	0.46	0.00
(40, 41]	7.0	2.5	1.46	0.44	0.01
(41, 42]	7.5	2.0	1.39	0.42	0.00
(42, 43]	7.0	3.0	1.42	0.41	0.00
(43, 44]	7.0	3.0	1.46	0.41	0.01
(44, 45]	7.0	3.0	1.46	0.41	0.00
(45, 46]	7.5	2.0	1.41	0.41	0.00
(46, 47]	8.0	1.5	1.33	0.38	0.00
(47, 48]	8.5	3.0	1.27	0.32	0.00
(50, 51]	8.5	1.5	1.29	0.23	0.00
(51, 52]	7.5	2.5	1.50	0.27	0.00
(52, 53]	8.0	2.5	1.40	0.22	0.00
(53, 54]	8.5	1.0	1.34	0.24	0.00
(54, 55]	8.5	2.5	1.30	0.20	0.00
(55, 56]	8.5	2.5	1.35	0.22	0.00
(56, 57]	8.0	3.5	1.41	0.21	0.00

Continued on next page

Current Bin [µA]	Core Threshold [p.e.]	Neighbor Threshold [p.e.]	Average Number of Islands	Gamma Efficiency	Pedestal Impurity
(57, 58]	8.5	3.0	1.36	0.21	0.00
(58, 59]	8.5	3.0	1.34	0.21	0.00
(66, 67]	9.0	3.0	1.29	0.30	0.00
(68, 69]	9.0	1.5	1.41	0.34	0.00

Table B.2: Pareto optimal cleaning levels, with conservative constraints: $\hat{N}_{\text{islands}} \leq 1.5$ and *pedestal impurity* < 0.01. The efficiencies where weighted with w(*gamma efficiency*)=1 and w(*pedestal impurity*)=0.1.

B.3 Comparison of Image Parameters from Data and MC

In addition to the image parameters presented in section 6.2.6 for the progressive cleaning levels, this section contains the counterparts derived with the conservative cleaning levels. Furthermore, feature distributions from more image parameters are presented in the following for both new cleaning level sets.

The conservative cleaning counter parts for `size` and `length` are illustrated in figure B.5 and figure B.6. In extension of these image parameters, also feature distributions of the `arrival_time_mean` and `concentration_cog` are depicted for both cleaning sets in figure B.7 to B.10.

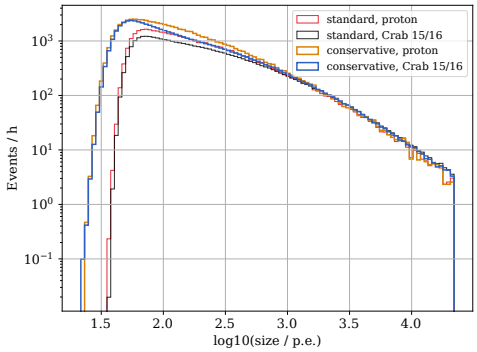

(a) No moonlight: $(0-2)\,\mathrm{NSB}_{\mathrm{Dark}}$.

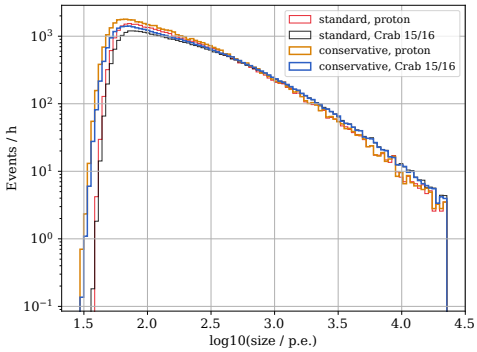

(b) Low moonlight: $(2-4)\,\mathrm{NSB}_{\mathrm{Dark}}$.

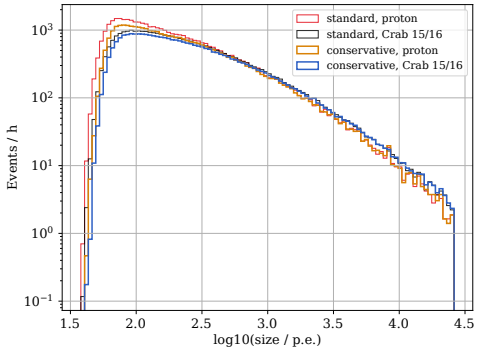

(c) Slight moonlight: $(4-8)\,\mathrm{NSB}_{\mathrm{Dark}}$.

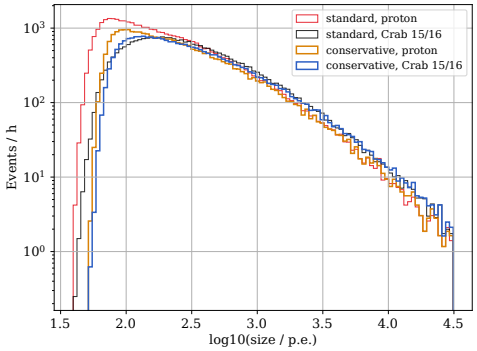

(d) Moderate moonlight: $(8-12)\,\mathrm{NSB}_{\mathrm{Dark}}$.

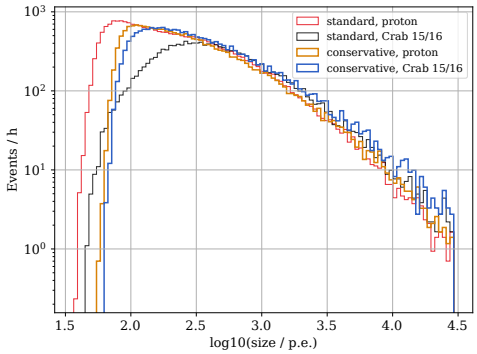

(e) Increased moonlight: $(12-16)\,\mathrm{NSB}_{\mathrm{Dark}}$.

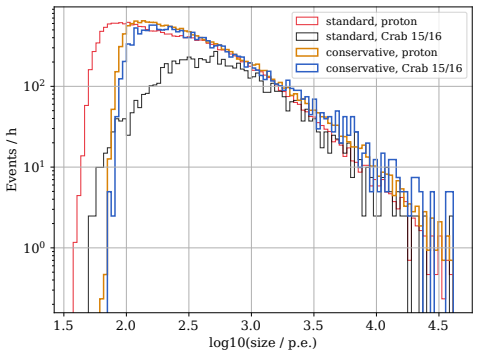

(f) Strong moonlight: $(16-24)\,\mathrm{NSB}_{\mathrm{Dark}}$.

Figure B.5: Comparison of observations and MC simulations based on the distributions of the feature `size` derived with conservative cleaning levels for six representative light conditions. The distributions are normalized to observation times. Each plot contains four feature distributions from the same image parameters and light conditions. These distributions show proton events from the standard cleaning (black and red) and the conservative cleaning (blue and orange) for Crab data (black and blue) and proton simulations (red and orange).

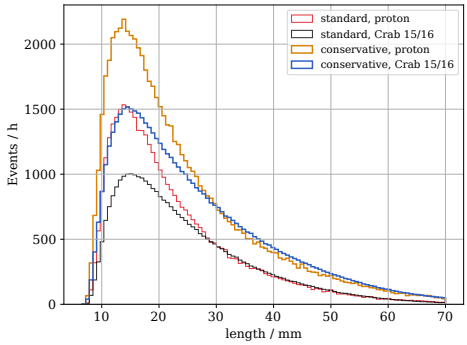

(a) No moonlight: $(0-2)\,\mathrm{NSB}_{\mathrm{Dark}}$.

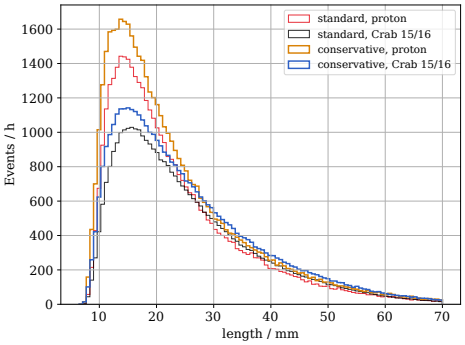

(b) Low moonlight: $(2-4)\,\mathrm{NSB}_{\mathrm{Dark}}$.

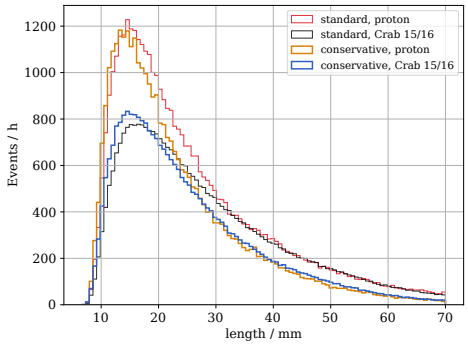

(c) Slight moonlight: $(4-8)\,\mathrm{NSB}_{\mathrm{Dark}}$.

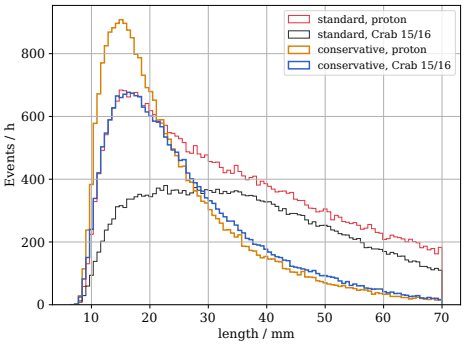

(d) Moderate moonlight: $(8-12)\,\mathrm{NSB}_{\mathrm{Dark}}$.

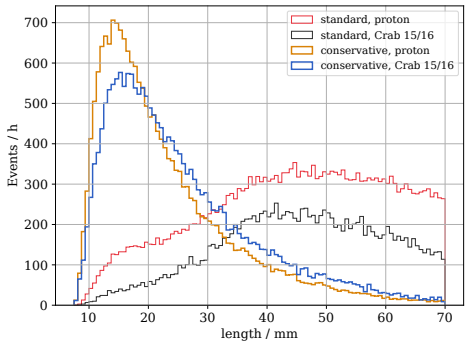

(e) Increased moonlight: $(12-16)\,\mathrm{NSB}_{\mathrm{Dark}}$.

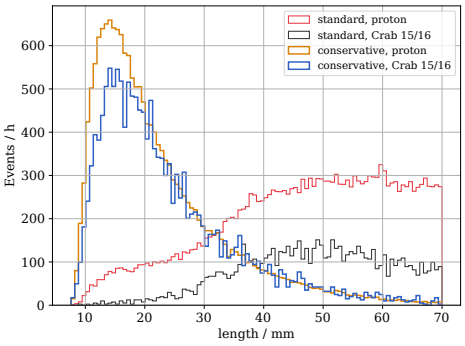

(f) Strong moonlight: $(16-24)\,\mathrm{NSB}_{\mathrm{Dark}}$.

Figure B.6: Comparison of observations and MC simulations based on the distributions of the feature `length` derived with conservative cleaning levels for six representative light conditions. The distributions are normalized to observation times. Each plot contains four feature distributions from the same image parameters and light conditions. These distributions show proton events from the standard cleaning (black and red) and the conservative cleaning (blue and orange) for Crab data (black and blue) and proton simulations (red and orange).

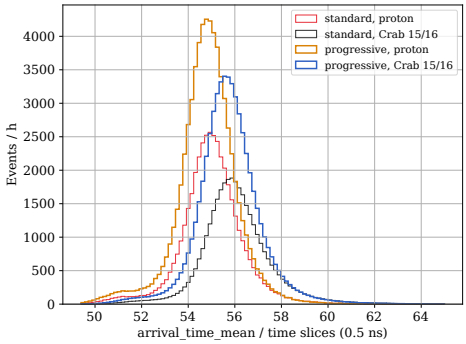

(a) No moonlight: $(0-2)\,\mathrm{NSB}_{\mathrm{Dark}}$.

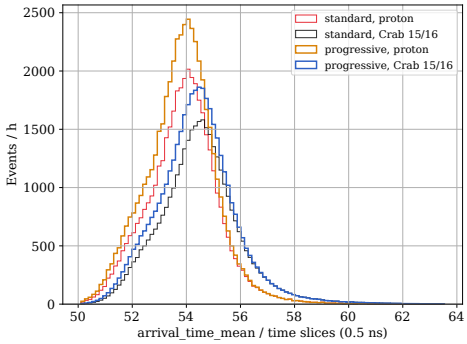

(b) Low moonlight: $(2-4)\,\mathrm{NSB}_{\mathrm{Dark}}$.

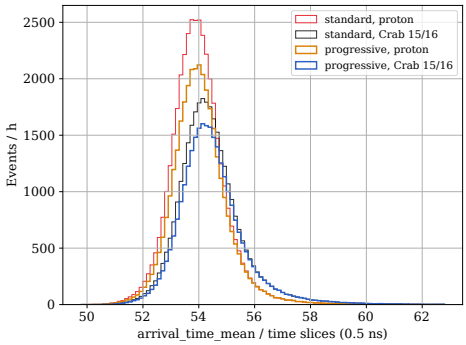

(c) Slight moonlight: $(4-8)\,\mathrm{NSB}_{\mathrm{Dark}}$.

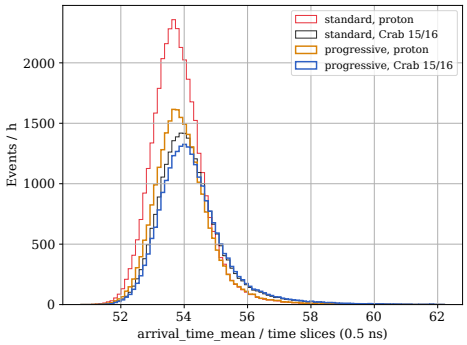

(d) Moderate moonlight: $(8-12)\,\mathrm{NSB}_{\mathrm{Dark}}$.

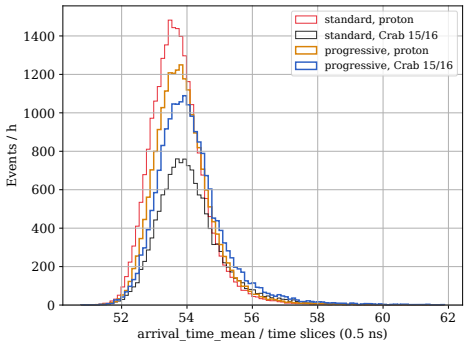

(e) Increased moonlight: $(12-16)\,\mathrm{NSB}_{\mathrm{Dark}}$.

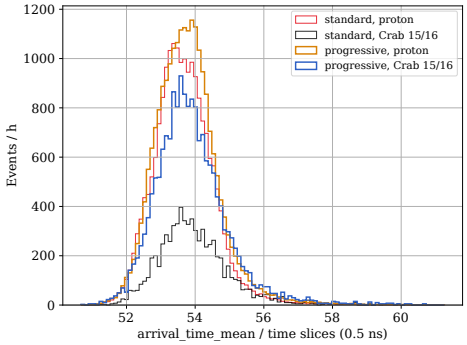

(f) Strong moonlight: $(16-24)\,\mathrm{NSB}_{\mathrm{Dark}}$.

Figure B.7: Comparison of observations and MC simulations based on the distributions of the feature `arrival_time_mean` derived with progressive cleaning levels for six representative light conditions. The distributions are normalized to observation times. Each plot contains four feature distributions from the same image parameters and light conditions. These distributions show proton events from the standard cleaning (black and red) and the progressive cleaning (blue and orange) for Crab data (black and blue) and proton simulations (red and orange).

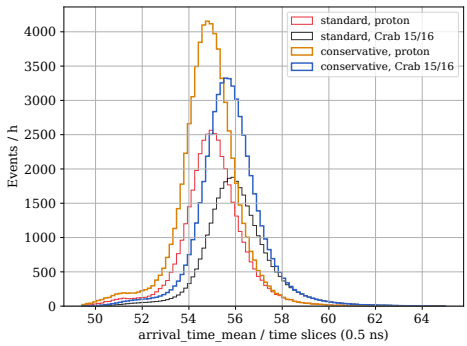

(a) No moonlight: $(0-2)\,\mathrm{NSB}_{\mathrm{Dark}}$.

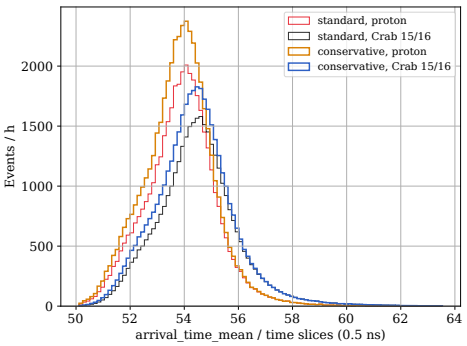

(b) Low moonlight: $(2-4)\,\mathrm{NSB}_{\mathrm{Dark}}$.

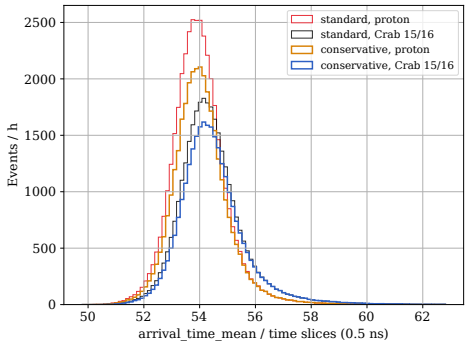

(c) Slight moonlight: $(4-8)\,\mathrm{NSB}_{\mathrm{Dark}}$.

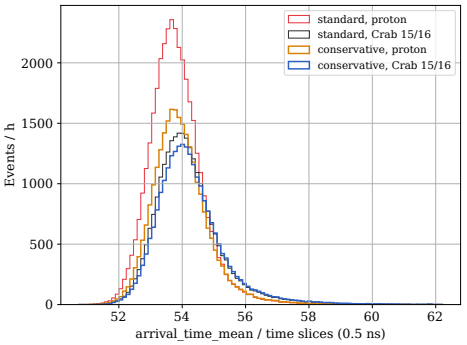

(d) Moderate moonlight: $(8-12)\,\mathrm{NSB}_{\mathrm{Dark}}$.

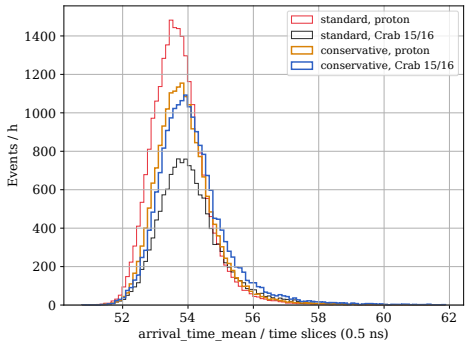

(e) Increased moonlight: $(12-16)\,\mathrm{NSB}_{\mathrm{Dark}}$.

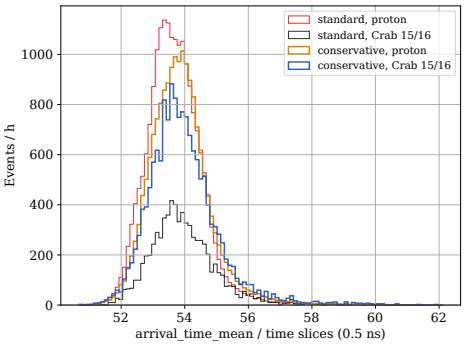

(f) Strong moonlight: $(16-24)\,\mathrm{NSB}_{\mathrm{Dark}}$.

Figure B.8: Comparison of observations and MC simulations based on the distributions of the feature `arrival_time_mean` derived with conservative cleaning levels for six representative light conditions. The distributions are normalized to observation times. Each plot contains four feature distributions from the same image parameters and light conditions. These distributions show proton events from the standard cleaning (black and red) and the conservative cleaning (blue and orange) for Crab data (black and blue) and proton simulations (red and orange).

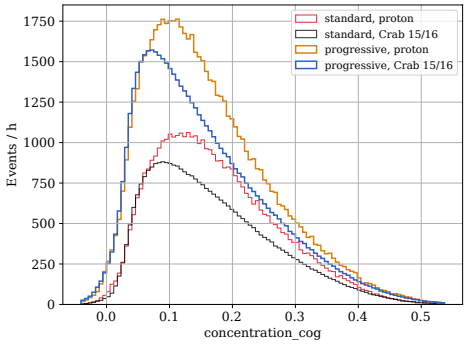

(a) No moonlight: $(0-2)\,\mathrm{NSB}_{\mathrm{Dark}}$.

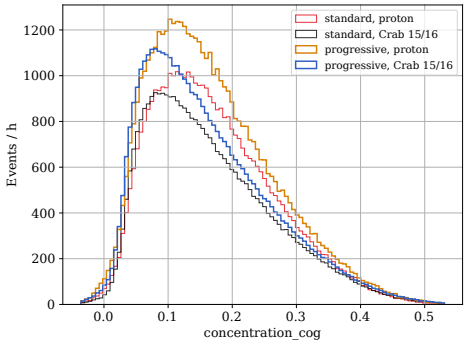

(b) Low moonlight: $(2-4)\,\mathrm{NSB}_{\mathrm{Dark}}$.

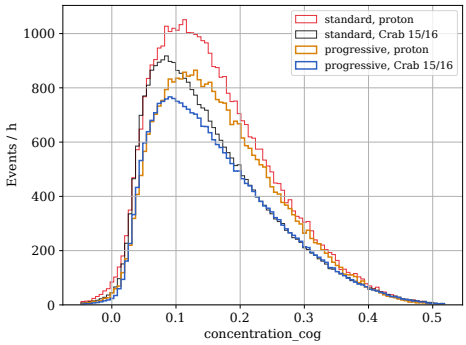

(c) Slight moonlight: $(4-8)\,\mathrm{NSB}_{\mathrm{Dark}}$.

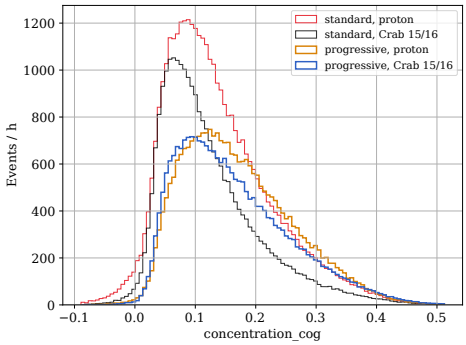

(d) Moderate moonlight: $(8-12)\,\mathrm{NSB}_{\mathrm{Dark}}$.

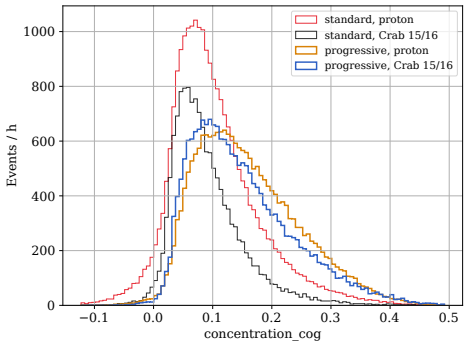

(e) Increased moonlight: $(12-16)\,\mathrm{NSB}_{\mathrm{Dark}}$.

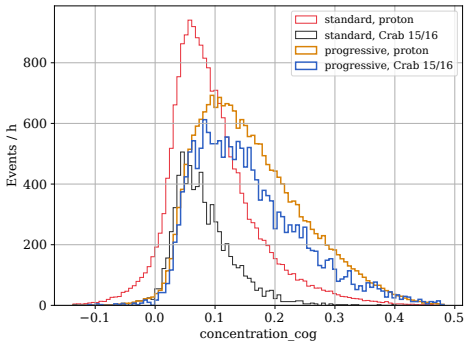

(f) Strong moonlight: $(16-24)\,\mathrm{NSB}_{\mathrm{Dark}}$.

Figure B.9: Comparison of observations and MC simulations based on the distributions of the feature `concentration_cog` derived with progressive cleaning levels for six representative light conditions. The distributions are normalized to observation times. Each plot contains four feature distributions from the same image parameters and light conditions. These distributions show proton events from the standard cleaning (black and red) and the progressive cleaning (blue and orange) for Crab data (black and blue) and proton simulations (red and orange).

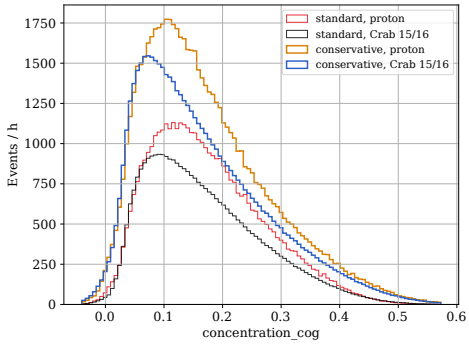

(a) No moonlight: $(0-2)\,\mathrm{NSB}_{\mathrm{Dark}}$.

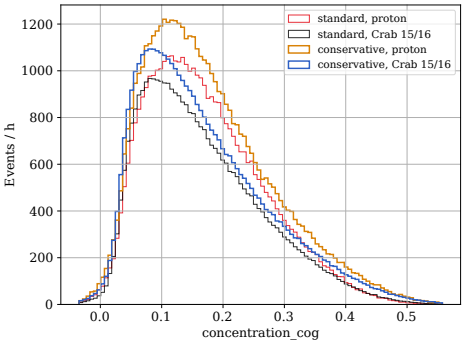

(b) Low moonlight: $(2-4)\,\mathrm{NSB}_{\mathrm{Dark}}$.

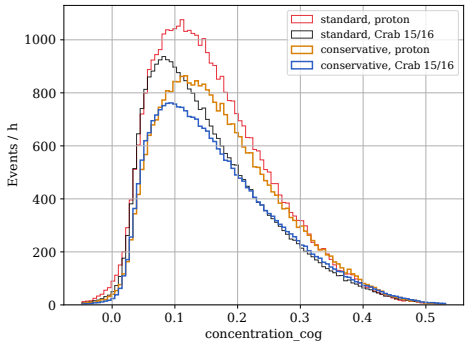

(c) Slight moonlight: $(4-8)\,\mathrm{NSB}_{\mathrm{Dark}}$.

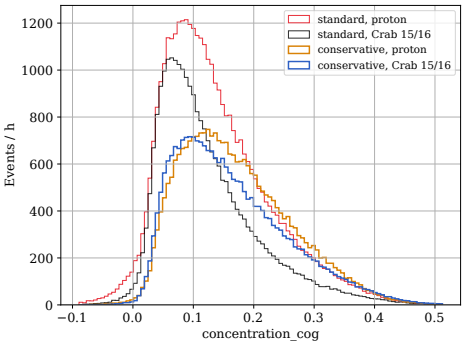

(d) Moderate moonlight: $(8-12)\,\mathrm{NSB}_{\mathrm{Dark}}$.

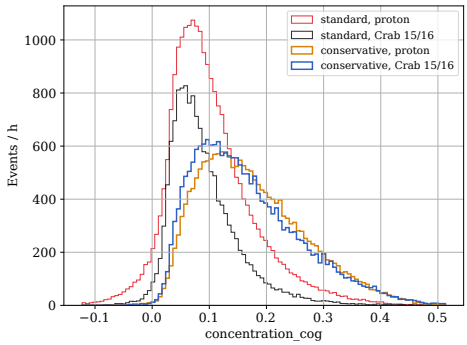

(e) Increased moonlight: $(12-16)\,\mathrm{NSB}_{\mathrm{Dark}}$.

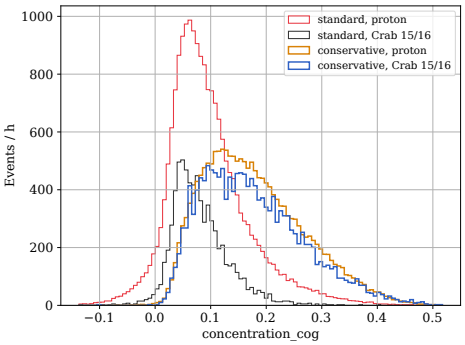

(f) Strong moonlight: $(16-24)\,\mathrm{NSB}_{\mathrm{Dark}}$.

Figure B.10: Comparison of observations and MC simulations based on the distributions of the feature `concentration_cog` derived with conservative cleaning levels for six representative light conditions. The distributions are normalized to observation times. Each plot contains four feature distributions from the same image parameters and light conditions. These distributions show proton events from the standard cleaning (black and red) and the conservative cleaning (blue and orange) for Crab data (black and blue) and proton simulations (red and orange).

B.4 Cut Selection for Angular Distance and Gammaness

This section provides plots for all six light conditions in addition to the dependency of significance of detection (LiMa) and the choice of maximum angular distance (θ_{max}) and `gammaness` threshold as illustrated in figure 6.17. These plots are depicted in figure B.11 to B.13 in partial figure (a) and (c) and have been compiled on the basis of features from progressive cleaning levels. Moreover, the same plots determine with image parameters from the standard cleaning levels are shown in figure B.11 to B.13 in partial figure (b) and (d) .

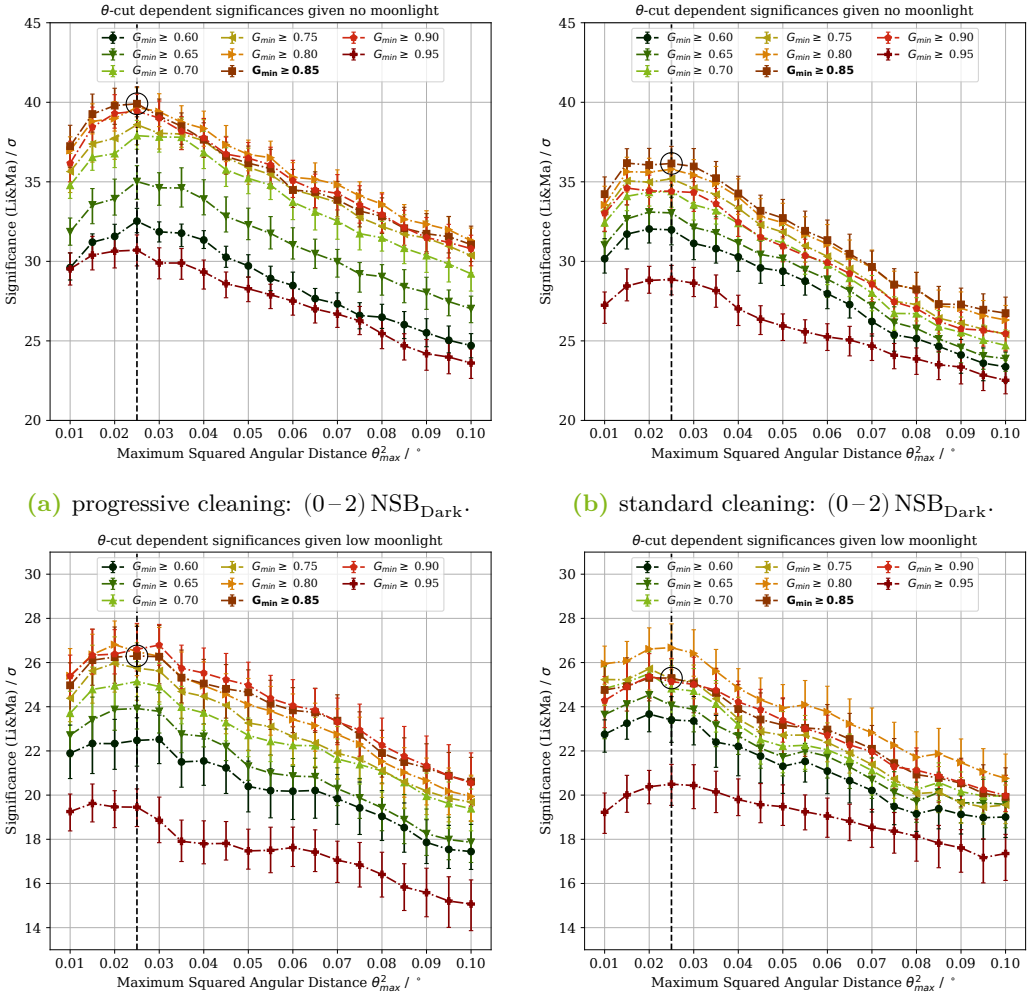

(a) progressive cleaning: $(0-2)\,\mathrm{NSB}_{\mathrm{Dark}}$.

(b) standard cleaning: $(0-2)\,\mathrm{NSB}_{\mathrm{Dark}}$.

(c) progressive cleaning: $(2-4)\,\mathrm{NSB}_{\mathrm{Dark}}$.

(d) standard cleaning: $(2-4)\,\mathrm{NSB}_{\mathrm{Dark}}$.

Figure B.11: Dependency of the significance of detection (Li&Ma) to the choice of maximum angular distance (θ^2_{max}) and prediction threshold given progressive (right) or standard cleaning (left) levels with no moonlight (top) or low moonlight (bottom). The significance is on the ordinate, the evaluated θ^2_{max} is on the abscissa, and the curves are grouped by the chosen prediction threshold. Lines do not indicate linearity but connect data points with the same prediction threshold. The data points mark the significance for the data set with the given combination of θ_{max} and prediction threshold. The significance was determined in a 100-fold bootstrapping, with the mean as a data point and the standard deviation as an estimator of the error bars. The θ^2_{max} chosen for this thesis is indicated by the dashed vertical line and the chosen `gammaness` threshold is printed in bold letters in the legend. The resulting significance is marked with a black circle.

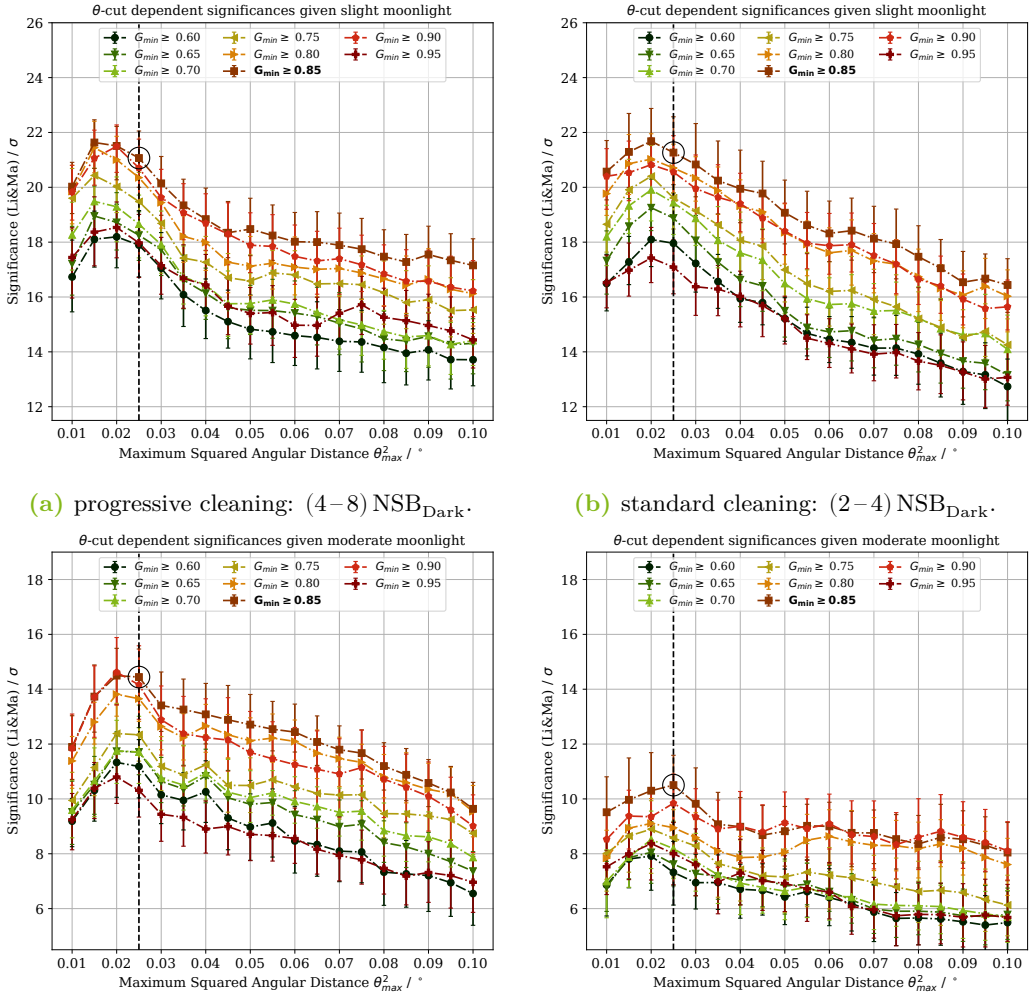

(a) progressive cleaning: $(4-8)\,\mathrm{NSB}_{\mathrm{Dark}}$.

(b) standard cleaning: $(2-4)\,\mathrm{NSB}_{\mathrm{Dark}}$.

(c) progressive cleaning: $(8-12)\,\mathrm{NSB}_{\mathrm{Dark}}$.

(d) standard cleaning: $(8-12)\,\mathrm{NSB}_{\mathrm{Dark}}$.

Figure B.12: Dependency of the significance of detection (Li&Ma) to the choice of maximum angular distance (θ^2_{max}) and prediction threshold given progressive (right) or standard cleaning (left) levels with slight moonlight (top) or moderate moonlight (bottom). The significance is on the ordinate, the evaluated θ^2_{max} is on the abscissa, and the curves are grouped by the chosen prediction threshold. Lines do not indicate linearity but connect data points with the same prediction threshold. The data points mark the significance for the data set with the given combination of θ_{max} and prediction threshold. The significance was determined in a 100-fold bootstrapping, with the mean as a data point and the standard deviation as an estimator of the error bars. The θ^2_{max} chosen for this thesis is indicated by the dashed vertical line and the chosen `gammaness` threshold is printed in bold letters in the legend. The resulting significance is marked with a black circle.

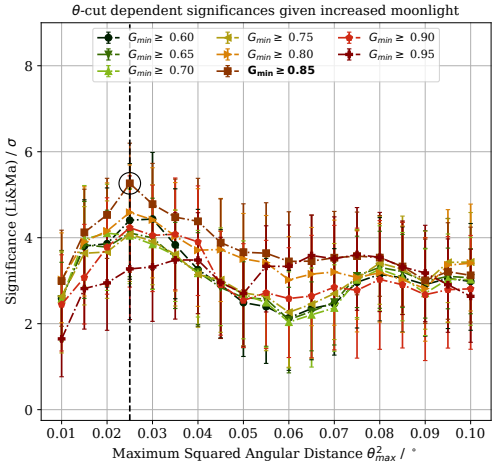

(a) progressive cleaning: $(12-16)\,\mathrm{NSB}_{\mathrm{Dark}}$.

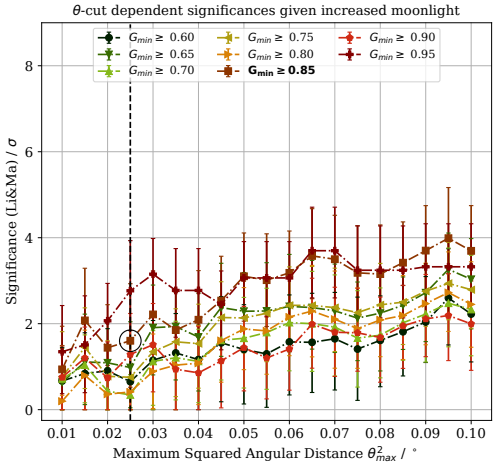

(b) standard cleaning: $(12-16)\,\mathrm{NSB}_{\mathrm{Dark}}$.

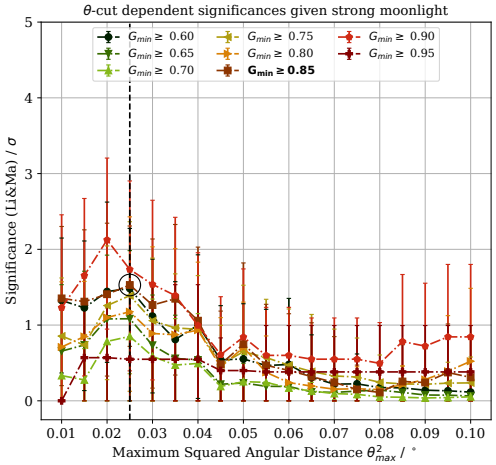

(c) progressive cleaning: $(16-24)\,\mathrm{NSB}_{\mathrm{Dark}}$.

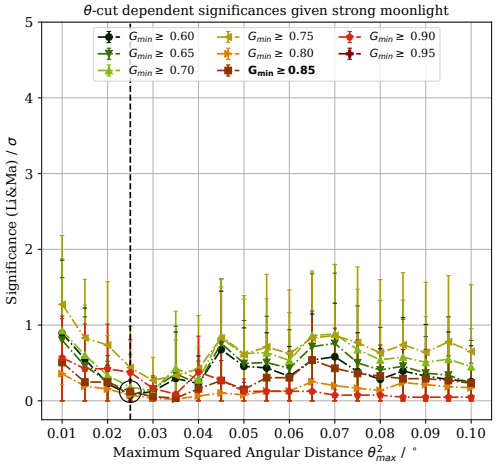

(d) standard cleaning: $(16-24)\,\mathrm{NSB}_{\mathrm{Dark}}$.

Figure B.13: Dependency of the significance of detection (Li&Ma) to the choice of maximum angular distance (θ^2_{max}) and prediction threshold given progressive (right) or standard cleaning (left) levels with increased moonlight (top) or strong moonlight (bottom). The significance is on the ordinate, the evaluated θ^2_{max} is on the abscissa, and the curves are grouped by the chosen prediction threshold. Lines do not indicate linearity but connect data points with the same prediction threshold. The data points mark the significance for the data set with the given combination of θ_{max} and prediction threshold. The significance was determined in a 100-fold bootstrapping, with the mean as a data point and the standard deviation as an estimator of the error bars. The θ^2_{max} chosen for this thesis is indicated by the dashed vertical line and the chosen `gammaness` threshold is printed in bold letters in the legend. The resulting significance is marked with a black circle.

C Appendix: NSB Performance

Chapter 6 discussed the NSB-dependent performance of the analysis presented in this thesis in comparison to the standard analysis used so far in *fact-tools*. In the main document, some of the performance plots were only presented for exemplary light conditions. Section C.1 thus provides additional plots of all light conditions for the source detection, sky maps, and energy migration. The latter was not shown in the main part of this thesis and is provided here additionally.

Furthermore, the values of flux points from the Crab Nebula's unfolded spectra, shown in section 7.7, are provided in this chapter. Tables with these flux points, their uncertainties, and the used energy bins are given in section C.2.

C.1 NSB Performance Plots for all Light Conditions

The distribution of the squared angular distance of reconstructed and actual source position (θ^2-plots) and sky maps at various NSB levels, with regard to Crab's locations, have been presented with a few example NSB levels. In order to present all six NSB levels, sky maps and θ^2-plots are illustrated in the following. Figure C.1 shows θ^2-plots achieved with the progressive cleaning levels, whereas the results from standard cleaning levels are provided in figure C.2. In the case of sky maps, the results from the progressive cleaning levels are presented in figure C.3 and the results from standard cleaning levels are depicted in figure C.4.

The performance of the energy regression has been reflected with bias and resolution plots in section 6.3.3. In order to provide insight to the underlying energy distribution with regard to a comparision of true and estimated energy, the energy migration matrices are illustrated in figure C.5 for the optimized analysis and in figure C.6 for the standard analysis.

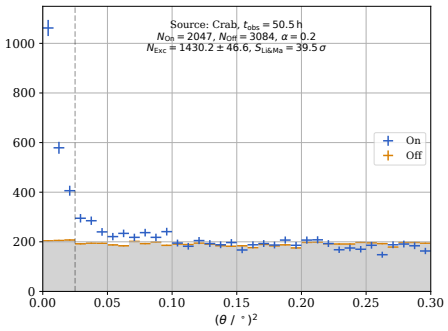

(a) No moonlight: $(0-2)\,\mathrm{NSB}_{\mathrm{Dark}}$.

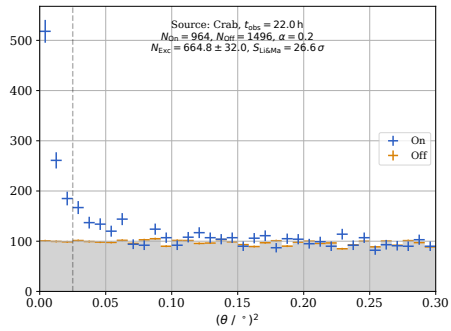

(b) Low moonlight: $(2-4)\,\mathrm{NSB}_{\mathrm{Dark}}$.

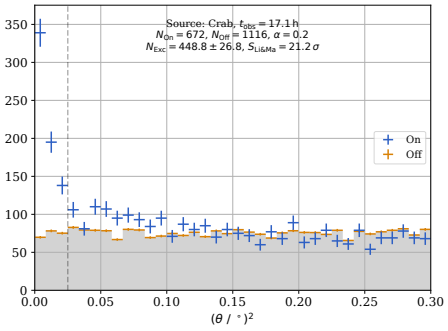

(c) Slight moonlight: $(4-8)\,\mathrm{NSB}_{\mathrm{Dark}}$.

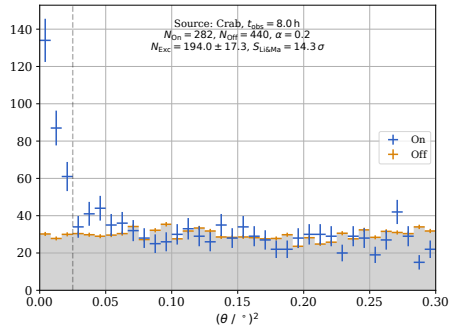

(d) Moderate moonlight: $(8-12)\,\mathrm{NSB}_{\mathrm{Dark}}$.

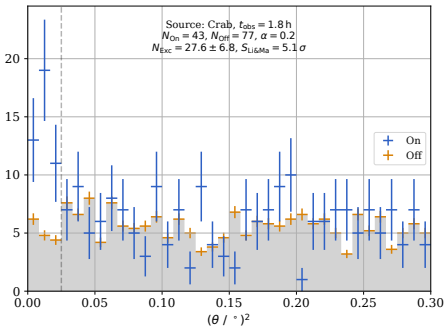

(e) Increased moonlight: $(12-16)\,\mathrm{NSB}_{\mathrm{Dark}}$.

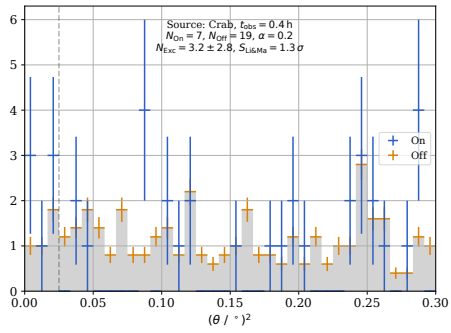

(f) Strong moonlight: $(16-24)\,\mathrm{NSB}_{\mathrm{Dark}}$.

Figure C.1: Examples for θ^2-plots of Crab Nebula observations at all six NSB samples ranging from $0\,\mathrm{NSB}_{\mathrm{Dark}}$ to $24\,\mathrm{NSB}_{\mathrm{Dark}}$. The results have been achieved with the **optimized analysis**. The squared distance to the observed source position of Crab are binned on the abscissa and the total number of events is given on the ordinate. Blue points represent data from the ON-position, while the average rates from the OFF-positions are indicated in orange. A `gammaness` cut of $G > 0.85$ has been applied to the Crab Nebula data in order to achieve the shown examples. The value of the θ^2-cut of $\theta^2_{\mathrm{max}} = 0.025°$ is indicated by the vertical grey, dashed line.

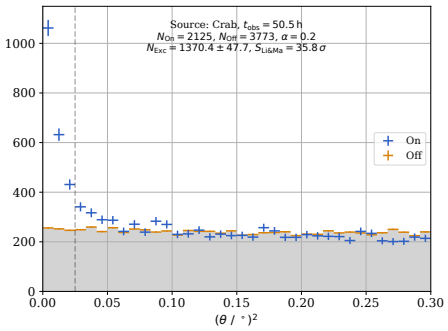

(a) No moonlight: $(0-2)\,\mathrm{NSB}_{\mathrm{Dark}}$.

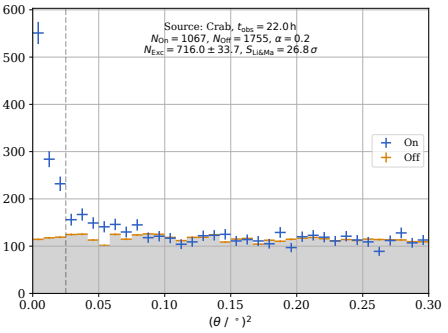

(b) Low moonlight: $(2-4)\,\mathrm{NSB}_{\mathrm{Dark}}$.

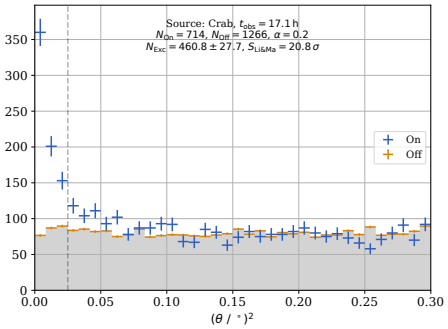

(c) Slight moonlight: $(4-8)\,\mathrm{NSB}_{\mathrm{Dark}}$.

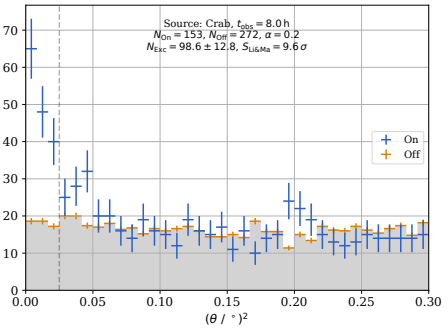

(d) Moderate moonlight: $(8-12)\,\mathrm{NSB}_{\mathrm{Dark}}$.

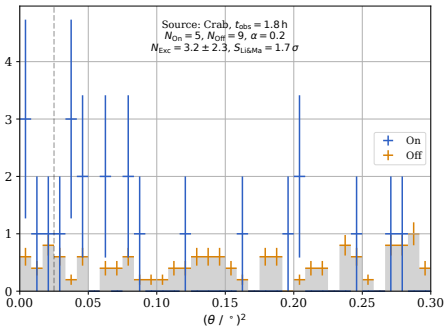

(e) Increased moonlight: $(12-16)\,\mathrm{NSB}_{\mathrm{Dark}}$.

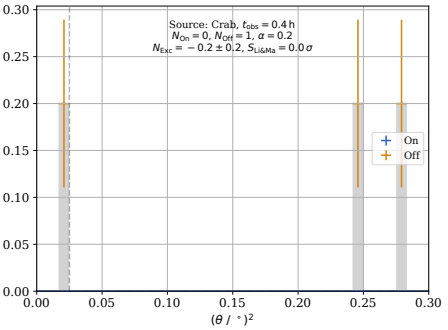

(f) Strong moonlight: $(16-24)\,\mathrm{NSB}_{\mathrm{Dark}}$.

Figure C.2: Examples for θ^2-plots of Crab Nebula observations at all six NSB samples ranging from $0\,\mathrm{NSB}_{\mathrm{Dark}}$ to $24\,\mathrm{NSB}_{\mathrm{Dark}}$. The results have been achieved with the **standard analysis**. The squared distance to the observed source position of Crab are binned on the abscissa and the total number of events is given on the ordinate. Blue points represent data from the ON-position, while the average rates from the OFF-positions are indicated in orange. A `gammaness` cut of $G > 0.85$ has been applied to the Crab Nebula data in order to achieve the shown examples. The value of the θ^2-cut of $\theta^2_{\mathrm{max}} = 0.025°$ is indicated by the vertical grey, dashed line.

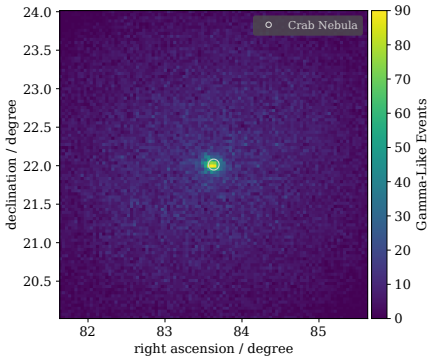

(a) No moonlight: $(0-2)\,\mathrm{NSB}_{\mathrm{Dark}}$.

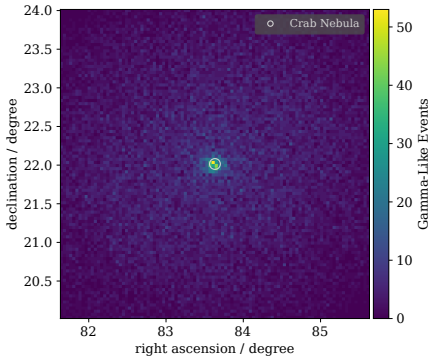

(b) Low moonlight: $(2-4)\,\mathrm{NSB}_{\mathrm{Dark}}$.

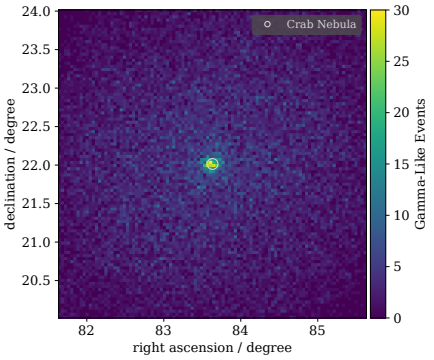

(c) Slight moonlight: $(4-8)\,\mathrm{NSB}_{\mathrm{Dark}}$.

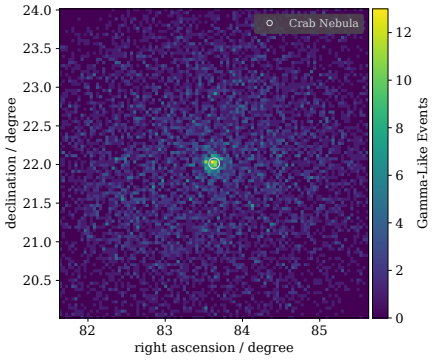

(d) Moderate moonlight: $(8-12)\,\mathrm{NSB}_{\mathrm{Dark}}$.

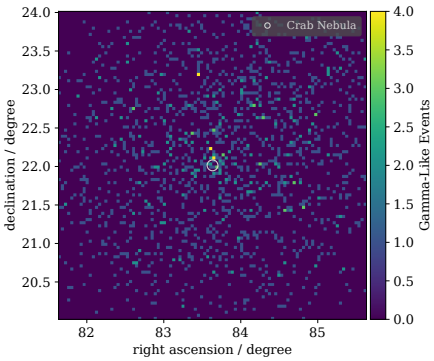

(e) Increased moonlight: $(12-16)\,\mathrm{NSB}_{\mathrm{Dark}}$.

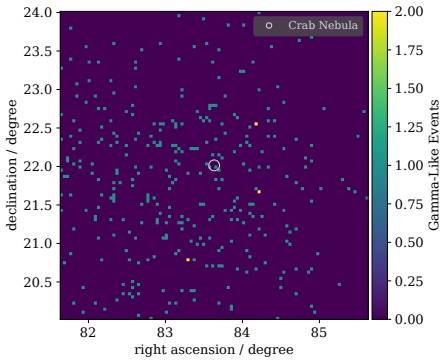

(f) Strong moonlight: $(16-24)\,\mathrm{NSB}_{\mathrm{Dark}}$.

Figure C.3: Sky maps of gamma-like events in the observed sky region with the source position of Crab in the centers. All six examples of NSB conditions are presented and range from $0\,\mathrm{NSB}_{\mathrm{Dark}}$ to $24\,\mathrm{NSB}_{\mathrm{Dark}}$. The source location is indicated by the grey circle. The results have been achieved with the **optimized analysis**. The coloring indicates the frequency of events from a certain direction given in equatorial coordinates right ascension and declination. The data are constrained to a `gammaness` of $G > 0.85$.

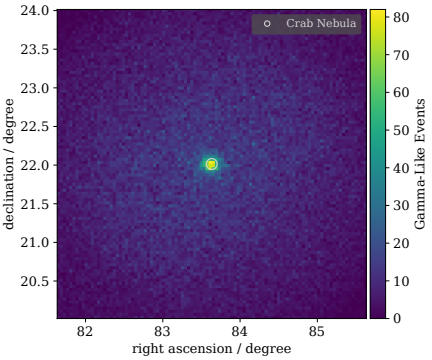

(a) No moonlight: $(0-2)\,\mathrm{NSB}_{\mathrm{Dark}}$.

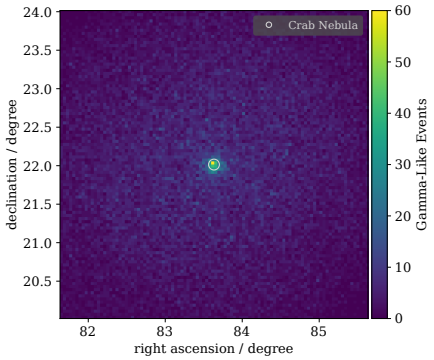

(b) Low moonlight: $(2-4)\,\mathrm{NSB}_{\mathrm{Dark}}$.

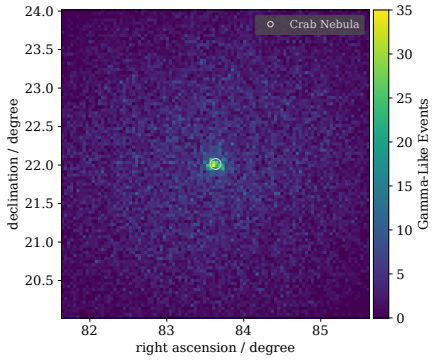

(c) Slight moonlight: $(4-8)\,\mathrm{NSB}_{\mathrm{Dark}}$.

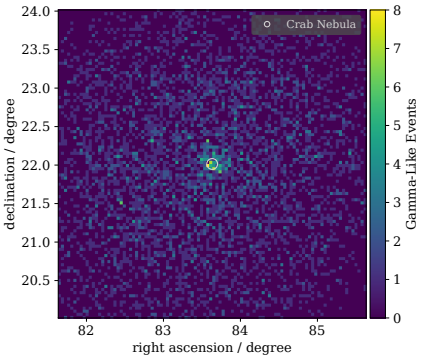

(d) Moderate moonlight: $(8-12)\,\mathrm{NSB}_{\mathrm{Dark}}$.

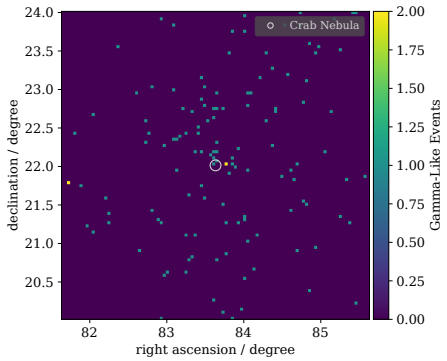

(e) Increased moonlight: $(12-16)\,\mathrm{NSB}_{\mathrm{Dark}}$.

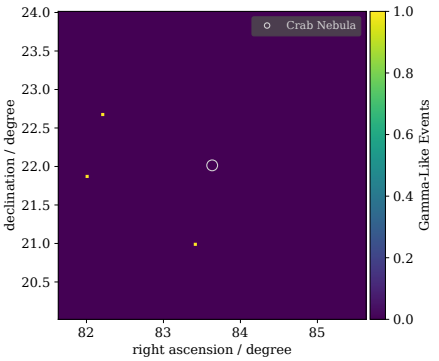

(f) Strong moonlight: $(16-24)\,\mathrm{NSB}_{\mathrm{Dark}}$.

Figure C.4: Sky maps of gamma-like events in the observed sky region with the source position of Crab in the centers. All six examples of NSB conditions are presented and range from $0\,\mathrm{NSB}_{\mathrm{Dark}}$ to $24\,\mathrm{NSB}_{\mathrm{Dark}}$. The source location is indicated by the grey circle. The results have been achieved with the **standard analysis**. The coloring indicates the frequency of events from a certain direction given in equatorial coordinates right ascension and declination. The data are constrained to a `gammaness` of $G > 0.85$.

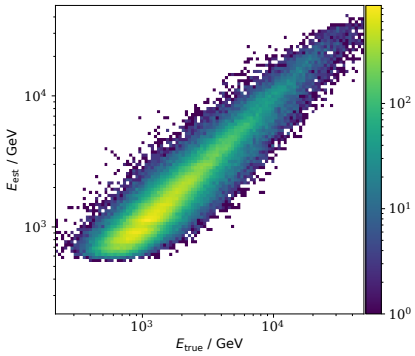

(a) No moonlight: $(0-2)\,\mathrm{NSB_{Dark}}$.

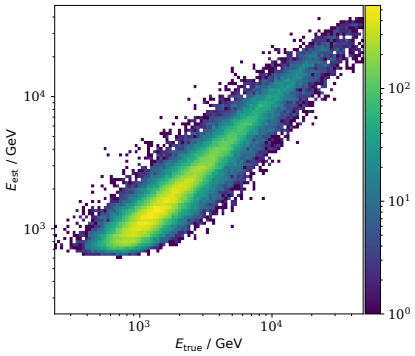

(b) Low moonlight: $(2-4)\,\mathrm{NSB_{Dark}}$.

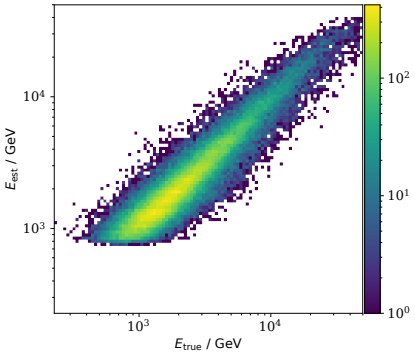

(c) Slight moonlight: $(4-8)\,\mathrm{NSB_{Dark}}$.

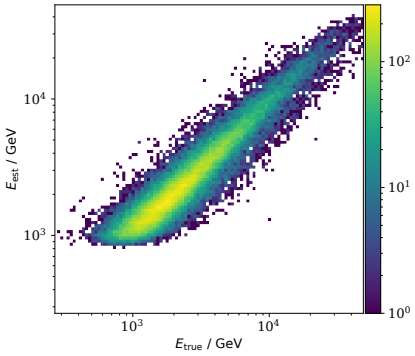

(d) Moderate moonlight: $(8-12)\,\mathrm{NSB_{Dark}}$.

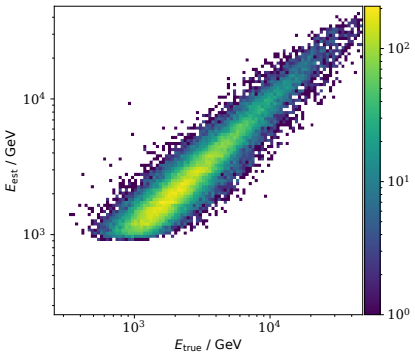

(e) Increased moonlight: $(12-16)\,\mathrm{NSB_{Dark}}$.

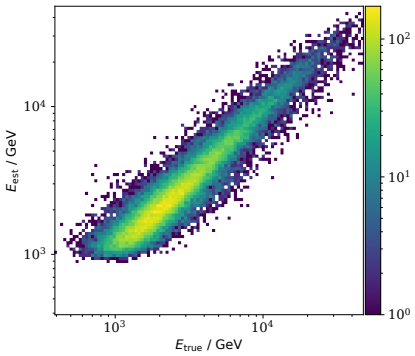

(f) Strong moonlight: $(16-24)\,\mathrm{NSB_{Dark}}$.

Figure C.5: Energy migration matrix of the energy regressor achieved with the **optimized analysis**. The true energy E_{true} of simulated showers is given on the abscissa. The estimated energy $E_{est.}$ is represented by the ordinate. The color map indicates the frequency of events. The bias and resolution plots in figure 6.16 are related to this distribution.

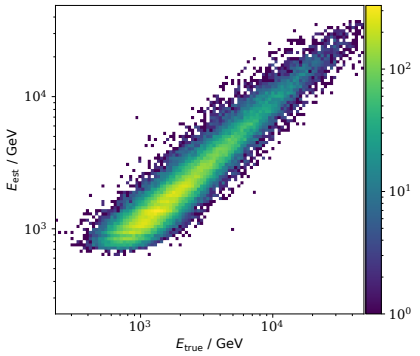

(a) No moonlight: $(0-2)\,\mathrm{NSB_{Dark}}$.

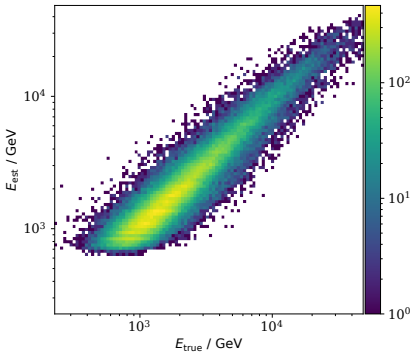

(b) Low moonlight: $(2-4)\,\mathrm{NSB_{Dark}}$.

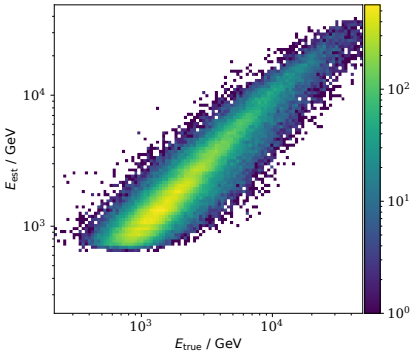

(c) Slight moonlight: $(4-8)\,\mathrm{NSB_{Dark}}$.

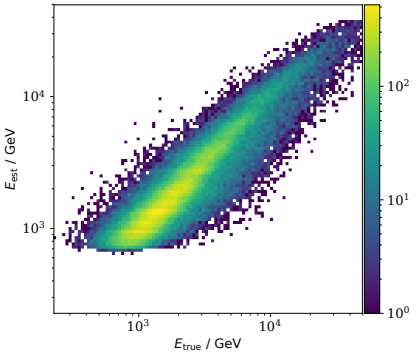

(d) Moderate moonlight: $(8-12)\,\mathrm{NSB_{Dark}}$.

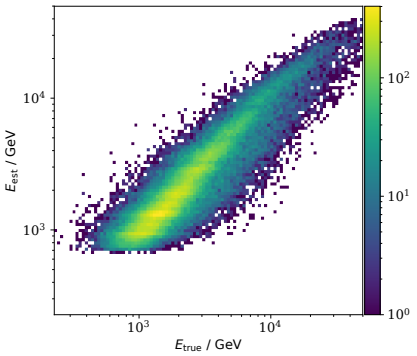

(e) Increased moonlight: $(12-16)\,\mathrm{NSB_{Dark}}$.

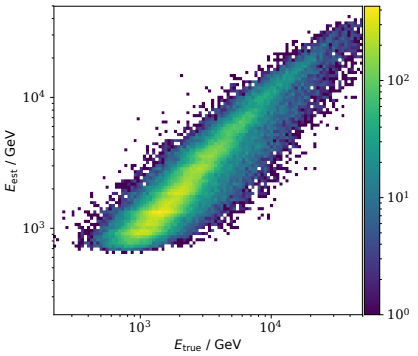

(f) Strong moonlight: $(16-24)\,\mathrm{NSB_{Dark}}$.

Figure C.6: Energy migration matrix of the energy regressor achieved with the **standard analysis**. The true energy E_{true} of simulated showers is given on the abscissa. The estimated energy $E_{est.}$ is represented by the ordinate. The color map indicates the frequency of events. The bias and resolution plots in figure 6.16 are related to this distribution.

C.2 Tables of the Unfolded Energy Spectra

The flux points of the Crab Nebula's unfolded spectra, presented in section 7.7, are listed in the following. The tables of the flux points unfolded with the optimized analysis are given in subsection C.2.1. The tables of the flux points unfolded with the standard analysis are given in subsection C.2.2.

C.2.1 Optimized Analysis

Tables that are containing values of the flux points of the Crab Nebula's unfolded spectra, which have been obtained with the optimized analysis, are given in tables C.1 to C.5.

Energy Range		Gamma-ray	Flux Uncertainties	
low	high	Flux	lower	upper
[GeV]	[GeV]	$\left[\frac{1}{\mathrm{GeV\,m^2\,s}}\right]$	$\left[\frac{1}{\mathrm{GeV\,m^2\,s}}\right]$	$\left[\frac{1}{\mathrm{GeV\,m^2\,s}}\right]$
300.00	533.48	3.94×10^{-9}	-2.84×10^{-9}	4.55×10^{-9}
533.48	948.68	8.39×10^{-10}	-1.31×10^{-10}	1.26×10^{-10}
948.68	1687.02	1.26×10^{-10}	-1.43×10^{-11}	1.41×10^{-11}
1687.02	3000.00	3.49×10^{-11}	-3.47×10^{-12}	3.55×10^{-12}
3000.00	5334.84	6.39×10^{-12}	-9.86×10^{-13}	1.00×10^{-12}
5334.84	9486.83	9.47×10^{-13}	-2.89×10^{-13}	3.04×10^{-13}
9486.83	16870.24	9.26×10^{-14}	-5.78×10^{-14}	8.01×10^{-14}
16870.24	30000.00	2.47×10^{-14}	-1.72×10^{-14}	2.73×10^{-14}
$t_{obs} = 50.50\,h$, $N_{On} = 2043$, $\alpha \cdot N_{Off} = 617$, $S_{Li\&Ma} = 39.5\,\sigma$				

Table C.1: Result of the unfolding of Crab Nebula data with the optimized analysis and NSB in the range of $(0-2)\,\mathrm{NSB_{Dark}}$. The energy range holds the values of the energy bins' low and high edge. The flux uncertainties are given relative to the gamma-ray flux. All values are rounded to two decimal places.

Energy Range		Gamma-ray	Flux Uncertainties	
low	high	Flux	lower	upper
[GeV]	[GeV]	$\left[\frac{1}{\mathrm{GeV\,m^2\,s}}\right]$	$\left[\frac{1}{\mathrm{GeV\,m^2\,s}}\right]$	$\left[\frac{1}{\mathrm{GeV\,m^2\,s}}\right]$
450.00	760.68	2.04×10^{-9}	-1.43×10^{-9}	1.95×10^{-9}
760.68	1285.85	4.51×10^{-10}	-8.92×10^{-11}	8.55×10^{-11}
1285.85	2173.59	9.88×10^{-11}	-1.55×10^{-11}	1.62×10^{-11}
2173.59	3674.23	1.97×10^{-11}	-4.16×10^{-12}	4.29×10^{-12}
3674.23	6210.91	3.57×10^{-12}	-1.24×10^{-12}	1.31×10^{-12}
6210.91	10498.91	8.27×10^{-13}	-3.67×10^{-13}	4.08×10^{-13}
10498.91	17747.32	1.17×10^{-13}	-7.84×10^{-14}	1.20×10^{-13}
17747.32	30000.00	2.11×10^{-14}	-1.56×10^{-14}	3.15×10^{-14}
$t_{obs} = 21.95\,\mathrm{h}$, $N_{On} = 964$, $\alpha \cdot N_{Off} = 299$, $S_{Li\&Ma} = 26.6\,\sigma$				

Table C.2: Result of the unfolding of Crab Nebula data with the optimized analysis and NSB in the range of $(2-4)\,\mathrm{NSB_{Dark}}$. The energy range holds the values of the energy bins' low and high edge. The flux uncertainties are given relative to the gamma-ray flux. All values are rounded to two decimal places.

Energy Range		Gamma-ray	Flux Uncertainties	
low	high	Flux	lower	upper
[GeV]	[GeV]	$\left[\frac{1}{\mathrm{GeV\,m^2\,s}}\right]$	$\left[\frac{1}{\mathrm{GeV\,m^2\,s}}\right]$	$\left[\frac{1}{\mathrm{GeV\,m^2\,s}}\right]$
500.00	897.41	2.38×10^{-9}	-1.48×10^{-9}	1.50×10^{-9}
897.41	1610.69	2.97×10^{-10}	-6.29×10^{-11}	6.40×10^{-11}
1610.69	2890.91	6.20×10^{-11}	-1.01×10^{-11}	1.02×10^{-11}
2890.91	5188.67	6.68×10^{-12}	-2.39×10^{-12}	2.52×10^{-12}
5188.67	9312.75	3.20×10^{-12}	-8.18×10^{-13}	8.73×10^{-13}
9312.75	16714.74	3.83×10^{-13}	-1.94×10^{-13}	2.27×10^{-13}
16714.74	30000.00	3.54×10^{-14}	-2.61×10^{-14}	5.34×10^{-14}
$t_{obs} = 17.09\,h$, $N_{On} = 670$, $\alpha \cdot N_{Off} = 223$, $S_{Li\&Ma} = 21.2\,\sigma$				

Table C.3: Result of the unfolding of Crab Nebula data with the optimized analysis and NSB in the range of $(4-8)\,\mathrm{NSB_{Dark}}$. The energy range holds the values of the energy bins' low and high edge. The flux uncertainties are given relative to the gamma-ray flux. All values are rounded to two decimal places.

Energy Range		Gamma-ray	Flux Uncertainties	
low	high	Flux	lower	upper
[GeV]	[GeV]	$\left[\frac{1}{\mathrm{GeV\,m^2\,s}}\right]$	$\left[\frac{1}{\mathrm{GeV\,m^2\,s}}\right]$	$\left[\frac{1}{\mathrm{GeV\,m^2\,s}}\right]$
550.00	1071.08	7.09×10^{-10}	-5.07×10^{-10}	8.57×10^{-10}
1071.08	2085.85	3.07×10^{-10}	-4.86×10^{-11}	5.01×10^{-11}
2085.85	4062.02	2.44×10^{-11}	-6.77×10^{-12}	7.28×10^{-12}
4062.02	7910.46	3.75×10^{-12}	-1.30×10^{-12}	1.45×10^{-12}
7910.46	15404.99	3.65×10^{-13}	-2.31×10^{-13}	3.30×10^{-13}
15404.99	30000.00	9.67×10^{-14}	-6.68×10^{-14}	1.10×10^{-13}
$t_{obs} = 8.03\,h$, $N_{On} = 282$, $\alpha \cdot N_{Off} = 88$, $S_{Li\&Ma} = 14.3\,\sigma$				

Table C.4: Result of the unfolding of Crab Nebula data with the optimized analysis and NSB in the range of $(8-12)\,\mathrm{NSB_{Dark}}$. The energy range holds the values of the energy bins' low and high edge. The flux uncertainties are given relative to the gamma-ray flux. All values are rounded to two decimal places.

Energy Range		Gamma-ray	Flux Uncertainties	
low	high	Flux	lower	upper
[GeV]	[GeV]	$\left[\frac{1}{\mathrm{GeV\,m^2\,s}}\right]$	$\left[\frac{1}{\mathrm{GeV\,m^2\,s}}\right]$	$\left[\frac{1}{\mathrm{GeV\,m^2\,s}}\right]$
600.00	1312.03	6.69×10^{-10}	-4.80×10^{-10}	8.13×10^{-10}
1312.03	2869.06	1.38×10^{-10}	-4.17×10^{-11}	4.56×10^{-11}
2869.06	6273.84	6.72×10^{-12}	-4.01×10^{-12}	5.60×10^{-12}
6273.84	13719.15	6.85×10^{-13}	-5.12×10^{-13}	1.06×10^{-12}
13719.15	30000.00	1.85×10^{-13}	-1.39×10^{-13}	3.01×10^{-13}
$t_{obs} = 1.82\,h$, $N_{On} = 43$, $\alpha \cdot N_{Off} = 15$, $S_{Li\&Ma} = 5.1\,\sigma$				

Table C.5: Result of the unfolding of Crab Nebula data with the optimized analysis and NSB in the range of $(12-16)\,\mathrm{NSB_{Dark}}$. The energy range holds the values of the energy bins' low and high edge. The flux uncertainties are given relative to the gamma-ray flux. All values are rounded to two decimal places.

C.2.2 Standard Analysis

Tables that are containing values of the flux points of the Crab Nebula's unfolded spectra, which have been obtained with the standard analysis, are given in tables C.6 to C.10.

Energy Range		Gamma-ray	Flux Uncertainties	
low	high	Flux	lower	upper
[GeV]	[GeV]	$\left[\frac{1}{\mathrm{GeV\,m^2\,s}}\right]$	$\left[\frac{1}{\mathrm{GeV\,m^2\,s}}\right]$	$\left[\frac{1}{\mathrm{GeV\,m^2\,s}}\right]$
300.00	533.48	3.38×10^{-8}	-2.16×10^{-8}	2.54×10^{-8}
533.48	948.68	6.98×10^{-10}	-4.09×10^{-10}	4.15×10^{-10}
948.68	1687.02	1.50×10^{-10}	-1.99×10^{-11}	1.96×10^{-11}
1687.02	3000.00	4.53×10^{-11}	-4.24×10^{-12}	4.09×10^{-12}
3000.00	5334.84	5.25×10^{-12}	-1.10×10^{-12}	1.07×10^{-12}
5334.84	9486.83	1.42×10^{-12}	-3.09×10^{-13}	3.30×10^{-13}
9486.83	16870.24	6.87×10^{-14}	-4.67×10^{-14}	6.95×10^{-14}
16870.24	30000.00	2.24×10^{-14}	-1.60×10^{-14}	2.59×10^{-14}
$t_{obs} = 50.50\,h$, $N_{On} = 2119$, $\alpha \cdot N_{Off} = 754$, $S_{Li\&Ma} = 35.8\,\sigma$				

Table C.6: Result of the unfolding of Crab Nebula data with the standard analysis and NSB in the range of $(0-2)\,\mathrm{NSB_{Dark}}$. The energy range holds the values of the energy bins' low and high edge. The flux uncertainties are given relative to the gamma-ray flux. All values are rounded to two decimal places.

Energy Range		Gamma-ray	Flux Uncertainties	
low	high	Flux	lower	upper
[GeV]	[GeV]	$\left[\frac{1}{\mathrm{GeV\,m^2\,s}}\right]$	$\left[\frac{1}{\mathrm{GeV\,m^2\,s}}\right]$	$\left[\frac{1}{\mathrm{GeV\,m^2\,s}}\right]$
450.00	760.68	2.20×10^{-9}	-1.50×10^{-9}	1.98×10^{-9}
760.68	1285.85	5.28×10^{-10}	-9.88×10^{-11}	9.97×10^{-11}
1285.85	2173.59	1.15×10^{-10}	-1.69×10^{-11}	1.77×10^{-11}
2173.59	3674.23	1.83×10^{-11}	-4.19×10^{-12}	4.37×10^{-12}
3674.23	6210.91	4.44×10^{-12}	-1.20×10^{-12}	1.28×10^{-12}
6210.91	10498.91	4.26×10^{-13}	-2.64×10^{-13}	3.41×10^{-13}
10498.91	17747.32	6.88×10^{-14}	-4.84×10^{-14}	8.22×10^{-14}
17747.32	30000.00	2.02×10^{-14}	-1.50×10^{-14}	2.99×10^{-14}
$t_{obs} = 21.95\,h$, $N_{On} = 1067$, $\alpha \cdot N_{Off} = 351$, $S_{Li\&Ma} = 26.8\,\sigma$				

Table C.7: Result of the unfolding of Crab Nebula data with the standard analysis and NSB in the range of $(2-4)\,\mathrm{NSB_{Dark}}$. The energy range holds the values of the energy bins' low and high edge. The flux uncertainties are given relative to the gamma-ray flux. All values are rounded to two decimal places.

Energy Range		Gamma-ray	Flux Uncertainties	
low	high	Flux	lower	upper
[GeV]	[GeV]	$\left[\frac{1}{\mathrm{GeV\,m^2\,s}}\right]$	$\left[\frac{1}{\mathrm{GeV\,m^2\,s}}\right]$	$\left[\frac{1}{\mathrm{GeV\,m^2\,s}}\right]$
500.00	897.41	1.37×10^{-9}	-8.72×10^{-10}	8.68×10^{-10}
897.41	1610.69	2.44×10^{-10}	-4.98×10^{-11}	5.12×10^{-11}
1610.69	2890.91	5.88×10^{-11}	-9.11×10^{-12}	9.33×10^{-12}
2890.91	5188.67	4.55×10^{-12}	-2.17×10^{-12}	2.38×10^{-12}
5188.67	9312.75	2.47×10^{-12}	-7.82×10^{-13}	8.15×10^{-13}
9312.75	16714.74	4.57×10^{-13}	-2.12×10^{-13}	2.53×10^{-13}
16714.74	30000.00	3.57×10^{-14}	-2.59×10^{-14}	5.17×10^{-14}
$t_{obs} = 17.09\,h$, $N_{On} = 713$, $\alpha \cdot N_{Off} = 253$, $S_{Li\&Ma} = 20.8\,\sigma$				

Table C.8: Result of the unfolding of Crab Nebula data with the standard analysis and NSB in the range of $(4-8)\,\mathrm{NSB_{Dark}}$. The energy range holds the values of the energy bins' low and high edge. The flux uncertainties are given relative to the gamma-ray flux. All values are rounded to two decimal places.

Energy Range		Gamma-ray	Flux Uncertainties	
low	high	Flux	lower	upper
[GeV]	[GeV]	$\left[\frac{1}{\mathrm{GeV\,m^2\,s}}\right]$	$\left[\frac{1}{\mathrm{GeV\,m^2\,s}}\right]$	$\left[\frac{1}{\mathrm{GeV\,m^2\,s}}\right]$
550.00	1071.08	6.25×10^{-10}	-3.98×10^{-10}	4.92×10^{-10}
1071.08	2085.85	1.69×10^{-10}	-3.96×10^{-11}	3.93×10^{-11}
2085.85	4062.02	1.32×10^{-11}	-6.56×10^{-12}	7.61×10^{-12}
4062.02	7910.46	2.97×10^{-12}	-1.48×10^{-12}	1.77×10^{-12}
7910.46	15404.99	2.60×10^{-13}	-1.83×10^{-13}	3.40×10^{-13}
15404.99	30000.00	8.22×10^{-14}	-6.11×10^{-14}	1.21×10^{-13}
$t_{obs} = 8.03\,h$, $N_{On} = 153$, $\alpha \cdot N_{Off} = 54$, $S_{Li\&Ma} = 9.6\,\sigma$				

Table C.9: Result of the unfolding of Crab Nebula data with the standard analysis and NSB in the range of $(8-12)\,\mathrm{NSB_{Dark}}$. The energy range holds the values of the energy bins' low and high edge. The flux uncertainties are given relative to the gamma-ray flux. All values are rounded to two decimal places.

Energy Range		Gamma-ray	Flux Uncertainties	
low	high	Flux	lower	upper
[GeV]	[GeV]	$\left[\frac{1}{\mathrm{GeV\,m^2\,s}}\right]$	$\left[\frac{1}{\mathrm{GeV\,m^2\,s}}\right]$	$\left[\frac{1}{\mathrm{GeV\,m^2\,s}}\right]$
600.00	1312.03	9.49×10^{-10}	-6.72×10^{-10}	1.15×10^{-9}
1312.03	2869.06	6.78×10^{-11}	-4.82×10^{-11}	8.35×10^{-11}
2869.06	6273.84	6.97×10^{-12}	-5.26×10^{-12}	1.15×10^{-11}
6273.84	13719.15	2.20×10^{-12}	-1.65×10^{-12}	3.56×10^{-12}
13719.15	30000.00	9.49×10^{-13}	-7.15×10^{-13}	1.66×10^{-12}
$t_{obs} = 1.82\,h$, $N_{On} = 5$, $\alpha \cdot N_{Off} = 2$, $S_{Li\&Ma} = 1.7\,\sigma$				

Table C.10: Result of the unfolding of Crab Nebula data with the standard analysis and NSB in the range of $(12-16)\,\mathrm{NSB_{Dark}}$. The energy range holds the values of the energy bins' low and high edge. The flux uncertainties are given relative to the gamma-ray flux. All values are rounded to two decimal places.

D Appendix: Hardware Changes

During the past nine years of operation, components of the FACT telescope system had been enhanced, optimized, repaired, and some had to be replaced. The hardware configuration of the system thus changed in parts from time to time. These changes would need to be taken into consideration for a full optimization of the analysis. The simulation then needs to be adapted to the hardware configurations.

However, the extend to which these changes affect the outcome of the analysis may vary with regard to the influence of the changed component. The correspondence of analysis results from winter 2013/14 and winter 2015/16 indicates a rather small influence during this period.

In the following, the hardware changes between March 2012 and May 2016 are listed for completeness and to provide an overview of the hardware status of FACT during the observations investigated in this thesis. It should be noted that most of the hardware changes were not considered in the presented study apart from an interpolation of malfunctioning pixels and a temperature related drift of the SiPMs' gain. The severest change to the optical system was a realignment of FACT's mirrors in May 2014. This change was not considered in the MC simulations, which still used the alignment model from before that time. It is thus advisable to use the post 2014 alignment model for further analysis of the Crab Nebula sample used in the presented study as it might allow for a more realistic simulation of the system and therefore a even better performance of the analysis.

Date	Change
2012-03-01	First operation of feedback system
2012-03-13	Replacement of bias crate controller
2012-04-13	Commissioning of feedback system
2012-04-20	(Approx.) feedback system commissioned
2012-08-13	Camera malfunctioning (night 13. to 14.)
2012-08-17	Camera repaired

Continued on next page

Date	Change
2012-10-30	Detached Mirror
2012-11-08	New pointing model
2012-11-20	Mirror alignment
2012-12-06	Broken bias channel
2013-01-10	Bias crate: replacement with spare
2013-01-10	Current measured in ch 263 is related to ch 262
2013-01-25	Mirror reattached and aligned
2013-01-26	Improvement of alignment of 4 mirrors
2013-03-12	Change of ratecontrol
2014-05-10	Mirror alignment
2014-05-19	Mirror alignment: now Davis-Cotton-Parabolic-Hybrid
2014-05-20	Camera repair
2014-05-20	Az gear repair
2014-05-21	Camera opened: Low Voltage supply repairs
2014-05-21	Painting of reflective surfaces on the mount
2014-05-21	Installation of allsky cam and weather station
2014-05-23	Actuator replacement
2014-05-24	New Pointing Model
2014-11-15	Broken DRS board
2015-01-08	Underflow voltage in CHID 729, 750
2015-01-08	Air conditioning target temperature set to 28°C
2015-05-26	Broken DRS board repaired
2015-05-26	FACT camera opened: humidity issues, replacement of FAD-board
2015-05-27	FACT camera opened
2015-05-28	FACT camera sealed; New FSC firmware
2015-08-31	Broken HV board 8 (CHIDs: 171 - 174)
2015-09-01	Broken HV board 41 (CHIDs: 184 - 188)
2015-11-05	LID actuator replacement

Continued on next page

Date	Change
2015-11-07	LID actuator replacement
2015-11-07	New Drive Software
2015-11-21	Camera dehumidification
2016-03-13	Broken HV board 272 (CHIDs: 1296 - 1299)

Table D.1: List of changes to the FACT hardware system from May 2012 until May 2016. Dates and events are taken from the FACT logbook.

List of Figures

List of Tables

Listings

Terms and Abbreviations

The following terms and abbreviations are provided as a service to the reader by means of a quick reference to terms frequently used in this thesis. The author of this thesis does not claim authorship for any of the definitions listed hereafter.

ADC

An analog-to-digital converter (ADC) is a system that converts an analog signal, e.g.„ light entering a sensor, into a digital signal. The inversion of this task is a digital-to-analog converter (DAC).

afterpulse

Effect of delayed avalanches in not fully recharged diodes, due to trapped charge carriers.

AGN

An active galactic nucleus (AGN) is a compact region at the center of a galaxy that has high luminosities reaching from radio to gamma ray wavebands. This radiation belived to result from the accretion of matter by a central supermassive black hole.

aict-tools

The *aict-tools* [84] are a collection of machine-learning scripts based on the *python* framework *scikit-learn*. They were developed by the FACT group of TU Dortmund University.

airglow

The airglow is emitted by excited atoms and molecules in the upper atmosphere, due to solar UV radiation during the day. Its intensity correlates with solar activity, with position on the sky and with time during the night. For details see [15].

APD

An Avalanche-Photo-Diode (APD) is a semiconductor photodiode that converts light into electricity via the photoelectric effect.

arrival time

The average arrival time of a photon bunch in a pixel of the FACT camera.

`arrival_time_mean`

Shower image parametrization: A *fact-tools* feature indicating the average arrival time of photons in all pixels of the camera.

`arrival_time_shower_mean`

A *fact-tools* feature indicating the average time of the arrival of photons on pixels associated with the shower.

a.s.l.

above sea level: a measure of a location's elevation in reference to a historic mean sea level.

AUC

The area under the (ROC-) curve is the definite integral of a curve, i.e., in machine-learning the area under the Reciever-Operator-Curve (ROC). It provides an aggregate measure of performance across all possible classification thresholds and allows for the comparison of machine-learning models.

bias

Mean value of the distribution of residuals $\frac{E_{Prediction}-E_{True}}{E_{True}}$.

Blazar

optically violent variable (OVV) quasars and BL Lac objects.

Calima

Sand particles from Sahara that occur at La Palma as an atmospheric phenomenon with winds from the east.

CERES

Executable in MARS CheObs, responsible for the simulation of the telescope and its electronics.

Cherenkov photon

aka Cherenkov radiation: Electromagnetic radiation emitted when a charged particle passes through a medium with a velocity larger then the medium's phase velocity.

clipping

Shortening of a electronic signal in time. In the case of FACT realised by adding an inverted, damped, and delayed version of the patch sum signals to the summed patches.

`COG`

Shower image parametrization: center of gravity of an air shower's light distribution in the focal plain.

`concentration_cog`

Shower image parametrization: Percentage of photons at the center of gravity (`COG`) compared to the total number of photons of the event.

`concentration_core`

Shower image parametrization: Percentage of photons inside the Hillas Ellipse aka. The pixels with a Mahalanobis Distance ≤ 1.

core pixel

Brightest pixels of a shower which are located in its core.

CORSIKA

Software for simulations of extensive air showers initiated by high energy cosmic particles.

Crab Nebula

A supernova remnant in the Taurus constellation from 1054CE. It is the brightest VHE gamma-ray source and is used for calibration as the standard candle in gamma-ray astronomy. Its central machine is the Crab Pulsar, a fastly spinning neutron star.

crosstalk

The effect of avalanches initiating simultaneous avalanches in neighboring G-APD cells.

cross-validation

Model validation in a statistical analysis to estimate the prediction error. It iteratively tests and trains models on independent subsamples drawn from the same overall sample. [60].

CTA

The the Cherenkov Telescope Array (CTA) will actually be two arrays of several IACTs with one array in the Northern Hemisphere and the other in the Southern Hemisphere. It will operate from some tens of GeV to about 300 TeV and is planned as an open observatory.

DAC

digital-to-analog converter.

DAQ

data acquisition.

dark count rate

Rate of thermally and field-assisted generated avalanches.

raw data level

Raw data of FACT: 1440 time series (one per pixel) of the signal amplitude in 300 *time slices* with 0.5 ns width.

pixel level

Data after the extraction step: Pixel-wise information about the number of photons and their mean arrival times.

shower level

Data after image cleaning: Event-wise parametrization of reconstructed shower images.

gamma level

Data after gamma/hadron separation: Reconstructed gamma-ray events with information about their energy, origin and gammaness.

Data-Monte-Carlo mismatch

Mismatch of data from simulations and observations with regard to their feature distributions.

dead-time

Time after an avalanche when a G-APD cannot be triggerd.

declination

Angular distance measured north/south of the celestial equator in the equatorial coordinate system.

`DISP`

Shower image parametrization: Method/Feature used for single telescope analyses to determine the orientation of the shower in the camera plane to reconstruct its origin. The feature is the distance between the COG and the reconstructed origin of the shower.

DRS

Domino ring-sampling chip(DRS) developed at the Paul-Scherrer-Institute to digitize and buffer analogue signals. The chip holds a chain of capacitors to store and buffer the signal.

DRS4

domino ring-sampling chip - type 4(DRS4) developed at the Paul-Scherrer-Institute to digitize and buffer analogue signals. The chip holds 1024 capacitors to store and buffer the signal.

DRS calibration

Calibration of the used data acquisition chip (DRS4). Constants are taken from special calibration runs.

DRS jump

Jump artifacts of the DRS4 chip that occur as jumps in the digitized time series.

DRS spike

Spike artifacts of the DRS4 chip that occur as spikes on the digitized time series.

extensive air shower

Cascade of secondary particles in the atmosphere initiated by a primary (cosmic) particle e.g. proton or photon.

extra-galactic background light

integrated emission from stars and galaxies of all types throughout the evolution of the universe.

EGS4

EGS (Electron Gamma Shower) is MC generator for the coupled transport of electrons and photons at energies between some keV to several hundreds of GeV.

FACT

The First G-APD Cherenkov Telescope (FACT) is the first imaging atmospheric Cherenkov telescope with a silicon photomultiplier (SiPM) camera. It is operating since October 2011 at the Roque de los Muchachos Observatory on La Palma (Canary islands).

fact-funfolding

The python package *fact-funfolding*[82] wrapps around *funfolding* and provides methods necessary for the unfolding of FACT observations.

fact-tools

The *fact-tools* are a collection of processors and stream implementations for the streams framework to analyse the data of the First G-APD Cherenkov Telescope.

AC-coupling

Alternating current coupling of circuits performed by e.g. a capacitor.

FITS file

Flexible Image Transport System (FITS) an open standard file format used in astronomy, which is used by FACT to store its raw data.

FLUKA

closed-source MC simulation for low-energy hadronic interactions.

FOV

field-of-view (FOV).

FPA

FACT preamplifier boards: The preamplifier units in use for FACT.

FTM

FACT trigger master board: The trigger master board that is in use for FACT.

FTU

FACT trigger unit boards: The boards that contain the trigger units which are in use for FACT.

funfolding

The python package *funfolding*[24] is a library with methods to perform spectral unfoldings.

gain

(here SiPM gain) The ratio of detected photons to the number of released charge carriers (i.e. the electronic signal) measured with the integral of a single avalanche signal in a SiPM.

gamma efficiency

Fraction of surviving gammas-ray events compared to the number of triggered gamma-ray events after a certain analysis step, e.g., the image cleaning.

gamma/hadron separation

Application of a prediction threshold to the classification of gamma and hadron events in oreder to distinguish between theses two classes.

`gammaness`

The confidence level (between 0 and 1) of the classifier for having detected a gamma event.

G-APD

A Geiger-mode-Avalanche-Photo-Diode (G-APD) aka single-photon Avalanche-Photo-Diode (SPAD) is a semi-conductor-based photon sensor that is operating with reverse bias voltage. An incoming photon initiates thus an avalanche of electron hole pairs and transfers accordingly the interaction with the photon into an electrical signal.

GenNSB

Term used in this thesis to name FACT's standard simulation method for NSB by generating NSB photons with Poisson statistics.

HEGRA

The former HEGRA Cherenkov Telescope array, which consisted of five IACTs stereo system at the Roque de los Muchachos Observatory on La Palma (Canary islands).

HEGRA CT3

HEGRA Cherenkov telescope 3 (HEGRA CT3), 3. IACT of the former HEGRA telescope array, which has been refurbished and is used as the foundation of FACT.

H.E.S.S.

The High Energy Steroscopic System (H.E.S.S.) is an IACT array with $4 \times 12\,\mathrm{m}$ and one 28 m operating in the GeV – TeV photon energy range. It is located near the Gamsberg in Namibia at an altitude of 1800 m a.s.l..

Hillas parameter

Shower image parametrizations: The first set of feature representations of air showers in the focal plane of an IACT, introdced by Hillas.

HV

high voltage supply (HV).

IACT

An imaging atmospheric Cherenkov telescope (IACT) or imaging air Cherenkov telescope is a technique to detect showers from very-high-energy gamma-rays photons by using Earth's atmosphere as detector volume and (secondary) Cherenkov photons as a proxy to observe the shower.

IceCube

IceCube is a particle detector at the South Pole aiming for astronomical neutrinos.

ICRC

The International Cosmic Ray Conference (ICRC) is biennially astro-particle physics conference organized by International Union of Pure and Applied Physics.

increased moonlight

Data sample with light conditions in the range $(48-64)\,\mu\mathrm{A}$ or $(12-16)\,\mathrm{NSB}_{\mathrm{Dark}}$.

inverse problem

The process of calculating from a set of observables the causal factors that produced them. In case of IACTs the following problem occurs: The energy of the primary particle can only be measured indirectly and the resolution for this is limited by the combination of detector and analysis. The true energy distribution is thus folded with their joined response and needs to be reconstructed via deconvolution [78].

Java

Java is a general-purpose, class-based, object-oriented programming language. Its design is orientated to the write-once-run-anywhere paradigm as it is platform independent.

`length`

Shower image parametrization: Spacial expansion of the semi-major axis of the shower's projection in the focal plane.

low moonlight

Data sample with light conditions in the range $(8-16)\,\mu\mathrm{A}$ or $(2-4)\,\mathrm{NSB}_{\mathrm{Dark}}$.

MAGIC

The Major Atmospheric Gamma-ray Imaging Cherenkov Telescopes (MAGIC), a $2 \times 17\,\mathrm{m}$ IACT stereo system at the Roque de los Muchachos Observatory on La Palma (Canary islands).

MARS

Modular Analysis and Reconstruction Software - Cherenkov Observatory Edition; C++ data analysis framework based on ROOT developed by Thomas Bretz.

MC

Monte Carlo simulation: A method to provide simulations based on random sampling of the desired processes [20].

Markov-Chain-Monte-Carlo

Method in Bayesian statistics for efficiently sampling a random variable from a posterior probability density function.

mean number of islands

Average number of islands – Shower image parametrization describing the number of separated clusters in the shower image – of several shower images.

MMCS

The MAGIC Monte Carlo Simulation (MMCS) is an inofficial private fork of CORSIKA modified for the needs of the MAGIC colaboration.

moderate moonlight

Data sample with light conditions in the range $(32-48)\,\mu A$ or $(8-12)\,\mathrm{NSB}_{\mathrm{Dark}}$.

bootstrapping

Sampling with replacement from a distribution. Used, e.g., to estimate the uncertainty of a value measured form this distribution.

MPPC

A Multi-Pixel Photon Counter (MPPC) aka silicon photomultiplier (SiPM) is a solid state photomultiplier comprised of a high density matrix of Geiger-mode-Avalanche-Photo-Diodes (G-APDs) .

MSE

The mean squared error (MSE) is a measurement of an estimator as the average of the squares of the errors: $\mathrm{MSE}(\hat{\theta}) = E_\theta\left[\left(\hat{\theta}-\theta\right)^2\right]$ with the estimator $\hat{\theta}$ and the unknown parameter θ.

neighbor pixel

pixels with Cherenkov photons in the neighborhood of core pixels, which are defining the outer fringe of a pixel cluster.

NKG

The Nishimura-Kamata-Greisen (NKG) formula is used by CORSIKA as lateral structure function for a pure electromagnetic cascade.

no moonlight

Data sample with light conditions in the range $(0-8)\,\mu A$ or $(0-2)\,\mathrm{NSB}_{\mathrm{Dark}}$.

NSB

The night sky background (NSB) aka light of the night sky (LONS) is referred as the combination of all light sources (e.g. star light, moonlight, etc.)that form a background to the desired astronomical observations.

`numIslands`

Number of islands - Shower image parametrization describing the number of separated clusters in the shower image.

ObsNSB

Observed night sky background superimposition - Newly developed simulation method for NSB for FACT that superimposes sampled random trigger events form real measurements and simulated air showers. The method was implemented within a Master's thesis in which it was called "Observed Background and Artificial Signal Superposition".

OFF-position

Location(s) with the same offset but at opposite locations as the source position in Wobble-Mode observations.

ON-position

Location of the source position in Wobble-Mode observations.

PDE

The photo detection efficiency first (PDE) is a measure for the sensitivity of an an silicon photomultiplier (SiPM). It is a function of wavelength, the applied over-voltage, and the fill factor.

PDF

probability density function (PDF).

p.e.

Unit of the number of photons, measured as a signal equivalent to a certain number of photons.

pedestal

Baseline measurement of a pixel's time series measured in a mode that triggers at a constant rate so mostly exclusively random photons are recorded but no Cherenkov photons. In time series with Cherenkov events, the pedestal refers to the underlying noise signal (including NSB) of the time series.

pedestal impurity

Fraction of surviving pedestals events compared to the number of triggered pedestal events after a certain analysis step, e.g., the image cleaning.

`ped_var`

Shower image parametrization: Variance of the signal of a pixel's time series in the integration window.

photon charge

Number of photons in in a camera pixel determined from the integrated signal of the time series.

PMMA

Polymethyl Methacrylate (PMMA), aka "plexiglass".

PMT

photomultiplier tubes (PMTs) aka photomultipliers are vacuum phototubes that use the photoelectric effect to transfer light into electricity by multiplying the current produced by incident light. They are extremely sensitive detectors of light in the ultraviolet, visible, and near-infrared range.

PSF

point spread function (PSF).

PWN

A pulsar wind nebula (PWN) aka plerion is the nebula of a supernova remnant (SNR) that is powered by pulsar winds generated by its pulsar, i.e., a central, highly magnetized, rotating neutron star.

python

Python is an interpreted, high-level, general-purpose programming language (*https://www.python.org*).

QGS-JETII

Hadronic MC generator for for high energy interactions, originally based on the Quark-Gluon String model.

random forest

Tree-based ensemble learning method for classification and regression.

recovery-time

Time after dead-time that is necessary to recharge a G-APD.

resolution

Standard deviation of the distribution of residuals $\frac{E_{Prediction}-E_{True}}{E_{True}}$.

right ascension

Angular distance measured eastwards along the celestial equator in the equatorial coordinate system.

ROC

The Receiver-Operator-Curve visualizes, e.g., the true positive rate (fraction of correctly predicted signals) versus the false positive rate (fraction of background events being incorrectly predicted as signals) by altering the prediction threshold of the evaluated model.

ROOT

C++ data analysis framework developed by CERN.

R^2-score

Indication for the goodness-of-fit and measure of how well data points are approximated by the regression predictions. Proportion of the variance in the dependent, predictable, true variable y from prediction f, calculated with: $R^2 = 1 - \frac{\sum_i (y_i - f_i)^2}{\sum_i (y_i - \bar{y})^2}$.

scikit-learn

The *scikit-learn* python package [89] is a free machine learning library.

SED

The spectral energy distribution (SED) visualizes the flux of emmited energy (or frequency) $E\Phi$ by an object as a function of the energy E at which it was emmitted. It is also interpreted as the power spectrum as it is a measure of the power observed at each frequency.

SiPM

SiPM: A solid-state (single) photon detector based on a matrix of single-photon avalanche diodes.

`size`

Shower image parametrization: Shower image parametrization: The total number of photons in the shower pixels.

slight moonlight

Data sample with light conditions in the range $(16-32)\,\mu A$ or $(4-8)\,NSB_{Dark}$.

supermassive black hole

super massive black hole.

SNR

A supernova remnant (SNR) is the general object that remains after the death of a star in an super nova explosion. It is determined by an expanding shock wave and consists of ejected material expanding from the explosion.

streams

streams is data stream analysis framework developed by Christian Bockermann at TU Dortmund University.

strong moonlight

Data sample with light conditions in the range $(64-96)\,\mu A$ or $(16-24)\,NSB_{Dark}$.

θ^2-plot

The distribution of the squared angular distance of reconstructed and actual source position (θ^2-plot) visualizes the distribution of gamma-like events with regard to the location of the (known) position of an gamma-ray source. It also contains the distribution of a remaining background as a (usually) flat underlying distribution.

`angular_distance` (θ)

Angular distance between reconstructed and actual source position.

two-level time-neighbor

The two-level time-neighbor cleaning is the common cleaning method used in FACT to cluster shower pixel, which is considering two thresholds in photon charge and demands a limited difference of the arrival time in neighbor pixels.

VERITAS

The Very Energetic Radiation Imaging Telescope Array System (VERITAS) is a ground-based gamma-ray observatory with an $4 \times 12\,m$ IACT array operating in the GeV –- TeV photon energy range. It is the successor of Whipple and is located at the Fred Lawrence Whipple Observatory on Mount Hopkins, Arizona, USA. The full array is operating since 2007.

VHE

Energy regime between 100 GeV and 100 TeV.

Whipple

The Whipple gamma-ray telescope was a 10 m diameter IACT at the Fred Lawrence Whipple Observatory on Mount Hopkins, Arizona, USA. It was pioneering the Imaging Atmospheric Cherenkov Technique (IACT) and was dismantled in 2013.

`width`

Shower image parametrization: Spacial expansion of the semi-minor axis of the shower's projection in the focal plane.

Wobble-Mode

off-axis measurements where the source position is not in camera center but located on one or several fixed position on a ring around the camera center.

XML

The Extensible Markup Language (XML) is used by *fact-tools* to define analysis processes outside of the compiled code.

Zodiacal light

Scattered sunlight from interplanetary dust particles in the ecliptic [15].

Bibliography

[1] B. Acharya et al. “Introducing the CTA concept”. *Astroparticle Physics* 43, 2013, pages 3–18. ISSN: 09276505.
DOI: 10.1016/j.astropartphys.2013.01.007.
https://linkinghub.elsevier.com/retrieve/pii/S0927650513000169.
Cited on p. 28.

[2] J. Adam et al. “Mirror position determination for the alignment of Cherenkov Telescopes”. *Nuclear Instruments and Methods in Physics Research Section A: Accelerators, Spectrometers, Detectors and Associated Equipment* 860, 2017, pages 1–5. ISSN: 0168-9002.
DOI: https://doi.org/10.1016/j.nima.2017.03.062.
http://www.sciencedirect.com/science/article/pii/S0168900217304217.
Cited on p. 18.

[3] F. A. Aharonian. “TeV gamma rays from BL Lac objects due to synchrotron radiation of extremely high energy protons”. *New Astronomy* 5:7, 2000, pages 377–395. ISSN: 1384-1076.
DOI: https://doi.org/10.1016/S1384-1076(00)00039-7.
http://www.sciencedirect.com/science/article/pii/S1384107600000397.
Cited on p. 6.

[4] F. A. Aharonian. *Very High Energy Cosmic Gamma Radiation: A Crucial Window on the Extreme Universe*. Vol. 2004. WORLD SCIENTIFIC, 2004, page 495. ISBN: 9812561730.
DOI: 10.1142/4657.
http://www.worldscientific.com/worldscibooks/10.1142/4657.
Cited on p. 11.

[5] F. A. Aharonian, P. Bhattacharjee, and D. N. Schramm. “Photon/proton ratio as a diagnostic tool for topological defects as the sources of extremely high-energy cosmic rays”. *Phys. Rev. D* 46:10, 1992, pages 4188–4192.
DOI: 10.1103/PhysRevD.46.4188.
https://link.aps.org/doi/10.1103/PhysRevD.46.4188.
Cited on p. 7.

[6] F. A. Aharonian et al. "The Crab Nebula and Pulsar between 500 GeV and 80 TeV: Observations with the HEGRA Stereoscopic Air Cerenkov Telescopes". *The Astrophysical Journal* 614:2, 2004, pages 897–913.
DOI: 10.1086/423931.
https://doi.org/10.1086/423931.
Cited on p. 66.

[7] M. Ahnen et al. "Data compression for the first G-APD Cherenkov Telescope". *Astronomy and Computing* 12, 2015, pages 191–199. ISSN: 2213-1337.
DOI: https://doi.org/10.1016/j.ascom.2015.06.007.
http://www.sciencedirect.com/science/article/pii/S2213133715000670.
Cited on pp. 38, 65, 70.

[8] M. Ahnen et al. "Performance of the MAGIC telescopes under moonlight". *Astroparticle Physics* 94, 2017, pages 29–41. ISSN: 0927-6505.
DOI: https://doi.org/10.1016/j.astropartphys.2017.08.001.
http://www.sciencedirect.com/science/article/pii/S092765051730110X.
Cited on pp. 2, 13–16, 24.

[9] J. Albert et al. "Observations of Markarian 421 with the MAGIC Telescope". *The Astrophysical Journal* 663:1, 2007, pages 125–138. ISSN: 0004-637X.
DOI: 10.1086/518221. ARXIV: 0603478 [astro-ph].
http://dx.doi.org/10.1086/518221.
Cited on p. 27.

[10] J. Aleksić et al. "Measurement of the Crab Nebula spectrum over three decades in energy with the MAGIC telescopes". *Journal of High Energy Astrophysics*, 2015. ISSN: 22144048.
DOI: 10.1016/j.jheap.2015.01.002. ARXIV: 1406.6892.
Cited on p. 126.

[11] J. Aleksić et al. "Performance of the MAGIC stereo system obtained with Crab Nebula data". *Astroparticle Physics* 35:7, 2012, pages 435–448. ISSN: 09276505.
DOI: 10.1016/j.astropartphys.2011.11.007.
http://linkinghub.elsevier.com/retrieve/pii/S0927650511002064.
Cited on pp. 54, 121.

[12] G. Ambrosi et al. "Characterization and possible astrophysics applications of UV sensitive SiPM devices". *Nuovo Cimento della Societa Italiana di Fisica C* 41:1-2, 2018. ISSN: 18269885.
DOI: 10.1393/ncc/i2018-18094-7.
http://prometeo.sif.it/papers/?pid=ncc11551.
Cited on p. 15.

[13] H. Anderhub et al. "Design and operation of FACT - the first G-APD Cherenkov telescope". *Journal of Instrumentation* 8:06, 2013, P06008–P06008. ISSN: 1748-0221.
DOI: 10.1088/1748-0221/8/06/P06008. ARXIV: arXiv:1304.1710v1.
http://iopscience.iop.org/1748-0221/8/06/P06008/.
Cited on pp. 14, 15, 18, 20, 23.

[14] S. Archambault et al. "Gamma-ray observations under bright moonlight with VERITAS". *Astroparticle Physics* 91, 2017, pages 34–43. ISSN: 0927-6505.
DOI: https://doi.org/10.1016/j.astropartphys.2017.03.001.
http://www.sciencedirect.com/science/article/pii/S0927650517300762.
Cited on pp. 2, 13–16, 24.

[15] C. Benn and S. Ellison. "Brightness of the night sky over La Palma". *New Astronomy Reviews* 42:6, 1998, pages 503–507. ISSN: 1387-6473.
DOI: 10.1016/S1387-6473(98)00062-1. ARXIV: 9909153 [astro-ph].
http://www.sciencedirect.com/science/article/pii/S1387647398000621.
Cited on pp. 12, 14, 217, 231.

[16] J. Beringer et al. (Particle Data Group Collaboration). "Review of Particle Physics". *Phys. Rev. D* 86, 1 2012, page 010001.
DOI: 10.1103/PhysRevD.86.010001.
https://link.aps.org/doi/10.1103/PhysRevD.86.010001.
Cited on p. 66.

[17] A. Biland et al. "FACT: status and experience from four years of operation of the first G-APD Cherenkov Telescope". In: *Ground-based and Airborne Telescopes VI*. Ed. by H. J. Hall, R. Gilmozzi, and H. K. Marshall. Vol. 9906. International Society for Optics and Photonics. SPIE, 2016, pages 486–492.
DOI: 10.1117/12.2232600.
https://doi.org/10.1117/12.2232600.
Cited on p. 15.

[18] A. Biland et al. “Calibration and performance of the photon sensor response of FACT — the first G-APD Cherenkov telescope”. *Journal of Instrumentation* 9:10, 2014, P10012–P10012.
DOI: 10.1088/1748-0221/9/10/p10012.
https://iopscience.iop.org/article/10.1088/1748-0221/9/10/P10012.
Cited on p. 40.

[19] A. Biland et al. “FACT: Towards Robotic Operation of an Imaging Air Cherenkov Telescope”, 2013.
ARXIV: 1307.7892.
https://arxiv.org/pdf/1307.7892.pdf%20http://arxiv.org/abs/1307.7892.
Cited on p. 28.

[20] V. Blobel and E. Lohrmann. “Statistische und numerische Methoden der Datenanalyse”. In: Teubner Studienbücher Physik. B. G. Teubner Stuttgart, Stuttgart, 1998. Chap. 5, page 358. ISSN: 1615-3766. ISBN: 978-3-519-03243-4.
DOI: 10.1007/978-3-663-05690-4.
Cited on pp. 35, 65, 225.

[21] C. Bockermann. “Mining Big Data Streams for Multiple Concepts”. PhD thesis. TU Dortmund University, 2015.
DOI: 10.17877/DE290R-16437.
http://hdl.handle.net/2003/34363.
Cited on pp. 37, 38.

[22] C. Bockermann and H. Blom. *The streams Framework*. Technical report. Version 0.9.6. Dortmund: Sonderforschungsbereich 876, TU Dortmund University, 2012.
DOI: 10.17877/DE290R-19178.
http://hdl.handle.net/2003/37182.
Cited on p. 37.

[23] C. Bockermann et al. “Online Analysis of High-Volume Data Streams in Astroparticle Physics”. In: *Machine Learning and Knowledge Discovery in Databases - European Conference, ECML PKDD 2015, Porto, Portugal, September 7-11, 2015, Proceedings, Part III*. Ed. by A. Bifet et al. Vol. 9286. Lecture Notes in Computer Science. Springer, 2015, pages 100–115.
DOI: 10.1007/978-3-319-23461-8_7.
https://link.springer.com/chapter/10.1007/978-3-319-23461-8_7.
Cited on pp. 36, 37.

[24] M. Börner. "Bestimmung des Energiespektrums von atmosphärischen Myonneutrinos mit 3 Jahren Daten des IceCube-Detektors". PhD thesis. TU Dortmund University, 2018.
DOI: 10.17877/DE290R-19089.
http://dx.doi.org/10.17877/DE290R-19089.
Cited on pp. 57, 58, 223.

[25] M. Börner and M. Nöthe. *funfolding. Python library to perform spectral unfoldings*. Python. GitHub.
https://pypi.org/project/funfolding/0.2.1/ visited on 09/07/2019.
Note: software repository.
Cited on p. 58.

[26] A. P. Bradley. "The use of the area under the ROC curve in the evaluation of machine learning algorithms". *Pattern Recognition* 30:7, 1997, pages 1145–1159. ISSN: 0031-3203.
DOI: 10.1016/S0031-3203(96)00142-2.
http://www.sciencedirect.com/science/article/pii/S0031320396001422.
Cited on p. 49.

[27] L. Breiman. "Random Forests". *Machine Learning* 45:1, 2001, pages 5–32. ISSN: 1573-0565.
DOI: 10.1023/A:1010933404324.
https://doi.org/10.1023/A:1010933404324.
Cited on pp. 45, 46.

[28] T. Bretz and D. Dorner. "MARS - CheObs ed. – A flexible Software Framework for future Cherenkov Telescopes". In: *Astroparticle, Particle and Space Physics, Detectors and Medical Physics Applications*. Ed. by C. Leroy et al. 2010, pages 681–687.
DOI: 10.1142/9789814307529_0111.
Cited on pp. 65, 67.

[29] T. Bretz et al. *Mars CheOps ed. C++ framework based on ROOT to analyse and simulate Cherenkov telescopes.* C++. SVN.
https://trac.fact-project.org/svn/trunk/Mars visited on 11/06/2019.
Note: software repository.
Cited on pp. 67, 68.

[30] T. Bretz, D. Dorner, F. A. Aharonian, W. Hofmann, and F. Rieger. "MARS — The Cherenkov Observatory edition". *AIP Conference Proceedings*, 2008, pages 664–667.
DOI: 10.1063/1.3076762.
http://scitation.aip.org/content/aip/proceeding/aipcp/10.1063/1.3076762.
Cited on pp. 65, 67.

[31] T. Bretz et al. "Long-term VHE γ-ray monitoring of bright blazars with a dedicated Cherenkov telescope". In: vol. 3. Universidad Nacional Autonoma de Mexico, 2008, pages 1495–1498. ISSN: 0000-2007.
https://indico.nucleares.unam.mx/event/4/session/40/contribution/974/material/paper/0.pdf.
Cited on pp. 1, 6, 27, 28.

[32] D. Britzger et al. "Studies of the Influence of Moonlight on Observations with the MAGIC Telescope". In: *Proceedings of the 31th International Cosmic Ray Conference (ICRC 2009)*. Lodz, Poland, 2009, pages 4–7.
ARXIV: 0907.0973.
http://arxiv.org/abs/0907.0973.
Cited on pp. 12, 81.

[33] K. A. Brügge et al. "FACT-Tools – Streamed Real-Time Data Analysis". In: *Proceedings of the 34th International Cosmic Ray Conference (ICRC 2015)*. The Hague, 2015.
DOI: 10.22323/1.236.0865.
Cited on p. 42.

[34] K. A. Brügge et al. *FACT-Tools. Extension to the streams framework to analyse data of the First G-APD Cherenkov Telescope.* Java. GitHub.
https://github.com/fact-project/fact-tools visited on 11/07/2019.
Note: software repository.
Cited on pp. 36, 38, 73.

[35] R. Bühler and R. Blandford. "The surprising Crab pulsar and its nebula: a review". *Reports on Progress in Physics* 77:6, 2014, page 066901.
DOI: 10.1088/0034-4885/77/6/066901. ARXIV: 1309.7046v3.
https://iopscience.iop.org/article/10.1088/0034-4885/77/6/066901.
Cited on p. 7.

[36] M. Bulinski. "OBASS Observed Background and Artifical Signal Superposition". MA thesis. Germany: TU Dortmund University, 2018.
https://nextcloud.e5.physik.tu-dortmund.de/index.php/s/6p7jsctcP5fE5wf.
Cited on pp. 70, 73.

[37] M. Bulinski and J. B. Buß. *EventList data base interface. Tools to create an event list data base, which works as an index for all of FACTs events.* Python. GitHub. 2018.
https://github.com/fact-project/EventList visited on 11/12/2019.
Note: software repository.
Cited on p. 73.

[38] S. Buschjäger, L. Pfahler, J. Buss, K. Morik, and W. Rhode. "On-Site Gamma-Hadron Separation with Deep Learning on FPGAs". In: *Joint European Conference on Machine Learning and Knowledge Discovery in Databases*. Springer, 2020.
Cited on p. 134.

[39] J. Buss et al. "FACT – Influence of SiPM Crosstalk on the Performance of an Operating Cherenkov Telescope". In: *Proceedings of the 34th International Cosmic Ray Conference (ICRC 2015)*. The Hague, 2015, page 863.
http://pos.sissa.it/cgi-bin/reader/conf.cgi?confid=236.
Cited on pp. 24, 69.

[40] M. Catanese. "Ground-Based Gamma-Ray Astronomy". *AIP Conference Proceedings* 510:1, 2000, pages 619–626.
DOI: 10.1063/1.1303276.
http://arxiv.org/abs/astro-ph/9911150.
Cited on p. 8.

[41] M. Catanese and T. C. Weekes. "Very High Energy Gamma-Ray Astronomy". *Publications of the Astronomical Society of the Pacific* 111:764, 1999, pages 1193–1222. ISSN: 0004-6280.
DOI: 10.1086/316435.
http://iopscience.iop.org/article/10.1086/316435.
Cited on p. 8.

[42] M. C. Chantell et al. "A hybrid version of the Whipple observatory's air Cherenkov imaging camera for use in moonlight". *Astroparticle Physics*, 1997. ISSN: 09276505.
DOI: 10.1016/S0927-6505(96)00055-2.
Cited on pp. 15, 16.

[43] M. Chantell et al. "Gamma-Ray Observations in Moonlight with the Whipple Atmospheric Cherenkov Hybrid Camera". In: *Proceedings of the 24th International Cosmic Ray Conference (ICRC 1995)*. Vol. 2. Rome, 1995, page 544.
http://articles.adsabs.harvard.edu/pdf/1995ICRC....2..544C.
Cited on p. 15.

[44] B. Degrange and G. Fontaine. "Introduction to high-energy gamma-ray astronomy". *Comptes Rendus Physique* 16:6-7, 2015, pages 587–599. ISSN: 1631-0705.
DOI: 10.1016/j.crhy.2015.07.003. ARXIV: 1604.05488.
http://www.sciencedirect.com/science/article/pii/S1631070515001292.
Cited on pp. 7, 120.

[45] N. Dinu et al. "Temperature and bias voltage dependence of the MPPC detectors". In: *IEEE Nuclear Science Symposuim & Medical Imaging Conference*. Vol. 1. Vol. 2 of. Ieee, 2010, pages 215–219. ISBN: 978-1-4244-9106-3.
DOI: 10.1109/NSSMIC.2010.5873750.
http://ieeexplore.ieee.org/lpdocs/epic03/wrapper.htm?arnumber=5873750.
Cited on p. 26.

[46] M. Doering, K. Bernloehr, G. Hermann, W. Hofmann, and H. Lampeitl. "Measurement of the Cherenkov light spectrum and of the polarization with the HEGRA-IACT-system". In: *Proceedings of International Cosmic Ray Conference (ICRC 2001)*. Hamburg, 2001.
ARXIV: astro-ph/0107149 [astro-ph].
Cited on p. 14.

[47] Y. Du and F. Retière. "After-pulsing and cross-talk in multi-pixel photon counters". *Nuclear Instruments and Methods in Physics Research Section A: Accelerators, Spectrometers, Detectors and Associated Equipment* 596:3, 2008, pages 396–401. ISSN: 0168-9002.
DOI: 10.1016/j.nima.2008.08.130.
http://www.sciencedirect.com/science/article/pii/S0168900208012643.
Cited on p. 26.

[48] S. Einecke. "The Data Mining Guide to the Galaxy: Active Galactic Nuclei in a Multi-Wavelength Context". PhD thesis. TU Dortmund University, 2017.
DOI: 10.17877/DE290R-18295.
Cited on pp. 5, 8.

[49] A. Fassò, A. Ferrari, J. Ranft, and P. R. Sala. "FLUKA: present status and future developments". In: *Proceedings of the 4th International Conference on Calorimetry in High-energy Physics*. Ed. by A. Menzione and A. Scribano. Vol. 9309194. World Scientific, 1993, pages 493–502.
http://www.fluka.org/content/publications/1993_elba.pdf.
Cited on p. 66.

[50] D. Foreman-Mackey et al. "emcee: The MCMC Hammer". *Publications of the Astronomical Society of the Pacific* 125:925, 2012, pages 306–312. ISSN: 00046280.
DOI: 10.1086/670067. ARXIV: 1202.3665.
http://dx.doi.org/10.1086/670067.
Cited on p. 58.

[51] I. Fredholm. "Sur une classe d'équations fonctionnelles". *Acta Mathematica* 27:1, 1903, pages 365–390. ISSN: 1871-2509.
DOI: 10.1007/BF02421317.
https://doi.org/10.1007/BF02421317.
Cited on p. 57.

[52] B. M. Gaensler and P. O. Slane. "The Evolution and Structure of Pulsar Wind Nebulae". *Annual Review of Astronomy and Astrophysics* 44:1, 2006, pages 17–47.
DOI: 10.1146/annurev.astro.44.051905.092528. ARXIV: astro-ph/0601081 [astro-ph].
Cited on p. 8.

[53] J. Goodman and J. Weare. "Ensemble samplers with affine invariance". *Communications in Applied Mathematics and Computational Science* 5:1, 2010, pages 65–80. ISSN: 21575452.
DOI: 10.2140/camcos.2010.5.65.
http://msp.org/camcos/2010/5-1/p04.xhtml.
Cited on p. 58.

[54] M. Grodzicka et al. "Effective dead time of APD cells of SiPM". In: *2011 IEEE Nuclear Science Symposium Conference Record*. 2012, pages 553–562. ISSN: 10957863. ISBN: 9781467301183.
DOI: 10.1109/NSSMIC.2011.6154111.
Cited on pp. 26, 27, 72.

[55] D. Guberman et al. "The Light-Trap: A novel concept for a large SiPM-based pixel for Very High Energy gamma-ray astronomy and beyond". *Nuclear Instruments and Methods in Physics Research, Section A: Accelerators, Spectrometers, Detectors and Associated Equipment* 923, 2019, pages 19–25. ISSN: 0168-9002.
DOI: 10.1016/j.nima.2019.01.052. ARXIV: 1901.05736.
http://www.sciencedirect.com/science/article/pii/S0168900219301056.
Cited on p. 134.

[56] C. Gueymard. "Updated transmittance functions for use in fast spectral direct beam irradiance models". In: vol. 6 of. San Jose, CA, 1994, pages 355–360.
https://www.researchgate.net/profile/Chris_Gueymard/publication/236314785_Updated_transmittance_functions_for_use_in_fast_spectral_direct_beam_irradiance_models/links/55d31b6f08ae7fb244f57eb1.pdf.
Cited on p. 14.

[57] C. Gueymard. *SMARTS2, A Simple Model of the Atmospheric Radiative Transfer of Sunshine: Algorithms and performance assessment Simple Model for the Atmospheric Radiative Transfer of Sunshine (SMARTS2) Algorithms and performance assessment*. Technical report.
http://www.fsec.ucf.edu/en/publications/pdf/fsec-pf-270-95.pdf.
Cited on p. 14.

[58] Hamamatsu. *MPPC (Multi-Pixel Photon Counter)*. Technical report. 2012.
http://www.hamamatsu.com.cn/UserFiles/DownFile/Related/20130812150251541.pdf.
Cited on pp. 23, 24.

[59] Hamamatsu. *MPPC (Multi-Pixel Photon Counter) S14160/S14161 series*. Technical report. 2019.
https://www.hamamatsu.com/resources/pdf/ssd/s14160_s14161_series_kapd1064e.pdf.
Cited on p. 15.

[60] T. Hastie, R. Tibshirani, and J. Friedman. *The Elements of Statistical Learning Data Mining, Inference, and Prediction*. 2nd ed. Springer, New York, 2017. ISBN: 978-0-387-84858-7.
DOI: 10.1007/978-0-387-84858-7.
https://web.stanford.edu/%7B~%7Dhastie/ElemStatLearn/printings/ESLII_print12.pdf.
Cited on pp. 45, 47, 48, 220.

[61] D. Heck, J. Knapp, J. N. Capdevielle, G. Schatz, and T. Thouw. *CORSIKA: a Monte Carlo code to simulate extensive air showers.* Technical report. 1998.
DOI: 10.5445/IR/270043064.
http://bibliothek.fzk.de/zb/abstracts/6019.htm.
Note: 51.02.03; LK 01; Wissenschaftliche Berichte, FZKA-6019 (Februar 98).
Cited on pp. 57, 65, 66.

[62] D. Heck and T. Pierog. *Extensive Air Shower Simulation with CORSIKA: A User's Guide.* Manual. 2013.
https://web.ikp.kit.edu/corsika/usersguide/corsika_tech.html.
Cited on pp. 66, 136.

[63] D. Hildebrand et al. "Using charged cosmic ray particles to monitor the data quality of FACT". In: *Proceedings of the 35th International Cosmic Ray Conference (ICRC2017).* Proceedings of Science, Busan, Korea, 2017. ISSN: 18248039.
DOI: 10.22323/1.301.0779.
https://doi.org/10.22323/1.301.0779.
Cited on p. 80.

[64] A. M. Hillas. "Cerenkov Light Images of EAS Produced by Primary Gamma Rays and by Nuclei". In: *19th International Cosmic Ray Conference (ICRC 1985), Volume 3.* Vol. 3. International Cosmic Ray Conference. 1985, page 445.
http://adsabs.harvard.edu/abs/1985ICRC....3..445H.
Cited on p. 43.

[65] J. Hinton. "Ground-based gamma-ray astronomy with Cherenkov telescopes". *New Journal of Physics* 11:5, 2008, page 055005.
DOI: 10.1088/1367-2630/11/5/055005. ARXIV: 0803.1609.
https://iopscience.iop.org/article/10.1088/1367-2630/11/5/055005.
Cited on p. 7.

[66] J. Holder. "TeV gamma-ray astronomy: A summary". *Astroparticle Physics* 39-40:1, 2012, pages 61–75. ISSN: 0927-6505.
DOI: 10.1016/j.astropartphys.2012.02.014. ARXIV: 1204.1267.
http://www.sciencedirect.com/science/article/pii/S0927650512000540.
Cited on p. 8.

[67] K. E. Jensen et al. "Afterpulsing in Geiger-mode avalanche photodiodes for 1.06μm wavelength". *Applied Physics Letters* 88, 2006, pages 1–4.
DOI: 10.1063/1.2189187.
https://doi.org/10.1063/1.2189187.
Cited on p. 26.

[68] J. Kildea et al. "The Whipple Observatory 10 m gamma-ray telescope, 1997-2006". *Astroparticle Physics* 28:2, 2007, pages 182–195. ISSN: 09276505.
DOI: 10.1016/j.astropartphys.2007.05.004.
http://www.sciencedirect.com/science/article/pii/S0927650507000746.
Cited on p. 1.

[69] H. V. Klapdor-Kleingrothaus and K. Zuber. *Teilchenastrophysik*. Teubner Studienbücher: Physik. Vieweg+Teubner Verlag, Wiesbaden, 1997. ISBN: 978-3-519-03094-2.
DOI: 10.1007/978-3-322-90548-2.
http://link.springer.com/10.1007/978-3-322-90548-2.
Cited on pp. 9, 11, 12.

[70] M. L. Knoetig et al. "FACT - Long-term stability and observations during strong Moon light". *Proceedings of the 33rd International Cosmic Rays Conference (ICRC 2013)* 2013-October, 2013.
ARXIV: 1307.6116.
https://arxiv.org/pdf/1307.6116.pdf.
Cited on pp. 15, 19, 24, 25, 28.

[71] D. Kranich et al. "TeV γ-ray observations of the Crab and Mkn 501 during moonshine and twilight". *Astroparticle Physics* 12:1-2, 1999, pages 65–74. ISSN: 0927-6505.
DOI: 10.1016/S0927-6505(99)00016-X. ARXIV: 9901330v1 [arXiv:astro-ph].
http://www.sciencedirect.com/science/article/pii/S092765059900016X.
Cited on pp. 13, 15, 16.

[72] H. Krawczynski et al. "Gamma-hadron separation methods for the VERITAS array of four imaging atmospheric Cherenkov telescopes". *Astroparticle Physics* 25:6, 2006, pages 380–390. ISSN: 0927-6505.
DOI: 10.1016/j.astropartphys.2006.03.011. ARXIV: 0604508 [astro-ph].
http://www.sciencedirect.com/science/article/pii/S0927650506000466.
Cited on p. 40.

[73] H. Krawczynski, Böttcher, Markus, and Reimer, Anita. "Unresolved Emission from the Core: Observations and Models". In: *Relativistic Jets from Active Galactic Nuclei*. Ed. by M. Böttcher, D. E. Harris, and H. Krawczynski. 1st ed. Wiley-VCH Verlag GmbH & Co. KGaA, Weinheim, Germany, 2012, pages 220–234. ISBN: 9783527641741.
DOI: 10.1002/9783527641741.
http://doi.wiley.com/10.1002/9783527641741.
Cited on p. 6.

[74] T.-P. Li and Y.-Q. Ma. "Analysis methods for results in gamma-ray astronomy". *The Astrophysical Journal* 272, 1983. ISSN: 0004-637X.
DOI: 10.1086/161295.
http://adsabs.harvard.edu/doi/10.1086/161295.
Cited on p. 54.

[75] MAGIC Collaboration and J. Albert. "Very high energy gamma-ray observations during moonlight and twilight with the MAGIC telescope", 2007.
ARXIV: astro-ph/0702475 [astro-ph].
http://arxiv.org/abs/astro-ph/0702475.
Cited on pp. 2, 13, 16.

[76] MAGIC Collaboration et al. "The major upgrade of the MAGIC telescopes, Part II: A performance study using observations of the Crab Nebula". *Astroparticle Physics* 72, 2016, pages 76–94. ISSN: 0927-6505.
DOI: 10.1016/j.astropartphys.2015.02.005. ARXIV: 1409.5594.
http://www.sciencedirect.com/science/article/pii/S0927650515000316.
Cited on pp. 55, 81, 83.

[77] K. Mannheim. "The proton blazar." *Astronomy and Astrophysics* 269, 1993, pages 67–76.
ARXIV: astro-ph/9302006 [astro-ph].
Cited on p. 6.

[78] N. Milke et al. "Solving inverse problems with the unfolding program TRUEE: Examples in astroparticle physics". *Nuclear Instruments and Methods in Physics Research, Section A: Accelerators, Spectrometers, Detectors and Associated Equipment* 697, 2013, pages 133–147. ISSN: 0168-9002.
DOI: 10.1016/j.nima.2012.08.105. ARXIV: 1209.3218.
http://www.sciencedirect.com/science/article/pii/S016890021201008X.
Cited on pp. 37, 57, 58, 225.

[79] R. Mirzoyan and E. Lorenz. *Measurement of The Night Sky Light Background at La Palma*. Technical report. 1994, pages 1–18.
http://www.astro.uni-wuerzburg.de/wikineu/images/8/85/MeasurementNSB.pdf.
Cited on p. 12.

[80] S. Müller et al. "Single Photon Extraction for FACT's SiPMs allows for Novel IACT Event Representation". In: *Proceedings of the 35th International Cosmic Ray Conference (ICRC 2017)*. Busan, South Korea, 2018, page 801. ISSN: 1824-8039.
DOI: 10.22323/1.301.0801.
https://pos.sissa.it/301/801/pdf.
Cited on p. 134.

[81] W. Nelson and Y. Namito. *The EGS4 Code System: Solution of gamma-ray and electron transport problems*. Technical report. 1990.
https://www.slac.stanford.edu/pubs/slacpubs/5000/slac-pub-5193.pdf.
Cited on p. 66.

[82] M. Nöthe. *fact-funfolding*. Python library to use the funfolding package for spectral unfoldings. Python. Version v0.3.3. GitHub.
https://github.com/fact-project/fact_funfolding visited on 11/05/2019.
Note: software repository.
Cited on pp. 59, 222.

[83] M. Nöthe. *Improving the Angular Resolution of FACT Using Machine Learning*. Technical report for Collaborative Research Center SFB 876 - Graduate School. TU Dortmund University, 2017, pages 171–174.
DOI: 10.17877/DE290R-19150.
https://sfb876.tu-dortmund.de/PublicPublicationFiles/sfbgk_etal_2017b.pdf.
Cited on pp. 44, 51.

[84] M. Nöthe, K. A. Brügge, and J. B. Buß. *aict-tools. Reproducible Artificial Intelligence for Cherenkov Telescopes*. Python. GitHub.
https://github.com/fact-project/aict-tools visited on 11/07/2019.
Note: software repository.
Cited on pp. 44, 217.

[85] S. Ostapchenko. "QGSJET-II: towards reliable description of very high energy hadronic interactions". In: *Nuclear Physics B - Proceedings Supplements*. Vol. 151. Vol. 1 of. 2016, pages 143–146. ISSN: 09205632.
DOI: 10.1016/j.nuclphysbps.2005.07.026.
https://linkinghub.elsevier.com/retrieve/pii/S0920563205009175.
Cited on p. 66.

[86] A. N. Otte et al. "Prospects of using silicon photomultipliers for the astroparticle physics experiments EUSO and MAGIC". *IEEE Transactions on Nuclear Science* 53:2, 2006, pages 636–640. ISSN: 0018-9499.
DOI: 10.1109/TNS.2006.870575.
http://ieeexplore.ieee.org/lpdocs/epic03/wrapper.htm?arnumber=1621377.
Cited on pp. 2, 24.

[87] A. N. Otte. "Observation of VHE Gamma-Rays from the Vicinity of magnetized Neutron Stars and Development of new Photon-Detectors for Future Ground based Gamma-Ray Detectors". PhD thesis. München: Fakultät für Physik, 2007.
http://nbn-resolving.de/urn/resolver.pl?urn:nbn:de:bvb:91-diss-20070924-620881-1-0.
Cited on p. 41.

[88] P. Padovani et al. "Active Galactic Nuclei: what's in a name?" *The Astronomy and Astrophysics Review* 25:1, 2017, page 2. ISSN: 0935-4956.
DOI: 10.1007/s00159-017-0102-9. ARXIV: 1707.07134.
http://dx.doi.org/10.1007/s00159-017-0102-9.
Cited on pp. 6, 7.

[89] F. Pedregosa et al. "Scikit-learn: Machine Learning in Python". *Journal of Machine Learning Research* 12, 2011, pages 2825–2830.
ARXIV: 1201.0490.
http://arxiv.org/abs/1201.0490.
Cited on pp. 44, 229.

[90] W. H. Press, S. A. Teukolsky, W. T. Vetterling, and B. P. Flannery. *Numerical Recipes 3rd Edition: The Art of Scientific Computing*. Third Edition. Cambridge University Press, USA, 2007. ISBN: 978-0-521-88068-8.
www.cambridge.org/9780521880688.
Cited on p. 68.

[91] S. Preuß, G. Hermann, W. Hofmann, and A. Kohnle. "Study of the photon flux from the night sky at La Palma and Namibia, in the wavelength region relevant for imaging atmospheric Cherenkov telescopes". *Nuclear Instruments and Methods in Physics Research Section A: Accelerators, Spectrometers, Detectors and Associated Equipment* 481:1-3, 2002, pages 229–240. ISSN: 01689002.
DOI: 10.1016/S0168-9002(01)01264-5.
http://www.sciencedirect.com/science/article/pii/S0168900201012645.
Cited on p. 12.

[92] G. Pühlhofer, O. Bolz, N. Goetting, and t. H. Collaboration. "The Technical Performance of the HEGRA System of Imaging Air Cherenkov Telescopes". *Astroparticle Physics* 20:3, 2003, pages 267–291. ISSN: 0927-6505.
DOI: 10.1016/j.astropartphys.2003.06.001.
http://www.sciencedirect.com/science/article/pii/S0927650503001944.
Cited on pp. 54, 111.

[93] D. Renker. "Geiger-mode avalanche photodiodes for Cherenkov detectors". *Journal of Instrumentation* 5:01, 2010, P01001–P01001.
DOI: 10.1088/1748-0221/5/01/P01001.
https://iopscience.iop.org/article/10.1088/1748-0221/5/01/P01001/pdf.
Cited on p. 26.

[94] D. Renker. "New trends on photodetectors". *Nuclear Instruments and Methods in Physics Research, Section A: Accelerators, Spectrometers, Detectors and Associated Equipment* 571:1-2 SPEC. ISS. 2007, pages 1–6. ISSN: 0168-9002.
DOI: 10.1016/j.nima.2006.10.016.
Cited on pp. 23–26.

[95] D. Renker and E. Lorenz. "Advances in solid state photon detectors". *Journal of Instrumentation* 4:4, 2009, P04004–P04004. ISSN: 17480221.
DOI: 10.1088/1748-0221/4/04/P04004.
https://iopscience.iop.org/article/10.1088/1748-0221/4/04/P04004.
Cited on pp. 24, 26, 72.

[96] J. Rico. "Overview of MAGIC results". In: vol. 273-275. 2016, pages 328–333. ISSN: 2405-6014.
DOI: 10.1016/j.nuclphysbps.2015.09.046.
http://www.sciencedirect.com/science/article/pii/S2405601415005350.
Cited on p. 7.

[97] S. Ritt. "Design and performance of the 6 GHz waveform digitizing chip DRS4". In: *2008 IEEE Nuclear Science Symposium Conference Record*. Ieee, 2008, pages 1512–1515. ISSN: 10823654. ISBN: 9781424427147.
DOI: 10.1109/NSSMIC.2008.4774700.
http://ieeexplore.ieee.org/lpdocs/epic03/wrapper.htm?arnumber=4774700.
Cited on p. 22.

[98] G. Romeo, G. Bonanno, G. Sironi, and M. C. Timpanaro. "Novel silicon photomultipliers suitable for dual-mirror small-sized telescopes of the Cherenkov telescope array". *Nuclear Instruments and Methods in Physics Research Section A: Accelerators, Spectrometers, Detectors and Associated Equipment* 908, 2018, pages 117–127. ISSN: 0168-9002.
DOI: 10.1016/j.nima.2018.08.035. ARXIV: 1806.00703.
http://www.sciencedirect.com/science/article/pii/S0168900218309884.
Cited on p. 15.

[99] T. Ruhe, D. Elsässer, W. Rhode, M. Nöthe, and K. Brügge. "Cherenkov Telescope Ring - An Idea for World Wide Monitoring of the VHE Sky". *EPJ Web Conf.* 207, 2019, page 03002.
DOI: 10.1051/epjconf/201920703002.
https://doi.org/10.1051/epjconf/201920703002.
Cited on pp. 1, 27, 28.

[100] T. F. Temme. "On the Hunt for Photons : Analysis of Crab Nebula Data obtained by the First G-APD Cherenkov Telescope". PhD thesis. TU Dortmund University, 2016.
DOI: 10.17877/DE290R-17773.
https://eldorado.tu-dortmund.de/handle/2003/35745.
Cited on pp. 44, 126.

[101] M. Urban et al. "The use of an ultra-violet camera in the atmospheric Cherenkov technique". *Nuclear Instruments and Methods in Physics Research, Section A: Accelerators, Spectrometers, Detectors and Associated Equipment* 368:2, 1996, pages 503–511. ISSN: 0168-9002.
DOI: 10.1016/0168-9002(95)00694-X.
http://www.sciencedirect.com/science/article/pii/016890029500694X.
Cited on pp. 15, 16.

[102] P. E. Vogler. "Design and commissioning of the trigger electronics for a novel Geiger-mode avalanche photodiode based camera for Imaging Atmospheric Cherenkov Telescopes". PhD thesis. ETH-Zürich, 2015.
DOI: 10.3929/ETHZ-A-010568419.
Cited on p. 20.

[103] R. M. Wagner. "Measurement of Very High Energy Gamma-Ray Emission from Four Blazars Using the MAGIC Telescope and a Comparative Blazar Study". PhD thesis. Munich, Tech. U., 2007, pages 1201–1203.
DOI: 10.1086/522380.
https://iopscience.iop.org/article/10.1086/522380.
Cited on pp. 55, 56.

[104] T. C. Weekes et al. "Atmospheric Cherenkov Gamma-Ray Observations Under Bright Moon Conditions". In: *Bulletin of the American Astronomical Society*. Vol. 18. 1986, page 700.
https://ui.adsabs.harvard.edu/abs/1986BAAS...18..700W.
Note: Provided by the SAO/NASA Astrophysics Data System.
Cited on p. 15.

[105] T. Weekes. *Very High Energy Gamma-Ray Astronomy*. CRC Press, Boca Raton, Florida, USA, 2003, page 221. ISBN: 9780429093241.
DOI: 10.1201/9781420033199.
https://doi.org/10.1201/9781420033199.
Cited on pp. 7, 9, 11, 12.

[106] D. Xu. "Exploring the Universe with Neutrinos: Recent Results from IceCube". *Nuclear and Particle Physics Proceedings* 287-288, 2017, pages 139–142. ISSN: 24056014.
DOI: 10.1016/j.nuclphysbps.2017.03.062. ARXIV: 1702.05244 [astro-ph.HE].
https://linkinghub.elsevier.com/retrieve/pii/S2405601417301311.
Cited on p. 6.

[107] K. Yamamoto et al. "Development of Multi-Pixel Photon Counter (MPPC)". In: *IEEE Nuclear Science Symposium Conference Record*. 2007, pages 1511–1515. ISBN: 978-1-4244-0922-8.
DOI: 10.1109/NSSMIC.2007.4437286.
http://ieeexplore.ieee.org/lpdocs/epic03/wrapper.htm?arnumber=4437286.
Cited on pp. 23–25.

Acknowledgements

The research and preparation of this dissertation was a challenging task that could hardly have been accomplished without the support and help of a number of persons. I am therefore deeply grateful to all of them for their valuable support.

First of all, I would like to thank Prof. Dr. Dr. Wolfgang Rhode for allowing me the opportunity of being part of his research group and, by this, diving into the fascinating fields of astroparticle physics and machine learning. I am grateful for years of support, encouragement, and gentle pressure as well as creative ideas for overcoming obstacles on my way.

Furthermore, I would like to thank Prof. Dr. Bernhard Spaan for his time and effort, he being the second assessor of my dissertation.

I am thankful for my colleges in the astroparticle physics group E5b (my old home) and the computer science group LS8 (my new home). I am appreciative of all the discussions we had and times shared on- and off-topic aswell as all of your valuable constructive critique. A special thank goes to Dr. Kai Brügge and Dr. Maximilian Nöthe for our friendship and companionship helping each other to stay sane, in fact.

Furthermore, I would like to thank Andrea Teichmann for her endless (administrative) support, encouragement, and lovely attitude. I am grateful for the (technical) support by Matthias Domke and Kai Warda and the opportunity to learn from them. A huge thank goes to Claudia von der Heyden for having my back at LS8, taking off weight from my shoulders so I could go the final last miles.

I thank the FACT collaboration for bringing to live such a fascinating and challenging project as FACT. I have learned a lot in this project, in many ways that I could not have imagined.

I would also like to thank the SFB 876 and project C3 in particular for the opportunity of a cross-domain collaboration, a glimpse into machine learning and other disciplines.Part of the work on this dissertation has been supported by Deutsche Forschungsgemeinschaft (DFG) - project number 124020371 - within the Collaborative Research Center SFB 876 “Providing Information by Resource-Constrained Analysis”, DFG project number 124020371, SFB project C3.

A big thank goes to Christian Bockermann for our fruitful collaboration in C3 and his mentoring.

Special thanks goes out to Prof Dr. Katharina Morik for letting me become part of her research group, her advice and guidance, and for giving me a new job opportunity.

Special thanks goes also to Dr. Stefan Michaelis for his mentorship in many different ways.

I am deeply grateful to Dr. Wendy Kopisch, Dr. Kai Brügge, Dr. Dominik Elsäßer, Lena Linnhoff, Mirko Bunse, and my wife Karina for proofreading my dissertation.

My deepest gratitude goes to my friends and family, especially to my wife and daughters, for their support and also their patience. I am blessed to have them.